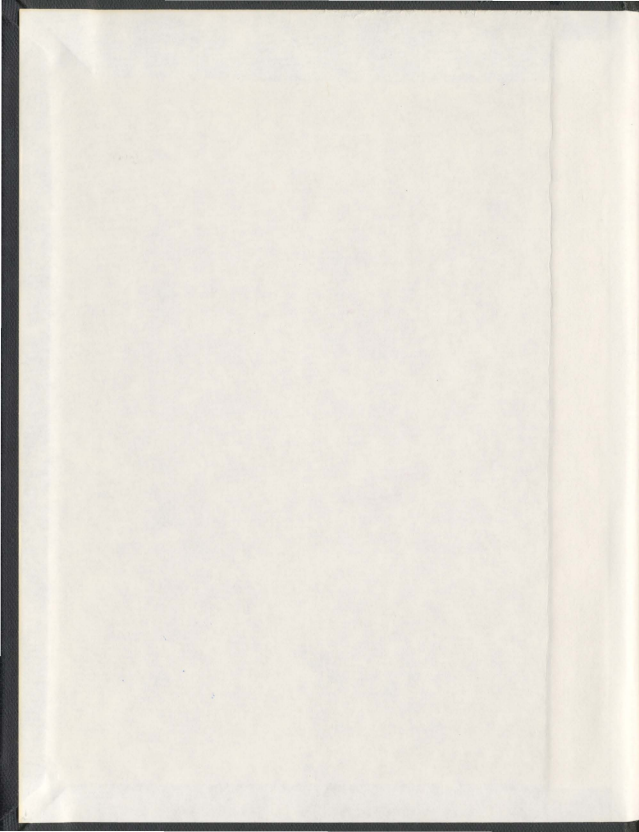


STRUCTURES OF BARE AND HYDRATED [AMINOACID-H]⁺
COMPLEXES DETERMINED BY INFRARED MULTIPLE
PHOTON DISSOCIATION SPECTROSCOPY

MICHAEL BURT



001311

**Structures of Bare and Hydrated $[M(\text{AminoAcid-H})]^+$
Complexes Determined by Infrared Multiple Photon
Dissociation Spectroscopy**

by

© Michael Burt

A thesis submitted to the
School of Graduate Studies
in partial fulfillment of the
requirements for the degree of
Doctor of Philosophy

Department of Chemistry
Memorial University of Newfoundland

September 2012

St. John's

Newfoundland

Abstract

Infrared multiple photon dissociation (IRMPD) spectroscopy was used to reveal the gas-phase structures of $[\text{Pb}(\text{AminoAcid-H})]^+$ complexes with and without a solvent molecule. The IRMPD-determined structures were supported by computed infrared spectra created from B3LYP/6-31+G(d,p) optimized geometries, and by MP2(full)/6-311++G(2d,2p)-derived 298 K enthalpies and Gibbs energies. Seven amino acid (Aa) complexes with nonpolar side chains (Ala, Val, Leu, Ile, Phe, Met and Pro) and two with polar side chains (Lys and Glu) were compared. The bare complexes adopt four isomers: A- and B-type complexes, where Pb^{2+} binds between the amine nitrogen and carbonyl oxygen of an amine- or carboxyl-deprotonated amino acid respectively; C-types, where Pb^{2+} forms a carboxylate salt with the amino acid; and D-types, which have Pb^{2+} bound to the amino acid side chain. The $[\text{Pb}(\text{Aa-H})\text{H}_2\text{O}]^+$ ions are generally the hydrated analogues of the $[\text{Pb}(\text{Aa-H})]^+$ complexes where water binds to Pb^{2+} . The water molecule remains intact in the B- and C-type structures, but the A-type complexes are the result of a proton shift, confirmed using H_2^{18}O , from the water to the deprotonated amine group. The water binding energies of the $[\text{Pb}(\text{Aa-H})]^+$ complexes were also determined using blackbody infrared radiative dissociation (BIRD), and their relative strengths reflect the structures of the $[\text{Pb}(\text{Aa-H})\text{H}_2\text{O}]^+$ complexes. To develop a broader understanding of $[\text{M}(\text{Aa-H})]^+$ ions, a series of $[\text{M}(\text{Ala-H})]^+$ and $[\text{M}(\text{BMAA-H})]^+$ complexes ($\text{M} = \text{Be}^{2+}$, Mg^{2+} , Ca^{2+} , Sr^{2+} , Ba^{2+} , Zn^{2+} , and Pb^{2+}) were also examined. This research demonstrates that these ions may adopt different tautomers from the $[\text{Pb}(\text{Aa-H})]^+$ complexes, indicating that the hardness and size of the metal cation dictates the ion's structure.

Acknowledgements

Many people encouraged or assisted me in the preparation of this thesis, but I particularly want to acknowledge my supervisor, Dr. Travis Fridgen, who gave me the freedom to choose the direction of our research. This responsibility helped me develop as a young scientist, and taught me to ask critical questions about my own work. The independence that Travis gave me has made him more of a friend than a supervisor, and contributed to a positive research environment. I am also grateful to past and present members of his research group; Chad Atkins, Sarah Decker, Ashley Power, Elizabeth Gillis, Ameneh Gholami, Maryam Moghaddam, and others, provided helpful comments about the research contained in this work and sat through several of my practice seminars. Additional thanks go to Sarah and Ashley, who assisted me with research throughout their undergraduate studies, and to Chad, who has been a valued friend since we worked together in Dr. Terry McMahon's group at the University of Waterloo. Our wide-ranging conversations were a highlight of my graduate program.

There are several members of the Department of Chemistry at Memorial University that also deserve special mention. I benefited from the advice of my supervisory committee members, Dr. Bob Davis and Dr. Peter Warburton, on the preparation of this thesis. Bob and Peter were also my physical chemistry instructors as an undergraduate, and I have always appreciated their friendliness and ability to apply chemistry to more lighthearted circumstances. Dr. Louise Dawe supervised me as part of the Graduate Program in Teaching. Louise is a committed educator, and I learned a great deal by teaching with her. Dr. Christopher Flinn, Dr. Christina Bottaro, and my external

examiner, Dr. Paul Mayer, helped improve this thesis with their careful attention and insightful questions. I am thankful for the fresh perspective they gave me.

I have always been fortunate to be surrounded by people that have encouraged my pursuits. Jonathan Thibault has been my closest friend for more than ten years, and has always provided a practical counterbalance for my musings. Conversations with Jon are always valuable; he has a directness that can be rare in academia, and it may be for the best that he chose engineering while I stuck to chemistry. My parents, Brian and Beverley, have always pushed me to achieve my goals, and as a consequence of having perhaps helped a bit too much, have spent the last few years trying to get me to relax. Their love and support has never gone unnoticed, or unfelt. I am also thankful for my younger brother Max, who has made it a goal to force me to take things less seriously, and for my grandparents who, like the rest of my family, have encouraged a sense of honesty within me that has greatly helped my growth as a man and a scientist. My deepest thanks go to Meghan, the love of my life. She has never failed to be supportive as long as we have been together, and has had limitless patience with me during the preparation of this thesis. I cannot imagine a better companion.

It never occurred to me that I would spend my formative years studying the chemistry of small molecules. I have always preferred explaining natural phenomena as a function of physical or mathematical abstractions, and came to university expecting to learn physics. That I chose to become a physical chemist is a testament to the quality (and tenacity) of my teachers. Those listed above have greatly helped me throughout my education, and many have proofread this thesis. If there remain errors, they are mine.

For Meghan and my family.

“Any road followed precisely to its end leads precisely nowhere. Climb the mountain just a little bit to test that it's a mountain. From the top of the mountain, you cannot see the mountain.”

Frank Herbert (1920 – 1986)

Table of Contents

Abstract	ii
Acknowledgements	iii
Table of Contents	vii
List of Tables	xi
List of Figures	xii
List of Symbols or Abbreviations	xxiii
List of Appendices	xxix
Co-authorship Statement	xxx

Chapter 1

Introduction	1
1.1. General Introduction	1
1.2. Determining the Structures of Biological Ions Using Mass Spectrometry	4
1.2.1. Amino Acids	12
1.2.2. Polypeptides and Proteins	18
1.2.3. Nucleobases and Nucleobase Pairs	22
1.2.4. Nucleobase Macroclusters	34
1.3. Motivation for Studying Lead(II)-Cationized Amino Acids	40
1.3.1. Lead Toxicity	41
1.3.2. Lead Chemistry	42
1.4. Objectives	45
References	47

Chapter 2

Experimental and Theory	54
2.1. Introduction	54
2.2. Instrumentation	55
2.2.1. Electrospray Ionization	55

2.2.2. Fourier Transform Ion Cyclotron Resonance Mass Spectrometry	60
2.2.3. Optical Parametric Oscillators	70
2.3. Experimental	73
2.3.1. Infrared Multiple Photon Dissociation Spectroscopy	75
2.3.2. Blackbody Infrared Radiative Dissociation	77
2.3.3. Sustained Off-Resonance Irradiation Collision-Induced Dissociation	81
2.4. Calculations	84
2.4.1. Electronic Structure Calculations	86
2.4.2. Master Equation Modeling	93
References	97

Chapter 3

Structures of bare and hydrated [Pb(AminoAcid-H)]⁺ complexes determined by infrared multiple photon dissociation spectroscopy	103
3.1. Introduction	103
3.2. Methods	107
3.2.1. IRMPD Spectroscopy	107
3.2.2. Calculations	109
3.3. Results and Discussion	110
3.3.1. Comparison of [Pb(Aa-H)] ⁺ and [Pb(Aa-H)H ₂ O] ⁺ Infrared Spectra.	110
3.3.2. [Pb(Ala-H)] ⁺ and [Pb(Ala-H)H ₂ O] ⁺	114
3.3.3. [Pb(Val-H)] ⁺ , [Pb(Leu-H)] ⁺ , [Pb(Ile-H)] ⁺ and their Monohydrated Analogues.	124
3.3.4. [Pb(Pro-H)] ⁺ and [Pb(Pro-H)H ₂ O] ⁺	129
3.3.5. [Pb(Lys-H)] ⁺ and [Pb(Lys-H)H ₂ O] ⁺	135
3.4. Conclusions: Pb²⁺ Stabilization by Amino Acid Conjugate Bases	142
References	144

Chapter 4

Gas-phase Structures of Pb²⁺ Cationized Phenylalanine and Glutamic Acid Determined by Infrared Multiple Photon Dissociation Spectroscopy and Computational Chemistry	149
4.1. Introduction	149
4.2. Methods	152
4.2.1. IRMPD Spectroscopy.....	152
4.2.2. Calculations.....	154
4.3. Results and Discussion	155
4.3.1. IRMPD Spectroscopy of [Pb(Aa-H)] ⁺ and [Pb(Aa-H)H ₂ O] ⁺	155
4.3.2. [Pb(Phe-H)] ⁺ and [Pb(Phe-H)H ₂ O] ⁺	158
4.3.3. [Pb(Glu-H)] ⁺ and [Pb(Glu-H)H ₂ O] ⁺	163
4.4. Conclusions	172
References	174

Chapter 5

Water Binding Energies of [Pb(AminoAcid-H)H₂O]⁺ Complexes Determined by Blackbody Infrared Radiative Dissociation	178
5.1. Introduction	178
5.2. Methods	182
5.2.1. BIRD Kinetic Measurements.....	182
5.2.2. Calculations.....	183
5.2.3. Master Equation Modeling.....	185
5.3. Results and Discussion	187
5.3.1. BIRD Kinetic Data.....	187
5.3.2. Arrhenius Parameters.....	189
5.3.3. Master Equation Modeling.....	192
5.3.4. Factors Affecting [Pb(Aa-H)H ₂ O] ⁺ Dissociation.....	195
5.3.4.1. Pb ²⁺ Stabilization by Amino Acid Conjugate Bases.....	195

5.3.4.2. Amino Acid Gas-Phase Basicity.....	199
5.3.5. Electrospray Solvents	202
5.4. Conclusions	203
References	207

Chapter 6

Gas-phase Structures of M^{2+}-Cationized Alanine and β-methylaminoalanine Investigated by Computational Chemistry and IRMPD Spectroscopy.....	212
6.1. Introduction.....	212
6.2. Methods.....	215
6.2.1. Ion Generation and Activation.....	215
6.2.2. Calculations.....	217
6.3. Results and Discussion.....	217
6.3.1. IRMPD Spectroscopy of $[M(\text{Ala-H})]^+$, $[M(\text{Ala-H})\text{H}_2\text{O}]^+$, and $[M(\text{BMAA-H})]^+$	217
6.3.2. Computational Comparisons of $[M(\text{Ala-H})]^+$ and $[M(\text{BMAA-H})]^+$ Complexes.....	220
6.3.3. Computed Structures of $[\text{Ba}(\text{BMAA-H})\text{H}_2\text{O}]^+$	230
6.4. Conclusions.....	232
References	234

Chapter 7

Summary.....	237
7.1. Overview	237
7.2. Future and Current Projects	240
Appendices.	244
VITA.....	286

List of Tables

Table 5.1. Measured $[\text{Pb}(\text{Aa-H})\text{H}_2\text{O}]^+$ Zero-Pressure Arrhenius Parameters	193
Table 5.2. Threshold Dissociation Energies	194
Table 5.3. Master Equation Arrhenius Pre-exponential Factors	197
Table 5.4. The Effect of Amino acid Basicity on Bond Lengths Around the Pb^{2+} Binding Site	201
Table 5.5. Measured E_0 in Different Electrospray Solvent Systems.....	204
Table C1. Vibrational Frequencies and Intensities of H_2O	263
Table C2. Observed Dissociation Rate Constants	264

List of Figures

- Figure 1.1.** Single-crystal X-ray structures of B-DNA and Z-DNA represented by skeletal (top) and space-filling (bottom) illustrations. B-DNA is a right-handed double helix that comprises ten base pairs per turn. By contrast, Z-DNA is left-handed and has twelve base pairs per turn. Figure adapted with permission from *Science* **1982**, 216, 475 – 485..... 3
- Figure 1.2.** The IRMPD spectrum of $[\text{Pb}(\text{Gly-H})]^+$ compared with three computed IR spectra. The computed spectra are determined from the B3LYP/6-31+G(d,p) optimized structures of Gly-A, -B, and -C. The 298 K relative enthalpies (in parentheses) were determined by the MP2/6-311++G(2d,p)//B3LYP/6-31+G(d,p) method and have units of kJ mol^{-1} . In both cases, the LANL2DZ basis set with effective core potential was applied to Pb^{2+} . Figure adapted with permission from *J. Phys. Chem. B* **2009**, 113, 14457 – 14464 7
- Figure 1.3.** A) The energy required to add successive water molecules to $[\text{M}(\text{H}_2\text{O})_n]^{2+}$ complexes. B) Arrhenius plots for the dissociation of $[\text{M}(\text{H}_2\text{O})_n]^{2+}$ complexes where $n = 4 - 7$. Complexes involving Mg^{2+} , Ca^{2+} , Sr^{2+} , and Ba^{2+} are indicated by \circ , \blacksquare , \bullet , and Δ respectively. The Arrhenius plot of $[\text{Mg}(\text{H}_2\text{O})_6]^{2+}$ exhibits an abrupt change in slope near 350 K, indicating that it has two temperature-dependent isomers. Figures adapted with permission from *Mass. Spectrom. Rev.* **2004**, 23, 127 – 158 and *J. Am. Chem. Soc.* **1999**, 121, 8898 – 8906..... 10
- Figure 1.4.** The generalized structures of canonical and zwitterionic amino acids. 13
- Figure 1.5.** The canonical tautomers of the ten amino acids investigated in this thesis .. 14
- Figure 1.6.** The IRMPD spectrum of $[\text{M}(\text{Ser})]^+$ ($\text{M}^+ = \text{Li}^+, \text{Na}^+, \text{K}^+, \text{Cs}^+, \text{and Rb}^+$) between $500 - 1800 \text{ cm}^{-1}$. The bands at $980, 1150, \text{and } 1230 \text{ cm}^{-1}$ (the side-chain CO stretch, NH_2 bend, and concerted COH bends, respectively) are indicative of structure A, whereas peaks at 1400 (carboxylic acid O-H bend) and 1680 cm^{-1} (the carboxylate anion CO stretch) are diagnostic of structures B and C, respectively. Figure adapted with permission from *J. Phys. Chem. A* **2008**, 112, 2248 – 2257..... 17
- Figure 1.7.** The IRMPD spectrum of $[\text{H}(\text{Leu-enkephalin})]^+$ compared with the computed IR spectra (bold lines) derived from the B3LYP/6-31+G(d,p) optimized structures of LE1 and LE2. Figure adapted with permission from *J. Am. Chem. Soc.* **2007**, 129, 5887 – 5897..... 19

Figure 1.8. The IRMPD spectrum (red) of cytochrome c. The blue lines are the smoothed averages of multiple scans. As the charge state increases, there is a noticeable blue shift in the band at $\sim 1660\text{ cm}^{-1}$, as well as the appearance of a band at 1480 cm^{-1} . Figure adapted with permission from *Mass Spectrom. Rev.* **2009**, *28*, 468 – 494 23

Figure 1.9. Numbering schemes for the canonical DNA and RNA nucleobases. 24

Figure 1.10. The IRMPD spectra for three $[\text{Li}(\text{B})\text{H}_2\text{O}]^+$ complexes (B = A, U, and T). **U1**, **T1**, and **A1** are the lowest Gibbs energy structures according to the MP2/6-311++G(2d,p)//B3LYP/6-31+G(d,p) method that best reflect the experimental data (* represents the location of thymine's methyl group). Figure adapted and reprinted with permission from *J. Phys. Chem. A* **2010**, *114*, 3449 – 3456 and *J. Phys. Chem. A* **2009**, *113*, 824 – 832..... 26

Figure 1.11. The IRMPD spectra (black) for three $[\text{Li}(\text{B})_2]^+$ and three $[\text{Li}(\text{B})_2\text{H}_2\text{O}]^+$ complexes (B = A, U, and T). **UU1**, **TT1**, and **AA1** are the lowest Gibbs energy structures according to the MP2/6-311++G(2d,p)//B3LYP/6-31+G(d,p) method that best reflect the experimental data. The computed IR spectra (red) for the lowest energy structures are also shown. Figure adapted and reprinted with permission from *J. Phys. Chem. A* **2010**, *114*, 3449 – 3456 and *J. Phys. Chem. A* **2009**, *113*, 824 – 832. 28

Figure 1.12. The addition of water to $[\text{Li}(\text{U})_2]^+$ strengthens the $\text{O4}_{\text{Ua}}\text{-N3}_{\text{Ub}}$ and $\text{N3}_{\text{Ua}}\text{-O2}_{\text{Ub}}$ hydrogen bonds by relaxing the uracil dimer. **UU2** is similar in enthalpy to **UU1** in Figure 1.10. Figure reprinted with permission from *Eur. J. Mass Spectrom.* **2012**, *18* (2), 235 – 250 30

Figure 1.13. The IRMPD spectrum of $[\text{Li}(\text{AT})\text{H}_2\text{O}^+]$ compared with two computed IR spectra calculated using B3LYP/6-31+G(d,p). **AT1** (red) is more energetically and enthalpically favourable than **AT2** (purple). The reported energies were determined using the MP2/6-311++G(2d,p)//B3LYP/6-31+G(d,p) method and are written as $\Delta\text{G}/\Delta\text{H}$. All units are in kJ mol^{-1} . Figure adapted with permission from *Int. J. Mass Spectrom.* **2010**, *297*, 2 – 8 32

Figure 1.14. SORI/CID spectra of the $[\text{Mg}(\text{Ura-H})(\text{Ura})]^+$, $[\text{Ca}(\text{Ura-H})(\text{Ura})]^+$, $[\text{Sr}(\text{Ura-H})(\text{Ura})]^+$, and $[\text{Ba}(\text{Ura-H})(\text{Ura})]^+$ complexes with a SORI power of 0.656 eV. Figure adapted with permission from *ChemPhysChem* **2012**, *13*, 1507 – 1513. 35

Figure 1.15. The IRMPD spectra of $[\text{Ca}(\text{U})_{10}]^{2+}$, $[\text{Ca}(\text{U})_{11}]^{2+}$, $[\text{Ca}(\text{U})_{12}]^{2+}$, and $[\text{Ca}(\text{U})_{14}]^{2+}$ in the N-H/O-H stretching region and $[\text{Ca}(\text{U})_{12}]^{2+}$ in the CO stretch/HCN bending region. The computed IR spectrum at the B3LYP/3-21G* level for $[\text{Ca}(\text{U})_{12}]^{2+}$ is

also shown for comparison. Figure reprinted with permission from the Ph.D. thesis of Elizabeth Gillis..... 37

Figure 1.16. A) Representative structures for the addition of uracil monomers to $[\text{Ca}(\text{U})_6]^{2+}$. The numbers indicate the order and location of uracil attachment. B) The addition of a fifth uracil monomer to the square planar (Bi, U_4I) and tetrahedral (Bii, U_4II) isomers creates different products: the square pyramidal U_5I , and a tetrahedral U_5II that contains a lone uracil monomer in a second shell. Figure adapted with permission from *Phys. Chem. Chem. Phys.* **2012**, *14*, 3304 – 3315..... 39

Figure 1.17. Holodirected and hemidirected coordination environments. Figure modified and reprinted from *Inorg. Chem.* **1998**, *37*, 1853 - 1867..... 43

Figure 2.1. A Bruker Apex Qe 7.0 T FT-ICR mass spectrometer coupled with an optical parametric oscillator..... 56

Figure 2.2. A schematic of the Bruker Apex Qe 7.0 T FT-ICR mass spectrometer highlighting the ion source, collision cell, and ICR cell. Figure adapted with permission from *J. Am. Soc. Mass Spectrom.* **2009**, *20*, 411 – 418..... 57

Figure 2.3. The electrospray process: A solution (a) is flowed through a capillary with a potential applied across a narrow opening at the other end. This produces charged droplets (b) that gradually shrink as solvent evaporates (c). Gas-phase ions are then produced according to the charged-residue (d) or ion evaporation (e) models. Figure adapted with permission from *Anal. Chem.* **1993**, *65*, 972A – 986A..... 59

Figure 2.4. The motion of positive and negative ions in a uniform magnetic field..... 62

Figure 2.5. Schematic diagram of a Penning trap. Figure reprinted from the Bruker Daltonics Apex-Qe Series Generation II User Manual. Version 2.0 (July 2008)..... 64

Figure 2.6. Ion motion in the ICR cell is described by three components: the cyclotron (ω_c), trapping (ω_z), and magnetron (ω_m) frequencies. Figure adapted with permission from *Anal. Chem.* **1991**, *63*, 215A – 229A..... 65

Figure 2.7. A packet of ions undergoing uniform cyclotron motion is detected as a sinusoidal signal. Figure adapted from the Bruker Daltonics Apex-Qe Series Generation II User Manual. Version 2.0 (July 2008)..... 67

Figure 2.8. A time-dependent ion signal can be converted to the m/z domain using a fast Fourier transform. Figure adapted from the Bruker Daltonics Apex-Qe Series Generation II User Manual. Version 2.0 (July 2008).....	69
Figure 2.9. Schematic representation of a KTP/OPO.....	71
Figure 2.10. The intensity of the KTP/OPO as a function of wavelength. Figure courtesy of Dr. André Peremans	72
Figure 2.11. The IRMPD process: a photon in resonance with the $v = 0 \rightarrow 1$ transition mode is absorbed by the ion, the $v = 1$ state is then depopulated by IVR, allowing multiple photon absorptions to occur. The ion will dissociate when enough energy is absorbed for the ion to surpass its lowest energy dissociation threshold, D_0 . Reproduced with permission from Dr. Travis Fridgen	76
Figure 2.12. The IRMPD spectra of $[\text{Pb}(\text{Gly-H})\text{H}_2\text{O}]^+$ (top) and its oxygen-18-labeled isotopomer (bottom). Isotopic labeling results in only the band at 3661 cm^{-1} shifting to a lower frequency, implying that the water molecule is no longer intact. Figure reprinted with permission from <i>J. Phys. Chem. B</i> 2009 , <i>113</i> , 14457 – 14464.....	80
Figure 2.13. Potential energy surfaces for the cases when: a) a structural rearrangement occurs prior to dissociation ($E_0 > D_0$) and b) there is no additional barrier to dissociation ($E_0 \approx D_0$).....	85
Figure 2.14. If the cyclotron frequency of an ion is in resonance with a radio-frequency field, it will become excited to larger orbits. By contrast, if the RF field is off-resonance the ion will be directed towards the center of the cell. A SORI pulse cycles through these two conditions, allowing the ion to accumulate internal energy without being ejected from the cell. Figure reprinted from the Bruker Daltonics Apex-Qe Series Generation II User Manual. Version 2.0 (July 2008).....	87
Figure 3.1. The three main types of complexes formed between Pb^{2+} and the conjugate bases of amino acids. Skeletal drawings of alanine, valine, leucine, isoleucine, proline, and lysine are also shown.	106
Figure 3.2. IRMPD spectra in the $3200 - 3800 \text{ cm}^{-1}$ region of six Pb^{2+} /amino acid conjugate base complexes.....	111
Figure 3.3. IRMPD spectra in the $3200 - 4000 \text{ cm}^{-1}$ region of six hydrated Pb^{2+} /amino acid conjugate base complexes.....	113

Figure 3.4. B3LYP/6-31+G(d,p) (LANL2DZ on Pb) computed structures for the bare and hydrated $[\text{Pb}(\text{Ala-H})]^+$ complexes. The reported energies are 298 K enthalpies and Gibbs energies (in parentheses) and have units of kJ mol^{-1} . The unbolded and bolded values were determined using the LANL2DZ and SDD methods, respectively, on Pb. The non-italicized values are B3LYP/6-31+G(d,p) (with LANL2DZ or SDD on Pb) and the italicized values are MP2(full)/6-311++G(2d,2p)//B3LYP/6-31+G(d,p) (with LANL2DZ or SDD on Pb)..... 115

Figure 3.5. Comparison of the $[\text{Pb}(\text{Ala-H})]^+$ IRMPD spectrum (black) with the B3LYP/6-31+G(d,p) calculated spectra for the isomers displayed in Figure 3.4..... 117

Figure 3.6. Comparison of the $[\text{Pb}(\text{Ala-H})\text{H}_2\text{O}]^+$ IRMPD spectrum (black) with the B3LYP/6-31+G(d,p) calculated spectra for the isomers displayed in Figure 3.4..... 118

Figure 3.7. Comparison of IRMPD and computed spectra for $[\text{Pb}(\text{Ala-H})\text{H}_2^{16}\text{O}]^+$ and $[\text{Pb}(\text{Ala-H})\text{H}_2^{18}\text{O}]^+$ 121

Figure 3.8. Comparison of the IRMPD spectrum of $[\text{Pb}(\text{Ala-H})\text{CH}_3\text{OH}]^+$ with the computed spectra of three isomeric structures. The 298 K enthalpies (and Gibbs energies in parentheses) have units of kJ mol^{-1} and are computed using B3LYP/6-31+G(d,p) (non italicized, with LANL2DZ on Pb) and MP2(full)/6-311++G(2d,2p)//B3LYP/6-31+G(d,p) (italicized, with LANL2DZ on Pb), respectively..... 123

Figure 3.9. The IRMPD spectra of $[\text{Pb}(\text{Val-H})]^+$, $[\text{Pb}(\text{Leu-H})]^+$, and $[\text{Pb}(\text{Ile-H})]^+$ compared with the B3LYP/6-31+G(d,p) computed spectra for the A-, B- and C-type isomers seen in Figure 3.10 125

Figure 3.10. Computed structures for the complexes between Pb^{2+} and the conjugate bases of Val, Leu, and Ile. The 298 K enthalpies (and Gibbs energies in parentheses) have units of kJ mol^{-1} and were computed using B3LYP/6-31+G(d,p) (non italicized, with LANL2DZ or SDD on Pb) and MP2(full)/6-311++G(2d,2p)//B3LYP/6-31+G(d,p) (italicized, with LANL2DZ or SDD on Pb)..... 126

Figure 3.11. The IRMPD spectra of $[\text{Pb}(\text{Val-H})\text{H}_2\text{O}]^+$, $[\text{Pb}(\text{Leu-H})\text{H}_2\text{O}]^+$, and $[\text{Pb}(\text{Ile-H})\text{H}_2\text{O}]^+$ compared with the B3LYP/6-31+G(d,p) computed spectra for the A-, B- and C-type isomers seen in Figure 3.12..... 127

Figure 3.12. Computed structures for the hydrated complexes between Pb^{2+} and the conjugate bases of either Val, Leu, or Ile. The 298 K enthalpies (and Gibbs energies in

parentheses) have units of kJ mol^{-1} and are computed using B3LYP/6-31+G(d,p) (non italicized, with LANL2DZ or SDD on Pb) and MP2(full)/6-311++G(2d,2p)//B3LYP/6-31+G(d,p) (italicized, with LANL2DZ or SDD on Pb)..... 128

Figure 3.13. Comparison of the IRMPD spectra of $[\text{Pb}(\text{Pro-H})]^+$ and $[\text{Pb}(\text{Pro-H})\text{H}_2\text{O}]^+$ with the computed spectra belonging to the structures shown in Figure 3.14..... 130

Figure 3.14. B3LYP/6-31+G(d,p) (LANL2DZ on Pb) computed structures for bare and hydrated Pb^{2+} /proline conjugate base complexes. The energies reported are 298 K enthalpies (and Gibbs energies in parentheses) and have units of kJ mol^{-1} . The unbolded and bolded values were determined using the LANL2DZ and SDD methods, respectively, on Pb. The non-italicized values are B3LYP/6-31+G(d,p) (with LANL2DZ or SDD on Pb) and the italicized values are MP2(full)/6-311++G(2d,2p)//B3LYP/6-31+G(d,p) (with LANL2DZ or SDD on Pb)..... 131

Figure 3.15. 298 K Gibbs energy (units of kJ mol^{-1}) diagram for the isomerization of the hydrated A-type structures to the hydrated C-type structures for alanine (A) and proline (B). The non-italicized and italicized values were determined by the B3LYP and MP2 methods, (with LANL2DZ on Pb), respectively..... 134

Figure 3.16. The B3LYP/6-31+G(d,p) optimized structures of $[\text{Pb}(\text{Lys-H})]^+$. The 298 K relative enthalpies and Gibbs energies (in parentheses) have units of kJ mol^{-1} and are provided at the B3LYP/6-31+G(d,p) (top) and MP2(full)/6-311++G(2d,2p) (bottom and italicized) levels of theory. Note that the LANL2DZ basis set with effective core potential were applied to Pb^{2+} for both levels of calculation..... 136

Figure 3.17. The IRMPD spectrum of $[\text{Pb}(\text{Lys-H})]^+$ (black) compared with four computed IR spectra. The computed spectra are from the B3LYP/6-31+G(d,p) optimized structures of Lys-Ci, -Bi, -Ai, and -Aiii shown in Figure 3.16 138

Figure 3.18. The B3LYP/6-31+G(d,p) optimized structures of $[\text{Pb}(\text{Lys-H})\text{H}_2\text{O}]^+$. The 298 K relative enthalpies and Gibbs energies (in parentheses) have units of kJ mol^{-1} and are provided at the B3LYP/6-31+G(d,p) (top) and MP2(full)/6-311++G(2d,2p) (bottom and italicized) levels of theory. Note that the LANL2DZ basis set and effective core potential were applied to Pb^{2+} for both levels of calculation..... 140

Figure 3.19. The IRMPD spectrum of $[\text{Pb}(\text{Lys-H})\text{H}_2\text{O}]^+$ (black) compared with four computed IR spectra. The computed spectra are from the B3LYP/6-31+G(d,p) optimized structures of LysW-Bi, -Ci, -Cii, and -Aiii shown in Figure 3.18 141

Figure 4.1. Four possible $[\text{Pb}(\text{Aa-H})]^+$ isomers. Skeletal drawings of phenylalanine, glutamic acid, and methionine are also shown 151

Figure 4.2: The IRMPD spectra of $[\text{Pb}(\text{Phe-H})]^+$, $[\text{Pb}(\text{Phe-H})\text{H}_2\text{O}]^+$, $[\text{Pb}(\text{Glu-H})]^+$, $[\text{Pb}(\text{Glu-H})\text{H}_2\text{O}]^+$, and $[\text{Pb}(\text{Met-H})]^+$ in the 3200 – 3800 cm^{-1} region 156

Figure 4.3. The IRMPD spectrum of $[\text{Pb}(\text{Phe-H})]^+$ (black) compared with four computed IR spectra. The computed spectra are from the B3LYP/6-31+G(d,p) optimized structures of Phe-Ai, -Bi, -Bii, and -Ci. The 298 K relative enthalpies and Gibbs energies (in parentheses) have units of kJ mol^{-1} and are provided at the B3LYP/6-31+G(d,p) (top) and MP2(full)/6-311++G(2d,2p) (bottom and italicized) levels of theory. In both cases, the LANL2DZ basis set with effective core potential was applied to Pb^{2+} 159

Figure 4.4. The IRMPD spectrum of $[\text{Pb}(\text{Phe-H})\text{H}_2\text{O}]^+$ (black) compared with three computed IR spectra. The computed spectra are from the B3LYP/6-31+G(d,p) optimized structures of PheW-Ai, -Bi, and -Ci. The 298 K relative enthalpies and Gibbs energies (in parentheses) have units of kJ mol^{-1} and are provided at the B3LYP/6-31+G(d,p) (top) and MP2(full)/6-311++G(2d,2p) (bottom and italicized) levels of theory. In both cases, the LANL2DZ basis set with effective core potential was applied to Pb^{2+} 162

Figure 4.5. The B3LYP/6-31+G(d,p) optimized structures of $[\text{Pb}(\text{Glu-H})]^+$. The 298 K relative enthalpies and Gibbs energies (in parentheses) have units of kJ mol^{-1} and are provided at the B3LYP/6-31+G(d,p) (top) and MP2(full)/6-311++G(2d,2p) (bottom and italicized) levels of theory. Note that the LANL2DZ basis set with effective core potential was applied to Pb^{2+} for both levels of calculation 164

Figure 4.6. The IRMPD spectrum of $[\text{Pb}(\text{Glu-H})]^+$ (black) compared with six computed IR spectra. The computed spectra are from the B3LYP/6-31+G(d,p) optimized structures of Glu-Ai, -Bi, -Ci, -Dzi, -Dci, and -Dcii shown in Figure 4.5..... 166

Figure 4.7. The B3LYP/6-31+G(d,p) optimized structures of $[\text{Pb}(\text{Glu-H})\text{H}_2\text{O}]^+$. The 298 K relative enthalpies and Gibbs energies (in parentheses) have units of kJ mol^{-1} and are provided at the B3LYP/6-31+G(d,p) (top) and MP2(full)/6-311++G(2d,2p) (bottom and italicized) levels of theory. Note that the LANL2DZ basis set with effective core potential was applied to Pb^{2+} for both levels of calculation 168

Figure 4.8. The IRMPD spectrum of $[\text{Pb}(\text{Glu-H})\text{H}_2\text{O}]^+$ (black) compared with five computed IR spectra. The computed spectra are from the B3LYP/6-31+G(d,p) optimized structures of GluW-Dzi, -Dzii, -Dziii, -Dziv, and -Dci shown in Figure 4.7 169

Figure 5.1. The A-, B-, C-, and D-type complexes formed between Pb^{2+} and the conjugate bases of amino acids. The ions resulting from single hydration are also shown

181

Figure 5.2. The lowest-energy structures of the nine $[\text{Pb}(\text{Aa-H})\text{H}_2\text{O}]^+$ complexes (Aa = Pro, Gly, Ala, Val, Leu, Ile, Phe, Lys, and Glu) determined using IRMPD spectroscopy. Each complex was optimized using the B3LYP/6-31+G(d,p) level of theory. In each case, the LANL2DZ basis set with relativistic core potential was applied to Pb

184

Figure 5.3. The dissociation of $[\text{Pb}(\text{Ala-H})\text{H}_2\text{O}]^+$ ($m/z = 314$ Da) into $[\text{Pb}(\text{Ala-H})]^+$ ($m/z = 296$ Da) and neutral water at 386.6 K monitored as a function of reaction time by FT-ICR mass spectrometry. The relative abundances of the ions are plotted after 6.01 s (a), 24.01 s (b), and 78.01 s (c)

188

Figure 5.4. a) The normalized intensities of $[\text{Pb}(\text{Ala-H})]^+$ and $[\text{Pb}(\text{Ala-H})\text{H}_2\text{O}]^+$ as a function of reaction time. Both ions exhibit first-order kinetic behaviour. b) The BIRD kinetic data for the dissociation of $[\text{Pb}(\text{Ala-H})\text{H}_2\text{O}]^+$ is fit to the integrated first-order rate law ($\ln[I_{\text{AaW}}/(I_{\text{AaW}}+I_{\text{Aa}})]$) versus reaction time) at 11 temperatures between 322 – 387 K.

190

Figure 5.5. Comparison of the Arrhenius plots ($\ln(k_{\text{obs}})$) versus $1/T$ for the $[\text{Pb}(\text{Aa-H})\text{H}_2\text{O}]^+$ complexes (Aa = Gly (\circ), Ala (\square), Val (Δ), Leu (\diamond), Ile (\bullet), Phe (\blacksquare), Lys (\blacktriangle), and Glu (\blacklozenge))

191

Figure 5.6. The Arrhenius plot of $[\text{Pb}(\text{Val-H})\text{H}_2\text{O}]^+$ (solid line) fit by k_{uni} values calculated using the master equation (dashed lines). The trial E_0 values, 8500 and 8700 cm^{-1} (black dashed lines) produce slopes that are slightly less and slightly more negative than the experimental line, hence the water binding energy is $8600 \pm 100 \text{ cm}^{-1}$ based on a comparison of the experimental Arrhenius plot with the master-equation calculated lines

196

Figure 6.1. The five principle $[\text{M}(\text{Aa-H})]^+$ isomers. Skeletal drawings of alanine and β -methylaminoalanine are also shown

213

Figure 6.2. The IRMPD spectrum of $[\text{Ba}(\text{Ala-H})\text{H}_2\text{O}]^+$ (black) compared with four computed IR spectra. The computed spectra are from the B3LYP/6-31+G(d,p) optimized structures of BaAlaW-Ai, -Bi, -Ci, and -Cii. The 298 K relative enthalpies and Gibbs energies (in parentheses) have units of kJ mol^{-1} and are provided at the B3LYP/6-31+G(d,p) (top) and MP2(full)/6-311++G(2d,2p) (bottom and italicized) levels of theory. In both cases, the LANL2DZ basis set with effective core potential was applied to Ba^{2+}

219

Figure 6.3. The B3LYP/6-31+G(d,p) optimized structures of [Ba(Ala-H)]⁺. The 298 K relative enthalpies and Gibbs energies (in parentheses) are provided at the B3LYP/6-31+G(d,p) (top) and MP2(full)/6-311++G(2d,2p) (bottom and italicized) levels of theory. Note that the LANL2DZ basis set with effective core potential was applied to Ba²⁺ for both levels of calculation 222

Figure 6.4. The difference in MP2(full)/6-311++G(2d,2p)//B3LYP/6-31+G(d,p) Gibbs energy (ΔG_{SB-CS}) between salt-bridge (C-type) and charge-solvated (B-type) [M(Aa-H)]⁺ isomers as a function of decreasing chemical hardness. [M(Ala-H)]⁺ and [M(BMAA-H)]⁺ complexes are represented by ● and ● respectively. Also shown are the ΔG_{SB-CS} values for the E-type [Zn(Ala-H)]⁺ and A-type [Pb(Ala-H)]⁺ structures relative to their C-type isomers (*) 224

Figure 6.5. The difference in MP2(full)/6-311++G(2d,2p)//B3LYP/6-31+G(d,p) Gibbs energy (ΔG_{SB-CS}) between salt-bridge (C-type) and charge-solvated (B-type) [M(Aa-H)]⁺ isomers as a function of the effective ionic radius of the metal cation. [M(Ala-H)]⁺ and [M(BMAA-H)]⁺ complexes are represented by ● and ● respectively..... 225

Figure 6.6. The B3LYP/6-31+G(d,p) optimized structures of [Ba(BMAA-H)]⁺. The 298 K relative enthalpies and Gibbs energies (in parentheses) are provided at the B3LYP/6-31+G(d,p) (top) and MP2(full)/6-311++G(2d,2p) (bottom and italicized) levels of theory. Note that the LANL2DZ basis set with effective core potential was applied to Ba²⁺ for both levels of calculation 228

Figure 6.7. The B3LYP/6-31+G(d,p) optimized structures of [Ba(BMAA-H)H₂O]⁺. The 298 K relative enthalpies and Gibbs energies (in parentheses) are provided at the B3LYP/6-31+G(d,p) (top) and MP2(full)/6-311++G(2d,2p) (bottom and italicized) level of theories. Note that the LANL2DZ basis set with effective core potential was applied to Ba²⁺ for both levels of calculation 231

Figure A1. Potential energy surface for the isomerization of A- to C-type [Pb(Ala-H)]⁺. The optimized geometries and reported Gibbs energies were determined using the B3LYP/6-31+G(d,p) method 245

Figure A2. Potential energy surface for the isomerization of A- to C-type [Pb(Pro-H)]⁺. The optimized geometries and reported Gibbs energies were determined using the B3LYP/6-31+G(d,p) method..... 246

Figure B1. The IRMPD spectrum of $[\text{Pb}(\text{Met-H})]^+$ (black) compared with three computed IR spectra. The computed spectra were derived from the B3LYP/6-31+G(d,p) optimized structures of Met-Ai, -Bi, and Ci shown in Figure B2..... 249

Figure B2. The B3LYP/6-31+G(d,p) optimized structures of $[\text{Pb}(\text{Met-H})]^+$. The 298 K relative enthalpies and Gibbs energies (in parentheses) have units of kJ mol^{-1} and are provided at the B3LYP/6-31+G(d,p) (top) and MP2(full)/6-311++G(2d,2p) (bottom and italicized) levels of theory. Note that the LANL2DZ basis set with effective core potential was applied to Pb^{2+} for both levels of calculation 250

Figure B3. Comparison of the IRMPD spectra for $[\text{Pb}(\text{Phe-H})\text{H}_2\text{O}]^+$, $[\text{Pb}(\text{Glu-H})\text{H}_2\text{O}]^+$, and $[\text{Pb}(\text{Ala-H})\text{H}_2\text{O}]^+$ 251

Figure B4. The B3LYP/6-31+G(d,p) optimized structures of (a) $[\text{Pb}(\text{Phe-H})]^+$ and (b) $[\text{Pb}(\text{Phe-H})\text{H}_2\text{O}]^+$. The B3LYP/6-31+G(d,p) energies are reported as $\Delta H_{298\text{K}}$ ($\Delta G_{298\text{K}}$) and have units of kJ mol^{-1} . The MP2(full)/6-311++G(2d,2p) energies are italicized. In each case, the LANL2DZ basis set with effective core potential was applied to Pb^{2+} ... 252

Figure B5. The IRMPD spectra (black) of (a) $[\text{Pb}(\text{Phe-H})]^+$ and (b) $[\text{Pb}(\text{Phe-H})\text{H}_2\text{O}]^+$ compared with computed IR spectra derived from the B3LYP/6-31+G(d,p) optimized structures in Figure B4..... 253

Figure B6. The B3LYP/6-31+G(d,p) optimized structures of $[\text{Pb}(\text{Glu-H})]^+$. The B3LYP/6-31+G(d,p) energies are reported as $\Delta H_{298\text{K}}$ ($\Delta G_{298\text{K}}$) and have units of kJ mol^{-1} . The MP2(full)/6-311++G(2d,2p) energies are italicized. In each case, the LANL2DZ basis set with effective core potential was applied to Pb^{2+} 255

Figure B7. The IRMPD spectrum (black) of $[\text{Pb}(\text{Glu-H})]^+$ compared with computed IR spectra derived from the B3LYP/6-31+G(d,p) optimized structures in Figure B6. 256

Figure B8. The B3LYP/6-31+G(d,p) optimized structures of $[\text{Pb}(\text{Glu-H})\text{H}_2\text{O}]^+$. The B3LYP/6-31+G(d,p) energies are reported as $\Delta H_{298\text{K}}$ ($\Delta G_{298\text{K}}$) and have units of kJ mol^{-1} . The MP2(full)/6-311++G(2d,2p) energies are italicized. In each case, the LANL2DZ basis set with effective core potential was applied to Pb^{2+} 257

Figure B9. The IRMPD spectrum (black) of $[\text{Pb}(\text{Glu-H})\text{H}_2\text{O}]^+$ compared with computed IR spectra derived from the B3LYP/6-31+G(d,p) optimized structures in Figure B8 ... 258

Figure C1. BIRD kinetic data for the dissociation of seven $[\text{Pb}(\text{Aa-H})\text{H}_2\text{O}^+]$ complexes (Aa = Gly, Val, Leu, Ile, Phe, Lys, and Glu) fit to the integrated first order rate law ($\ln[I_{\text{AaW}}/(I_{\text{AaW}}+I_{\text{Aa}})]$ versus reaction time) 266

Figure C2. The Arrhenius plot of $[\text{Pb}(\text{Val-H})\text{H}_2\text{O}^+]$ (solid line) fit by k_{uni} values obtained by master equation modeling using frequency scaling factors (α) between 0.90 – 1.10 (dashed lines) 270

Figure C3. IRMPD spectra in the 3200 - 3800 cm^{-1} region for $[\text{Pb}(\text{Ala-H})\text{H}_2\text{O}^+]$ solvated in 50/50 18.2 M Ω $\text{H}_2\text{O}/\text{MeOH}$ and 50/50 18.2 M Ω $\text{H}_2\text{O}/\text{MeCN}$. The spectra are compared to computed infrared spectra for A- (green), B- (blue), and C-type (red) $[\text{Pb}(\text{Ala-H})\text{H}_2\text{O}^+]$ complexes 272

Figure D1. The B3LYP/6-31+G(d,p) optimized structures of seven $[\text{M}(\text{Ala-H})]^+$ complexes ($\text{M}^{2+} = \text{Be}^{2+}, \text{Mg}^{2+}, \text{Ca}^{2+}, \text{Sr}^{2+}, \text{Ba}^{2+}, \text{Zn}^{2+},$ and Pb^{2+}). The 298 K relative enthalpies and Gibbs energies (in parentheses) have units of kJ mol^{-1} and are provided at the B3LYP/6-31+G(d,p) (top) and MP2(full)/6-311++G(2d,2p) (bottom and italicized) levels of theory. Note that the LANL2DZ basis set with effective core potential was applied to $\text{Sr}^{2+}, \text{Ba}^{2+},$ and Pb^{2+} for both levels of calculation 275

Figure D2. The B3LYP/6-31+G(d,p) optimized structures of seven $[\text{M}(\text{BMAA-H})]^+$ complexes ($\text{M}^{2+} = \text{Be}^{2+}, \text{Mg}^{2+}, \text{Ca}^{2+}, \text{Sr}^{2+}, \text{Ba}^{2+}, \text{Zn}^{2+},$ and Pb^{2+}). The 298 K relative enthalpies and Gibbs energies (in parentheses) have units of kJ mol^{-1} and are provided at the B3LYP/6-31+G(d,p) (top) and MP2(full)/6-311++G(2d,2p) (bottom and italicized) level of theories. Note that the LANL2DZ basis set with effective core potential was applied to $\text{Sr}^{2+}, \text{Ba}^{2+},$ and Pb^{2+} for both levels of calculation 278

List of Symbols, Nomenclature or Abbreviations

Symbols

ΔG	= Gibbs energy change
ΔH	= enthalpy change
ΔG^\ddagger	= Gibbs energy of activation
ΔH^\ddagger	= enthalpy of activation
ΔS^\ddagger	= entropy of activation
ΔU_{corr}	= thermal energy difference between the transition state and the reactant
a	= distance between the trapping plates of a Penning trap
\AA	= angstrom (10^{-10} m)
A	= Arrhenius pre-exponential factor
$A(h\nu)$	= Einstein coefficient for spontaneous emission
$B(h\nu)$	= Einstein coefficient for induced emission
B	= magnetic field strength
D_0	= 0 K dissociation energy
e	= elementary charge
E	= internal energy/radio frequency field
E_0	= critical dissociation energy
E_a	= Arrhenius activation energy
E_a^∞	= limiting rapid-exchange Arrhenius activation energy
E_{elec}	= electronic energy

E_{rot}	= rotational energy
E_{trans}	= translational energy
E_{vib}	= vibrational energy
E_{ZP}	= zero-point energy
f	= focal length
G	= Gibbs energy
G^\ddagger	= sum of states for the transition state
h	= Planck's constant
H	= enthalpy
I	= intensity
J	= total angular momentum
$k_{l,rad}$	= rate constants for radiative absorption
$k_{-l,rad}$	= rate constants for radiative emission
k_B	= Boltzmann constant
k_d	= unimolecular dissociation rate constant
k_{ij}	= rate constants for all state-to-state transitions
k_{obs}	= observed (measured) rate constant
k_{uni}	= thermal unimolecular dissociation rate constant
m	= mass
m/z	= mass-to-charge ratio
N	= number of atoms in a molecule/density of states
P_i	= probabilities of an oscillator having m quanta of energy in the i state

Q	= canonical partition function/Rayleigh limiting charge
r	= radius
S	= entropy
t	= time
T^{-1}	= inverse temperature
v	= velocity
V_t	= trapping voltage
z	= charge
α	= cell constant/frequency scaling factor
ϵ_0	= permittivity of the vacuum
λ	= surface tension
μ	= transition dipole moment
ν	= frequency
$\rho(h\nu)$	= Planck's black-body radiation distribution
σ	= reaction degeneracy
ω	= angular (cyclotron) frequency
ω_m	= magnetron frequency
ω_{obs}	= observed cyclotron frequency
ω_t	= trapping frequency

Abbreviations

A = adenine

Ala	= alanine
ALS	= amyotrophic lateral sclerosis
Arg	= arginine
B3LYP	= Becke, 3-parameter, Lee-Yang-Parr density functional theory
BIRD	= blackbody infrared radiative dissociation
BMAA	= β -methylaminoalanine
C	= cytosine
CID	= collision-induced dissociation
CLIO	= Centre Laser Infrarouge d'Orsay (Orsay, France)
CP	= Counterpoise correction
Cys	= cysteine
DFT	= density functional theory
DNA	= deoxyribonucleic acid
EDTA	= ethylenediaminetetraacetic acid
ESI	= electrospray ionization
FEL	= free electron laser
FELIX	= Free Electron Laser for Infrared eXperiments (Nieuwegein, Netherlands)
FT-ICR	= Fourier transform ion cyclotron resonance
FT-ICR MS	= Fourier transform ion cyclotron resonance mass spectrometry
G	= guanine
GB	= gas-phase basicity

Glu	= glutamic acid
Gly	= glycine
His	= histidine
ICR	= ion cyclotron resonance
Ile	= isoleucine
IRC	= intrinsic reaction coordinate
IRMPD	= infrared multiple photon dissociation spectroscopy
IVR	= intramolecular vibrational energy redistribution
KTP	= potassium titanyl phosphate, KTiOPO_4
LANL2DZ	= Los Alamos National Laboratories 2 Double Zeta basis set with effective core potential
Leu	= leucine
Lys	= lysine
MALDI	= matrix-assisted laser desorption ionization
Met	= methionine
MP2	= Møller-Plesset second-order perturbation theory
MS	= mass spectrometry
NBO	= natural bond order
Nd:YAG	= neodymium-doped yttrium aluminum garnet, $\text{Nd:Y}_3\text{Al}_5\text{O}_{12}$
OPO	= optical parametric oscillator
Phe	= phenylalanine
Pro	= proline

RF	= radio frequency
RNA	= ribonucleic acid
RRKM	= Rice-Ramsperger-Kassel-Marcus theory
SDD	= Stuttgart/Dresden basis set with effective core potential
Ser	= serine
SORI-CID	= sustained off-resonance collision-induced dissociation
T	= thymine
Tyr	= tyrosine
U	= uracil
Val	= valine
VRC-TST	= variational reaction coordinate transition state theory

List of Appendices

Appendix A – Supporting Information for Chapter 3.....	244
Appendix B – Supporting Information for Chapter 4.....	248
Appendix C – Supporting Information for Chapter 5.....	262
Appendix D.– Supporting Information for Chapter 6.....	274

Co-authorship Statement

The experiments described in Chapters 3 – 6 were designed by the principal author in collaboration with Dr. Travis Fridgen, and are an extension of the research presented in the M.Sc. thesis of Chad Atkins. IRMPD spectroscopy and BIRD kinetic measurements were performed using a Bruker Apex Qe 7 T Fourier transform ion cyclotron resonance mass spectrometer (FT-ICR) installed by Dr. Fridgen at Memorial University; Dr. André Peremans helped couple the FT-ICR with the tunable optical parametric oscillator required for IRMPD spectroscopy. Electronic structure calculations and master equation modeling used the Gaussian 09 and VariFlex software packages and were carried out on the ACENet and Westgrid computational networks. The principal author conducted the majority of experiments and data analysis, and was responsible for preparing the research for publication. Dr. Fridgen contributed to the final versions of each paper. In Chapter 3, some of the computational chemistry was performed by Sarah Decker, while Mark Rowsell and Chad Atkins were responsible for determining the structures of $[\text{Pb}(\text{Ala-H})]^+$ and $[\text{Pb}(\text{Ala-H})\text{H}_2\text{O}]^+$. Ms. Decker also performed some of the BIRD measurements in Chapter 5.

Chapter 1

Introduction

1.1. General Introduction. The adage “form follows function” is perhaps the simplest way to describe the chemical behaviour of natural molecules. Evolutionary or environmental challenges restrict the range of products that can viably fill a specific role, and this fact is exploited by chemists to design useful materials like pharmaceuticals and catalysts. A commercial drug, for instance, results from screening thousands of potential candidate molecules that have small variations in structure. The converse to the above statement is also true, meaning that clues to the potential behaviour of a specific molecule can be revealed by examining its configuration. For this reason, a large part of chemical research involves determining the structures of molecules in order to grasp the fundamental forces that dictate their behaviour.

Particular attention has been given to the structures of biomolecules since simple perturbations to these systems, such as a change in acidity or the introduction of metal ions, will often promote activation, isomerization or ion-molecule reactions that drastically alter how they act in physiological systems.¹⁻¹³ A well known occurrence is the disruption of base pairing in DNA and RNA due to the abundance of ambient salt.¹⁴ The hydrogen bonds between nucleobase pairs play a key role in maintaining the double helical structure of these biopolymers, but metal ions can stabilize higher energy nucleobase tautomers through coordinate bonding.¹⁵⁻¹⁸ This results in base mispairing and, consequently, biological mutations.¹⁹ Cationic interactions are also capable of

drastically altering the structure of DNA; alkaline earth and transition metal cations have been known to stabilize triple-stranded DNA, and protonated nucleobases can initiate the conversion of B-DNA to Z-DNA (Figure 1.1).^{20,21} The picture is similar for other biological molecules; chelating metals with amino acids is a proven method for stabilizing non-canonical tautomers in the gas phase, and will also distort the tertiary structure of peptides.^{1,2,11,12}

In light of the extensive isomerism that ions can induce in biomolecules, determining the structures of these complexes is intriguing medically as well as chemically. For instance, one of the motives behind structurally characterizing metal cation bound biomolecules is the knowledge that Cu^{2+} catalyzes the aggregation of synthetic amyloid beta. This produces reactive oxygen-containing species that may be related to the oxidative stress associated with the progression of Alzheimer's disease.²²⁻²⁶ Certain amino acids, such as histidine and carnosine, or tyrosine and phenylalanine when conjugated with a polyaminocarboxylic acid like EDTA, can limit this oxidative stress by chelating the metal ions. For this reason, a detailed understanding of the metal cation-amino acid binding motif could reveal the mechanism for this process and possibly lead to new treatments.^{27,28}

This work focuses on the use of mass spectrometry and gas-phase ion activation techniques to probe the structures and physical properties of metal-cationized amino acids. Knowledge of these complexes is necessary to help characterize larger peptides, and is also required to understand the role of metal ions in biologically important systems. In particular, Chapters 3 – 5 explore the structures and water binding energies of

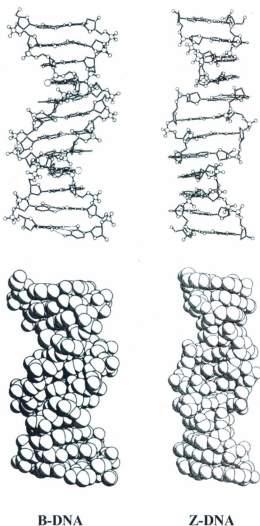


Figure 1.1. Single-crystal X-ray structures of B-DNA and Z-DNA represented by skeletal (top) and space-filling (bottom) illustrations. B-DNA is a right-handed double helix that comprises ten base pairs per turn. By contrast, Z-DNA is left-handed and has twelve base pairs per turn. Figure adapted with permission from *Science* **1982**, 216, 475 – 485.²⁹

lead(II)-amino acid complexes. Lead chelation can cause severe physiological consequences ranging from heme synthesis to hypertension. This makes the characterization of these complexes medically significant, as they could aid in the design of lead-selective chelating agents.³⁰ Chapter 6 describes lead(II) and alkaline earth complexes with β -methylaminoalanine (BMAA), a nonproteinogenic amino acid found in cycad seeds. Ingestion of BMAA has been linked to the onset of the neurodegenerative disorder amyotrophic lateral sclerosis (ALS), hence, determining the structures and reactivity of these complexes could shed light on possible therapies. The rest of this chapter is devoted to reviewing the contemporary use of three gas-phase techniques; infrared multiple photon dissociation (IRMPD) spectroscopy, blackbody infrared radiative dissociation (BIRD) kinetic experiments, and collision-induced dissociation (CID); to determine the structures of biological ions.

1.2. Determining the Structures of Biological Ions Using Mass Spectrometry. Any substance produced by a living entity can be considered a biomolecule. This is a broad definition that encompasses small compounds, such as the amino acids used to create proteins, as well as larger species like enzymes or DNA. When this statement is combined with the knowledge that there are an essentially limitless number of unique organisms on Earth, it quickly becomes clear that the natural complexity of biomolecules necessitates a highly sensitive and versatile analytical technique. For many years, this role has been performed by mass spectrometry (MS);³¹⁻³³ a method that identifies a molecular ion based on its mass-to-charge (m/z) ratio, and which can also be used to infer structural information about the species under study by inducing it to fragment. The

fundamentals of mass spectrometry have been detailed in many texts, but a brief overview is given here.^{34,35}

Mass spectrometry experiments share three key principles: the analyte must be converted into a gas-phase ion, a mass analyzer is required to group ions according to their m/z , and a sensitive detector is needed to determine the abundance of ions at a specific m/z . Beyond these requirements, mass spectrometry is extremely versatile, and can be combined with several gas-phase techniques to determine the structures of ions. A particularly robust approach is infrared multiple photon dissociation (IRMPD) spectroscopy, which is a structure-sensitive technique realized by coupling a mass spectrometer with an intense and tunable infrared light source.^{1,2,13,36} In a similar manner to conventional infrared spectroscopy, IRMPD spectroscopy provides evidence for the structure (or structures) of an ion by the observed positions of characteristic infrared absorption bands. These are used to identify specific functional groups of a molecule (carbonyl groups, amines, carboxylic acids, etc...) and are often compared with theoretical infrared spectra derived using computational chemistry in order to determine more detailed structures.^{15,37-44} This method, which is described in more detail in Section 2.3.1, has become increasingly popular among gas-phase ion chemists due to the addition of mass spectrometers to the free electron lasers (FEL) at the Free Electron Laser for Infrared eXperiments (FELIX, Nijmegen, the Netherlands)⁴⁵ and the Centre Laser Infrarouge d'Orsay (CLIO, Orsay, France)⁴⁶, as well as the availability of tunable tabletop light sources such as optical parametric oscillators (OPO).^{1,2,36}

A salient feature of IRMPD spectroscopy is that ion activation methods can be used to determine structural information. In IRMPD experiments, the ion is activated using an intense source of light; if the impinging photons are in resonance with one of the vibrational transitions of the ion, then a single photon absorption will occur. Anharmonic coupling between this transition and the ion's other vibrational modes then depopulates the absorbing vibrational excited state through fast ($10^{-12} - 10^{-14}$ s) intramolecular vibrational-energy redistribution (IVR), freeing it for further photon absorption. This process is repeated until the ion absorbs enough energy to dissociate, and the subsequent fragmentation is observed in the mass spectrum as a decrease in parent ion intensity with respect to the fragment ions.

The IRMPD spectrum of lead-cationized glycine (Gly), which is deprotonated and of the form $[\text{Pb}(\text{Gly-H})]^+$, is shown in Figure 1.2 as an example.³⁷ The peak at 3552 cm^{-1} is in a similar position to the carboxylic acid O-H stretch observed for matrix-isolated glycine (3560 cm^{-1}) as well as for the sodium- and proton-bound dimers of glycine (3555 and 3569 cm^{-1} respectively),^{38,47} indicating that $[\text{Pb}(\text{Gly-H})]^+$ is deprotonated at the amine group rather than the carboxylic acid. This peak assignment is consistent with the computed infrared spectrum of the most stable amine-deprotonated $[\text{Pb}(\text{Gly-H})]^+$ isomer, Gly-A, where Pb^{2+} is bound between the carbonyl oxygen and amine nitrogen. The IRMPD spectrum of $[\text{Pb}(\text{Gly-H})]^+$ was presented as the first evidence that metal-cationized amino acids can be amine-deprotonated, but it should be noted that the lack of any observed amine N-H stretches between $3300 - 3450 \text{ cm}^{-1}$ makes it impossible to spectroscopically rule out the existence of two isomers with intact amine groups, Gly-B

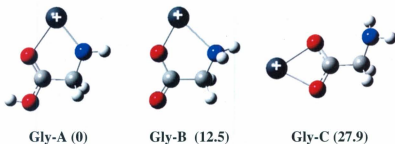
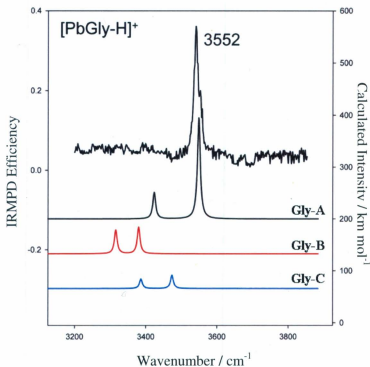


Figure 1.2: The IRMPD spectrum of $[\text{Pb}(\text{Gly}-\text{H})]^+$ compared with three computed IR spectra. The computed spectra are determined from the B3LYP/6-31+G(d,p) optimized structures of Gly-A, -B, and -C. The 298 K relative enthalpies (in parentheses) were determined by the MP2/6-311++G(2d,p)//B3LYP/6-31+G(d,p) method and have units of kJ mol^{-1} . In both cases, the LANL2DZ basis set with effective core potential was applied to Pb^{2+} . Figure adapted with permission from *J. Phys. Chem. B* **2009**, *113*, 14457 – 14464.³⁷

and Gly-C, based on the IRMPD spectrum alone. However, both of these isomers are $12.5 - 27.9 \text{ kJ mol}^{-1}$ less enthalpically stable than Gly-A, suggesting that the amine-deprotonated complex is the most likely gas-phase structure of $[\text{Pb}(\text{Gly-H})]^+$.

It is also possible to infer structural information by activating ions using other methods, such as collision-induced dissociation (CID)⁴⁸ or blackbody infrared radiative dissociation (BIRD)⁴⁹. Each of these techniques, as well as the instrumentation required to perform them, are described in more detail in Chapter 2. CID involves fragmenting the ion of interest by colliding it with a neutral bath gas such as argon. The ion's structure can then be determined by identifying the fragment ions using mass spectrometry and piecing them together. Collisions between the ion and bath gas result in some of the ion's kinetic energy being transferred into internal energy. The extent of fragmentation depends on the amount of internal energy deposited into the ion and, as a consequence, is dependent on the ion's initial kinetic energy, the nature of the bath gas, and the number of collisions it undergoes.

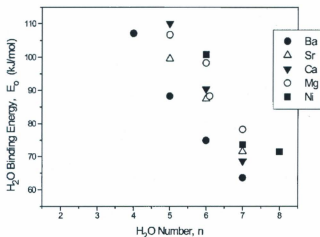
BIRD relies on the ion of interest absorbing enough ambient blackbody photons to dissociate. In low-pressure environments (10^{-10} mbar), these experiments allow thermal unimolecular dissociation rate constants, k_{uni} , to be determined using mass spectrometry by monitoring the relative normalized intensities of the parent and fragment ions as a function of time. Arrhenius activation energies, E_a , can then be determined from a plot of $\ln(k_{\text{uni}})$ against inverse temperature (T^{-1}). If dissociation occurs through a barrierless process, such as desolvation, E_a can be used to determine the binding energy of the

fragment ion. This requires deriving the limiting rapid-exchange value of E_a , a process which is described in more detail in Section 2.3.2.⁴⁹

BIRD experiments can reveal a number of interesting structural features: an abrupt change in the slope of an Arrhenius plot is evidence for the existence of temperature-dependent isomers, and different structural configurations can often be distinguished by their solvent binding energies. Furthermore, the effect of adding solvent or additional monomers to a complex can be examined. This last point was illustrated by Williams and coworkers by using BIRD to determine the sequential water binding energies of a series of divalent metal cations.⁴⁹⁻⁵¹ Figure 1.3A demonstrates that $[\text{Mg}(\text{H}_2\text{O})_n]^{2+}$ and $[\text{Ni}(\text{H}_2\text{O})_n]^{2+}$ have sharp drops in water binding energies when a seventh water is added. This trend is not observed for the Ca^{2+} , Sr^{2+} , or Ba^{2+} complexes, and can be explained by the smaller ionic radii of Mg^{2+} and Ni^{2+} preventing the added water molecule from becoming part of the inner hydration sphere.⁵² The $[\text{Mg}(\text{H}_2\text{O})_6]^{2+}$ complex is also interesting as its Arrhenius plot (Figure 1.3B) has a change in slope near 350 K. This was attributed to the thermal stabilization of a higher energy isomer that has one (or possibly two) of its six waters in a second hydration shell, but no conclusive structural evidence was reported.

In order to activate biomolecular ions, they must be trapped long enough for the consequence of their dissociation to be observed. In typical IRMPD experiments for example, the ion of interest is isolated in a quadrupole ion trap or Fourier transform ion cyclotron resonance (FT-ICR) mass spectrometer before irradiation.^{1,2,36} FT-ICR mass spectrometers are particularly useful due to their high sensitivity and resolution as well as

A)



B)

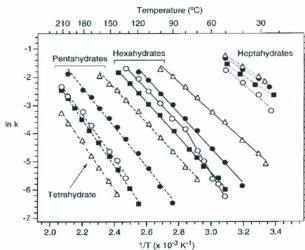


Figure 1.3: A) The energy required to add successive water molecules to $[M(H_2O)_n]^{2+}$ complexes. B) Arrhenius plots for the dissociation of $[M(H_2O)_n]^{2+}$ complexes where $n = 4 - 7$. Complexes involving Mg^{2+} , Ca^{2+} , Sr^{2+} , and Ba^{2+} are indicated by \circ , \blacksquare , \bullet , and Δ respectively. The Arrhenius plot of $[Mg(H_2O)_6]^{2+}$ exhibits an abrupt change in slope near 350 K, indicating that it has two temperature-dependent isomers. Figures adapted with permission from *Mass. Spectrom. Rev.* **2004**, 23, 127 – 158 and *J. Am. Chem. Soc.* **1999**, 121, 8898 – 8906.^{49, 51}

excellent mass accuracy. This type of instrument, which is used for the experiments described in Chapters 3 – 6, allows the trapped ions to establish an equilibrium distribution of energies in the ICR cell. Hence, in addition to structurally characterizing gas-phase complexes using IRMPD spectroscopy, FT-ICR MS can be used to monitor the behaviour of ions using the other activation methods described above. For example, at ambient ICR pressures (10^{-10} mbar), the dissociation energies of weakly-bound ionic complexes can be determined using blackbody infrared radiative dissociation (BIRD).⁴⁹ Furthermore, since the ICR cell is able to perform multiple steps of mass selection, it is possible to perform in-cell CID by pulsing a 10^{-8} mbar burst of unreactive bath gas into the ICR cell. Using the same approach, reaction mechanisms can also be probed by leaking small amounts of gas (10^{-9} – 10^{-7} mbar) into the ICR cell and determining ion-molecule rate constants by monitoring the intensities of the reactant and product ions as a function of time.

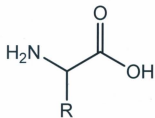
IRMPD spectroscopy, BIRD, and CID are excellent methods for determining gas-phase structures, but it has only been over the past two decades that they have been extensively applied to biological ions. This is partly due to the difficulty of isolating intact gas-phase biological ions from solution- or solid-phase samples. Traditional ionization techniques, such as electron impact, often cause biomolecules to extensively fragment, and further require that the analyte already be present in the gas phase whereas most biomolecules exist in solution. These problems have been circumvented by the rise of “soft” ionization techniques, such as electrospray ionization (ESI) and matrix-assisted laser desorption ionization (MALDI), which introduce biomolecules into the gas-phase in

a nondestructive manner.⁵³ ESI is especially useful because it generates ions directly from solution, whereas MALDI extracts the ions from a matrix. For this reason, ESI is typically used for the analysis of biomolecules since ions can be prepared in solution using conventional benchtop chemistry.⁵⁴ ESI also has the advantage that it can be coupled with liquid-phase separation methods, such as liquid chromatography or electrophoresis. This has made it a valuable tool for identifying individual proteins from complex mixtures.³²

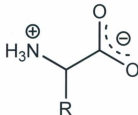
Each of the gas-phase techniques described in this section enable the intrinsic properties of ions to be explored. Sections 1.2.1 – 1.2.5 will discuss the use of IRMPD spectroscopy, BIRD, and CID with respect to determining the structures of biological ions. Since the focus of this work is determining the structures and reactivity of metal cationized biological ions using a variety of mass spectrometric techniques, particular attention will be given to complexes involving metals.

1.2.1. Amino Acids.[†] Every naturally occurring amino acid can be zwitterionic in the presence of polar solvents, but removing them from solution causes even the most basic amino acids to favour their canonical tautomers (Figure 1.4, the specific amino acids analyzed in this thesis are shown in Figure 1.5).⁵⁵ For this reason, there has been considerable interest in using gas-phase techniques to explore the physical properties of zwitterions. One approach uses microsolvation to determine the limiting number of solvent molecules necessary for isomerization to take place. Gas-phase glycine, for

[†] Parts of Sections 1.2.1, 1.2.3, and 1.2.4 are adapted from work previously published in *Eur. J. Mass Spectrom.* **2012**, *18* (2), 235 - 250.



Canonical



Zwitterionic

Figure 1.4. The generalized structures of canonical and zwitterionic amino acids.

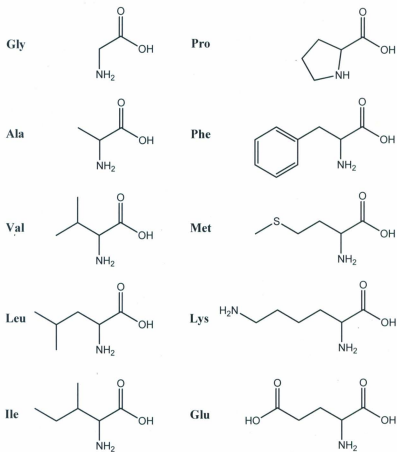


Figure 1.5. The canonical tautomers of the ten amino acids investigated in this thesis.

instance, requires between two and six water molecules to stabilize its zwitterionic structure,^{56,57} while alanine, phenylalanine, and tryptophan are zwitterions in the presence of at least four waters.^{56,58} It should also be noted that canonical and zwitterionic amino acids can coexist in the gas phase. In the case of tryptophan, calculations suggest that a non-negligible amount of canonical amino acids are present up to at least six added water molecules.⁴³

Currently, the majority of research into the structures of gas-phase amino acid complexes uses metal chelation to stabilize different tautomers.^{1,2,59} Metal ions are interesting for many reasons: for example, they are suspected to promote the formation of certain peptides,⁶⁰ and metal complexation with the aromatic groups of amino acid side chains has helped reveal the nature of cation- π interactions.⁶¹ Metal cations can stabilize zwitterions through an ionic interaction with the deprotonated carboxylate group known as a salt bridge, and the imparted stability is dependent on both the size and valency of the chelating metal atom, as well as the gas-phase basicity of the amino acid.^{59,62-64} Strongly polarizing cations induce the formation of salt bridges by enhancing charge separation in the amino acid. However, since the most polarizing cations are small, they are also easily charge solvated by the basic sites of the amino acid. For this reason, aliphatic amino acids are more likely to produce salt bridge structures in the presence of smaller cations, whereas the presence of additional basic sites in more functionalized amino acids favours charge-solvated tautomers.⁶⁴ Consequently, amino acids with additional heteroatoms or aromatic rings generally produce salt bridges with larger

cations, since the ionic radius of the metal cation is less effectively shielded by the amino acid.

The most extensively studied metal(M)-amino acid(Aa) complexes are of the form $[M(\text{Aa})]^{+2}$.^{12,37,62,65-72} IRMPD spectra supported by density functional theory (DFT) calculations were used to confirm that lithium-cationized arginine (Arg) is charge-solvated and that $[M(\text{Arg})]^+$ complexes involving K^+ , Rb^+ , and Cs^+ are zwitterionic. $[\text{Na}(\text{Arg})]^+$ exists as a mixture of both isomers.⁷⁰ A similar trend appears in structural investigations of other metal-ion amino acid complexes. Armentrout and coworkers used IRMPD spectroscopy to demonstrate that serine (Ser) forms charge-solvated structures with Li^+ , Na^+ , K^+ , and Rb^+ where each metal ion forms a three-coordinate bond with serine's amine nitrogen, carbonyl oxygen, and hydroxyl group (Figure 1.6).⁶² However, a bidentate charge-solvated structure was shown to contribute to the gas-phase populations of both $[\text{K}(\text{Ser})]^+$ and $[\text{Rb}(\text{Ser})]^+$, while $[\text{Cs}(\text{Ser})]^+$ exhibited bands indicative of the salt bridge isomer. Lysine and tryptophan do not form zwitterions with alkali metal cations, but IRMPD spectra indicate that a change of structure still occurs when the cation size is increased from Na^+ to K^+ .^{73,74}

In addition to the size of the metal, its valency is important with respect to zwitterion stabilization. Dicationic metals have been shown computationally and experimentally to stabilize salt bridge structures more than singly-charged metal cations.^{59,65,66,69} A notable example is tryptophan, where IRMPD spectroscopy and computational techniques have been used to demonstrate that charge-solvated structures

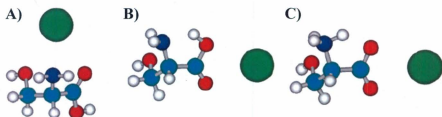
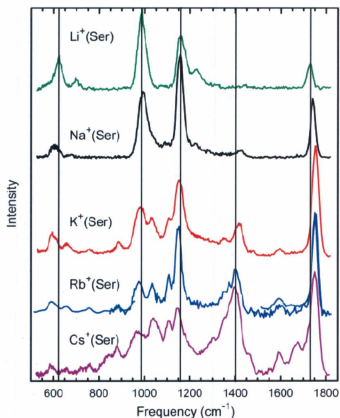


Figure 1.6. The IRMPD spectrum of $[\text{M}(\text{Ser})]^+$ ($\text{M}^+ = \text{Li}^+, \text{Na}^+, \text{K}^+, \text{Cs}^+$, and Rb^+) between 500 – 1800 cm^{-1} . The bands at 980, 1150, and 1230 cm^{-1} (the side-chain CO stretch, NH_2 bend, and concerted COH bends, respectively) are indicative of structure A, whereas peaks at 1400 (carboxylic acid O-H bend) and 1680 cm^{-1} (the carboxylate anion CO stretch) are diagnostic of structures B and C, respectively. Figure adapted with permission from *J. Phys. Chem. A* **2008**, *112*, 2248 – 2257.⁶²

are favoured for complexes with every alkali metal cation as well as Ag^+ .⁷⁴ However, when divalent cations are involved, salt bridge structures were shown to be stable for some of the larger alkaline earth cations (Ca^{2+} , Sr^{2+} , and Ba^{2+}).^{59,74} A similar pattern is true for glycine (Gly); $[\text{Be}(\text{Gly})]^{2+}$ is charge solvated while $[\text{Mg}(\text{Gly})]^{2+}$, $[\text{Ca}(\text{Gly})]^{2+}$, $[\text{Sr}(\text{Gly})]^{2+}$, and $[\text{Ba}(\text{Gly})]^{2+}$ are zwitterionic.⁶⁵ Further investigation into glycine complexes by Russo and coworkers using DFT demonstrated that divalent first row-transition metals (Mn^{2+} , Fe^{2+} , Co^{2+} , Ni^{2+} , Cu^{2+} , and Zn^{2+}) also produce glycine zwitterions.⁶³

1.2.2. Polypeptides and Proteins. The utility of IRMPD spectroscopy is partially limited by the size of the ion being studied.^{1,2} Larger molecules have a greater number of vibrational modes by definition, and this can create complex or crowded IR spectra that are difficult to interpret. For this reason, research into the structures of proteins typically focuses on smaller polypeptides containing two to five amino acid residues. A biologically relevant example is the use of IRMPD spectroscopy to determine the gas-phase structure of protonated Leu-enkephalin (Tyr-Gly-Gly-Phe-Leu), a pentapeptide which acts as a neurotransmitter.¹⁰ The IRMPD spectrum of $[\text{H}(\text{Leu-enkephalin})]^+$ (Figure 1.7) revealed that its structure is a mixture of two roughly isoenergetic isomers that are both protonated at the terminal amine group, but stabilized by different functional groups. The most stable structure, **LE1**, has the NH_3^+ moiety stabilized by multiple carbonyl oxygen atoms, the Tyr-Gly and Phe-Leu amide linkages, and the aromatic side chain of Tyr. **LE2** has a similar configuration, but is instead stabilized by the Gly-Phe

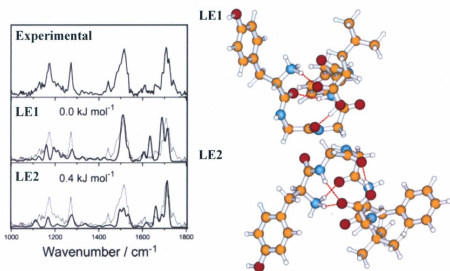


Figure 1.7. The IRMPD spectrum of $[H(\text{Leu-enkephalin})]^+$ compared with the computed IR spectra (bold lines) derived from the B3LYP/6-31+G(d,p) optimized structures of LE1 and LE2. Figure adapted with permission from *J. Am. Chem. Soc.* **2007**, *129*, 5887 - 5897.¹⁰

linkage instead of the two described for **LE1**. The antisymmetric NH_3^+ bending mode is predicted to appear at 1632 cm^{-1} for **LE1** and 1660 cm^{-1} for **LE2**, and this difference lead the authors to suggest that **LE2** is the most likely $[\text{H}(\text{Leu-enkephalin})]^+$ tautomer in the gas-phase. However, the broad peak centered at 1500 cm^{-1} , as well as the shoulder at $\sim 1200\text{ cm}^{-1}$, indicates that **LE1** is also present.

The case of $[\text{H}(\text{Leu-enkephalin})]^+$ demonstrates that IRMPD spectroscopy can be used to determine the most favourable protonation or metalation sites on specific peptides.⁷⁵⁻⁷⁷ This is particularly useful because predicting these binding sites is not always as straightforward as comparing the proton affinities or gas-phase basicities of different amino acid residues. For example, the Ala-Ala dipeptide is protonated at the terminal amine group,⁷⁵ but Ala-Ala-Ala and the structurally similar Gly-Gly-Gly have two gas-phase populations: one that is protonated at the N-terminal nitrogen like Ala-Ala, and another protonated at the N-terminal carbonyl oxygen.⁷⁷ The structures of the N-protonated alanine di- and tripeptides have planar backbones and *trans* configurations about the amide linkages, while the O-protonated tripeptide has a cyclic structure stabilized by hydrogen bonding. It should be noted that the IRMPD spectrum of $[\text{H}(\text{AlaAla})]^+$ is also explained by a roughly isoenergetic structure where the carboxylic acid is perpendicular to the NH_3^+ moiety. It's clear then, that the alanine residues are able to rotate with respect to one another, and it is likely this rotation that enables hydrogen bonds to stabilize the O-protonated $[\text{H}(\text{AlaAlaAla})]^+$ isomer. IRMPD spectroscopy has also revealed that protonated or metal chelated peptides can be stabilized through interactions with functionalized amino acid side chains. For example, Ala-His is known

to be protonated at histidine's (His) imidazole group,⁷⁶ while sodium- and potassium-bound Phe-Ala and Ala-Phe are partly stabilized by a π -interaction with phenylalanine's aromatic ring.⁷⁸

Non-covalently bound amino acids can also be studied using IRMPD spectroscopy by isolating proton-bound complexes in the gas phase. The proton-bound dimers^{*} of glycine, alanine, and valine were determined to contain charge-solvated amino acids,⁴² while zwitterionic structures of proline and lysine have been found in $[\text{H}(\text{Pro})_2]^+$ and $[\text{H}(\text{Lys})_2]^+$,^{79,80} respectively. An interesting example is the case of proton-bound serine.⁸¹ The most stable structure of $[\text{H}(\text{Ser})_2]^+$ contains two charge-solvated amino acids. However, zwitterionic serine is stabilized as more monomers are added to the system, and $[\text{H}(\text{Ser})_3]^+$ appears to be completely zwitterionic. This trend was identified by comparing the IRMPD spectra of several $[\text{H}(\text{Ser})_n]^+$ ($n = 2 - 8$) complexes; as the number of serine monomers is increased, there is a noticeable weakening of the carboxylic acid O-H band, and a simultaneous increase in intensity of the N-H stretch arising from the protonated amine moiety. Cation-bound complexes have also been examined using IRMPD spectroscopy. The sodium-bound dimer of glycine contains canonical amino acids, but has a different structure than its proton-bound analogue.³⁸ The binding proton of $[\text{H}(\text{Gly})_2]^+$ lies between the amine nitrogen of one monomer and the carbonyl oxygen of the other, but $[\text{Na}(\text{Gly})_2]^+$ has the sodium ion stabilized by a four coordinate interaction with the amine nitrogen and carbonyl oxygen of each glycine.

^{*}Proton bound dimers are distinct from *protonated dimers*. The former describes two separate monomers bound to a single proton, while the latter indicates that the monomers are conjugated. The same is true for the terms metal- or cation-bound dimer.

To the best of the author's knowledge, the largest biomolecules to be studied by IRMPD spectroscopy are bovine ubiquitin and cytochrome c.^{9,82} These compounds are much too large for detailed structures to be determined, however intriguing structural features can still be observed. For instance, the IRMPD spectrum of cytochrome c (Figure 1.8), which combines 104 amino acid residues, contains three distinguishable vibrational bands that vary in intensity as a function of the ion's charge state. The two bands at 1660 cm^{-1} and 1535 cm^{-1} belong to C=O stretch and N-H bending modes respectively, and indicate that the backbone of the protein is an α -helix. This is supported by the observation that the CO stretch shifts to lower energy as the ion charge state increases, suggesting that there is less intramolecular hydrogen bonding throughout the α -helix. The vibrational stretch at 1480 cm^{-1} is intriguing; it has no analogue in solution, but may be due to a change in secondary structure caused by the reduced hydrogen bonding.

1.2.3. Nucleobases and Nucleobase Pairs. Ionized nucleic acid bases or nucleotides often adopt different structures from their free forms (Figure 1.9). Protons or metal ions can stabilize higher energy isomers, and frequently change the function of these biomolecules. The stabilization of nucleotide phosphate groups by metal ions, and the rupturing of the hydrogen bonds between base pairs due to metal coordination with the nucleobase are just two consequences of the presence of metal ions. Considering their implications with respect to DNA deformation and biological mutations, metal ion/nucleobase complexes have recently been receiving increased attention. The most interest has been given to complexes involving adenine (A), thymine (T), and uracil (U), which form the AT and AU base pairs in DNA and RNA, respectively.^{8,15,18,40,41,43,44,83}

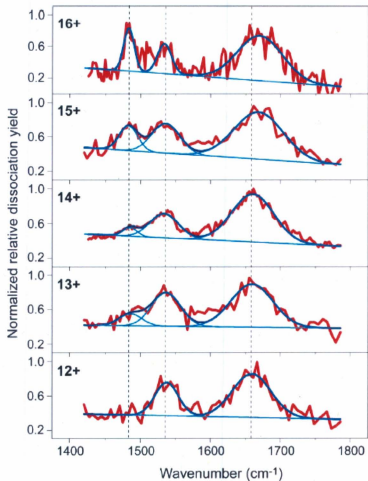


Figure 1.8. The IRMPD spectrum (red) of cytochrome c. The blue lines are the smoothed averages of multiple scans. As the charge state increases, there is a noticeable blue shift in the band at $\sim 1660\text{ cm}^{-1}$, as well as the appearance of a band at 1480 cm^{-1} . Figure adapted with permission from *Mass Spectrom. Rev.* **2009**, *28*, 468 – 494.⁸²

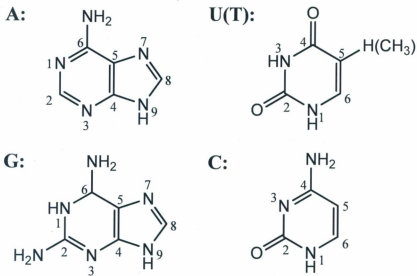


Figure 1.9. Numbering schemes for the canonical DNA and RNA nucleobases.

This research was partly spurred by the discovery of monovalent cations attached to AT-tracts in the minor groove of DNA; ambient water molecules from the spine of hydration help integrate the cations into the groove by stabilizing them between four oxygen atoms from DNA and two from the water molecules.¹⁴

The IRMPD spectra of three $[\text{Li}(\text{B})\text{H}_2\text{O}]^+$ complexes (nucleobase (B) = A, T, and U) are compared in the N-H/O-H stretching region in Figure 1.10.^{15,40} The spectra for the pyrimidine bases are virtually identical; $[\text{Li}(\text{U})\text{H}_2\text{O}]^+$ and $[\text{Li}(\text{T})\text{H}_2\text{O}]^+$ each contain a symmetric O-H stretch around 3640 cm^{-1} and two N-H stretches at approximately 3455 cm^{-1} and 3430 cm^{-1} . These features are consistent with the theoretical IR spectra derived from the lowest-energy structures for these complexes, **UI** and **TI**, but there is a notable absence of the antisymmetric O-H stretch predicted to appear at 3725 cm^{-1} . This is attributed to poor coupling between the antisymmetric O-H stretch and the other vibrational modes of the ion, which reduces the efficiency of IVR. The symmetric O-H stretch is more strongly coupled than the antisymmetric stretch because it vibrates along the bond axis rather than perpendicular to it, explaining why it is observed in the IRMPD spectrum while the antisymmetric stretch is not.⁸⁴

UI and **TI** each have the lithium cation bound to the O4 position of the canonical diketo structures, and water bound directly to Li^+ (Figure 1.9 contains the nucleobase numbering schemes). These structures were supported by calculated Gibbs energies that demonstrated that Li^+ binds more favourably to the O4 position than to the O2 position, and concurs with earlier CID results which likewise indicated that Li^+

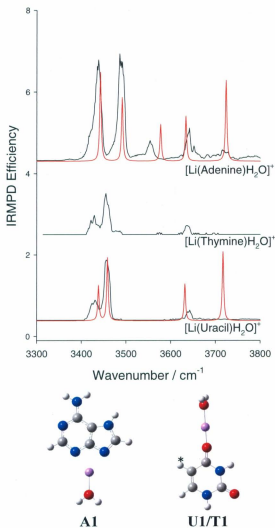


Figure 1.10. The IRMPD spectra for three $[\text{Li}(\text{B})\text{H}_2\text{O}]^+$ complexes (B = A, U, and T). U1, T1, and A1 are the lowest Gibbs energy structures according to the MP2/6-311++G(2d,p)//B3LYP/6-31+G(d,p) method that best reflect the experimental data (* represents the location of thymine's methyl group). Figure adapted and reprinted with permission from *J. Phys. Chem. A* **2010**, *114*, 3449 - 3456 and *J. Phys. Chem. A* **2009**, *113*, 824 - 832.^{15,40}

preferably binds to the O4 position.⁸⁵ The IRMPD spectrum of $[\text{Li}(\text{A})\text{H}_2\text{O}]^+$ unequivocally demonstrates that Li^+ binds to an adenine tautomer that is higher in energy than the canonical form. The spectrum contains three N-H stretches at 3438, 3486, and 3554 cm^{-1} as well as the symmetric and antisymmetric water O-H stretches at 3642 and 3728 cm^{-1} , respectively. The antisymmetric O-H stretch is weaker than the symmetric O-H stretch, as was the case for $[\text{Li}(\text{U})\text{H}_2\text{O}]^+$ and $[\text{Li}(\text{T})\text{H}_2\text{O}]^+$. These features indicate that $[\text{Li}(\text{A})\text{H}_2\text{O}]^+$ is the lithiated A7 tautomer (**A1**, which has an N7-H bond) where Li^+ is bound between the N3 and N9 positions. This is despite the fact that as a free base this isomer is 30 – 35 kJ mol^{-1} of Gibbs energy less stable than the canonical A9 tautomer.⁸⁶ Furthermore, Russo had previously predicted a non-canonical imino structure for $[\text{Li}(\text{A})]^+$ where the cation is bound between the N6 and N7 positions and one of the N6 hydrogens is on N1, and similar results were reported for a series of Na^+ , Mg^{2+} , and Zn^{2+} -adenine complexes.^{18,87} Although Russo's proposed structure was determined to be the lowest Gibbs energy structure by 5.2 kJ mol^{-1} , there was no evidence to support its existence in the gas phase. IRMPD spectroscopy was also used to determine that the gas-phase structures of $[\text{K}(\text{A})]^+$ and $[\text{Cs}(\text{A})]^+$ were A7 tautomers like $[\text{Li}(\text{A})\text{H}_2\text{O}]^+$. This should be expected; as the size of the metal cation increases, it becomes more polarizable and is unable to stabilize the imine tautomer as effectively.

Figure 1.11 contains the IRMPD spectra of $[\text{Li}(\text{B})_2]^+$ and $[\text{Li}(\text{B})_2\text{H}_2\text{O}]^+$ complexes between $\sim 2500 - 4000 \text{ cm}^{-1}$.^{15,40} With the exception of the bands attributed to water in the O-H stretching region, the spectra for $[\text{Li}(\text{U})_2]^+$ and $[\text{Li}(\text{T})_2]^+$ are nearly identical to those

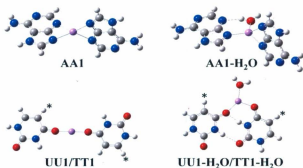
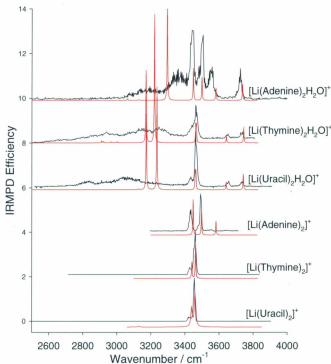
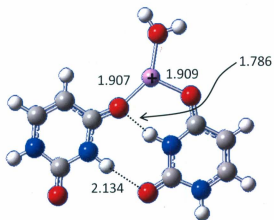
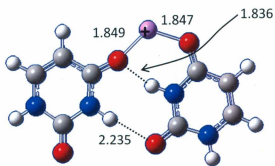


Figure 1.11. The IRMPD spectra (black) for three $[\text{Li}(\text{B})_2]^+$ and three $[\text{Li}(\text{B})_2\text{H}_2\text{O}]^+$ complexes (B = A, U, and T). UU1, TT1, and AA1 are the lowest Gibbs energy structures according to the MP2/6-311++G(2d,p)//B3LYP/6-31+G(d,p) method that best reflect the experimental data. The computed IR spectra (red) for the lowest energy structures are also shown. Figure adapted and reprinted with permission from *J. Phys. Chem. A* **2010**, *114*, 3449 - 3456 and *J. Phys. Chem. A* **2009**, *113*, 824 - 832.^{15,40}

of $[\text{Li}(\text{U})\text{H}_2\text{O}]^+$ and $[\text{Li}(\text{U})\text{H}_2\text{O}]^+$, and the same is true for the case of adenine. The lithium-bound nucleobase dimers are therefore symmetric, and this is confirmed by the computed IR spectra of the lowest energy symmetric structures (**UU1**, **TT1**, and **AA1**) matching the IRMPD spectra. Hydrating these dimers (**UU1-H₂O**, **TT1-H₂O**, and **AA1-H₂O**), however, produces a noticeable difference; there is a significant number of new features in the 2500 – 3400 cm^{-1} region of the $[\text{Li}(\text{B})_2\text{H}_2\text{O}]^+$ spectra. The addition of water to these dimers causes the structures to relax in such a way that stronger hydrogen bonds are formed between the uracils, breaking the symmetry seen for the bare dimers. This is demonstrated in Figure 1.12, where the addition of water to $[\text{Li}(\text{U})_2]^+$ reduces the lengths of the $\text{O4}_{\text{Ua}}-\text{N3}_{\text{Ub}}$ and $\text{N3}_{\text{Ua}}-\text{O2}_{\text{Ub}}$ hydrogen bonds by 0.050 and 0.101 Å with respect to **UU2**, an isomer similar in energy to **UU1** that is the precursor to **UU1-H₂O**. These hydrogen bonded N-H stretches are responsible for the broad bands observed in the IRMPD spectra of $[\text{Li}(\text{U})_2\text{H}_2\text{O}]^+$ and $[\text{Li}(\text{T})_2\text{H}_2\text{O}]^+$; water can be ruled out as a hydrogen bond donor for these ions by the presence of its symmetric and antisymmetric O-H stretches in the IRMPD spectra. By contrast, a noticeable difference between $[\text{Li}(\text{A})_2\text{H}_2\text{O}]^+$ and the pyrimidine dimers is the lack of the symmetric O-H stretch, indicating that water participates in hydrogen bonding with one or both adenine monomers. No single structure can completely account for the IRMPD spectrum of any $[\text{Li}(\text{B})_2\text{H}_2\text{O}]^+$ complex; there are at least three additional isomers of $[\text{Li}(\text{A})_2\text{H}_2\text{O}]^+$ and four for $[\text{Li}(\text{U})_2\text{H}_2\text{O}]^+$ and $[\text{Li}(\text{T})_2\text{H}_2\text{O}]^+$ that are calculated to be similar in Gibbs energy ($< 4 \text{ kJ mol}^{-1}$) to the lowest energy structures. These tautomers differ by the number of



UU1-H₂O



UU2

Figure 1.12. The addition of water to $[\text{Li}(\text{U})_2]^+$ strengthens the $\text{O4}_{\text{Ua}}\text{-N3}_{\text{Ub}}$ and $\text{N3}_{\text{Ua}}\text{-O2}_{\text{Ub}}$ hydrogen bonds by relaxing the uracil dimer. UU2 is similar in enthalpy to UU1 in Figure 1.10. Figure reprinted with permission from *Eur. J. Mass Spectrom.* **2012**, *18* (2), 235 - 250.¹³

hydrogen bonds between the bases, the nitrogen and oxygen atoms involved with hydrogen bonding, and the orientation of the nucleobases with respect to one another. The IRMPD spectra of the $[\text{Li}(\text{B})_2\text{H}_2\text{O}]^+$ complexes therefore arise from a mixture of isomers.

In addition to characterizing the metal-bound nucleobase homodimers described above, IRMPD spectroscopy has also been used to determine the influence of cations on Watson-Crick base pairs.⁴¹ Previous investigations of $[\text{M}(\text{AT})^{+/2+}]$ heterodimers considered the interaction strictly in terms of the canonical forms because those tautomers were expected to be predominant in the gas-phase.^{4,88} However, the IRMPD spectrum of $[\text{Li}(\text{AT})\text{H}_2\text{O}]^+$ shown in Figure 1.13 has provided evidence of non-Watson-Crick binding.⁴¹ There are six recognizable vibrational modes; 3658 and 3734 cm^{-1} are the symmetric and antisymmetric O-H stretches of water, adenine's NH_2 symmetric and antisymmetric stretches appear at 3554 and 3442 cm^{-1} , and the bands at 3502 and 3472 cm^{-1} are caused by the $\text{N7}_\text{A}\text{-H}$ and $\text{N1}_\text{T}\text{-H}$ stretches. In standard Watson-Crick base pairing, adenine's NH_2 group is hydrogen bonded to O4_T , so the appearance of both NH_2 stretches indicates that the $[\text{Li}(\text{AT})]^+$ complex does not follow this model. It should be noted, however, that this experiment does not account for the presence of ribose or deoxyribose, which bind at N9_A and N1_T , respectively. The IRMPD spectrum is also compared with the computed IR spectra determined from the two most stable structures according to Gibbs energy and enthalpy (**AT1** and **AT2**). Both structures are consistent with the experimental spectrum, and cannot be distinguished in the observed

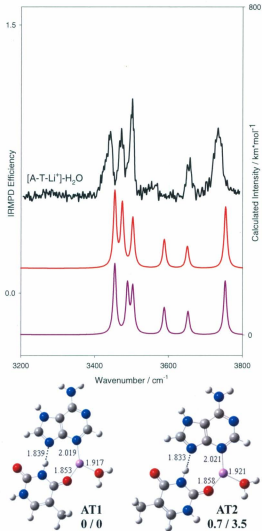


Figure 1.13. The IRMPD spectrum of $[\text{Li}(\text{AT})\text{H}_2\text{O}^+]$ compared with two computed IR spectra calculated using B3LYP/6-31+G(d,p). **AT1** (red) is more energetically and enthalpically favourable than **AT2** (purple). The reported energies were determined using the MP2/6-311++G(2d,p)//B3LYP/6-31+G(d,p) method and are written as $\Delta\text{G}/\Delta\text{H}$. All units are in kJ mol^{-1} . Figure adapted with permission from *Int. J. Mass Spectrom.* **2010**, 297, 2 - 8.⁴¹

spectroscopic range. **AT2** is 0.7 kJ mol^{-1} less stable than **AT1** using relative Gibbs energies, and is 3.5 kJ mol^{-1} more enthalpically unfavourable. Both structures show that $[\text{Li}(\text{AT})\text{H}_2\text{O}^+]$ is stabilized by a hydrogen bond between $\text{N}3_{\text{T}}$ and $\text{N}9_{\text{A}}$ and an electrostatic interaction between Li^+ , $\text{N}3_{\text{A}}$, and either $\text{O}4_{\text{T}}$ (**AT1**) or $\text{O}2_{\text{T}}$ (**AT2**). Water binds directly to the lithium ion through its oxygen atom. The $\text{O}4_{\text{T}}\text{-Li}^+\text{-N}3_{\text{A}}$ bond is consistent with earlier reports^{40,85} that the bidentate Li^+ interaction between $\text{N}3$ and $\text{N}9$ observed in the isolated $[\text{Li}(\text{A})\text{H}_2\text{O}]^+$ complex does not stabilize the lithium-bound nucleobase pair as well as the hydrogen bonding between $\text{N}3_{\text{T}}$ and $\text{N}9_{\text{A}}$.

Many other metal-ion nucleobase complexes have been investigated. Lamsabhi *et al.* used tandem mass spectrometry experiments and theoretical calculations to demonstrate that the reaction of uracil with Cu^{2+} produces singly-charged $[\text{Cu}(\text{U}-\text{H})]^+$ complexes with Cu^{2+} bound between the $\text{N}1$ and $\text{O}2$ positions, and also determined the collisionally-activated pathways for unimolecular dissociation.⁸⁹ This was expanded upon by examining $[\text{Cu}(\text{U})(\text{U}-\text{H})]^+$ using sustained off-resonance collision-induced dissociation (SORI-CID), IRMPD activation, thorough isotopic labeling, and computational chemistry.⁹⁰ Both $[\text{Cu}(\text{U}-\text{H})]^+$ and, surprisingly, $[\text{Cu}(\text{U})(\text{U}-\text{H})]^+$ complexes lose HNCO as the primary fragmentation pathway, followed by loss of NCO for $[\text{Cu}(\text{U}-\text{H})]^+$ and HCN for $[\text{Cu}(\text{U})(\text{U}-\text{H})]^+$. The dissociation of $[\text{Cu}(\text{U})(\text{U}-\text{H})]^+$ requires extensive isomerization, however, the lowest energy structure is stabilized by a hydrogen bond between $\text{O}2_{\text{U-H}}$ and $\text{O}4_{\text{U}}$ and has a four-coordinate Cu^{2+} bound between $\text{N}3_{\text{U-H}}$, $\text{O}4_{\text{U-H}}$, $\text{N}3_{\text{U}}$, and $\text{O}2_{\text{U}}$. A similar approach was used to characterize $[\text{Pb}(\text{U}-\text{H})]^+$ and $[\text{Pb}(\text{T}-\text{H})]^+$, while the structures of $[\text{Ca}(\text{U})]^{2+}$ and its thio-derivatives were probed by DFT and shown

to have Ca^{2+} bound between the O2 and N3 positions of uracil's O4-enol (or enethiol) tautomer.^{91,92} The unimolecular reactivity of uracil complexes with divalent metal ions is significantly different from the alkali metal-uracil clusters described earlier.¹⁶ The only fragmentation observed for the alkali metal ion containing clusters was the loss of the nucleobase, however, in the presence of a dication the base polarization increases, resulting in bond activation and eventual cleavage. Depending on the metal ion, this will change the observed fragmentation; collisions with $[\text{Ca}(\text{U})]^{2+}$ produce CaOH^+ , while the enhanced charge transfer in Cu^{2+} and Pb^{2+} complexes strengthens the acidity of uracil and produces deprotonated clusters. Hence, CuOH^+ and PbOH^+ products are not observed. A broader investigation of $[\text{M}(\text{U})(\text{U-H})]^+$ complexes with almost every metal cation that has +2 as the most common oxidation state has also been conducted.^{93,94} This study showed that whether or not uracil loss is observed depends on the size of the metal dication, and demonstrated a correlation between the size of the metal dication and the uracil binding energy. The complexes containing the smallest metal dications bind uracil the strongest (Figure 1.14), indicating that the metal-uracil bond is best characterized as an electrostatic ion-dipole interaction.

1.2.4. Nucleobase Macroclusters. The natural pairing of nucleobases makes them potential candidates for molecular self-assembly.⁹⁵ Metal ions can direct this process by stabilizing nucleobase complexes through strong ion-dipole interactions. The discovery of larger nucleobase clusters in biological systems has sparked an interest in their physiological involvement. Guanine quartets, which consist of four planar hydrogen

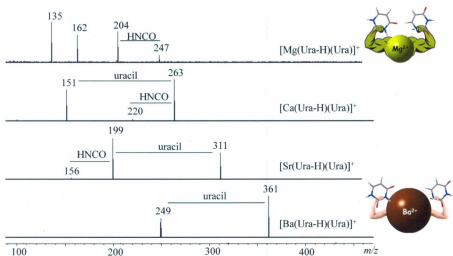


Figure 1.14. SORI/CID spectra of the $[\text{Mg}(\text{Ura-H})(\text{Ura})]^+$, $[\text{Ca}(\text{Ura-H})(\text{Ura})]^+$, $[\text{Sr}(\text{Ura-H})(\text{Ura})]^+$, and $[\text{Ba}(\text{Ura-H})(\text{Ura})]^+$ complexes with a SORI power of 0.656 eV. Figure adapted with permission from *ChemPhysChem* **2012**, *13*, 1507 – 1513.⁹⁴

bonded guanosine monomers coordinated to an alkali metal cation, are involved in telomere formation and are consequently associated with cancer or cellular aging.^{96,97} Large nucleobase adducts are known to form stable magic number clusters; Na⁺ yields tetramers with uracil, thymine, and guanine, while K⁺, Cs⁺ and NH₄⁺ produce uracil and thymine pentamers.⁹⁸⁻¹⁰⁰ Hydrogen bonding between the nucleobases stabilizes these clusters; however additional bonding between sugar residues may promote higher-order cluster formation. For instance, deoxycytidine and deoxyadenosine form smaller complexes with alkali metals than cytidine or adenosine. Zins and coworkers combined tandem mass spectrometry with DFT calculations to demonstrate that Ca²⁺-uracil clusters can contain as many as 14 nucleobases.¹⁰¹ It was suggested that six nucleobases form a hexameric core about the cation via strong ion-molecule interactions, and that additional nucleobases attach to the inner core through weaker non-covalent interactions.

Four [Ca(U)_n]²⁺ (n = 10, 11, 12, and 14) IRMPD spectra between 3000 – 3800 cm⁻¹, and one for the n = 12 case in the 1550 – 1900 cm⁻¹ region, are shown in Figure 1.15.¹⁰² The spectra in the higher energy region show broad bands spanning from 3000 to 3400 cm⁻¹ indicative of hydrogen bonded N-H stretching, and the spectrum for n = 12 in the lower-energy region suggests C=O stretching and HCN bending modes. Neither set of infrared spectra are very useful for structural characterization. In an attempt to assign a more definitive structure to these uracil clusters, Gillis and coworkers used blackbody infrared radiative dissociation (BIRD) and IRMPD activation to model the dissociation kinetics and structures of several [Ca(U)_n]²⁺ (n = 4 - 14) complexes.¹⁰³ For these clusters,

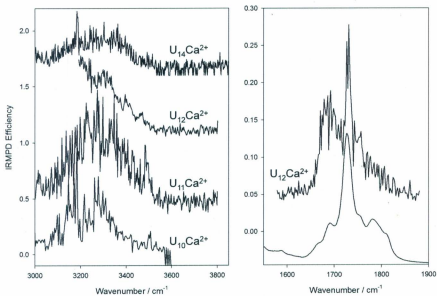


Figure 1.15. The IRMPD spectra of $[\text{Ca}(\text{U})_{10}]^{2+}$, $[\text{Ca}(\text{U})_{11}]^{2+}$, $[\text{Ca}(\text{U})_{12}]^{2+}$, and $[\text{Ca}(\text{U})_{14}]^{2+}$ in the N-H/O-H stretching region and $[\text{Ca}(\text{U})_{12}]^{2+}$ in the CO stretch/HCN bending region. The computed IR spectrum at the B3LYP/3-21G* level for $[\text{Ca}(\text{U})_{12}]^{2+}$ is also shown for comparison. Figure reprinted with permission from the Ph.D. thesis of Elizabeth Gillis.¹⁰²

examining the dissociation chemistry revealed more useful structural information than IRMPD spectroscopy. Master equation modeling of the BIRD data returned a much higher threshold dissociation energy for $[\text{Ca}(\text{U})_6]^{2+}$ than the larger clusters, confirming the existence of the hexameric core. For $[\text{Ca}(\text{U})_n]^{2+}$ clusters where $n > 6$, the experimental activation energies displayed an odd-even alternation in stabilities (even numbered clusters are slower to dissociate) which signifies the presence of uracil dimers (Figure 1.16A) about the inner core. Calculated binding energies were consistent with this odd-even alternation with even numbered clusters having a higher binding energy than the odd numbered clusters. Electrospray ionization MS data showed that the $[\text{Ca}(\text{U})_n]^{2+}$ ($n = 6, 8, 10, 12, 14$) complexes were significantly more abundant than the odd-numbered counterparts, further demonstrating that the even numbered complexes are magic number clusters.

Another interesting feature of this work was that two distinct gas-phase populations of $[\text{Ca}(\text{U})_5]^{2+}$ were found by CO_2 -laser IRMPD kinetics. Roughly half of the $[\text{Ca}(\text{U})_5]^{2+}$ ion population dissociated at a different rate, hence two non-interconverting populations of ions must be present. The first is the expected precursor of the $[\text{Ca}(\text{U})_6]^{2+}$ inner core (**U₅1**, Figure 1.16B), while the second has uracil non-covalently bound to a tetrahedral $[\text{Ca}(\text{U})_4]^{2+}$ complex (**U₅2**). The lowest energy structure of $[\text{Ca}(\text{U})_4]^{2+}$, **U₄2**, has a distorted tetrahedral geometry where one pair of uracil molecules are stabilized by two hydrogen bonds. A slightly concave square planar $[\text{Ca}(\text{U})_4]^{2+}$ complex (**U₄1**) was also found in the characteristic quartet configuration, where each nucleobase interacts with one another through hydrogen bonding. **U₄1** is 32.8 kJ mol^{-1} higher in Gibbs energy

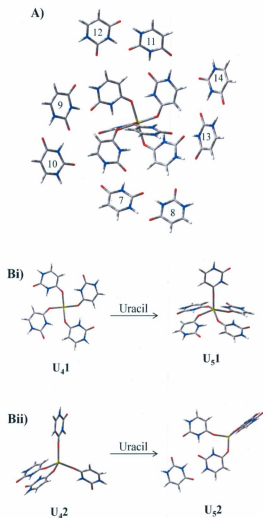


Figure 1.16. A) Representative structures for the addition of uracil monomers to $[\text{Ca}(\text{U})_6]^{2+}$. The numbers indicate the order and location of uracil attachment. B) The addition of a fifth uracil monomer to the square planar (Bi, U₄1) and tetrahedral (Bii, U₄2) isomers creates different products: the square pyramidal U₅1, and a tetrahedral U₅2 that contains a lone uracil monomer in a second shell. Figure adapted with permission from *Phys. Chem. Chem. Phys.* **2012**, *14*, 3304 – 3315.¹⁰³

than U_42 , but is the precursor for the most stable $[Ca(U)_5]^{2+}$ structure, the square pyramidal U_51 . By contrast, the addition of uracil to U_42 results in the nucleobase being placed in a second solvent shell around a tetrahedral core. This structure (U_52), however, is at least 120 kJ mol^{-1} higher in Gibbs energy than U_51 . The observation of U_52 was concluded to be the result of the experimental process, as uracil may condense with the thermodynamically stable tetrahedral $[Ca(U)_4]^{2+}$ complex. The minimum energy structures for the larger clusters ($n \geq 7$) are more uncertain due to the significantly greater number of degrees of freedom. However, since the oscillatory trend of calculated binding energies suggests the tendency for outer shell uracils to form dimers, odd-numbered complexes will contain a lone uracil attached to the inner core. The proposed odd-numbered structures indicate that the lone uracil forms two hydrogen bonds with one of the $[Ca(U)_6]^{2+}$ monomers; the addition of another base closes the "loop" with the hexameric core by forming two hydrogen bonds with the lone uracil but only one with the core. It is telling that the difference in activation energies between successive complexes ($n = 7 - 14$) was between $10 - 15 \text{ kJ mol}^{-1}$, roughly the strength of an extra hydrogen bond.

1.3. Motivation for Studying Lead(II)-Cationized Amino Acids. A survey of the preceding sections demonstrates that much is known about the structures of metal-bound biomolecules. However, most of this research has focused on structures that include alkali or alkaline earth metals, and information on complexes with heavier ions is limited. To remedy this gap, the experiments described in Chapters 3 – 6 of this work examine the structures of lead(II)-cationized amino acids. Lead is interesting for several reasons: it is

unique among *p*-block metals in that it chelates with every amino acid, and gas-phase lead(II) complexes with amino acids are deprotonated ($[\text{Pb}(\text{Aa-H})]^+$), a form which has not been as well documented as the $[\text{M}(\text{Aa})]^{+2+}$ complexes described earlier. Furthermore, lead chelation has important consequences in biochemical processes ranging from heme synthesis to hypertension and anemia, making the characterization of these complexes physiologically relevant.³⁰ This section elaborates on these motivations for studying lead-cationized amino acids, and also explores lead's unique chemistry.

1.3.1. Lead Toxicity. Lead has several physical properties that make it an excellent material for industrial purposes. It is soft, malleable, and has a lower boiling point than many other metals. For these reasons, lead has been used throughout human history to produce a variety of everyday items such as batteries, paints, and building materials. However, its applications are becoming increasingly limited because it is known to be a potent poison. Chronic exposure to lead can cause death, and symptoms include cognitive impairment, palsy, and anemia.^{104,105} Lead poisoning primarily occurs through respiration or ingestion and is particularly dangerous for children. Perhaps the best known example is the case of tetraethyllead, which was introduced in 1923 as an anti-knocking agent in gasoline. This increased lead levels in the atmosphere to such a degree, that by the time it was finally banned more than fifty years later, the average lead level in the blood of American children was four times higher.¹⁰⁶

Treatment of lead poisoning generally requires chelating the lead with proteins or enzymes. Dimercaptosuccinic acid (DMSA, $\text{C}_4\text{H}_6\text{O}_4\text{S}_2$) and ethylenediaminetetraacetic

acid (EDTA, $C_{10}H_{16}N_2O_8$) are particularly useful for this, but are unfortunately nonspecific, as they can remove essential metals from the body as well.³⁰ Considering lead's ability to bind to thiol groups, there have been attempts to develop more Pb-selective chelating agents by incorporating ligands with sulfur atoms, however, none are commonly used for Pb treatment. The toxicity of lead is a consequence of its ability to complex with specific biomolecules. For example, it inhibits the enzyme for heme synthesis, porphobilinogen synthase, and ferrochelatase, which incorporates iron into the heme precursor. In order to understand the chemistry of biological lead complexes, it is important to determine the structure of the preferred lead binding sites. This will allow chelating agents to be designed that specifically remove lead, and not other metals.

1.3.2. Lead Chemistry. The electronic configuration of lead is $[Xe]4f^{14}5d^{10}6s^26p^2$, however, unlike the lighter elements of group 14, its most common oxidation state is +2 rather than +4. This is attributed to the inert pair effect, which explains the difficulty of removing or sharing the valence *s* electrons of post-transition metals as a consequence of relativity.¹⁰⁷⁻¹⁰⁹ In the case of lead(II) for example, the velocity of the 6*s* pair of electrons causes the orbital to contract, meaning that the energy required to remove this lone pair from Pb is higher than removing the corresponding 5*s* lone pair from Sn. The result is that lead(II) contains a relatively inert lone pair of electrons that can influence the arrangement of ligands around the cation. If the lone pair is stereochemically inactive, the lead(II) coordination is said to be holodirected and metal-ligand bonds are distributed evenly throughout the coordination sphere (Figure 1.17).¹¹⁰ On the other hand, if the lone

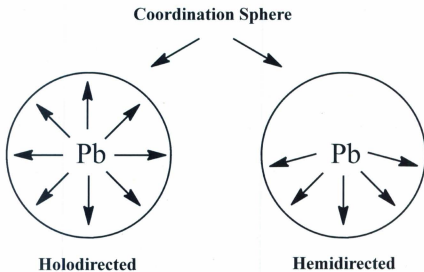


Figure 1.17. Holodirected and hemidirected coordination environments. Figure modified and reprinted from *Inorg. Chem.* **1998**, *37*, 1853 - 1867.¹¹⁰

pair orbital contains some *p* character, it will be stereochemically active and ligands will bind to only one side of the coordination sphere. This arrangement is said to be hemidirected, and is characterized by a noticeable void in the distribution of ligands about the cation. For a generic lead complex where every ligand (L) is identical, the Pb-L bond lengths will be the same in holodirected structures, while in the hemidirected case, the influence of the lone pair will lengthen any nearby Pb-L bonds, and shorten those directly opposite to it.¹¹¹

A comparison of more than 300 lead-containing crystal structures revealed that lead's coordination environment depends primarily on its oxidation state and coordination number. The absence of the 6s lone pair of electrons ensures that all lead(IV) complexes are holodirected, but their presence does not necessarily imply that lead(II) enforces hemidirected geometries. In fact, lead(II) complexes can be both holo- and hemidirected, and the relative favourability of these two arrangements depends on the number of coordinating ligands. When the coordination number is between 2 and 5, lead(II) complexes are hemidirected; both geometries are observed when the coordination number is 6 to 8; and lead(II) complexes with 9 or more ligands are holodirected. This trend suggests that steric effects minimize the influence of the lone pair as the environment around the cation becomes more crowded. In the intermediate cases (6 – 8 ligands), the predilection of lead(II) to form holo- or hemidirected arrangements depends on the nature of the ligands. In general, holodirected geometries are associated with more polarizable ligands (i.e. Cl, Br, and I), while hemidirected structures are typically

observed for complexes with less polarizable ligands, such as oxygen and nitrogen. Furthermore, a complex is more likely to be hemidirected if the ligands are conjugated or if they are able to stabilize each other in some way. For example, molecular orbital calculations on four-coordinate hemidirected complexes demonstrated that the typical energy required to enforce a holodirected geometry, that is, to make the lone pair stereochemically inactive, is roughly $35 - 50 \text{ kJ mol}^{-1}$. This gap increases if the ligands are stabilized by hydrogen bonding, implying that ligand interaction also plays a role in geometry.¹¹⁰

1.4. Objectives. The primary focus of this thesis is the structural characterization of gaseous lead(II)-cationized amino acids by IRMPD spectroscopy. These experiments are motivated by the physiological impact of Pb^{2+} complexes described in Section 1.3, as well as by their unique chemistry. Pb^{2+} interacts with the conjugate bases of amino acids to produce complexes of the form $[\text{Pb}(\text{Aa-H})]^+$, and the structures of these ions may be influenced by a stereochemically active lone pair of electrons found in lead's $6s$ orbital. Neither of these features has been well characterized with respect to the gas-phase structures of amino acids, and this research aims to fill that gap.

Chapters 3 and 4 examine the IRMPD-determined structures of bare and hydrated $[\text{Pb}(\text{Aa-H})]^+$ complexes involving seven amino acids with nonpolar side chains (Aa = proline (Pro), alanine (Ala), valine (Val), leucine (Leu), isoleucine (Ile), phenylalanine (Phe), methionine (Met) and two with polar side chains (lysine (Lys), and glutamic acid (Glu)). These are investigated in order to determine whether or not the amino acid side

chain significantly influences ion structure, as well as to gauge the stabilization of Pb^{2+} by different functional groups. These experiments are complemented in Chapter 5 by the use of BIRD kinetic measurements and master equation modeling to determine the water binding energies of the $[\text{Pb}(\text{Aa-H})\text{H}_2\text{O}]^+$ complexes. This provides insight into how solvation influences the structures of these ions, which is of interest because solvent stabilizes zwitterionic amino acid tautomers in bulk solution. Chapter 6 extends the IRMPD characterization of metal-cationized amino acids to $[\text{M}(\text{Ala-H})]^+$ and $[\text{M}(\text{BMAA-H})]^+$ complexes involving Be^{2+} , Mg^{2+} , Ca^{2+} , Sr^{2+} , Ba^{2+} and Zn^{2+} . Comparisons between these experiments and those in Chapters 3 and 4 will help determine the influence of metal cation size on amino acid structure.

References

1. Fridgen, T. D. *Mass. Spectrom. Rev.* **2009**, *28*, 586 – 607.
2. Polfer, N. C.; Oomens, J. *Mass Spectrom. Rev.* **2009**, *28*, 468 – 494.
3. Finney, L. A.; O'Halloran, T. V. *Science* **2003**, *300*, 931 - 936.
4. Burda, J. V.; Šponer, J.; Leszczynski, J.; Hobza, P. J. *Phys. Chem. B* **1997**, *101*, 9670 - 9677.
5. Chakrabarti, P. *Protein Eng.* **1990**, *4 (1)*, 49 - 56.
6. Dunbar, R. C.; Oomens, J.; Orlova, G.; Bohme, D. K. *Int. J. Mass Spectrom.* **2011**, *308*, 330 - 337.
7. Dunbar, R. C.; Steill, J. D.; Oomens, J. *J. Am. Chem. Soc.* **2011**, *133*, 1212 - 1215.
8. Bakker, J. M.; Salpin, J.-Y.; Maître, P. *Int. J. Mass Spectrom.* **2009**, *283*, 214 - 221.
9. Oh, H.-B.; Breuker, K.; Sze, S. K.; Ge, Y.; Carpenter, B. K.; McLafferty, F. W. *P. Natl. Acad. Sci.* **2002**, *99 (25)*, 15863 - 15868.
10. Polfer, N. C.; Oomens, J.; Suhai, S.; Paizs, B. *J. Am. Chem. Soc.* **2007**, *129*, 5887 - 5897.
11. Polfer, N. C.; Paizs, B.; Snoek, L. C.; Compagnon, I.; Suhai, S.; Meijer, G.; von Helden, G.; Oomens, J. *J. Am. Chem. Soc.* **2005**, *127*, 8571 - 8579.
12. Bush, M. F.; O'Brien, J. T.; Prell, J. S.; Saykally, R. J.; Williams, E. R. *J. Am. Chem. Soc.* **2007**, *129*, 1612 - 1622.
13. Burt, M. B.; Fridgen, T. D. *Eur. J. Mass Spectrom.* **2012**, *18 (2)*, 235 - 250.
14. McFail-Isom, L.; Sines, C. C.; Williams, L. D. *Curr. Opin. Struct. Biol.* **1999**, *9*, 298 - 304.
15. Rajabi, K.; Gillis, E. A. L.; Fridgen, T. D. *J. Phys. Chem. A* **2010**, *114*, 3449 - 3456.
16. Trujillo, C.; Lamsabhi, A. M.; M6, O.; Yáñez, M.; Salpin, J.-Y., *Int. J. Mass Spectrom.* **2011**, *306*, 27 - 36.
17. Russo, N.; Toscano, M.; Grand, A. *J. Am. Chem. Soc.* **2001**, *123*, 10272 - 10279.

18. Kabeláč, M.; Hobza, P. *J. Phys. Chem. B* **2006**, *110*, 14515 - 14523.
19. Pyle, A. M. *J. Biol. Inorg. Chem.* **2002**, *7*, 679 - 690.
20. Potaman, V. N.; Soyfer, V. N. *J. Biomo. Struct. Dyn.* **1994**, *11*, 1035 - 1040.
21. Chen, F.-M. *Biochemistry* **1984**, *23*, 6159 - 6165.
22. Hajieva, P.; Behl, C. *Curr. Pharm. Design* **2006**, *12*, 699 - 704.
23. Drew, S. C.; Barnham, K. J. *Acc. Chem. Res.* **2011**, *44*, 1146 - 1155.
24. Faller, P. *ChemBioChem* **2009**, *10*, 2837 - 2845.
25. Smith, D. G.; Cappai, R.; Barnham, K. J. *Biochim. Biophys. Acta* **2007**, *1768*, 1976 - 1990.
26. Barnham, K. J.; Bush, A. I. *Curr. Opin. Chem. Biol.* **2008**, *12*, 222 - 228.
27. Velez, S.; Nair, N. G.; Reddy, V. P. *Colloids Surf. B* **2008**, *66*, 291 - 294.
28. Fisher, A. E. O.; Naughton, D. P. *Biomed. Pharmacother.* **2005**, *59*, 158 - 162.
29. Dickerson, R. E.; Drew, H. R.; Conner, B. N.; Wing, R. M.; Fratini, A. V.; Kopka, M. L. *Science* **1982**, *216*, 475 - 485.
30. Patrick, L. *Altern. Med. Rev.* **2006**, *11*, 2 - 22.
31. Aebersold, R.; Mann, M. *Nature* **2003**, *422*, 198 - 207.
32. Link, A. J.; Eng, J.; Schieltz, D. M.; Carmack, E.; Mize, G. J.; Morris, D. R.; Garvik, B. M.; Yates, J. R. I. *Nat. Biotechnol.* **1999**, *17*, 676 - 682.
33. Tipton, J. D.; Tran, J. C.; Catherman, A. D.; Ahlf, D. R.; Durbin, K. R.; Kelleher, N. L. *J. Biol. Chem.* **2011**, *286*, 25451 - 25458.
34. Harris, D. C., *Quantitative Chemical Analysis*. 6th ed.; W. H. Freeman: 2002.
35. Skoog, D. A.; Holler, F. J.; Crouch, S. R., *Principles of Instrumental Analysis*. 6th ed.; Brooks Cole: 2006.
36. Eyler, J. R. *Mass Spectrom. Rev.* **2009**, *28*, 448 - 467.

37. Atkins, C. G.; Banu, L.; Rowsell, M.; Blagojevic, V.; Bohme, D. K.; Fridgen, T. D. *J. Phys. Chem. B* **2009**, *113*, 14457 - 14464.
38. Atkins, C. G.; Rajabi, K.; Gillis, E. A. L.; Fridgen, T. D. *J. Phys. Chem. A* **2008**, *112*, 10220 - 10225.
39. Burt, M. B.; Decker, S. G. A.; Atkins, C. G.; Rowsell, M.; Peremans, A.; Fridgen T. D. *J. Phys. Chem. B* **2011**, *115*, 11506 - 11518.
40. Gillis, E. A. L.; Rajabi, K.; Fridgen, T. D. *J. Phys. Chem. A* **2009**, *113*, 824 - 832.
41. Gillis, E. A. L.; Fridgen, T. D. *Int. J. Mass Spectrom.* **2010**, *297*, 2 - 8.
42. Rajabi, K.; Fridgen, T. D. *J. Phys. Chem. A* **2008**, *112*, 23 - 30.
43. Rajabi, K.; Theel, K.; Gillis, E. A. L.; Beran, G.; Fridgen, T. D. *J. Phys. Chem. A* **2009**, *113*, 8099 - 8107.
44. Ali, O. Y.; Fridgen, T. D. *Int. J. Mass Spectrom.* **2011**, *308*, 167 - 174.
45. Oepts, D.; van der Meer, A. F. G.; van Amersfoort, P. W. *Infrared Phys. Technol.* **1995**, *36*, 297 - 308.
46. Ortega, J. M.; Berset, J. M.; Chaput, R.; Glotin, F.; Humbert, G.; Jaroszynski, D.; Joly, P.; Kergosien, B.; Lesrel, J. *Nucl. Instrum. Methods Phys. Res., Sect. A* **1996**, *375*, 618 - 625.
47. Stepanian, S. G.; Reva, I. D.; Radchenko, E. D.; Rosado, M. T. S.; Duarte, M. L. T. S.; Fausto, R.; Adamowicz, L. *J. Phys. Chem. A* **1998**, *102*, 1041 - 1054.
48. Heeren, R. M. A.; Kleinnijenhuis, A. J.; McDonnell, L. A.; Mize, T. H. *Anal. Bioanal. Chem.* **2004**, *378*, 1048 - 1058.
49. Dunbar, R. C. *Mass Spectrom. Rev.* **2004**, *23*, 127 - 158.
50. Rodriguez-Cruz, S. E.; Jockusch, R. A.; Williams, E. R. *J. Am. Chem. Soc.* **1998**, *120*, 5842 - 5843.
51. Rodriguez-Cruz, S. E.; Jockusch, R. A.; Williams, E. R. *J. Am. Chem. Soc.* **1999**, *121*, 8898 - 8906.
52. Shannon, R. D. *Acta Cryst.* **1976**, *32*, 751 - 767.

53. Benesch, J. L. P.; Ruotolo, B. T.; Simmons, D. A.; Robinson, C. V. *Chem. Rev.* **2007**, *107*, 3544 - 3567.
54. Kebarle, P.; Tang, L. *Anal. Chem.* **1993**, *65*, 972 - 986.
55. Chappo, C. J.; Paul, J. B.; Provencal, R. A.; Roth, K.; Saykally, R. J. *J. Am. Chem. Soc.* **1998**, *120*, 12956 - 12957.
56. Xu, S.; Nilles, J. M.; Bowen, K. H. *J. Chem. Phys.* **2003**, *119*, 10696 - 10701.
57. Jensen, J. H.; Gordon, M. S. *J. Am. Chem. Soc.* **1995**, *117*, 8159 - 8170.
58. Tajkhorshid, E.; Jalkanen, K. J.; Suhai, S. *J. Phys. Chem. B* **1998**, *102*, 5899 - 5913.
59. Dunbar, R. C.; Polfer, N. C.; Oomens, J. *J. Am. Chem. Soc.* **2007**, *129*, 14562 - 14563.
60. Rode, B. M. *Peptides* **1999**, *20*, 773 - 786.
61. Ma, J. C.; Dougherty, D. A. *Chem. Rev.* **1997**, *97*, 1303 - 1324.
62. Armentrout, P. B.; Rodgers, M. T.; Oomens, J.; Steill, J. D. *J. Phys. Chem. A* **2008**, *112*, 2248 - 2257.
63. Marino, T.; Toscano, M.; Russo, N.; Grand, A. *J. Phys. Chem. B* **2006**, *110*, 24666 - 24673.
64. Drayß, M. K.; Armentrout, P. B.; Oomens, J.; Schäfer, M. *Int. J. Mass Spectrom.* **2010**, *297*, 18 - 27.
65. Strittmatter, E. F.; Lemoff, A. S.; Williams, E. R. *J. Phys. Chem. A* **2000**, *104*, 9793 - 9796.
66. Constantino, E.; Rodríguez-Santiago, L.; Sodupe, M.; Tortajada, J. *J. Phys. Chem. A* **2005**, *109*, 224 - 230.
67. Moision, R. M.; Armentrout, P. B. *J. Phys. Chem. A* **2002**, *106*, 10350 - 10362.
68. Kapota, C.; Lemaire, J.; Maître, P.; Ohanessian, G. *J. Am. Chem. Soc.* **2004**, *126*, 1836 - 1842.
69. Bush, M. F.; Oomens, J.; Saykally, R. J.; Williams, E. R. *J. Am. Chem. Soc.* **2008**, *130*, 6463 - 6471.

70. Forbes, M. W.; Bush, M. F.; Polfer, N. C.; Oomens, J.; Dunbar, R. C.; Williams, E. R.; Jockusch, R. A. *J. Phys. Chem. A* **2007**, *111*, 11759-11770.
71. Price, W. D.; Jockusch, R. A.; Williams, E. R. *J. Am. Chem. Soc.* **1997**, *119*, 11988 - 11989.
72. Jockusch, R. A.; Price, W. D.; Williams, E. R. *J. Phys. Chem. A* **1999**, *103*, 9266 - 9274.
73. Bush, M. F.; Forbes, M. W.; Jockusch, R. A.; Oomens, J.; Polfer, N. C.; Saykally, R. J.; Williams, E. R. *J. Phys. Chem. A* **2007**, *111*, 7753 - 7760.
74. Polfer, N. C.; Oomens, J.; Dunbar, R. C. *Phys. Chem. Chem. Phys.* **2006**, *8*, 2744 - 2751.
75. Lucas, B.; Grégoire, G.; Lemaire, J.; Maitre, P.; Ortega, J.-M.; Rupenyany, A.; Reimann, B.; Schermann, J.-P.; Desfrancois, C. *Phys. Chem. Chem. Phys.* **2004**, *6*, 2659 - 2663.
76. Lucas, B.; Grégoire, G.; Lemaire, J.; Maitre, P.; Glotin, F.; Schermann, J.-P.; Desfrancois, C. *Int. J. Mass Spectrom.* **2005**, *243*, 105 - 113.
77. Wu, R.; McMahon, T. B. *J. Am. Chem. Soc.* **2007**, *129*, 11312 - 11313.
78. Polfer, N. C.; Oomens, J.; Dunbar, R. C. *ChemPhysChem* **2008**, *9*, 579 - 589.
79. Oh, H.-B.; Lin, C.; Hwang, H. Y.; Zhai, H.; Breuker, K.; Zabrouskov, V.; Carpenter, B. K.; McLafferty, F. W. *J. Am. Chem. Soc.* **2005**, *127*, 4076 - 4083.
80. Wu, R.; McMahon, T. B. *J. Am. Chem. Soc.* **2007**, *129*, 4864 - 4865.
81. Kong, X.; Tsai, I.-A.; Sabu, S.; Han, C.-C.; Lee, Y. T.; Chang, H.-C.; Tu, S.-Y.; Kung, A. H.; Wu, C.-C. *Angew. Chem. Int. Ed.* **2006**, *45*, 4130 - 4134.
82. Oomens, J.; Polfer, N.; Moore, D. T.; van der Meer, L.; Marshall, A. G.; Eyler, J. R.; Meijer, G.; von Helden, G. *Phys. Chem. Chem. Phys.* **2005**, *7*, 1345 - 1348.
83. Salpin, J.-Y.; Guillaumont, S.; Tortajada, J.; MacAleese, L.; Lemaire, J.; Maitre, P. *ChemPhysChem* **2007**, *8*, 2235 - 2244.
84. Pankewitz, T.; Lagutschenkov, A.; Niedner-Schatteburg, G.; Xantheas, S. S.; Lee, Y.-T. *J. Chem. Phys.* **2007**, *126*, 074307.
85. Rodgers, M. T.; Armentrout, P. B. *J. Am. Chem. Soc.* **2000**, *122*, 8548 - 8558.

86. Hanus, M.; Kabeláč, M.; Rejnek, J.; Ryjáček, F.; Hobza, P. *J. Phys. Chem. B* **2004**, *108*, 2087 - 2097.
87. Russo, N.; Toscano, M.; Grand, A. *J. Phys. Chem. B* **2001**, *105*, 4735 - 4741.
88. Anwander, E. H. S.; Probst, M. M.; Rode, B. M. *Biopolymers* **1990**, *29*, 757 - 769.
89. Lamsabhi, A. M.; Alcamí, M.; Mó, O.; Yáñez, M.; Tortajada, J.; Salpin, J.-Y. *ChemPhysChem* **2007**, *8*, 181 - 187.
90. Ali, O. Y.; Fridgen, T. D. *ChemPhysChem* **2012**, *13*, 588 - 596.
91. Guillaumont, S.; Tortajada, J.; Salpin, J.-Y.; Lamsabhi, A. M. *Int. J. Mass Spectrom.* **2005**, *243*, 279 - 293.
92. Trujillo, C.; Lamsabhi, A. M.; Mó, O.; Yáñez, M.; Salpin, J.-Y. *Org. Biomol. Chem.* **2008**, *6*, 3695 - 3702.
93. Ali, O. Y. *Structures of Metal Dication-Uracil Complexes in the Gas Phase and Matrix Isolated Hydrogen-Bonded Complexes*. Memorial University of Newfoundland, St. John's, 2011.
94. Fridgen, T. D.; Ali, O. Y.; Randell, N. M.; Fridgen, T. D., Primary Fragmentation Pathways of Gas Phase $[M(\text{Uracil H})(\text{Uracil})]^+$ Complexes ($M=\text{Zn, Cu, Ni, Co, Fe, Mn, Cd, Pd, Mg, Ca, Sr, Ba, and Pb}$): Loss of Uracil versus H₂CO. *ChemPhysChem* **2012**, *13*, (6), 1507 - 1513.
95. Davis, J. T. *Angew. Chem. Int. Ed.* **2004**, *43*, 668 - 698.
96. Shafer, R. H.; Smirnov, I. *Biopolymers* **2000**, *56*, 209 - 227.
97. Katayama, S.; Shiota, G.; Oshimura, M.; Kawasaki, H. *J. Cancer Res. Clin. Oncol.* **1999**, *125*, 405 - 410.
98. Cheong, C.; Moore, P. B. *Biochemistry* **1992**, *31*, 8406 - 8414.
99. Koch, K. J.; Aggerholm, T.; Nanita, S. C.; Cooks, R. G. *J. Mass Spectrom.* **2002**, *37*, 676 - 686.
100. Aggerholm, T.; Nanita, S. C.; Koch, K. J.; Cooks, R. G. *J. Mass Spectrom.* **2003**, *38*, 87 - 97.
101. Zins, E.-L.; Rochut, S.; Pepe, C. *J. Mass Spectrom.* **2009**, *44*, 813 - 820.

102. Gillis, E. A. L. *Structures and Energetics of Non-Covalently Bound Gaseous Ions by Infrared Photodissociation*. Memorial University of Newfoundland, St. John's, 2011.
103. Gillis, E. A. L.; Demireva, M.; Nanda, K.; Beran, G. J. O.; Williams, E. R.; Fridgen, T. D. *Phys. Chem. Chem. Phys.* **2012**, *14*, 3304-3315.
104. Grandjean, P. *Environ. Res.* **1978**, *17*, 303 - 321.
105. Needleman, H. L.; Schell, A.; Bellinger, D.; Leviton, A.; Allred, E. N. *N. Engl. J. Med.* **1990**, *322*, 83 - 88.
106. Needleman, H. L. *Environ. Res.* **2000**, *84*, 20 - 35.
107. Pitzer, K. S. *Acc. Chem. Res.* **1979**, *12*, 271 - 276.
108. Pyykkö, P.; Desclaux, J.-P. *Acc. Chem. Res.* **1979**, *12*, 276 - 281.
109. Pyykkö, P. *Chem. Rev.* **1988**, *88*, 563 - 594.
110. Shimoni-Livny, L.; Glusker, J. P.; Bock, C. W. *Inorg. Chem.* **1998**, *37*, 1853 - 1867.
111. Hancock, R. D.; Reibenspies, J. H.; Maumela, H. *Inorg. Chem.* **2004**, *43*, 2981 - 2987.

Chapter 2

Experimental and Theory

2.1. Introduction. Gas-phase techniques allow the intrinsic properties of ions, such as structure and reactivity, to be investigated in the absence of bulk solvents.¹⁻⁵ This is particularly helpful for understanding the physical chemistry of biological ions since, as was discussed in Chapter 1, the addition of a single metal ion or solvent molecule to these species often results in measurable structural changes. Comparing the structures of bare gas-phase ions with their solvated or metal cationized counterparts can therefore reveal the forces controlling the structures of these complexes as well as the influence of the metal ions and solvents themselves.

The majority of research into the structures of biomolecules typically involves isolating the species of interest in a low-pressure environment using tandem mass spectrometry and then activating it to examine its behaviour.¹⁻²⁶ The experiments described in Chapters 3 – 6 use a Fourier transform ion cyclotron resonance mass spectrometer (FT-ICR MS) to isolate metal cationized amino acids long enough for them to be activated by one of three techniques: infrared multiple photon dissociation (IRMPD) spectroscopy, blackbody infrared radiative dissociation (BIRD), or collision-induced dissociation (CID). Each of these techniques, as well as the computational methods that are often used to support them, will be detailed throughout this chapter.

2.2. Instrumentation. The experiments presented in this work use a Bruker Apex Qe 7.0 T FT-ICR mass spectrometer coupled with an optical parametric oscillator (Figure 2.1). The FT-ICR MS is depicted in more detail in Figure 2.2, and can be broadly separated into four segments: the gas-phase ion source, quadrupole region, ion transfer optics, and ICR cell. The gas-phase ions are initially generated from the solution phase using electrospray ionization (ESI), and are subsequently accelerated through a quadrupole mass filter into a hexapole collision cell. Solvated ions can be prepared in this cell by minimizing the collision (Ar) gas flow and introducing solvent (10^{-2} mbar) through a microvalve that separates the collision cell from a degassed solvent reservoir; this is particularly useful for creating singly hydrated complexes.²⁷ The bare or solvated ions are then injected into the “zero”-pressure (10^{-10} mbar) ICR cell using ion transfer optics, where they are isolated as well as detected. A notable feature of ICR cells is that they are able to store ions for extended periods of time, allowing them to be activated through different methods. For example, the trapped ions can be irradiated by light from the optical parametric oscillator (OPO) to perform IRMPD spectroscopy, induced to undergo in-cell CID by a 10^{-8} mbar pulse of collision gas, or allowed to dissociate by absorbing ambient blackbody photons by BIRD. The following sections will describe three components of this instrumentation: the ESI source, the ICR cell, and the optical parametric oscillator (OPO).

2.2.1. Electrospray Ionization. Generating gas-phase ions from solution requires energy to remove the solvent or matrix. There are many techniques capable of achieving this:



Figure 2.1. A Bruker Apex Qe 7.0 T FT-ICR mass spectrometer coupled with an optical parametric oscillator.

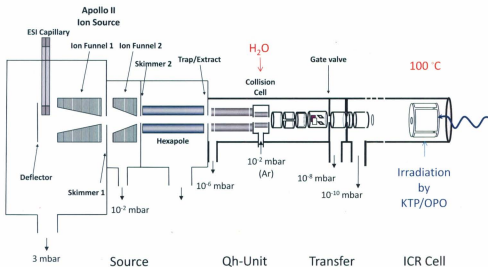


Figure 2.2. A schematic of the Bruker Apex Qe 7.0 T FT-ICR mass spectrometer highlighting the ion source, collision cell, and ICR cell. Figure adapted with permission from *J. Am. Soc. Mass Spectrom.* **2009**, *20*, 411 – 418.²⁷

matrix-assisted laser desorption ionization, fast atom (or particle) bombardment, and plasma desorption; however, each of these methods often delivers sufficient energy to the species of interest to cause fragmentation or further ionization. Electrospray ionization, by contrast, bestows very little additional internal energy to the molecule and is considered to be one of the softest methods available to transfer ions from solution to the gas phase.²⁸⁻³² In addition to its non-destructive nature, ESI has the additional benefit that the ions are generated from solutions containing typical organic solvents (water, methanol, etc.). This means that a desired ion can be prepared using conventional solution-phase chemistry and then isolated in the gas phase.

The general electrospray process is demonstrated in Figure 2.3 and will briefly be introduced here. An ionic solution is first prepared by solvating the species of interest, typically in a solution of water and polar liquids. This solution then flows into a narrow capillary with an opening at the other end. An electric field is generated at this orifice by applying a potential across the opening; this causes the area near the surface of the liquid to acquire a net charge. In positive ion mode, for example, cations are forced towards the surface of the liquid while anions are pulled away. The accumulated charge causes the surface to destabilize through Coulombic repulsion, and the liquid is drawn out in the shape of a cone towards the mass spectrometer. If the potential across the capillary is strong enough, sufficient charge will accumulate to eject discrete droplets from the cone. At this stage, the charged droplets will begin splitting into smaller droplets as solvent evaporates. For a spherical droplet of radius, r , and surface tension, λ , this process is

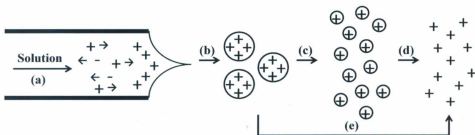


Figure 2.3. The electrospray process: A solution (a) is flowed through a capillary with a potential applied across a narrow opening at the other end. This produces charged droplets (b) that gradually shrink as solvent evaporates (c). Gas-phase ions are then produced according to the charged-residue (d) or ion evaporation (e) models. Figure adapted with permission from *Anal. Chem.* **1993**, *65*, 972A – 986A.²⁸

governed by the Rayleigh equation (Eq. 2.1), which determines the limiting charge, Q , at which a droplet can stay together. ϵ_0 is the permittivity of the vacuum.²⁸

$$Q = 64\pi^2\epsilon_0\lambda r^3 \quad (2.1)$$

In order to reduce the size of the droplets as quickly as possible, the solution is typically formulated with volatile organic solvents and the solvent evaporation rate is increased by heating the ESI source. Eventually, the charged droplets become small enough to produce gas-phase ions. The exact mechanism for this final step is uncertain, but there are at least two possibilities: the charged-residue model, which predicts that solvent evaporation eventually results in a droplet containing just one ion which is subsequently desolvated, and the ion evaporation model, which predicts that ions will statistically evaporate from larger charged droplets.²⁸ In general, the charged-residue model is the dominant mechanism for large ions, such as proteins, whereas small clusters are thought to be produced through ion evaporation.³³

2.2.2. Fourier Transform Ion Cyclotron Resonance Mass Spectrometry. Ion cyclotron resonance mass spectrometry is based on the principle that the mass-to-charge ratio of an ion can be distinguished by its cyclotron frequency. When an ion of mass, m , and charge, z , is introduced into a spatially uniform magnetic field, B , it is subject to the magnetic component of the Lorentz force (Eq. 2.2, where e is the elementary charge).³⁴

$$\vec{F} = (ze)\vec{v} \times \vec{B} \quad (2.2)$$

If the magnetic field is perpendicular to the velocity, v , of the ion, it will cause the

ion to revolve as in Figure 2.4. Since the Lorentz force directs the ion's centripetal motion, it is straightforward to demonstrate that m/z is inversely proportional to the cyclotron frequency, ω (Eq. 2.3).³⁵⁻³⁷

$$\frac{m}{z} = \frac{e\vec{B}}{\omega} \quad (2.3)$$

The significant feature of this equation is that the mass-to-charge ratio of an ion in a magnetic field is independent of the ion's velocity; every ion with the same m/z will have identical cyclotron frequencies regardless of their translational energy when they enter the ICR cell. This means that, unlike traditional double-focusing mass spectrometers, no energy resolution is necessary. Taking the differential of Eq. 2.3 reveals that the mass resolution of an ICR cell is directly proportional to the magnetic field strength (Eq. 2.4).³⁶ The 7.0 T magnet of the Bruker Apex Qe FT-ICR mass spectrometer, for example, has a resolving power greater than 10^5 , which is more than sufficient for the experiments described here.

$$\frac{m}{\Delta m} = \frac{-ze\vec{B}}{m\Delta\omega} \quad (2.4)$$

From another viewpoint, the resolution of an FT-ICR mass spectrometer is essentially the number of cyclotron orbits an ion can undergo during the detection process. Hence, in order to precisely measure an ion's cyclotron frequency, it must be confined in the ICR cell for a sufficient length of time to maximize the resolution. The Lorentz force restricts the motion of ions to orbits, but there is nothing stopping the ions

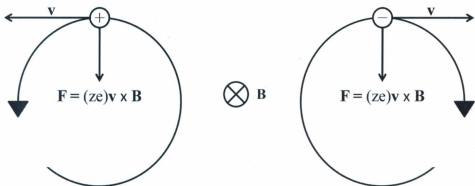


Figure 2.4. The motion of positive and negative ions in a uniform magnetic field.

from simply escaping in the axial direction. For this reason, an axial electric field is applied at both ends of the cell to contain the ions. This configuration, where ions are radially trapped by a magnetic field and axially confined by an electric field, is known as a Penning trap and is shown in Figure 2.5. The Penning trap of the Bruker Apex Qe 7.0 T FT-ICR mass spectrometer is a (mostly) closed cylinder composed of two trapping plates, two excitation plates, and two detection plates located in the center of the magnetic field. The diameter of the cell as well as the distance between the trapping plates are both 60 mm. The potential of the front trapping plate is 0.5 V while that of the rear is 1.5 V; both plates have the same polarity as the trapped ions. This creates a potential well that enables the ions to enter the cell, but which prevents them from leaving through the other side.

The trapped ions oscillate axially since the electric field strength varies linearly near the center of the ICR cell. This trapping oscillation, ω_t , is described by Eq. 2.5 where V_t is the trapping voltage, a is the distance between the trapping plates, and α is a constant that depends on the shape of the cell.

$$\omega_t = \left(\frac{4ze\alpha V_t}{ma^2} \right)^{\frac{1}{2}} \quad (2.5)$$

The crossed electric and magnetic fields also introduce a radial “magnetron” motion (Figure 2.6) that counteracts the magnetic component of the Lorentz force. This occurs because the ions pressed towards the center of the cell bulge outwards along a plane of constant electrostatic potential. The magnetron frequency, ω_m (Eq. 2.6), reduces the observed cyclotron frequency, ω_{obs} , according to Eq. 2.7. It should be noted, however,

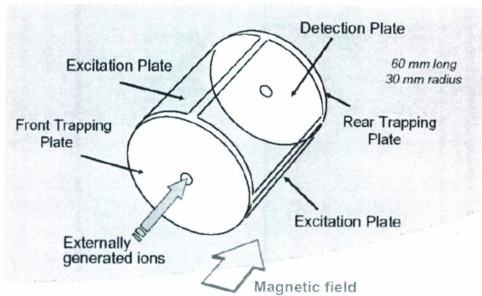


Figure 2.5. Schematic diagram of a Penning trap. Figure reprinted from the Bruker Daltonics Apex-Qe Series Generation II User Manual. Version 2.0 (July 2008).

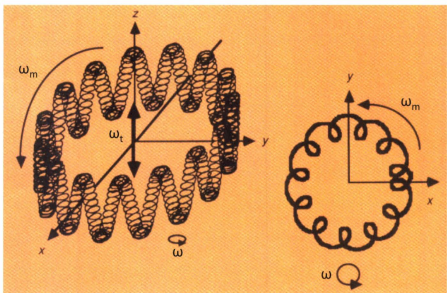


Figure 2.6. Ion motion in the ICR cell is described by three components: the cyclotron (ω), trapping (ω_t), and magnetron (ω_m) frequencies. Figure adapted with permission from *Anal. Chem.* **1991**, *63*, 215A – 229A.³⁶

that this shift is independent of m/z .

$$\omega_m = \left(\frac{\alpha V_T}{2\alpha^2 \bar{B}} \right)^{\frac{1}{2}} \quad (2.6)$$

$$\omega_{obs} = \omega - \omega_m \quad (2.7)$$

The Penning trap allows ions to be stored long enough for a precise determination of their cyclotron frequencies. In principle the ions could be held indefinitely, but in practice collisions between the trapped ions and background gases, as well as the absorption of ambient photons, limits the data acquisition period to $\sim 10^5$ s. Typical FT-ICR experiments are performed at low pressures (10^{-10} mbar) in order to increase m/z resolution. As the ions orbit, their electric fields induce a charge in the two detection plates. These plates are of opposite polarity, so the induced charge varies as a function of their distance from the ion. This results in a transient sinusoidal signal that reveals the frequency and magnitude of the orbiting ions as a function of time (Figure 2.7). This detection method is ideal for a single ion, but when multiple ions are injected into the ICR cell their cyclotron orbits will be in different orbital phases. Since the charge induced on the detector plates by completely out of phase ions (180° apart) will balance out, the incoherent motion of a large number of ions effectively reduces the observed net electrical signal to zero. The solution to this problem is using the excitation plates to irradiate the trapped ions with a radio frequency field, E , in resonance with their cyclotron frequencies. This provides phase coherence for the ions and accelerates them into larger orbits where they can be more efficiently detected. The radius, r , of the new orbit is a function of the length, t , of the excitation event (Eq 2.8).

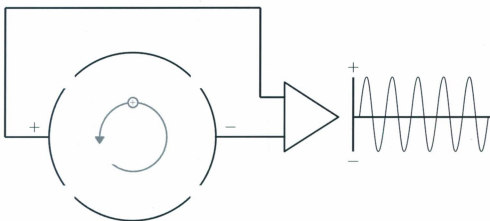


Figure 2.7. A packet of ions undergoing uniform cyclotron motion is detected as a sinusoidal signal. Figure reprinted from the Bruker Daltonics Apex-Qe Series Generation II User Manual, Version 2.0 (July 2008).

$$r = \frac{Et}{2B} \quad (2.8)$$

Ions with the same mass-to-charge ratio will orbit together as an ion packet, and can be distinguished from other ion packets by their cyclotron frequency. Eq. 2.8 also demonstrates why FT-ICR mass spectrometry is highly selective: specific ions, isotopes for example, can be ejected from the ICR cell by exciting them to the cell boundaries. In a similar manner, a single m/z can be isolated by sweeping the cell with every frequency besides that of the ion of interest.

The acquisition of a mass spectrum consists of four steps. The ICR cell is initially purged by changing the relative potentials of the trapping plates to axially eject any remaining ions from earlier experiments; the process is then reversed to inject new ions into the cell and the trapping conditions are restored. Once the ions are confined in the cell, excitation and detection occur in rapid succession (1 – 10 ms). As was mentioned earlier, ion detection results in a transient sinusoidal waveform from which mass spectral data can be extracted. In ideal cases involving a single m/z , the cyclotron frequency can be directly determined from the periodicity of the wave. However, because experiments involving multiple ions or isotopes complicate the signal due to wave superpositioning, fast Fourier transforms are used to convert the waveform into a mass spectrum (Figure 2.8). A description of fast Fourier transform algorithms is beyond the scope of this work, but in brief, they quickly and accurately approximate the solutions of discrete Fourier transforms.

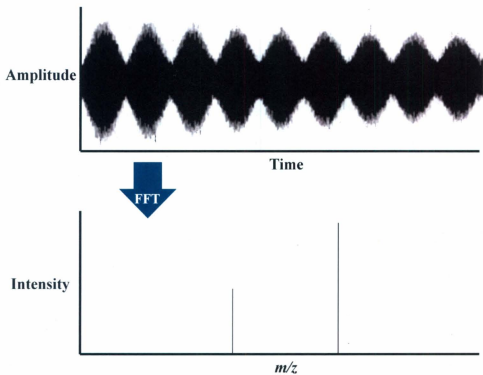


Figure 2.8: A time-dependent ion signal can be converted to the m/z domain using a fast Fourier transform. Figure adapted from the Bruker Daltonics Apex-Qe Series Generation II User Manual, Version 2.0 (July 2008).

2.2.3. Optical Parametric Oscillators. Optical parametric oscillators are nonlinear crystals that convert a stream of high energy photons, such as coherent light from a laser, into two lower energy waves.³⁸ They operate on the principle that the response of an electric field to a polarized dielectric material will depend on the angle of the light with respect to the crystal axis. The frequencies of the output waves, called the signal and idler, can therefore be controlled by rotating the crystal.

The OPO installed at Memorial University is an 8 x 12 x 25 mm KTP crystal (potassium titanyl phosphate, KTiOPO_4) pumped collinearly by the 1064 nm fundamental line of a Brilliant B Nd:YAG laser (neodymium-doped yttrium aluminum garnet, $\text{Nd:Y}_3\text{Al}_5\text{O}_{12}$) (Figure 2.9).^{39,40} The crystal is cut in the ZX plane with an angle of 47.2° with respect to the Z-axis. Rotating the face struck by light (Y-axis) by $\pm 8^\circ$ allows the pump wave to produce signal and idler waves between 1.5 – 2.1 and 2.1 – 3.5 μm respectively. The OPO is placed in a 35 mm cavity containing two dichroic mirrors; the input mirror is highly reflective with respect to the signal wave, whereas the output mirror reflects 30% of the signal wave but is transparent to both the pump and idler waves. This simultaneously produces perpendicular beams with bandwidths of about 3 cm^{-1} ; the signal beam is parallel to the crystal's rotational axis while the idler beam is directed towards the ICR cell to be used for infrared spectroscopy. The pump wave is emitted into the cavity through the input mirror in 6 ns (850 mJ) pulses at 10 Hz, but the energy of the output pulses are a function of their wavelengths (Figure 2.10). For the idler beam, the energy maximum occurs at 2.6 μm where the conversion efficiency of the laser

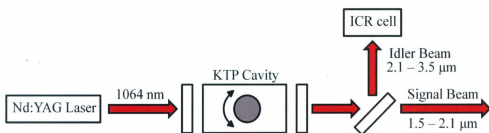


Figure 2.9. Schematic representation of a KTP/OPO.

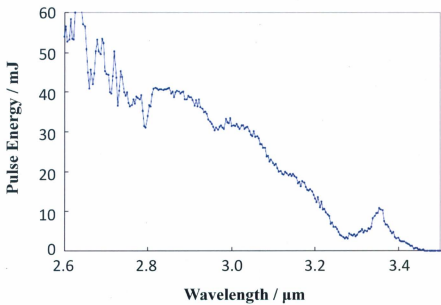


Figure 2.10. The intensity of the KTP/OPO as a function of wavelength. Figure courtesy of Dr. André Peremans.

pulse is 20%. The idler output drops with increasing wavelength until about 3.4 μm , where it stops entirely. This restricts the usable range for infrared spectroscopy to 2.5 – 3.13 μm (4000 – 3200 cm^{-1}).

The slight divergence (0.5°) and astigmatism of the idler beam are corrected using a spherical 3000 mm focal length (f) Au mirror and a cylindrical CaF_2 lens ($f = 400$ mm). The beam is focused towards the ICR cell by a second CaF_2 ($f = 200$ mm) lens along a path purged of CO_2 and H_2O by dry air and gaseous N_2 . The beam then enters the ICR cell through a BaF_2 window and irradiates the trapped ions.

2.3. Experimental. The lengthy trapping times made possible by FT-ICR mass spectrometers, combined with their ability to be mated with a variety of ion injection and excitation devices, make them ideal environments for determining an ion's thermochemistry, structure, and reactivity.^{36,41} The FT-ICR MS described in Section 2.2 is coupled with a KTP/OPO and uses electrospray ionization to generate gas-phase ions. This allows several in-cell ion activation techniques to be performed: infrared multiple photon dissociation (IRMPD) spectroscopy, blackbody infrared radiative dissociation (BIRD), and sustained off-resonance irradiation collision-induced dissociation (SORI-CID). These techniques, which are briefly introduced here, are described in detail throughout Sections 2.3.1 – 2.3.3.

IRMPD spectroscopy is a structure-sensitive technique that requires an intense and tunable infrared light source.^{2,3,5,41} This approach determines structural features of a gas-phase ion by irradiating the analyte over a range of energies and monitoring the extent of its dissociation as a function of the frequency of the impinging radiation. Any

observed vibrational bands are then assigned to specific functional groups of the molecule, and these conclusions are typically supported by comparing the experimental IRMPD spectrum with theoretical infrared spectra determined from electronic structure calculations.^{1-3,5-23,41-45}

SORI-CID can also be used to reveal information about an ion's structure. In these experiments, a collision gas is pulsed into the ICR cell which causes the trapped ions to become collisionally activated. Depending on the amount of energy deposited into the ion, one (or more) of its dissociation thresholds can be surpassed, allowing its fragmentation pathways to be determined by mass spectrometry. Since the FT-ICR MS is a tandem-in-time instrument, SORI-CID can be performed on the fragment ions as well as the parent ions. This reveals the primary, secondary, and tertiary fragmentation pathways of the ion.

A notable feature of FT-ICR mass spectrometers is that ions are passively trapped according to their charge and kinetic energy, allowing them to be thermalized in the ICR cell. Hence, in addition to structurally characterizing gas-phase complexes using IRMPD spectroscopy or SORI-CID, the dissociation energies and kinetic behaviour of weakly-bound ionic complexes can be determined using blackbody infrared radiative dissociation (BIRD); a process where the trapped ions are activated through the absorption of ambient infrared photons.^{4,25,26,46-48} Unimolecular dissociation reaction rate constants are determined by monitoring the extent of dissociation as a function of reaction time, and dissociation energies can be extracted using master equation analyses by repeating the BIRD experiment at multiple temperatures.

2.3.1. Infrared Multiple Photon Dissociation Spectroscopy. When a molecule is exposed to infrared light, it will absorb radiation that is in resonance with its vibrational modes. Since these frequencies are dependent on the structure of the molecule, infrared spectroscopy is commonly used to reveal the existence of specific functional groups. Conventional infrared absorption spectroscopy involves irradiating the species of interest over a range of infrared frequencies and measuring the attenuation of the radiation. This allows structural features to be determined by examining the shape, intensity, and frequency of any observed vibrational stretches in the infrared spectrum. Although infrared absorption spectroscopy is well-established for solution- and solid-phase molecules, it cannot be applied to gas-phase ions because it is too insensitive at low ion densities. Over the past 30 years, an alternative method of infrared spectroscopy has emerged that couples trapping mass spectrometers with high-intensity infrared light sources, such as the FT-ICR MS/OPO combination described here. This technique is known as infrared multiple photon dissociation (IRMPD) spectroscopy, and relies on measuring the changes in a mass spectrum due to multiple photon absorptions.^{2,3,5,41}

The IRMPD mechanism is shown in Figure 2.11. It begins by the absorption of a single photon in resonance with one of the ion's $\nu = 0 \rightarrow 1$ vibrational transitions. Once the ion becomes vibrationally excited, the $\nu = 1$ state is quickly ($\sim 10^{-13}$ s) depopulated through intramolecular vibrational energy redistribution (IVR). This process statistically spreads the absorbed energy throughout the ion's other internal energy states, and enables it to absorb another photon. With a sufficiently intense source of photons, this cycle will

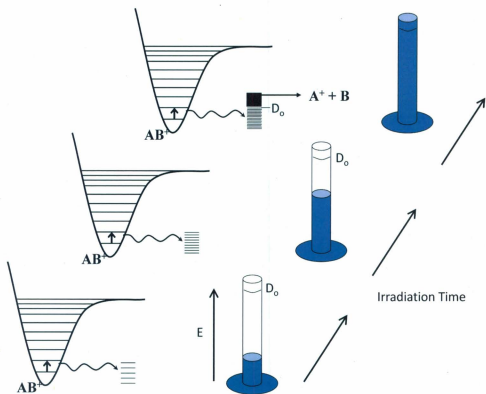


Figure 2.11. The IRMPD process: a photon in resonance with the $v = 0 \rightarrow 1$ transition mode is absorbed by the ion, the $v = 1$ state is then depopulated by IVR, allowing multiple photon absorptions to occur. The ion will dissociate when enough energy is absorbed for the ion to surpass its lowest energy dissociation threshold, D_0 . Reproduced with permission from Dr. Travis Fridgen.

repeat itself until the ion's lowest energy dissociation threshold is reached, resulting in fragmentation. The IRMPD spectrum, which is a plot of the IRMPD yield (Eq. 2.9) as a function of wavelength, is acquired by scanning the trapped ions with the KTP/OPO over the 3200 – 3800 cm^{-1} range, and using the FT-ICR mass spectrometer to determine the relative intensities of the parent, I_{parent} , and fragment, $I_{\text{fragments}}$ ions at each frequency.

$$\text{IRMPD Yield} = -\log_{10}\left(\frac{I_{\text{parent}}}{I_{\text{parent}} + \sum_i I_{\text{fragment}(i)}}\right) \quad (2.9)$$

IRMPD experiments require efficient IVR and radiation intensity capable of inducing the ion under study to dissociate. The extent of IVR is dependent on the structure of the ion since it occurs due to the anharmonic coupling between vibrational modes. If the statistical distribution of energy throughout the structure is blocked; as sometimes happens when certain moieties act as energy bottlenecks; IVR will be non-statistical and there will be no guarantee that the IRMPD-activated ions will fragment through their lowest energy dissociation channel.^{49,50} This is generally only a problem for large ions and is not an issue with the experiments described here. The other experimental concern is that the light source will not provide enough energy to induce the ion to dissociate. This can be mitigated to some extent by raising the temperature of the ICR cell to increase the ion's internal energy. For example, the KTP/OPO described in Section 2.2.3 was not intense enough to dissociate $[\text{Pb}(\text{Gly-H})]^+$ (Figure 1.2) at room temperature, but was successful when the ICR cell temperature was set to 73 °C.¹² The heating jacket around the ICR cell used for these experiments can only be varied between 20 – 120 °C however, so this method will not work for strongly bound complexes. In such cases, it's often useful to “tag” the ion with an easily removable solvent molecule

such as water. The energy required to remove a single water molecule is typically much smaller than the lowest energy dissociation threshold of the bare complex, and so an IRMPD spectrum can be acquired by monitoring the extent of IRMPD-induced water loss. Acquiring IRMPD spectra of solvated ions also reveals information about the solvent's effect on ionic structure; this is particularly interesting for the amino acids studied in Chapters 3 – 6 because water is known to stabilize zwitterionic tautomers in the solution phase (Section 1.2.1). If neither heating nor tagging is suitable for the ion under study, the light source itself can be changed. Switching a bench-top laser is obviously impractical, but an IRMPD spectrum can be acquired at a facility that couples a free electron laser (FEL) to a mass spectrometer; FELIX⁵¹, at the Radboud University Nijmegen in the Netherlands, and CLIO (Centre Laser Infrarouge Orsay) in France,⁵² both have this capacity.⁵² FELs have a tunable range between 500 – 2000 cm^{-1} and are significantly more intense than commercially available OPOs. However, IRMPD spectra in this region, like those of the $[\text{M}(\text{Ser})]^+$ ions shown in Figure 1.4, are usually quite congested.

Structural information is determined from an ion's IRMPD spectrum by examining the shape and position of the observed vibrational modes. It is also tempting to consider the band intensities, which partly reflect the relative energies of different dissociation channels. However, as was illustrated by the missing antisymmetric O-H stretch of $[\text{Li}(\text{Uracil})\text{H}_2\text{O}]^+$ and $[\text{Li}(\text{Thymine})\text{H}_2\text{O}]^+$ discussed in Chapter 1 (Figure 1.8), inefficient IVR can reduce the observed intensities of vibrational modes. A second consideration is that the intensity of the KTP/OPO varies as a function of wavelength

(Figure 2.10). Both of these factors must be kept in mind when trying to make meaningful comparisons between experimental and computed intensities.

Vibrational bands are not always easy to interpret. The complexity of an IRMPD spectrum increases with the size of the ion, the number of functional groups it contains, and its extent of hydrogen bonding. Structural information can be masked if an ion contains too many overlapping vibrational modes, while hydrogen bonding shifts the vibrational stretches of N-H and O-H groups to lower energies and significantly broadens the observed bands; this can occur to such a degree that the band will become indistinguishable from the spectrum's baseline.^{13,53,54} Another issue occurs when the ion of interest has more than one stable structure in the gas phase. In these cases, the features of the IRMPD spectrum will reflect each tautomer. It is therefore not always possible to assign a unique structure to an ion using IRMPD spectroscopy. Fortunately, there are several techniques that can be used to extract additional information from an IRMPD spectrum. One example is to perform an isotopic labeling experiment to identify specific bands. For instance, Atkins et al. used H₂¹⁸O to prove that the two O-H stretches in the IRMPD spectrum of [Pb(Gly-H)H₂O]⁺ resulted from a PbO-H and a carboxylic acid O-H stretch instead of two water O-H stretches (Figure 2.12).¹² Assigned band positions can also be supported by comparing them with predicted vibrational frequencies derived from electronic structure calculations. This approach will be described in more detail in Section 2.4.1.

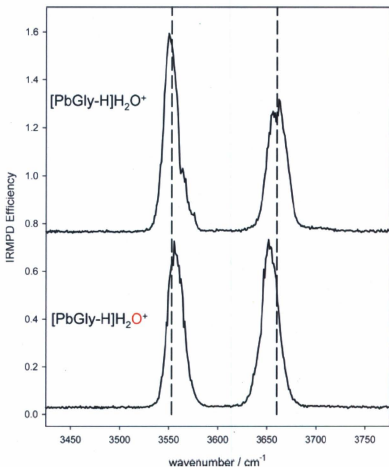


Figure 2.12. The IRMPD spectra of $[\text{Pb}(\text{Gly-H})\text{H}_2\text{O}]^+$ (top) and its oxygen-18-labeled isotomer (bottom). Isotopic labeling results in only the band at 3661 cm^{-1} shifting to a lower frequency, implying that the water molecule is no longer intact. Figure reprinted with permission from *J. Phys. Chem. B* **2009**, *113*, 14457 – 14464.¹²

2.3.2. Blackbody Infrared Radiative Dissociation. One of the attractive features of FT-ICR mass spectrometry is that ions can be trapped in an extremely low pressure (10^{-10} mbar) environment where the collision frequency between ions and neutral molecules is effectively zero. This prevents collisional activation, and allows the ions to be stored for extended periods of time. Ions cannot be trapped indefinitely, however, because they will still accumulate energy by absorbing infrared photons from the ambient blackbody radiation field. This ion activation mechanism is known as blackbody infrared radiative dissociation (BIRD), and is responsible for unimolecular dissociation in “zero”-pressure environments.^{4,46}

BIRD is typically combined with FT-ICR MS to probe the dissociation kinetics and binding energies of weakly bound ($\sim 70 - 200 \text{ kJ mol}^{-1}$) ionic complexes. There are two requirements for BIRD experiments that make detection in an ICR cell an excellent choice: BIRD reactions take seconds or longer so the ions must be trapped, and the isolated ions must not be activated through non-thermal processes. For example, if an ion were translationally or collisionally excited beyond its lowest energy dissociation threshold, its observed rate of decay would reflect the kinetics of non-thermal activation, and not the kinetics of thermal unimolecular dissociation. It has already been demonstrated that ICR cells are capable of trapping ions long enough to carry out BIRD experiments, but they also provide a collision-free environment that is free of radio-frequency electric fields. This allows the ions to be trapped in such a way that they are only activated through photon absorption.

The goal of an individual BIRD experiment is to determine the unimolecular dissociation rate constant, k_{uni} , for the ion of interest at a specific temperature, T . This can be accomplished by monitoring the ion's normalized intensity in the ICR cell, I , as a function of time, t , and fitting these parameters to the integrated first-order rate law (Eq. 2.10).

$$[I] = [I]_0 e^{-k_{uni}t} \quad (2.10)$$

Before injection into the ICR cell, the ions are thermalized by briefly storing them in a collision cell pressurized by 10^{-2} mbar of argon gas. This eliminates any excess ion velocity and further reduces the risk of collision-induced dissociation in the ICR cell. Once the precursor ions are trapped, they are isolated using a sweep of radio frequency potentials to eject unwanted species. This ensures that any fragment ions observed during the experiment arise solely from the precursor ion and not an unrelated complex. The sweep window is typically kept wide (± 10 Da with respect to the ion of interest) in order to avoid non-thermal ion activation. k_{uni} is established by acquiring mass spectra at different stages of the BIRD reaction and plotting the normalized ion intensities as a function of reaction time.

Determining k_{uni} at multiple temperatures allows the Arrhenius activation energy, E_a , and pre-exponential factor, A , for the dissociation of the ionic complex to be extracted from the Arrhenius relation (Eq. 2.11).

$$k_{uni} = A e^{-E_a/k_B T} \quad (2.11)$$

The utility of these values, however, depends on the size of the complex being studied as well as the rate of the reaction. If the rate of photon exchange between an ion

and its surroundings is faster than the rate of unimolecular dissociation, the ion is said to be in the rapid-exchange limit and will maintain its equilibrium distribution of internal energies even though only the most energetic molecules are dissociating. In this scenario, the measured E_0 is equivalent to the limiting rapid-exchange Arrhenius activation energy, E_a^∞ , and can be related to the threshold dissociation energy, E_0 , if the reaction is barrierless. This relation is given by Eq. 2.12, where $k_B T$ is the thermal energy and ΔU_{corr} is the thermal energy difference between the transition state and the reactant compared to their respective ground states. At 0 K, the threshold dissociation energy is therefore a good approximation to E_a^∞ .

$$E_0 = E_a^\infty - k_B T - \Delta U_{corr} \quad (2.12)$$

Eq. 2.12 relies on the fact that the energy and enthalpy of activation, ΔU^\ddagger and ΔH^\ddagger respectively, are equivalent for a unimolecular process and are related to E_a^∞ by Eq. 2.13. The entropy of activation, ΔS^\ddagger , can be determined from the limiting rapid-exchange pre-exponential factor, A^∞ , by Eq 2.14.

$$\Delta U^\ddagger = \Delta H^\ddagger = E_a^\infty - k_B T \quad (2.13)$$

$$A^\infty = \frac{k_B T}{h} e^{\left(1 + \left(\frac{\Delta S^\ddagger}{k_B}\right)\right)} \quad (2.14)$$

Small molecules, such as the amino acid complexes discussed in Chapters 3 – 6, have slower rates of photon exchange than unimolecular decay. This means that the equilibrium distribution of internal energies is truncated by the continuous removal of the most energetic ions. This is known as the slow-exchange (or “sudden-death”) limit, and implies that the observed decay rate depends only on the rate of photon absorption since

ions will rapidly dissociate when excited above E_0 . The measured rate constant therefore does not reflect the rate of unimolecular dissociation. Under the slow-exchange condition, E_a significantly underestimates E_0 , and kinetic modeling must be used to extract meaningful results from the BIRD experiments. This will be described in greater detail in Section 2.4.3.

Most BIRD research has focused on barrierless dissociation reactions, such as desolvation or covalent bond cleavage, where E_0 is equivalent to the 0 K dissociation energy, D_0 (Figure 2.13). This enables binding energies to be determined for a variety of complexes, including the energy necessary to protonate several amino acids and organic bases, as well as the energy required to fragment larger peptides.^{4,24-26,55,56} Of particular interest with regards to this text is the hydration of amino acids. Amino acids can adopt either a charge-solvated or zwitterionic structure, hence their fragmentation pathways and water detachment rates could be used to discriminate between isomers.

2.3.3. Sustained Off-Resonance Irradiation Collision-Induced Dissociation. The IRMPD and BIRD techniques rely on measuring the consequence of ion activation. In some circumstances however, the dissociation threshold of the ion of interest is too high in energy for these methods to be useful. In this event, structural information about the parent ion can be determined by collisionally activating the ions and observing any fragmentation. Although collision-induced dissociation at first seems at odds with the “zero”-pressure environment of the ICR cell, it is possible to perform in-cell CID by irradiating the ions with a low-energy, off-resonance radio-frequency pulse.^{57,58} This

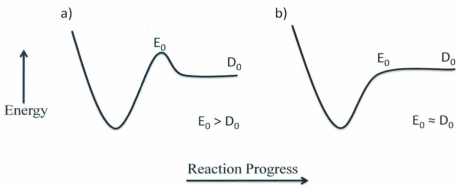


Figure 2.13. Potential energy surfaces for the cases when: a) a structural rearrangement occurs prior to dissociation ($E_0 > D_0$) and b) there is no additional barrier to dissociation ($E_0 \approx D_0$).

process, known as sustained off-resonance irradiation collision-induced dissociation (SORI-CID), causes the ions to undergo acceleration and deceleration cycles during the RF pulse so that they can gradually accumulate internal energy without being ejected from the cell (Figure 2.14). If the RF pulse is performed in conjunction with a high pressure (10^{-8} mbar) burst of collision gas, such as argon, the excited ions will collide with the bath gas and dissociate. The fragment ions can then be detected in the ICR cell after a short delay to pump away the electrically neutral bath gas. Since the FT-ICR is a tandem mass spectrometer, the fragment ions themselves can be isolated and subjected to SORI-CID. This allows structural information about the parent and fragment ions to be determined.

2.4. Calculations. Gas-phase biological ions, such as the amino acids described in Chapters 3 – 6, are typically modeled using *ab initio* or semiempirical calculations to extract additional structural or thermochemical information from the experimental data.^{2,3,5} IRMPD spectroscopy, for example, is an excellent tool for identifying specific functional groups, but more detailed structures can be revealed by comparing IRMPD spectra with computed infrared spectra derived from potential structures for the ion under study.^{6,8,12-15,43-45,59-61} This is a standard method that relies on determining the relative energies of a series of possible ion geometries and then calculating the harmonic vibrational frequencies of the most stable isomers. This technique, as well as one that uses a master equation analysis to recover an ion's threshold dissociation energy from a series of BIRD experiments, are described in detail in Sections 2.4.1 and 2.4.2.

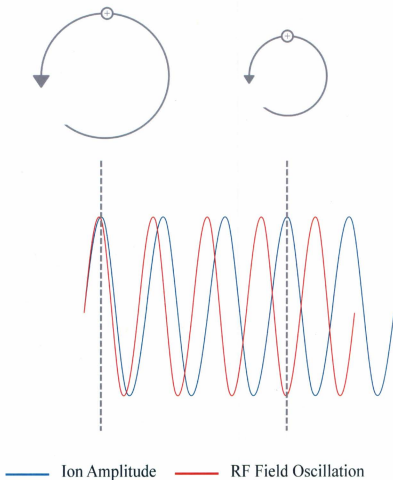


Figure 2.14. If the cyclotron frequency of an ion is in resonance with a radio-frequency field, it will become excited to larger orbits. By contrast, if the RF field is off-resonance the ion will be directed towards the center of the cell. A SORI pulse cycles through these two conditions, allowing the ion to accumulate internal energy without being ejected from the cell. Figure adapted from the Bruker Daltonics Apex-Qe Series Generation II User Manual. Version 2.0 (July 2008).

2.4.1. Electronic Structure Calculations. The most stable structure of an ion can be determined by calculating the geometric arrangement of atoms with the lowest electronic energy. This can be accomplished using a variety of computational methods, but the general approach is typically the same; a series of “guess” structures are optimized by an energy minimization algorithm in order to find the global minimum on the ion’s potential energy surface.⁶² These candidate structures have different internuclear distances, bond angles, and torsional angles, and are varied in such a way as to reduce molecular strain or to increase hydrogen bonding. It should be noted that this technique relies on the researcher finding the most stable structure of the ion, so a purported “lowest energy” structure may in fact only provide an upper limit for the true global energy minimum.

The calculations presented in this work use a two-step process: local minima were found by geometrically optimizing candidate structures using density functional theory (DFT), and then single-point energy calculations are carried out on the optimized structures using a more accurate *ab initio* method. Both steps are performed using Gaussian 09.⁶³ DFT is a semi-empirical process that calculates a molecule’s electronic energy using its ground-state electron probability density. The DFT treatment used here is the popular B3LYP (Becke, 3-parameter, Lee-Yang-Parr) hybrid functional, which is frequently used to optimize systems containing small biological ions. A full description of this method can be found elsewhere, but in brief, B3LYP calculates an ion’s electronic energy by mixing a Hartree-Fock electron exchange-energy functional with DFT exchange- and correlation-energy functionals that treat electron density as a function of position.^{62,64-66}

Once the equilibrium geometry is established by the B3LYP method, a vibrational frequency analysis is performed that considers the ion as a series of harmonic oscillators.⁶² In this model, the vibrational energy, E_{vib} , of an N -atom molecule is the sum of the energy of each normal vibrational mode (Eq. 2.15, where h is Planck's constant).

$$E_{vib} \approx \sum_{n=1}^{3N-6} \left(v_n + \frac{1}{2} \right) h \nu_n \quad (2.15)$$

The frequency, ν , of each of the n normal modes is found by taking the second-derivative of the ion's internal energy with respect to its Cartesian nuclear coordinates (with origin at the center of mass) and then determining the force constants from the eigenvalues of a mass-weighted force constant matrix. This process occurs after geometry optimization because calculated frequencies are only real when they are determined at a stationary point on the ion's potential energy surface. Gaussian 09 also determines the relative intensities, I , of the vibrational frequencies by calculating the change in dipole moment, $d\mu$, caused by the vibration. This is accomplished using Eq. 2.16, where dq is the change in the ion's geometry.⁶⁷

$$I \propto \left(\frac{d\mu}{dq} \right)^2 \quad (2.16)$$

Vibrational frequency analyses allow the theoretical IR spectrum of a specific structure to be compared with an experimental IRMPD spectrum. The presence or absence of bands in both spectra can then be used to characterize the structure of the gas-phase ion. There are, however, two considerations which should be kept in mind when comparing experimental and theoretical IR spectra. The first is that the analysis described above assumes the ion is a harmonic oscillator. In order to account for anharmonicity, the

computed frequencies must be scaled by an empirical factor that depends on the nature of the system being studied, the IR range under consideration, and the choice of computational theory; a scaling factor of 0.955 is applied to the computed IR spectra presented in Chapters 3 – 6.^{13,68} The second is that the intensities of the computed vibrational frequencies only account for the absorption of one photon, whereas IRMPD spectra by definition are produced from the absorption of multiple photons. This generally has a negligible effect on band comparisons if the ion structure is accurately predicted and there is efficient IVR.⁶⁹

Gaussian 09 treats the geometrically optimized ion as an ideal gas in a canonical ensemble. This means that performing a vibrational frequency analysis also allows the ion's intrinsic thermochemistry to be determined by statistical mechanics.⁷⁰ The total internal energy of the ion is the sum of the electronic, vibrational, rotational, translational, and zero-point energies (Eq. 2.17.)

$$E = E_{elec} + E_{vib} + E_{rot} + E_{trans} + E_{ZP} \quad (2.17)$$

Enthalpy, H , and Gibbs energy, G , can be calculated from the internal energy by the following thermochemical relations (Eq. 2.18 and 2.19), where k_B and S represent the Boltzmann constant and entropy respectively. S is found by Eq. 2.20, where Q is the canonical partition function.

$$H = E + k_B T \quad (2.18)$$

$$G = H - TS \quad (2.19)$$

$$S = \left(\frac{d}{dT} (k_B T \ln Q) \right)_V \quad (2.20)$$

Since E_{elec} is by far the greatest contributor to the total energy of the molecule, single-point electronic energy calculations are performed on the optimized B3LYP geometries using an *ab initio* method in order to refine the thermochemical data. This step is necessary because DFT methods do not account for long-range electron correlation well and, as a consequence, fail to model dispersion forces.⁷¹ Møller-Plesset second-order (MP2) perturbation theory, which accounts for two-body electron correlations, is used to approximate the solution to the Schrödinger equation.⁷² The MP2-derived energies are then substituted into Eq. 2.17 to determine more accurate thermochemical values.⁷² This two-step approach for determining relative thermochemistries raises the question as to why a frequency analysis is not simply done at the MP2 level of theory. The answer is that this process would require significantly more computational time. Combining the B3LYP and MP2 methods reduces the overall computational cost of a calculation while retaining most of the accuracy of the MP2 level of theory.

An essential requirement for the B3LYP and MP2 calculations is choosing a basis set that can accurately model the ion. These are linear combinations of atomic orbitals used to determine the ion's molecular orbitals. The basis set used in conjunction with the B3LYP method is denoted as 6-31+G(d,p) (also written as 6-31+G**). This is a split-valence double-zeta basis set that represents each inner shell atomic orbital by a single basis function made by linearly combining six primitive Gaussian functions; the valence shell atomic orbitals, by contrast, are defined by two basis functions: one prepared by combining three primitive Gaussians, and another which is a single Gaussian function.⁶²

The more expansive split-valence triple-zeta 6-311++G(2d,2p) basis set, which represents the valence shell atomic orbitals by three basis functions, is used for the MP2 calculations. The + and ++ notations in the basis sets described above reflect the addition of diffuse functions that account for electron density at large distances from the nuclei. Consequently, these are important for anions, ions with lone pairs, or hydrogen-bonded species. The single + implies that an additional set of highly diffuse s , p_x , p_y , and p_z functions are applied to each non-hydrogen atom, while the ++ indicates that an extra s function is included for every hydrogen atom. The polarization functions (in brackets) account for the fact that when atoms form molecules, the resulting polarization distorts their distribution of charge. Polarization is accounted for by including functions that allow the atomic orbitals to behave asymmetrically (d and p orbitals, for instance). The 6-31+G(d,p) basis set adds a set of five d orbitals to each atom between Li - Ca, and a set of three p orbitals to hydrogen and helium. The 6-311++G(2d,2p), by contrast, adds two sets of d and p orbitals. It should be noted that in Gaussian 09 6-31+G(d,p) and 6-311++G(2d,2p) can only be applied to the elements between H - Kr. For larger atoms (Na - La and Hf- Bi), such as the Pb-containing complexes considered in Chapters 3 - 6, the LANL2DZ (Los Alamos National Laboratories 2-Double-Zeta) basis set is used.⁷³ This replaces the inner shell atomic orbitals with a relativistic core potential, and applies two basis functions to the valence electrons.

One final comment should be made about using electronic structure calculations to determine transition state structures. Since transition states exist as saddle points on potential energy surfaces, one of their vibrational modes will be imaginary and their

existence can be verified by the vibrational analysis described above. It is often desirable to know the energy barrier posed by a transition state in order to comment on potential reaction mechanisms. For example, if the most stable predicted structure for a compound is not reflected in the experimental IRMPD spectrum, the potential energy barrier with respect to its formation may explain why it is not observed in the gas phase. The minimum energy path between the reactant, transition state, and product, can be identified using the intrinsic reaction coordinates (IRC) method. This technique takes the expected geometry of a given transition state, and makes small perturbations to its structure until it finds the lowest energy pathway connecting the reactant and product geometries.^{74,75}

2.4.2. Master Equation Modeling. An issue with interpreting BIRD data is that accurate thermodynamic information can only be extracted if the ion is sufficiently large for its photon exchange rates to be faster than its decay rate. For this reason, the unimolecular dissociation kinetics of small ions are generally determined by solving the master equation (Eq. 2.21). This model simulates the change in population, dN/dt , of a system's internal energy states (i, j) over time using a set of coupled linear first-order ordinary differential equations which consider the detailed rate constants of all state-to-state transitions (k_{ij}) and dissociation processes (k_d).^{4,76}

$$\frac{dN_i}{dt} = -k_d N_i(t) + \sum_j k_{ij} N_j(t) \quad (2.21)$$

The master equation can be solved automatically using computational software, VariFlex for example,⁷⁷ if it is written as a matrix and diagonalized. This allows temperature-dependent thermal unimolecular dissociation rate constants, k_{uni} , to be recovered from the lowest eigenvalue of the matrix of coefficients; a process that requires knowledge of the detailed rate constants, k_{ij} and k_d . VariFlex uses E/J -resolved (reaction energy, E , and total angular momentum, J) variable reaction coordinate transition state theory (VRC-TST) to minimize k_d derived by Rice-Ramsperger-Kassel-Marcus (RRKM) theory.^{49,50} Formally, RRKM theory requires assigning vibrational frequencies and rotational constants to the dissociating molecule as well as the transition state. As was mentioned in Section 2.4.1, this can be accomplished by performing geometry optimizations followed by frequency calculations. However, if the reverse association reaction is barrierless, as is expected for the reactions modeled in Chapter 5, the transition state structure for dissociation is hard to isolate. VRC-TST instead defines the reaction coordinate as the bond being broken through dissociation and varies its length until the calculated RRKM rate constants (Eq. 2.22) are minimized.⁷⁸⁻⁸² This is accomplished by variationally minimizing the sum-of-states for the transition state, G^\ddagger , by sampling over the reaction coordinate using Monte Carlo methods.⁸¹ This method determines G^\ddagger by separating radial and angular motion and then integrating over the three Cartesian coordinates of the total angular momentum as well as a radial coordinate and its conjugate momentum. The density of states, N , is calculated by the Beyer-Swinehart direct counting algorithm.⁸³ σ is the reaction degeneracy.

$$k_d = \frac{\sigma G^\ddagger(E, J)}{hN(E, J)} \quad (2.22)$$

Since collisional processes are negligible in ICR cells, k_{ij} is simply the sum of the rate constants for radiative absorption ($k_{i,rad}$) and emission ($k_{-i,rad}$) (Eq. 2.23).

$$k_{ij} = k_{i,rad} + k_{-i,rad} \quad (2.23)$$

The detailed rate constants for blackbody absorption (Eq. 2.24) and spontaneous and induced emission (Eq. 2.25) are:

$$k_{i,rad}(\Delta E_{i \rightarrow j} = h\nu) = \sum_m \rho(h\nu) \mathbf{B}(h\nu) P_i^{mh\nu} \quad (2.24)$$

$$k_{-i,rad}(\Delta E_{j \rightarrow i} = h\nu) = \sum_m [\mathbf{A}(h\nu) + \rho(h\nu) \mathbf{B}(h\nu) P_j^{mh\nu}] \quad (2.25)$$

Where $\rho(h\nu)$ is Planck's black-body radiation distribution, and P_i and P_j are the probabilities of the ν th oscillator having m quanta of energy in the i and j states, respectively (Eq. 2.26). $\mathbf{A}(h\nu)$ and $\mathbf{B}(h\nu)$ are the Einstein coefficients for spontaneous and induced emission; these can be calculated according to Eq. 2.27 and 2.28.

$$P = \frac{e^{-mh\nu/k_B T}}{(1 - e^{-h\nu/k_B T})} \quad (2.26)$$

$$\mathbf{A}(h\nu) = 8\pi h (\nu/c)^3 \mathbf{B}(h\nu) \quad (2.27)$$

$$\mathbf{B}(h\nu) = \frac{2\pi^2 \mu^2}{6\epsilon_0 h^2} \quad (2.28)$$

Where μ is the transition dipole moment of the oscillator, h is Planck's constant, and ϵ_0 is the dielectric constant.

The radiative exchange rate constants, k_{ij} , were calculated by VariFlex using the method proposed by Dunbar.⁸⁴⁻⁸⁹ An internal temperature is assigned to the ion that corresponds with its internal energy, and the vibrational modes described above are

assumed to be in thermal equilibrium with this temperature. The Einstein coefficients for each IR active vibrational mode are found by integrating over the associated IR absorption intensities. Boltzmann statistics are then used to determine the rate constants for radiative absorption and emission.

References

1. Burt, M. B.; Fridgen, T. D. *Eur. J. Mass Spectrom.* **2012**, *18* (2), 235 – 250.
2. Fridgen, T. D. *Mass Spectrom. Rev.* **2009**, *28*, 586 - 607.
3. Polfer, N. C.; Oomens, J. *Mass Spectrom. Rev.* **2009**, *28*, 468 - 494.
4. Dunbar, R. C. *Mass Spectrom. Rev.* **2004**, *23*, 127 - 158.
5. Polfer, N. C. *Chem. Soc. Rev.* **2011**, *40*, 2211 - 2221.
6. Polfer, N. C.; Oomens, J.; Moore, D. T.; von Helden, G.; Meijer, G.; Dunbar, R. C. *J. Am. Chem. Soc.* **2006**, *128*, 517 - 525.
7. Dunbar, R. C.; Polfer, N. C.; Oomens, J. *J. Am. Chem. Soc.* **2007**, *129*, 14562 - 14563.
8. Armentrout, P. B.; Rodgers, M. T.; Oomens, J.; Steill, J. D. *J. Phys. Chem. A* **2008**, *112*, 2248 - 2257.
9. Gapeev, A.; Dunbar, R. C. *J. Am. Chem. Soc.* **2001**, *123*, 8360 - 8365.
10. Dunbar, R. C.; Oomens, J.; Orlova, G.; Bohme, D. K. *Int. J. Mass Spectrom.* **2011**, *308*, 330 – 337.
11. Dunbar, R. C.; Steill, J. D.; Oomens, J. *J. Am. Chem. Soc.* **2011**, *133*, 1212 - 1215.
12. Atkins, C. G.; Banu, L.; Rowsell, M.; Blagojevic, V.; Bohme, D. K.; Fridgen, T. D. *J. Phys. Chem. B* **2009**, *113*, 14457 - 14464.
13. Atkins, C. G.; Rajabi, K.; Gillis, E. A. L.; Fridgen, T. D. *J. Phys. Chem. A* **2008**, *112*, 10220 - 10225.
14. Gillis, E. A. L.; Fridgen, T. D. *Int. J. Mass Spectrom.* **2010**, *297*, 2 - 8.
15. Gillis, E. A. L.; Rajabi, K.; Fridgen, T. D. *J. Phys. Chem. A* **2009**, *113*, 824 - 832.
16. Ali, O. Y.; Fridgen, T. D. *Int. J. Mass Spectrom.* **2011**, *308*, 167 – 174.
17. Forbes, M. W.; Bush, M. F.; Polfer, N. C.; Oomens, J.; Dunbar, R. C.; Williams, E. R.; Jockusch, R. A. *J. Phys. Chem. A* **2007**, *111*, 11759 - 11770.
18. Bakker, J. M.; Sinha, R. K.; Besson, T.; Brugnara, M.; Tosi, P.; Salpin, J.-Y.; Maitre, P. *J. Phys. Chem. A* **2008**, *112*, 12393 - 12400.

19. Polfer, N. C.; Oomens, J. *Phys. Chem. Chem. Phys.* **2007**, *9*, 3804 - 3817.
20. Polfer, N. C.; Paizs, B.; Snoek, L. C.; Compagnon, I.; Suhai, S.; Meijer, G.; von Helden, G.; Oomens, J. *J. Am. Chem. Soc.* **2005**, *127*, 8571 - 8579.
21. Salpin, J.-Y.; Gamiotte, L.; Tortajada, J.; Besson, T.; Maitre, P. *Int. J. Mass Spectrom.* **2010**, *304*, 154 - 164.
22. Drayß, M. K.; Armentrout, P. B.; Oomens, J.; Schäfer, M. *Int. J. Mass Spectrom.* **2010**, *297*, 18 - 27.
23. Bush, M. F.; O'Brien, J. T.; Prell, J. S.; Wu, C.-C.; Saykally, R. J.; Williams, E. R. *J. Am. Chem. Soc.* **2009**, *131*, 13270 - 13277.
24. Jockusch, R. A.; Lemoff, A. S.; Williams, E. R. *J. Am. Chem. Soc.* **2001**, *123*, 12255 - 12265.
25. Rodriguez-Cruz, S. E.; Jockusch, R. A.; Williams, E. R. *J. Am. Chem. Soc.* **1998**, *120*, 5842 - 5843.
26. Rodriguez-Cruz, S. E.; Jockusch, R. A.; Williams, E. R. *J. Am. Chem. Soc.* **1999**, *121*, 8898 - 8906.
27. Rajabi, K.; Easterling, M. L.; Fridgen, T. D. *J. Am. Soc. Mass Spectrom.* **2009**, *20*, 411 - 418.
28. Kebarle, P.; Tang, L. *Anal. Chem.* **1993**, *65*, 972 - 986.
29. Loo, J. A. *Mass Spectrom. Rev.* **1997**, *16*, 1 - 23.
30. Gaskell, S. J. *J. Mass Spectrom.* **1997**, *32*, 677 - 688.
31. Smith, R. D.; Loo, J. A.; Edmonds, C. G.; Barinaga, C. J.; Udseth, H. R. *Anal. Chem.* **1990**, *62*, 882 - 899.
32. Senko, M. W.; Hendrickson, C. L.; Paša-Tolić, L.; Marto, J. A.; White, F. M.; Guan, S.; Marshall, A. G. *Rapid Commun. Mass Spectrom.* **1996**, *10*, 1824 - 1828.
33. Cole, R. B. *J. Mass Spectrom.* **2000**, *35*, 763 - 772.
34. Fishbane, P. M.; Gasiorowicz, S. G.; Thornton, S. T., *Physics for Scientists and Engineers*. 3rd ed.; Pearson Prentice Hall: 2005.

35. Marshall, A. G.; Hendrickson, C. L. *Int. J. Mass Spectrom.* **2002**, *215*, 59 - 75.
36. Marshall, A. G.; Grosshans, P. B. *Anal. Chem.* **1991**, *63*, 215A - 229A.
37. Marshall, A. G.; Hendrickson, C. L.; Jackson, G. S. *Mass Spec. Rev.* **1998**, *17*, 1 - 35.
38. Armstrong, J. A.; Bloembergen, N.; Ducuing, J.; Pershan, P. S. *Phys. Rev.* **1962**, *127*, 1918 - 1939.
39. Kato, K. *J. Quantum Electron.* **1991**, *27*, 1137 - 1140.
40. Yang, S. T.; Eckardt, R. C.; Byer, R. L. *Opt. Lett.* **1993**, *18*, 971 - 973.
41. Eyler, J. R. *Mass Spectrom. Rev.* **2009**, *28*, 448 - 467.
42. Burt, M. B.; Decker, S. G. A.; Atkins, C. G.; Rowsell, M.; Peremans, A.; Fridgen, T. D. *J. Phys. Chem. B* **2011**, *115*, 11506 - 11518.
43. Rajabi, K.; Fridgen, T. D. *J. Phys. Chem. A* **2008**, *112*, 23 - 30.
44. Rajabi, K.; Gillis, E. A. L.; Fridgen, T. D. *J. Phys. Chem. A* **2010**, *114*, 3449 - 3456.
45. Rajabi, K.; Theel, K.; Gillis, E. A. L.; Beran, G.; Fridgen, T. D. *J. Phys. Chem. A* **2009**, *113*, 8099 - 8107.
46. Dunbar, R. C.; McMahon, T. B. *Science* **1998**, *279*, 194 - 197.
47. Stevens, S. M., Jr.; Dunbar, R. C.; Price, W. D.; Sena, M.; Watson, C. H.; Nichols, L. S.; Riveros, J. M.; Richardson, D. E.; Eyler, J. R. *J. Phys. Chem. A* **2004**, *108*, 9892 - 9900.
48. Stevens, S. M., Jr.; Dunbar, R. C.; Price, W. D.; Sena, M.; Watson, C. H.; Nichols, L. S.; Riveros, J. M.; Richardson, D. E.; Eyler, J. R. *J. Phys. Chem. A* **2002**, *106*, 9686 - 9694.
49. Steinfeld, J. I.; Francisco, J. S.; Hase, W. L., *Chemical Kinetics and Dynamics*. 2nd ed.; Prentice Hall: 1999.
50. Forst, W., *Unimolecular Reactions: A Concise Introduction*. Cambridge University Press: 2003.
51. Oepts, D.; van der Meer, A. F. G.; van Amersfoort, P. W. *Infrared Phys. Technol.* **1995**, *36*, 297 - 308.

52. Ortega, J. M.; Berset, J. M.; Chaput, R.; Glotin, F.; Humbert, G.; Jaroszynski, D.; Joly, P.; Kergosien, B.; Lesrel, J. *Nucl. Instrum. Methods Phys. Res., Sect. A* **1996**, *375*, 618 – 625.
53. Wang, Y.-S.; Chang, H.-C.; Jiang, J.-C.; Lin, S. H.; Lee, Y. T.; Chang, H.-C. *J. Am. Chem. Soc.* **1998**, *120*, 8777 - 8788.
54. Chiavassa, T.; Roubin, P.; Pizzala, L.; Verlaque, P.; Allouche, A.; Marinelli, F. *J. Phys. Chem.* **1992**, *96*, 10659 - 10665.
55. Lemoff, A. S.; Bush, M. F.; Williams, E. R. *J. Am. Chem. Soc.* **2003**, *125*, 13576 - 13584.
56. Jockusch, R. A.; Lemoff, A. S.; Williams, E. R. *J. Phys. Chem. A* **2001**, *105*, 10929 - 10942.
57. Senko, M. W.; Speir, J. P.; McLafferty, F. W. *Anal. Chem.* **1994**, *66*, 2801 - 2808.
58. Herrmann, K. A.; Somogyi, A.; Wysocki, V. H.; Drahos, L.; Vékey, K. *Anal. Chem.* **2005**, *77*, 7626 - 7638.
59. Fridgen, T. D.; MacAleese, L.; Maitre, P.; McMahon, T. B.; Boissel, P.; Lemaire, J. *Phys. Chem. Chem. Phys.* **2005**, *7*, 2747 - 2755.
60. Armentrout, P. B.; Gabriel, A.; Moision, R. M. *Int. J. Mass Spectrom.* **2009**, *283*, 56 - 68.
61. O'Brien, J. T.; Prell, J. S.; Steill, J. D.; Oomens, J.; Williams, E. R. *J. Phys. Chem. A* **2008**, *112*, 10823 - 10830.
62. Levine, I. N. *Quantum Chemistry*. 5th ed.; Prentice Hall: 2000.
63. Frisch, M. J.; Trucks, G. W.; Schlegel, H. B.; Scuseria, G. E.; Robb, M. A.; Cheeseman, J. R.; Scalmani, G.; Barone, V.; Mennucci, B.; Petersson, G. A.; Nakatsuji, H.; Caricato, M.; Li, X.; Hratchian, H. P.; Izmaylov, A. F.; Bloino, J.; Zheng, G.; Sonnenberg, J. L.; Hada, M.; Ehara, M.; Toyota, K.; Fukuda, R.; Hasegawa, J.; Ishida, M.; Nakajima, T.; Honda, Y.; Kitao, O.; Nakai, H.; Vreven, T.; Montgomery, J. A. Jr.; Peralta, J. E.; Ogliaro, F.; Bearpark, M.; Heyd, J. J.; Brothers, E.; Kudin, K. N.; Staroverov, V. N.; Kobayashi, R.; Normand, J.; Raghavachari, K.; Rendell, A.; Burant, J. C.; Iyengar, S. S.; Tomasi, J.; Cossi, M.; Rega, N.; Millam, J. M.; Klene, M.; Knox, J. E.; Cross, J. B.; Bakken, V.; Adamo, C.; Jaramillo, J.; Gomperts, R.; Stratmann, R. E.; Yazyev, O.; Austin, A. J.; Cammi, R.; Pomelli, C.; Ochterski, J. W.; Martin, R. L.; Morokuma, K.; Zakrzewski, V. G.; Voth, G. A.; Salvador, P.; Dannenberg, J. J.; Dapprich, S.; Daniels, A. D.; Farkas, O.; Foresman, J.

- B.; Ortiz, J. V.; Cioslowski, J.; Fox, D. J. Gaussian 09, Revision A.01; Gaussian, Inc.: Wallingford, CT, 2009.
64. Becke, A. D. *Phys. Rev. A* **1988**, *38*, 3098 - 3100.
65. Becke, A. D. *J. Chem. Phys.* **1993**, *98*, 5648 - 5652.
66. Lee, C.; Yang, W.; Parr, R. G. *Phys. Rev. B* **1988**, *37*, 785 - 789.
67. Lewars, E. G., *Computational Chemistry: Introduction to the Theory and Applications of Molecular and Quantum Mechanics*. 2nd ed.; Springer: 2010
68. Kamariotis, A.; Boyarkin, O. V.; Mercier, S. R.; Beck, R. D.; Bush, M. F.; Williams, E. R.; Rizzo, T. R. *J. Am. Chem. Soc.* **2006**, *128*, 905 - 916.
69. von Helden, G.; Oomens, J.; Sartakov, B. G.; Meijer, G. *Int. J. Mass Spectrom.* **2006**, *254*, 1 - 19.
70. Engel, T.; Reid, P., *Physical Chemistry*. Pearson Benjamin Cummings: 2006.
71. Johnson, E. R.; Wolkow, R. A.; DiLabio, G. A. *Chem. Phys. Lett.* **2004**, *394*, 334 - 338.
72. Møller, C.; Plesset, M. S. *Phys. Rev.* **1934**, *46*, 618 - 622.
73. Wadt, W. R.; Hay, J. H. *J. Chem. Phys.* **1985**, *82*, 284 - 298.
74. Schlegel, H. B.; Peng, C.; Ayala, P. Y.; Frisch, M. J. *J. Comput. Chem.* **1996**, *17*, 49 - 56.
75. Fukui, K. *Acc. Chem. Res.* **1981**, *14*, 363 - 368.
76. Williams, E. R.; Price, W., D. *J. Phys. Chem. A* **1997**, *101*, 8844 - 8852.
77. Klippenstein, S. J.; Wagner, A. F.; Dunbar, R. C.; Wardlaw, D. M.; Robertson, S. H. *VariFlex*, 1.00; 1999.
78. Klippenstein, S. J. *J. Chem. Phys. Lett.* **1990**, *170*, 71 - 77.
79. Klippenstein, S. J. *J. Chem. Phys.* **1991**, *94*, 6469 - 6482.
80. Klippenstein, S. J. *J. Chem. Phys.* **1992**, *96*, 367 - 371.
81. Klippenstein, S. J. *J. Phys. Chem.* **1994**, *98*, 11459 - 11464.

82. Robertson, S. H.; Wagner, A. F.; Wardlaw, D. M. *Faraday Discuss.* **1995**, *102*, 65 - 83.
83. Beyer, T.; Swinehart, D. F. *Commun. ACM* **1973**, *16*, 379.
84. Dunbar, R. C. *J. Chem. Phys.* **1989**, *90*, 7369 - 7375.
85. Dunbar, R. C. *J. Chem. Phys.* **1991**, *95*, 2537 - 2548.
86. Dunbar, R. C. *J. Phys. Chem.* **1994**, *98*, 8705 - 8712.
87. Dunbar, R. C.; McMahon, T. B.; Thölmann, D.; Tonner, D. S.; Salahub, D. R.; Wei, D. *J. Am. Chem. Soc.* **1995**, *117*, 12819 - 12825.
88. Lin, C.-Y.; Dunbar, R. C. *J. Phys. Chem.* **1996**, *100*, 655-659.
89. Dunbar, R. C.; Zaniwski, R. C. *J. Chem. Phys.* **1992**, *96* (7), 5069-5075.

Chapter 3

Structures of bare and hydrated $[\text{Pb}(\text{AminoAcid-H})]^+$ complexes determined by infrared multiple photon dissociation spectroscopy[†]

3.1. Introduction. Lead(II) engenders ailments ranging from hypertension to anemia.¹ This toxicity can be reduced through chelation with peptides or proteins,¹⁻⁵ but despite the implications of lead(II)-peptide complexes in biochemistry, information about their structures remains incomplete. A starting point for understanding the nature of these ions is the structural characterization of smaller lead(II)/amino acid (Aa) complexes. Electrospray ionization mass spectrometry has previously indicated that these complexes are deprotonated and of the form $[\text{Pb}(\text{Aa-H})]^+$, but their actual structures were not determined.⁶⁻⁸ In this chapter, infrared multiple-photon dissociation (IRMPD) spectroscopy and electronic structure calculations are used to resolve this issue by structurally characterizing $[\text{Pb}(\text{Aa-H})]^+$ and $[\text{Pb}(\text{Aa-H})\text{H}_2\text{O}]^+$ complexes involving five amino acids with nonpolar side chains (proline (Pro), alanine (Ala), valine (Val), leucine (Leu), and isoleucine (Ile)) and one amino acid containing a polar and basic side chain (lysine (Lys)).

IRMPD spectroscopy is a form of consequence spectroscopy that allows structural features of gas-phase ions to be directly determined.⁹⁻¹¹ This technique involves trapping the ions of interest in a mass spectrometer and then irradiating them with a tunable infrared source, such as a tabletop OPO laser⁹⁻¹⁷ or the free electron lasers at CLIO¹⁸ and FELIX.¹⁹ If the impinging radiation is in resonance with a vibrational mode of the

[†] Adapted from work previously published in *J. Phys. Chem. B*, **2011**, *115*, 11506 - 11518.

isolated ion, then the ion will absorb a photon. This vibrational energy is rapidly redistributed throughout the ion's other internal energy modes, allowing multiple photons to be absorbed at the same wavelength. Dissociation may occur once the ion absorbs enough energy to surpass its dissociation threshold. An ion's vibrational spectrum can therefore be revealed by scanning over a range of wavelengths and monitoring the extent of dissociation. The assignment of observed vibrational modes is often supported by comparing them to computed IR absorption spectra derived from electronic structural calculations, allowing detailed structures of the complexes to be determined.

The appeal of gas-phase ion techniques such as IRMPD stems from their ability to explore the intrinsic properties of the ion without the complications of bulk solvent. The activity and function of cationic amino acid complexes are partly dictated by the distribution of electrostatic forces throughout the molecule. In the condensed phases, for example, solvents such as water can alter the structure of amino acids and proteins.²⁰ For a given ion, an in depth comparison of gas- and solution-phase data can provide insight into the role of the solvents themselves. In the present study, the solvent absence allows for a better understanding of the interactions between lead(II) and the deprotonated amino acid binding sites as well as the result of singly hydrating $[\text{Pb}(\text{Aa-H})]^+$.

A large volume of work has recently been directed at determining the structures of stable gas-phase amino acid complexes through microsolvation,²¹⁻³³ dimerization,^{13,34-40} and metal chelation.^{13,41-59} Most of this research has focused on $[\text{M}(\text{Aa})]^{+2+}$ ions where M is an alkali or alkaline earth metal. The *p*-block amino acid complexes, however, have largely been ignored. Unlike other *p*-block metals, lead complexes with every amino

acid, and, as was mentioned above, the dominant gas-phase lead(II)-amino acid complexes formed by electrospray ionization are deprotonated.⁷ $[M(\text{Aa-H})]^+$ ions are not as well characterized as $[M(\text{Aa})]^+$ or $[M(\text{Aa})]^{2+}$ structures, although Ohanessian and coworkers have rigorously explored the structure and fragmentation pathways of $[\text{Zn}(\text{Gly-H})]^+$ using low-energy CID,⁶⁰⁻⁶³ and prior work by Atkins and coworkers used IRMPD spectroscopy to characterize the structure of $[\text{Pb}(\text{Gly-H})]^+$.¹² Their $[\text{Pb}(\text{Gly-H})]^+$ IRMPD spectrum revealed a strong IR absorption band around 3540 cm^{-1} which was assigned to the carboxylic acid O-H stretch. The proton lost in $[\text{Pb}(\text{Gly-H})]^+$ must therefore belong to the amine group since the carboxylic acid functional group remains intact. This was supported by DFT and *ab initio* electronic structure calculations that predicted the lowest energy structure of $[\text{Pb}(\text{Gly-H})]^+$ to be one where Pb^{2+} is covalently bound between the deprotonated amine group and the carbonyl oxygen of the carboxylic acid group (A in Figure 3.1). Further IRMPD spectroscopy experiments on $[\text{Pb}(\text{Gly-H})\text{H}_2\text{O}]^+$, its isotopomer $[\text{Pb}(\text{Gly-H})\text{H}_2^{18}\text{O}]^+$, $[\text{Pb}(\text{Gly-H})\text{CH}_3\text{OH}]^+$, and the glycine ethyl ester helped to confirm the structure of $[\text{Pb}(\text{Gly-H})]^+$.

Pb^{2+} can interact with deprotonated amino acids in several ways. Figure 3.1 shows three $[\text{Pb}(\text{Aa-H})]^+$ isomers. A is amine-deprotonated while B and C are carboxyl-deprotonated. Pb^{2+} binds between the amine group and the carboxylic acid in A and B, and lies between the two oxygens in C.¹² The following discussion will reveal that the predilection for a metal-cationized amino acid to adopt an A-, B-, or C-type structure is strongly dependent on the nature of the amino acid side chain.

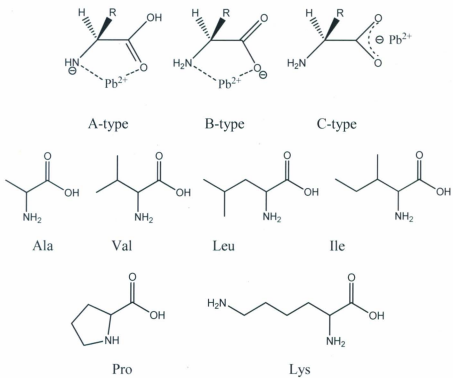


Figure 3.1. The three main types of complexes formed between Pb^{2+} and the conjugate bases of amino acids. Skeletal drawings of alanine, valine, leucine, isoleucine, proline, and lysine are also shown.

3.2. Methods.

3.2.1. IRMPD Spectroscopy. $[\text{Pb}(\text{Aa-H})]^+$ complexes were prepared by mixing approximately 0.1 mM $\text{Pb}(\text{NO}_3)_2$ (> 99%, Fluka Chemika) and 0.1 mM Aa (Aa = Ala, Val, Leu, Ile, Pro and Lys) (Nutritional Biochemicals Corporation) in a 50/50 mixture of 18.2 M Ω water (Millipore) and methanol (99.8%, ACP Chemicals). The $[\text{Pb}(\text{Aa-H})]^+$ solution was passed into the Apollo II ion source of a Bruker Apex Qe 7 T Fourier transform ion cyclotron resonance (FT-ICR) mass spectrometer at a flow rate of 100 $\mu\text{L h}^{-1}$. The voltage across the source exit capillary was 294 V. The $[\text{Pb}(\text{Aa-H})]^+$ ions were then mass selected by a quadrupole mass filter and allowed to accumulate in a hexapole collision cell for 0.8 – 2.0 s before being transferred to the ICR cell. Once in the ICR cell, the ions were irradiated using a potassium titanyl phosphate optical parametric oscillator (KTP OPO) for 2 – 7 s over the spectroscopic range of 3200 – 4000 cm^{-1} at intervals of 1.5 cm^{-1} . Two to six mass spectra were averaged per wavelength step. IRMPD spectra were prepared by plotting the IRMPD yield as a function of the OPO radiation frequency. The IRMPD yield is defined as the base 10 logarithm of the normalized precursor ion intensity.

The preparation of solvated complexes involved an extra step.⁶⁴ The collision cell has both an argon gas inlet line and a vapour inlet line. The argon flow is minimized while the desired solvent is added to the collision cell through the vapour inlet by opening a micro-valve. The solvents were degassed by a series of freeze-pump-thaw cycles prior to use.

The KTP OPO is pumped collinearly using a Brilliant B Nd:YAG laser (Big Sky Laser). The pump source is a 1064 nm fundamental line emitted in 6 ns (850 mJ) pulses at 10 Hz through a dichroic cavity mirror; this input mirror is highly reflective with respect to the signal wavelength (1.528 – 2.128 μm). The KTP crystal (8 x 12 x 25 mm) is enclosed in an OPO cavity which is only resonant with the signal wave. The output mirror is transparent at the pump wavelength and the idler wavelength (2.128 – 3.500 μm), but is 30% reflective with respect to the signal wavelength. The dichroic input and output mirrors allow the KTP OPO to produce two perpendicular beams: the signal and idler. The idler beam is used for near infrared spectroscopy between 2.128 – 3.500 μm , although in practice the useful range for IRMPD spectroscopy experiments is approximately 2.5 – 3.13 μm (4000 – 3200 cm^{-1}). The OPO (Euroscan) has a 3 cm^{-1} bandwidth and the output pulse varies as a function of the wavelength used. The maximum efficiency occurs at 2.6 μm where the conversion efficiency for an 800 mJ pump pulse is 20%; producing a 60 mJ idler pulse. The idler output then decreases somewhat linearly as wavelength increases; energy output above 3.2 μm is about 10 mJ, and energy output ceases between 3.4 and 3.5 μm . The idler beam divergence (0.5°) and astigmatism are corrected using a spherical Au mirror ($f = 3000$ mm) as well as a cylindrical ($f = 400$ mm) CaF_2 lens. The beam is then focused into the ICR cell by a second CaF_2 ($f = 200$ mm) lens. The KTP OPO idler beam is transmitted into the ICR cell through a path purged of CO_2 and H_2O . The radiation enters the ICR vacuum chamber through a BaF_2 window and then irradiates the ion packet in the ICR cell. An effective overlap between the laser and ion cloud is achieved by irradiating the ions with

a resonant frequency and adjusting the optical equipment to maximize the observed dissociation. The ICR cell itself is surrounded by a homemade heating jacket thermalized near 100 °C. This facilitates dissociation of the lead-complexes and increases the observed signal intensities.

3.2.2. Calculations. The Gaussian 09 software package was employed for all calculations.⁶⁵ Roughly 20 - 40 unique structures were considered for each complex, but for clarity only 3 - 7 of the lowest energy minima are reported here for each isomer. Each set of structures was created by varying the sites of deprotonation and lead chelation, as well as by altering bond and torsional angles to maximize hydrogen bonding or to relieve molecular strain. Geometry optimizations and harmonic frequency calculations were performed on every isomer using B3LYP density functional theory in conjunction with the LANL2DZ basis set with relativistic core potential for lead and the 6-31+G(d,p) basis set for all other atoms. This method is abbreviated here as B3LYP/6-31+G(d,p), although it should be remembered that the LANL2DZ basis set is always used for lead. The vibrational modes were scaled by a factor of 0.955 to compare with the experimental IRMPD spectra.^{12,13}

Single point energy calculations were performed on each optimized structure at the MP2 level of theory using the LANL2DZ basis set and core potential for lead and the larger 6-311++G(2d,2p) basis set for the other atoms. The 298 K Gibbs energies and enthalpies are reported as MP2(full)/6-311++G(2d,2p)//B3LYP/6-31+G(d,p). Like the B3LYP method, this is an abbreviation which omits the LANL2DZ basis set.

Thermodynamic data for the bare and hydrated Pro and Ala complexes were also calculated by replacing the LANL2DZ basis set with the SDD effective core potential for lead; geometry optimizations as well as single point energies were recalculated using this approach.⁶⁶ The MP2(full)/6-311++G(2d,2p)//B3LYP/6-31+G(d,p) method was still employed for all other atoms. This change in methodology arose from an observed discrepancy, discussed in more detail below, between the experimental results and the minimum energy structure of $[\text{Pb}(\text{Pro-H})]^+$ calculated by the LANL2DZ method.

Transitions states were also determined for isomerization reactions involving $[\text{Pb}(\text{Pro-H})]^+$, $[\text{Pb}(\text{Ala-H})]^+$, $[\text{Pb}(\text{Pro-H})\text{H}_2\text{O}]^+$, and $[\text{Pb}(\text{Ala-H})\text{H}_2\text{O}]^+$. These were authenticated by the presence of one imaginary vibrational mode that corresponds to the correct reaction coordinate.

3.3. Results and Discussion.

3.3.1. Comparison of $[\text{Pb}(\text{Aa-H})]^+$ and $[\text{Pb}(\text{Aa-H})\text{H}_2\text{O}]^+$ Infrared Spectra. The IRMPD spectra in the 3200 - 3800 cm^{-1} range for six $[\text{Pb}(\text{Aa-H})]^+$ complexes are compared in Figure 3.2. In each case, the only fragmentation induced by radiation from the KTP OPO laser was H_2O loss, although $[\text{Pb}(\text{Val-H})]^+$ also lost a small amount of CO over its O-H stretch region (12% of the H_2O loss).

The $[\text{Pb}(\text{Aa-H})]^+$ complexes containing Ala, Val, Leu, and Ile exhibit similar absorbance patterns. Each spectrum contains a weak absorbance in the N-H stretch region at approximately 3410 - 3440 cm^{-1} and a strong absorbance centered around 3560

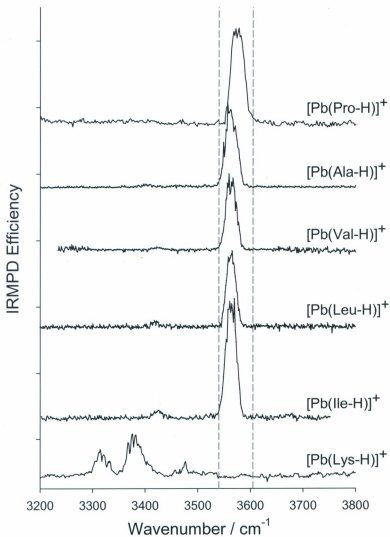


Figure 3.2. IRMPD spectra in the 3200 - 3800 cm⁻¹ region of six Pb²⁺/amino acid conjugate base complexes.

cm^{-1} in the O-H stretch region. The former is assigned as an amine N-H stretch while the latter is designated as a carboxylic acid O-H stretch. The spectrum of $[\text{Pb}(\text{Pro-H})]^+$ is similar to the above spectra except that nothing is observed in the N-H stretch region. Deprotonation is therefore occurring at the amine moiety and not the carboxylic acid for the $[\text{Pb}(\text{Aa-H})]^+$ complexes involving nonpolar amino acids (Aa = Ala, Val, Leu, Ile, and Pro).

The IRMPD spectrum of $[\text{Pb}(\text{Lys-H})]^+$ is clearly different than the spectra of the five complexes discussed above (Figure 3.2). Most notably it lacks the strong feature at $\sim 3560 \text{ cm}^{-1}$ assigned to the O-H stretch. This suggests that $[\text{Pb}(\text{Lys-H})]^+$ is deprotonated at the carboxylic acid end of the amino acid. Furthermore, the IRMPD spectrum of $[\text{Pb}(\text{Lys-H})]^+$ also contains three observable peaks in the N-H stretching region at 3315, 3380 and 3480 cm^{-1} .

Six $[\text{Pb}(\text{Aa-H})\text{H}_2\text{O}]^+$ complexes were produced in the storage hexapole by singly hydrating the $[\text{Pb}(\text{Aa-H})]^+$ ions, and their IRMPD spectra are collected in Figure 3.3. The only fragmentation pathway observed upon irradiation by the KTP OPO was H_2O loss. However, Ala, Val, Leu, and Ile also exhibited a much smaller secondary loss of another H_2O (10% relative to the first loss) over the carboxylic acid O-H stretch region; this is attributed to IRMPD of the $[\text{Pb}(\text{Aa-H})]^+$ fragment ions. The IRMPD spectra of $[\text{Pb}(\text{Pro-H})\text{H}_2\text{O}]^+$ and $[\text{Pb}(\text{Lys-H})\text{H}_2\text{O}]^+$ are clearly different from those of the $[\text{Pb}(\text{Aa-H})\text{H}_2\text{O}]^+$ complexes containing Ala, Val, Leu, and Ile. The $[\text{Pb}(\text{Aa-H})\text{H}_2\text{O}]^+$ (Aa = Ala, Val, Leu, and Ile) IRMPD spectra each contain weak absorptions due to amine N-H stretching

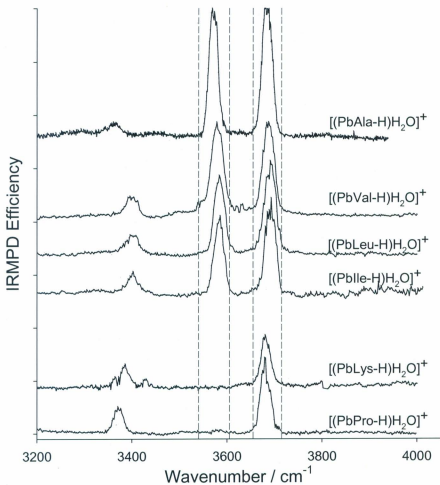


Figure 3.3. IRMPD spectra in the 3200 - 4000 cm^{-1} region of six hydrated Pb^{2+} /amino acid conjugate base complexes.

between 3250 and 3400 cm^{-1} and two much stronger absorptions at 3580 and 3690 cm^{-1} . These latter two bands are in similar positions to the carboxylic acid O-H stretch and PbO-H stretch, respectively, of $[\text{Pb}(\text{Gly-H})\text{H}_2\text{O}]^+$.¹²

The IRMPD spectra of $[\text{Pb}(\text{Lys-H})\text{H}_2\text{O}]^+$ and $[\text{Pb}(\text{Pro-H})\text{H}_2\text{O}]^+$ have only one band in the O-H stretching region at about 3680 cm^{-1} . Since the bare $[\text{Pb}(\text{Lys-H})]^+$ complex did not have a carboxylic acid O-H stretch it might be expected that attaching water to $[\text{Pb}(\text{Lys-H})]^+$ would result in the water symmetric and antisymmetric stretching absorptions, but this can be dismissed spectroscopically based on the observation of only one O-H stretch. Transfer of a proton back to the carboxylate group can also be ruled out based on the absence of the COO-H band. A structure where water is coordinated to lead and intramolecularly hydrogen bonded to another basic site in the molecule may explain the spectrum. The IRMPD spectrum of $[\text{Pb}(\text{Pro-H})\text{H}_2\text{O}]^+$ is interesting; it does not have a carboxylic acid O-H stretch but the bare complex, $[\text{Pb}(\text{Pro-H})]^+$, did. This suggests that, during solvation in the storage hexapole, $[\text{Pb}(\text{Pro-H})]^+$ isomerizes from an amine-deprotonated structure to a carboxylic acid-deprotonated structure.

The IRMPD spectra described above will now be compared with computed IR spectra in order to determine more detailed structures.

3.3.2. $[\text{Pb}(\text{Ala-H})]^+$ and $[\text{Pb}(\text{Ala-H})\text{H}_2\text{O}]^+$. The lowest-energy structures for the $[\text{Pb}(\text{Ala-H})]^+$ and $[\text{Pb}(\text{Ala-H})\text{H}_2\text{O}]^+$ complexes are shown in Figure 3.4. The relative enthalpies and 298 K Gibbs energies, computed using both the LANL2DZ and SDD

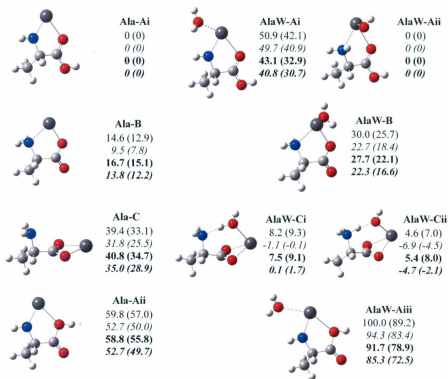


Figure 3.4. B3LYP/6-31+G(d,p) (LANL2DZ on Pb) computed structures for the bare and hydrated $[\text{Pb}(\text{Ala-H})]^+$ complexes. The reported energies are 298 K enthalpies and Gibbs energies (in parentheses) and have units of kJ mol^{-1} . The unbolded and bolded values were determined using the LANL2DZ and SDD methods, respectively, on Pb. The non-italicized values are B3LYP/6-31+G(d,p) (with LANL2DZ or SDD on Pb) and the italicized values are MP2(full)/6-311++G(2d,2p)//B3LYP/6-31+G(d,p) (with LANL2DZ or SDD on Pb).

methods discussed earlier, are also presented. It is evident that the lowest energy structure of $[\text{Pb}(\text{Ala-H})]^+$, Ala-Ai, is amine-deprotonated with Pb^{2+} bound between HN^- and the carbonyl oxygen. Ala-Ai is also significantly lower in energy than the carboxyl-deprotonated isomers, Ala-B and Ala-C. Ala-B coordinates Pb^{2+} similarly to Ala-Ai, while in Ala-C Pb^{2+} interacts with the carboxylate anion. The nearly 90° OCCN dihedral angle for Ala-C is lower in energy than structures with a 0° OCCN angle by 2.5 kJ mol^{-1} . The $3200 - 3800 \text{ cm}^{-1}$ region of the computed infrared spectra for these structures are also unaffected by the difference in OCCN dihedral angle and so only the lowest energy isomers are shown.

Adding water to each of these complexes results in the isomers depicted on the right hand side of Figure 3.4. There are two types of structures, one where water is intact and another where it donates a proton to the deprotonated amine group. For three of the structures with an intact water, AlaW-Ai, AlaW-B, and AlaW-Aiii, proton transfer results in AlaW-Aii. For AlaW-Ci, proton transfer results in AlaW-Cii. Whereas the non-solvated C-type tautomer, Ala-C, was predicted to be 25.5 kJ mol^{-1} higher in Gibbs energy than Ala-Ai, solvating dramatically changes this picture. Solvation of Ala-Ai produces AlaW-Ai, an isomer which is $30.7 - 40.9 \text{ kJ mol}^{-1}$ higher in Gibbs energy than AlaW-Ci, the complex formed by solvating Ala-C. The subsequent proton-transfer from water back to HN^- produces AlaW-Aii, which is roughly isoenergetic with the lowest energy isomer, AlaW-Cii, according to MP2 methods.

Figures 3.5 and 3.6 compare the $[\text{Pb}(\text{Ala-H})]^+$ and $[\text{Pb}(\text{Ala-H})\text{H}_2\text{O}]^+$ IRMPD

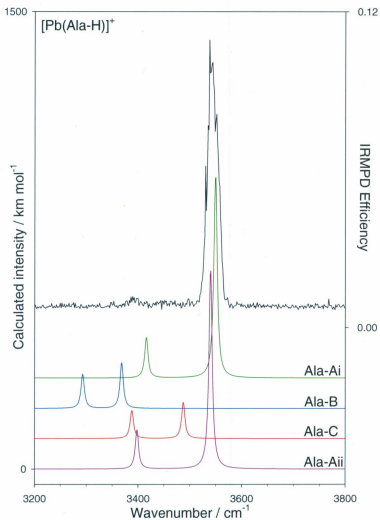


Figure 3.5. Comparison of the [Pb(Ala-H)]⁺ IRMPD spectrum (black) with the B3LYP/6-31+G(d,p) calculated spectra for the isomers displayed in Figure 3.4.

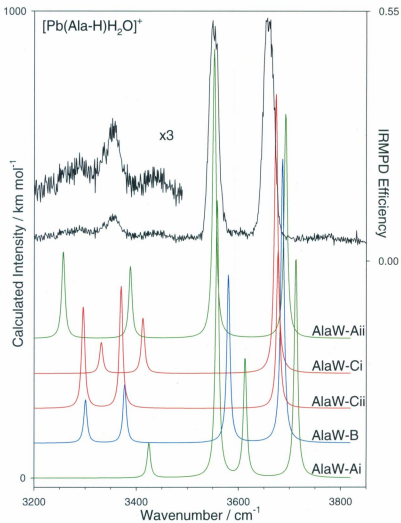


Figure 3.6. Comparison of the $[\text{Pb}(\text{Ala-H})\text{H}_2\text{O}]^+$ IRMPD spectrum (black) with the B3LYP/6-31+G(d,p) calculated spectra for the isomers displayed in Figure 3.4.

spectra with the B3LYP/6-31+G(d,p) computed IR spectra of the isomers shown in Figure 3.4. There is a distinct similarity between the experimental spectrum of $[\text{Pb}(\text{Ala-H})]^+$ and the computed spectra of Ala-Ai and Ala-Aii. These structures are difficult to distinguish spectroscopically, but Ala-Aii is calculated to be 50.0 kJ mol^{-1} higher in Gibbs energy and is not expected to be present in the gas phase. It is therefore highly probable that the species responsible for the experimental spectrum is the lowest energy structure, Ala-Ai. The strong band at 3560 cm^{-1} and the weak band at 3410 cm^{-1} are therefore assigned to the carboxylic acid O-H stretch and the N-H stretch of Ala-Ai, respectively.

The IRMPD spectrum of $[\text{Pb}(\text{Ala-H})\text{H}_2\text{O}]^+$ is compared with five computed spectra in Figure 3.6. The experimental spectrum has only two strong bands in the O-H stretch region. This rules out AlaW-Ai and AlaW-Aiii, the complexes formed simply by adding water to Ala-Ai and Ala-Aii, respectively, which are both expected to have symmetric and antisymmetric water stretches in addition to a carboxylic acid O-H stretch. AlaW-Aii and AlaW-B both compare very well with the experimental spectrum. AlaW-Aii suggests that water has transferred a proton to the deprotonated site on the amino acid, leaving a PbO-H stretch observed at 3690 cm^{-1} and a carboxylic acid O-H stretch at 3580 cm^{-1} . AlaW-B could be formed by simply adding water to Ala-B. AlaW-B is significantly higher in energy than AlaW-Aii but it is possible to experimentally rule out AlaW-B as a contributor to the IRMPD spectrum by adding oxygen-18 labeled water to the electrosprayed complex in the hexapole cell. If both observed bands were due to water stretches, then each would be expected to shift. If the 3680 cm^{-1} band was due to

the carboxylic acid O-H stretch then that band would not shift upon addition of oxygen-18 labeled water. The IRMPD spectra determined when normal water and oxygen-18 labeled water were added to $[\text{Pb}(\text{Ala-H})]^+$ are shown in Figure 3.7 in black and blue, respectively. The predicted spectra for AlaW-Aii and AlaW-B with both normal and oxygen-18 labeled water added to Pb are also shown. The 3690 cm^{-1} peak red-shifts by $\sim 7\text{ cm}^{-1}$ after labeling, a change that is outside the bandwidth of the KTP OPO. This shift, combined with the absence of a shift in the 3580 cm^{-1} absorption, rules out AlaW-B and, in fact, any structure where there is free water bound to the $[\text{Pb}(\text{Ala-H})]^+$ complex.

AlaW-Ci and AlaW-Cii are computed to be similar in energy to AlaW-Aii but are expected to have only one band in the O-H stretch region. While the presence of the 3680 cm^{-1} band does confirm the presence of a structure such as AlaW-Aii, it does not necessarily rule out the presence of AlaW-Ci and AlaW-Cii. In fact, the N-H stretch region is more complex than the two N-H stretching vibrations of AlaW-Aii would suggest; there is observable IRMPD intensity at about 3450 cm^{-1} between the carboxylic acid O-H stretch and the most intense N-H stretching vibration (observed at 3370 cm^{-1}) that might be consistent with one or both of the AlaW-C isomers being present in addition to AlaW-Aii. Furthermore, the band observed at the lowest frequency is broad and may be so due to it being composed of more than one vibration, although it could also be that in AlaW-Aii the N-H bond has a small degree of interaction with the oxygen of the PbOH moiety. Based on the present data, it is difficult to rule out the AlaW-C structures, but it is quite apparent from the intense carboxylic acid O-H stretch that

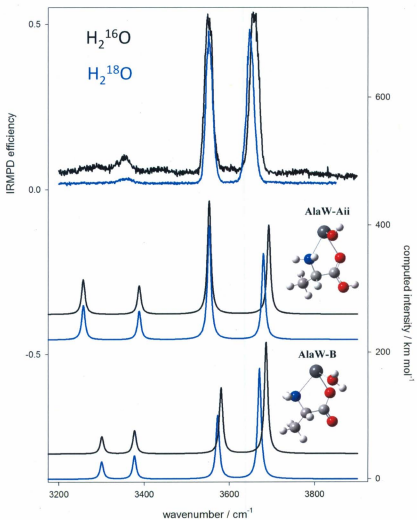


Figure 3.7. Comparison of IRMPD and computed spectra for $[\text{Pb}(\text{Ala-H})\text{H}_2^{16}\text{O}]^+$ and $[\text{Pb}(\text{Ala-H})\text{H}_2^{18}\text{O}]^+$.

there is a significant contribution from AlaW-Aii. If the AlaW-C structures are present, it likely means that isomerization occurs during the solvation of Ala-Ai in the hexapole storage cell.

An IRMPD spectrum was also recorded for $[\text{Pb}(\text{Ala-H})]^+$ solvated by methanol, $[\text{Pb}(\text{Ala-H})\text{CH}_3\text{OH}]^+$. This spectrum, shown in Figure 3.8, exhibits IRMPD intensity in the N-H stretch region and, similar to the $[\text{Pb}(\text{Ala-H})]^+$ and $[\text{Pb}(\text{Ala-H})\text{H}_2\text{O}]^+$ IRMPD spectra, a strong band at about 3560 cm^{-1} consistent with a carboxylic acid O-H stretch. There is also a weaker band at 3640 cm^{-1} . If we were observing a structure similar to AlaW-Aii for $[\text{Pb}(\text{Ala-H})\text{H}_2\text{O}]^+$ we would not expect to see a band in this region since the PbOH moiety is changed to PbOCH_3 . Furthermore, solvating Ala-C would not produce a structure that exhibits the carboxylic acid O-H stretch and, unless the hydrogen bonding similar to that observed for the AlaW-C structures were absent, there would also be no methanol free O-H stretch. Figure 3.8 compares the experimental IRMPD spectrum with the computed spectra of three possible structures: AlaM-Ai, AlaM-Aii, and AlaM-C. It is apparent that we cannot rule out any of these isomers. Even AlaM-Ai, which is predicted to be 34.5 kJ mol^{-1} higher in Gibbs energy than AlaM-Aii, cannot be ruled out. AlaM-Ai is most likely responsible for the 3640 cm^{-1} band. This is the entrance channel complex between methanol and Ala-Ai and its presence suggests that some of this complex gets kinetically trapped in this structure and that proton transfer to the deprotonated amine is not complete.

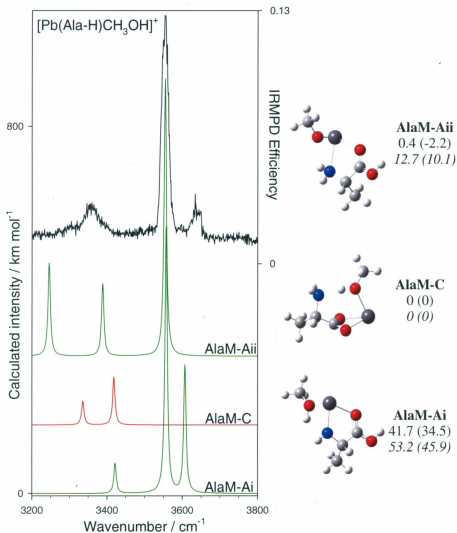


Figure 3.8. Comparison of the IRMPD spectrum of $[\text{Pb}(\text{Ala-H})\text{CH}_3\text{OH}]^+$ with the computed spectra of three isomeric structures. The 298 K enthalpies (and Gibbs energies in parentheses) have units of kJ mol^{-1} and are computed using B3LYP/6-31+G(d,p) (non italicized, with LANL2DZ on Pb) and MP2(full)/6-311++G(2d,2p)//B3LYP/6-31+G(d,p) (italicized, with LANL2DZ on Pb), respectively.

3.3.3. [Pb(Val-H)]⁺, [Pb(Leu-H)]⁺, [Pb(Ile-H)]⁺ and their Monohydrated Analogues.

The IRMPD spectra of the bare [Pb(Val-H)]⁺, [Pb(Leu-H)]⁺, and [Pb(Ile-H)]⁺ complexes are compared with computed IR spectra in Figure 3.9. The three lowest-energy structures for each of these complexes are shown in Figure 3.10. These spectra are very similar to the IRMPD spectrum of [Pb(Ala-H)]⁺ in Figure 3.5, and it is clear by comparing the computed and experimental spectra that, in each case, the main contributor to the gas-phase population is the lowest energy isomer (Val-A, Leu-A and Ile-A).

The IRMPD spectra for the monohydrated complexes, [Pb(Val-H)H₂O]⁺, [Pb(Leu-H)H₂O]⁺, and [Pb(Ile-H)H₂O]⁺ are shown in Figure 3.11. Also in Figure 3.11, and compared to the experimental spectra, are the computed spectra for the lowest-energy hydrated structures. The computed structures and relative energies for the most stable hydrated complexes are shown in Figure 3.12. The B3LYP calculated energies predict the A- and C-type ions to be similar in energy, while the MP2 calculations predict the C-type structures to be 4.6 and 11.0 kJ mol⁻¹ lower in Gibbs energy than the A-type structures. The features of the IRMPD spectra, however, clearly belong to the A-type structures. In a similar manner to the case of [Pb(Ala-H)H₂O]⁺, the B-type structures can be ruled out by isotopic labeling experiments that show only a shift in the PbO-H stretching vibration. The calculations also show the B-type ions to be significantly higher in energy. For the non-hydrated species, the A-type complexes were computed to be the lowest in Gibbs energy over the C-type structures by at least 25.4 kJ mol⁻¹ and the spectra are consistent with the A-type structures. That these structures seem to be the main species present in

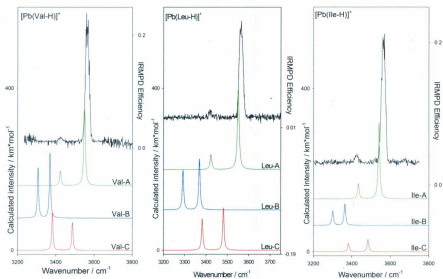


Figure 3.9. The IRMPD spectra of $[\text{Pb}(\text{Val-H})]^+$, $[\text{Pb}(\text{Leu-H})]^+$, and $[\text{Pb}(\text{Ile-H})]^+$ compared with the B3LYP/6-31+G(d,p) computed spectra for the A-, B- and C-type isomers seen in Figure 3.10.

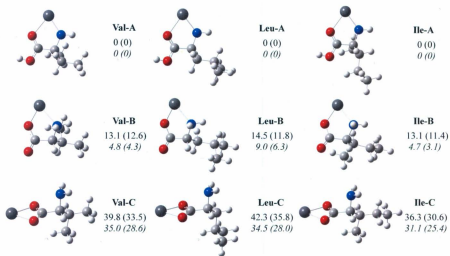


Figure 3.10. Computed structures for the complexes between Pb^{2+} and the conjugate bases of Val, Leu, and Ile. The 298 K enthalpies (and Gibbs energies in parentheses) have units of kJ mol^{-1} and were computed using B3LYP/6-31+G(d,p) (non italicized, with LANL2DZ or SDD on Pb) and MP2(full)/6-311++G(2d,2p)//B3LYP/6-31+G(d,p) (italicized, with LANL2DZ or SDD on Pb).

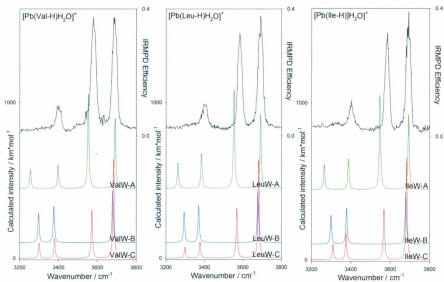


Figure 3.11. The IRMPD spectra of $[\text{Pb}(\text{Val-H})\text{H}_2\text{O}]^+$, $[\text{Pb}(\text{Leu-H})\text{H}_2\text{O}]^+$, and $[\text{Pb}(\text{Ile-H})\text{H}_2\text{O}]^+$ compared with the B3LYP/6-31+G(d,p) computed spectra for the A-, B- and C-type isomers seen in Figure 3.12.

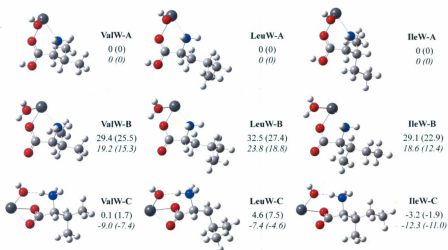


Figure 3.12. Computed structures for the hydrated complexes between Pb^{2+} and the conjugate bases of either Val, Leu, or Ile. The 298 K enthalpies (and Gibbs energies in parentheses) have units of kJ mol^{-1} and are computed using B3LYP/6-31+G(d,p) (non italicized, with LANL2DZ or SDD on Pb) and MP2(full)/6-311++G(2d,2p)//B3LYP/6-31+G(d,p) (italicized, with LANL2DZ or SDD on Pb).

the hydrated system as well suggests that the A-type structures are being solvated and that the energy barrier for isomerization to the hydrated C structures is too high to be overcome on the timescale of the present experiments. It could also suggest that the calculations artificially stabilize the C structures with respect to the A structures. This will be elaborated upon in the next section.

3.3.4. [Pb(Pro-H)]⁺ and [Pb(Pro-H)H₂O]⁺. The IRMPD spectrum of [Pb(Pro-H)]⁺ is compared to the computed spectra of its three lowest energy isomers in Figure 3.13; the structures are shown in Figure 3.14. The spectrum exhibits a carboxylic acid O-H stretch, but there is no observable N-H stretch, suggesting that proline is, like the other systems discussed so far, amine deprotonated. The calculations predict that the carboxyl-deprotonated Pro-B is 11.5 kJ mol⁻¹ lower in Gibbs energy than Pro-Ai using MP2 theory in conjunction with the LANL2DZ method. Calculations employing the SDD basis set and core potential yield slightly different results in that the two isomers are virtually identical in energy. The experimental spectrum, however, is most consistent with Pro-Ai. That simply changing a basis set produces different minimum energy structures demonstrates the importance that experiments have in revealing structural information. One cannot solely rely on calculations.

The IRMPD spectrum of [Pb(Pro-H)H₂O]⁺ (Figures 3.3 and 3.13) is markedly different from the amino acid complexes discussed above. The strong carboxylic acid O-H stretch observed between 3560 and 3580 cm⁻¹ for the bare and hydrated [Pb(Ala-H)]⁺, [Pb(Val-H)]⁺, [Pb(Leu-H)]⁺, and [Pb(Ile-H)]⁺ complexes as well as for the [Pb(Pro-H)]⁺

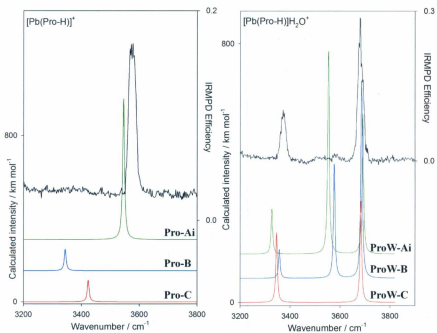


Figure 3.13. Comparison of the IRMPD spectra of $[\text{Pb}(\text{Pro-H})]^+$ and $[\text{Pb}(\text{Pro-H})\text{H}_2\text{O}]^+$ with the computed spectra belonging to the structures shown in Figure 3.14.

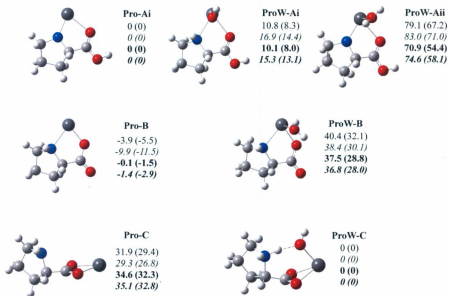


Figure 3.14. B3LYP/6-31+G(d,p) (LANL2DZ on Pb) computed structures for bare and hydrated Pb^{2+} /proline conjugate base complexes. The energies reported are 298 K enthalpies (and Gibbs energies in parentheses) and have units of kJ mol^{-1} . The unbolded and bolded values were determined using the LANL2DZ and SDD methods, respectively, on Pb. The non-italicized values are B3LYP/6-31+G(d,p) (with LANL2DZ or SDD on Pb) and the italicized values are MP2(full)/6-311++G(2d,2p)//B3LYP/6-31+G(d,p) (with LANL2DZ or SDD on Pb).

structure is absent. Figure 3.13 also compares the experimental spectrum of $[\text{Pb}(\text{ProH})\text{H}_2\text{O}]^+$ with three computed IR spectra. The absence of a band in the 3560 and 3580 cm^{-1} region means that ProW-Ai and ProW-B cannot explain the observed spectrum. The computed spectrum of ProW-C, however, does. ProW-C is computed to be lower in 298 K Gibbs energy than ProW-Ai by approximately 14.4 or 13.1 kJ mol^{-1} , depending on whether the LANL2DZ or SDD basis set with effective core potential, respectively, was used for lead.

These experiments show that after hydration, or during the hydration process, electrosprayed Pro-Ai isomerizes to Pro-C so that the observed hydrated isomer is ProW-C. The question is why does this same process not happen for Ala-A, Val-A, Leu-A, and Ile-A, all of which are observed in the IRMPD experiments, as are the corresponding hydrated A-type isomers, AlaW-A, ValW-A, LeuW-A, and IleW-A? To answer this question, the potential energy surfaces for the isomerization of Ala-A to Ala-C and for Pro-A to Pro-C were computed using the method of intrinsic reaction coordinates (Figures A1 and A2 in Appendix A, respectively).⁶⁷ For $[\text{Pb}(\text{Ala-H})]^+$, the path from Ala-Ai to Ala-C goes through Ala-Aii and then Ala-B, and a similar mechanism was found for the isomerization of Pro-Ai to Pro-C. There are two energy barriers required for these reactions, the highest being for the transformation of the Aii isomers to the B isomers, which requires 207 kJ mol^{-1} and 223 kJ mol^{-1} of Gibbs energy for the Ala and Pro systems, respectively. Since the expected thermal energies of both Pro-Ai and Ala-Ai are roughly 30 and 25 kJ mol^{-1} , these energy barriers are far too high for these reactions to

take place in the gas phase. There are also no thermodynamic grounds for isomerization since both rearrangements are uphill processes requiring some 30 kJ mol^{-1} .

As stated previously, $[\text{Pb}(\text{Ala-H})]^+$ and $[\text{Pb}(\text{Pro-H})]^+$ adopt A-type isomers. It is the hydrated structures that differ. A likely place for isomerization to occur is in the storage hexapole, which has a modest pressure ($\sim 10^{-2}$ mbar) of water vapour. One could envisage that after the first addition of water, a second water could assist in any proton transfer isomerizations. A water-assisted isomerization of the hydrated A-type complexes to the B-type isomers was found with a barrier just above 30 kJ mol^{-1} (Figures 3.15A and B for alanine and proline, respectively). The second step in both cases is a change in lead binding from N and O to the two carboxylate oxygens. This final isomerization is not assisted by water and has a Gibbs energy barrier of 166 kJ mol^{-1} for the Ala case but only 82 kJ mol^{-1} for the Pro system. The expected thermal energies of $[\text{Pb}(\text{Ala-H})\text{H}_2\text{O}]^+$ and $[\text{Pb}(\text{Pro-H})\text{H}_2\text{O}]^+$ are approximately 35 and 40 kJ mol^{-1} , respectively. While there is very likely some uncertainty in the magnitudes of these Gibbs energy barriers their relative heights are probably trustworthy. It is clear that the rate constant for the isomerization of AlaW-B to AlaW-C will be orders of magnitude smaller than for the ProW-B to ProW-C isomerization, and is, in fact, 10^{14} slower based on the MP2 Gibbs energies at 298 K . This would account for why ProW-C is observed in the IRMPD spectrum of $[\text{Pb}(\text{Pro-H})\text{H}_2\text{O}]^+$, as well as explain why the main isomer for $[\text{Pb}(\text{Ala-H})\text{H}_2\text{O}]^+$ is ProW-Aii.

The significant difference in the Gibbs energy barriers also brings up the question as to the source of this difference. Proline, being a secondary amine, is significantly

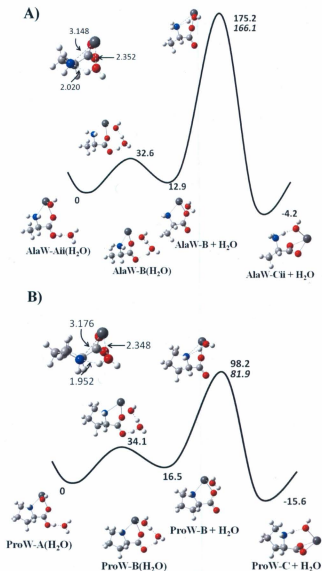


Figure 3.15. 298 K Gibbs energy (units of kJ mol^{-1}) diagram for the isomerization of the hydrated A-type structures to the hydrated C-type structures for alanine (A) and proline (B). The non-italicized and italicized values were determined by the B3LYP and MP2 methods, (with LANL2DZ on Pb), respectively.

more basic than alanine; the gas-phase basicity of proline is 928 kJ mol^{-1} , while alanine's is 888 kJ mol^{-1} .⁶⁸ This means that the transition state for the proline isomerization is better stabilized by a much stronger water O-H...N hydrogen bond, 1.952 \AA in the proline transition state versus 2.020 \AA for the alanine transition state (Figures 3.15A and B). The greater basicity of Pro also results in a slightly longer Pb-N bond for the transition state, making it more product-like and less tight. That proline is more basic than alanine, valine, leucine, and isoleucine, and is better at stabilizing the transition state from N and O bound Pb to carboxylate-bound Pb could explain why isomerization is observed to occur in the proline case but not for any of the others.

3.3.5. [Pb(Lys-H)]⁺ and [Pb(Lys-H)H₂O]⁺. The basic side chain of lysine contains an ϵ -amine group that can interact with the lead cation. A comparison of the lowest energy [Pb(Lys-H)]⁺ isomers in Figure 3.16 demonstrates that this interaction significantly stabilizes structures where the side chain is interacting with lead (Lys-Ai, -Bi, and -Ci) relative to those where it is absent (Lys-Aii, -Bii, and -Cii). Without the ϵ -amine interaction the Aii, Bii, and Cii structures have similar relative energies to the systems discussed previously; Lys-Aii and -Bii have comparable thermodynamic stabilities while Lys-Cii is higher in Gibbs energy by $29.6 - 31.8 \text{ kJ mol}^{-1}$. Lys-Bii and -Cii, which are both deprotonated at the carboxylic acid, are stabilized by the side chain interaction to a much greater extent (86.4 and $126.5 \text{ kJ mol}^{-1}$, respectively) than Lys-Aii (57.8 kJ mol^{-1}) which is amine-deprotonated. This extra stabilization of Pb²⁺ by the side chain renders

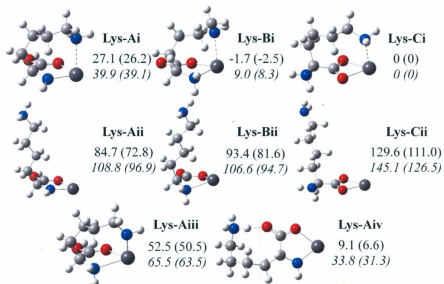


Figure 3.16. The B3LYP/6-31+G(d,p) optimized structures of $[\text{Pb}(\text{Lys-H})]^+$. The 298 K relative enthalpies and Gibbs energies (in parentheses) have units of kJ mol^{-1} and are provided at the B3LYP/6-31+G(d,p) (top) and MP2(full)/6-311++G(2d,2p) (bottom and italicized) levels of theory. Note that the LANL2DZ basis set with effective core potential were applied to Pb^{2+} for both levels of calculation.

Lys-Bi and -Ci significantly lower in energy than the Lys-Ai structure, and makes Lys-Ci the lowest energy isomer. Structures where deprotonation occurs at the amine side chain (Lys-Aiii), and where the carboxylic acid OH is hydrogen bonded to the side chain amine group (Lys-Aiv), are also higher in energy than Lys-Ci. It should be noted that Lys-Aiv is a zwitterionic structure that results from a proton transfer from the carboxylic acid group to the side chain. The resulting -NH_3^+ is hydrogen bonded to the -COO^- group. The Gibbs energy of this structure is actually slightly lower (7.8 kJ mol^{-1}) than Lys-Ai, but it is still 31.3 kJ mol^{-1} higher in energy than Lys-Ci.

The IRMPD spectrum of $[\text{Pb}(\text{Lys-H})]^+$ is shown in Figure 3.17 and is compared with the computed IR spectra of the four lowest energy $[\text{Pb}(\text{Lys-H})]^+$ structures. The experimental spectrum exhibits three main features in the N-H stretching region at 3360, 3390 and 3430 cm^{-1} . Unlike the spectra of the bare $[\text{Pb}(\text{Aa-H})]^+$ complexes involving nonpolar amino acids, there is no carboxylic acid O-H stretch. This spectroscopically rules out all the amine-deprotonated isomers except for Lys-Aiv, and is consistent with these structures being computed to be significantly higher in energy. The structure with the computed spectrum that is most consistent with the experimental spectrum is Lys-Ci which is also the one predicted to be the lowest in enthalpy and Gibbs energy at the MP2 level of theory. While experimentally, Lys-Bi and Lys-Aiii cannot be ruled out as contributing to the infrared spectrum, their computed Gibbs energies suggest that, if they exist, they will be minor contributors to the gas-phase population.

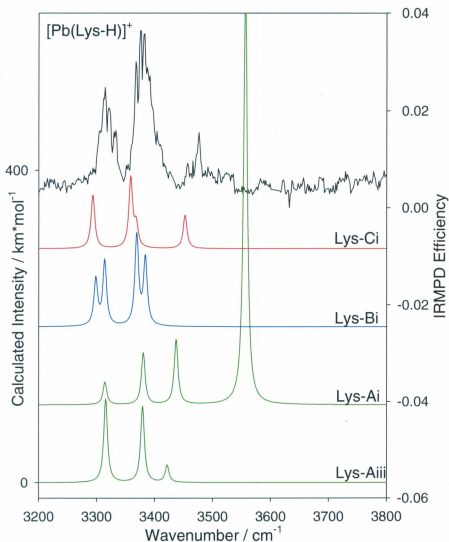


Figure 3.17. The IRMPD spectrum of $[\text{Pb}(\text{Lys-H})]^+$ (black) compared with four computed IR spectra. The computed spectra are from the B3LYP/6-31+G(d,p) optimized structures of Lys-Ci, -Bi, -Ai, and -Aiii shown in Figure 3.16.

The lowest energy structures of seven $[\text{Pb}(\text{Lys-H})\text{H}_2\text{O}]^+$ isomers are shown in Figure 3.18. The most stable complex is a three coordinate B-type ion (LysW-Bi). The lead cation of LysW-Bi is hydroxylated and a proton has been transferred from the water to the ϵ -amine; the side chain is also hydrogen bonded to the deprotonated oxygen atom. The B structure where water is intact (LysW-Bii) is 51.2 kJ mol^{-1} higher in Gibbs energy than LysW-Bi. Unlike the bare complexes, the C structure (LysW-Ci) is predicted to be slightly (7.5 kJ mol^{-1}) higher in energy than the B structure. LysW-Cii with water intact is, again, four coordinate but is only predicted to be 5.7 kJ mol^{-1} higher in Gibbs energy than LysW-Ci. LysW-Ai and LysW-Aii are 38.3 and 70.0 kJ mol^{-1} higher in Gibbs energy than LysW-Bi. The lowest-energy A-type structure, LysW-Aiii (similar to Lys-Aiii in Fig. 3.16), is also significantly higher in energy, 29.1 kJ mol^{-1} , than the lowest energy structure.

The computed spectra of the four lowest energy $[\text{Pb}(\text{Lys-H})\text{H}_2\text{O}]^+$ isomers are compared to the IRMPD spectrum in Figure 3.19. Any of the complexes with intact water, such as LysW-Cii, will obviously not match the experimental spectrum as there would be two bands in the OH stretch region. Similarly, LysW-Ai cannot reproduce the IRMPD spectrum because there would be a carboxylic acid O-H stretch as well as a PbO-H stretch. LysW-Bi is the most consistent with the experimental spectrum and actually reproduces it quite well; it is also the lowest energy isomer. There are three observed N-H stretches expected from this structure since two of the N-H bonds are hydrogen bonded and predicted to occur at much lower frequencies out of the range of these experiments.

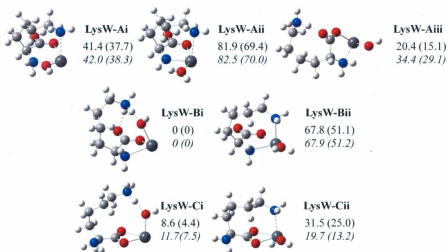


Figure 3.18. The B3LYP/6-31+G(d,p) optimized structures of $[\text{Pb}(\text{Lys-H})\text{H}_2\text{O}]^+$. The 298 K relative enthalpies and Gibbs energies (in parentheses) have units of kJ mol^{-1} and are provided at the B3LYP/6-31+G(d,p) (top) and MP2(full)/6-311++G(2d,2p) (bottom and italicized) levels of theory. Note that the LANL2DZ basis set and effective core potential were applied to Pb^{2+} for both levels of calculation.

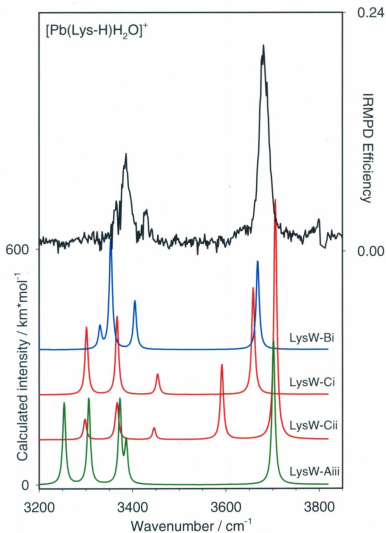


Figure 3.19. The IRMPD spectrum of $[\text{Pb}(\text{Lys-H})\text{H}_2\text{O}]^+$ (black) compared with four computed IR spectra. The computed spectra are from the B3LYP/6-31+G(d,p) optimized structures of LysW-Bi, -Ci, -Cii, and -Aiii shown in Figure 3.18.

There is no experimental or theoretical evidence for any of the other structures contributing to the spectrum. A B-type structure for the solvated $[\text{Pb}(\text{Lys-H})]^+$ complex and a C-type structure for the bare complex means that during solvation an isomerization reaction occurs where lead changes binding sites from N and O to COO^- , similar to the proline complexes. A determination of the potential energy surface for this isomerization is beyond the scope of this work.

3.4. Conclusions: Pb^{2+} Stabilization by Amino Acid Conjugate Bases. IRMPD spectroscopy and electronic structure calculations confirmed that $[\text{Pb}(\text{Aa-H})]^+$ complexes are deprotonated at the amine group (A-type structures) for amino acids with nonpolar side chains or amino acids where the side chains do not interact with lead. This can be rationalized using hard-soft acid-base theory; Pb^{2+} is typically considered a soft (or intermediate) Lewis acid and prefers to bond covalently to soft bases.^{69,70} The carboxylate anion is a hard base while the NH_2 , NH , NH^+ , or N^- group would all be considered much softer; this accounts for the preferred binding by lead. That the A-type structures are preferred means that there is extra stabilization of Pb^{2+} by the NH^+ or N^- functional groups over the NH_2 or NH moieties that overcomes the higher energy required to deprotonate the amine group relative to the carboxylic acid. The extra stabilization of Pb^{2+} by lysine's basic side chain makes the C-type structure, deprotonated at the carboxylic acid, more stable than the amine deprotonated A-type structure.

When the complexes are hydrated, the calculations predict that the C-type structures are the lowest in energy due to the stabilization of Pb^{2+} by the extra

coordination of water and the hydrogen bonding between the protonated amine and the O of the PbOH moiety. The experimental IRMPD spectra, however, are more consistent with the A-type structures having an intact carboxylic acid when the amino acid is Ala, Val, Leu and Ile, and these conclusions are supported by IRMPD experiments with oxygen-18 labeled water that demonstrate a red-shift for the PbO-H stretch upon isotopic substitution, but no shift for the corresponding carboxylic acid O-H stretch. The existence of the A-type isomers is explained by the presence of an insurmountable isomerization barrier between the hydrated A- and C-type complexes. The case of proline is an exception; the bare proline complex is an amine deprotonated A-type structure but the hydrated complex is a C-type structure. This means that proline isomerization must occur during hydration. A mechanism for isomerization of the A-type structure to the C-type structure, part of which is a base (water) catalyzed proton transfer, was determined and is consistent with Pro having a much lower barrier ($\sim 80 \text{ kJ mol}^{-1}$) for isomerization than the case of Ala. This lower barrier is explained in terms of the greater basicity of proline, which stabilizes lead in the transition state. Experiment and theory also show that the lowest energy structure of $[\text{Pb}(\text{Lys-H})\text{H}_2\text{O}]^+$ is a B-type structure deprotonated at the carboxylic acid. In this case, the basic side chain provides the extra stability.

References

1. Patrick, L. *Altern. Med. Rev.* **2006**, *11*, 2 - 22.
2. Velez, S.; Nair, N. G.; Reddy, V. P. *Colloids Surf. B* **2008**, *66*, 291 - 294.
3. Fisher, A. E. O.; Naughton, D. P. *J. Struct. Chem.* **2006**, *47*, 87 - 90.
4. Fisher, A. E. O.; Naughton, D. P. *J. Struct. Chem.* **2007**, *48*, 711 - 714.
5. Fisher, A. E. O.; Naughton, D. P. *Biomed. Pharmacother.* **2005**, *59*, 158 - 162.
6. Burford, N.; Eelman, M.D.; LeBlanc, W.G. *Can. J. Chem.* **2004**, *82*, 1254 - 1259.
7. Burford, N.; Eelman, M.D.; LeBlanc, W.G.; Cameron, S.; Robertson, K.N. *Chem. Commun.* **2004**, 332 - 333.
8. Burford, N.; Eelman, M.D.; Groom, K. *J. Inorganic. Chem.* **2005**, *99*, 1992 - 1997.
9. Fridgen, T. D. *Mass. Spectrom. Rev.* **2009**, *28*, 586 - 607.
10. Eyler, J. R. *Mass Spectrom. Rev.* **2009**, *28*, 448 - 467.
11. Polfer, N. C.; Oomens, J. *Mass Spectrom. Rev.* **2009**, *28*, 468 - 494.
12. Atkins, C. G.; Banu, L.; Rowsell, M.; Blagojevic, V.; Bohme, D. K.; Fridgen, T. D. *J. Phys. Chem. B.* **2009**, *113*, 14457 - 14464.
13. Atkins, C. G.; Rajabi, K.; Gillis, E. A. L.; Fridgen, T. D. *J. Phys. Chem. A.* **2008**, *112*, 10220 - 10225.
14. Cagmat, E. B.; Szczepanski, J.; Pearson, W. L.; Powell, D. H.; Eyler, J. R.; Polfer, N. C. *Phys. Chem. Chem. Phys.* **2010**, *12*, 3474 - 3479.
15. Bush, M. F.; O'Brien, J. T.; Prell, J. S.; Wu, C.-C.; Saykally, R. J.; Williams, E. R. *J. Am. Chem. Soc.* **2009**, *131*, 13270 - 13277.
16. Bush, M. F.; O'Brien, J. T.; Prell, J. S.; Saykally, R. J.; Williams, E. R. *J. Am. Chem. Soc.* **2007**, *129*, 1612 - 1622.
17. Oh, H.; Breuker, K.; Sze, S. K.; Ge, Y.; Carpenter, B. K.; McLafferty, F. W. *Proc. Natl. Acad. Sci. U.S.A.* **2002**, *99*, 15863 - 15868.

18. Oepts, D.; van der Meer, A. F. G.; van Amersfoort, P. W. *Infrared Phys. Technol.* **1995**, *36*, 297 - 308.
19. Ortega, J. M.; Berset, J. M.; Chaput, R.; Glotin, F.; Humbert, G.; Jaroszynski, D.; Joly, P.; Kergosien, B.; Lesrel, J. *Nucl. Instrum. Methods Phys. Res., Sect. A* **1996**, *375*, 618 - 625.
20. Kamariotis, A.; Boyarkin, O. V.; Mercier, S. R.; Beck, R. D.; Bush, M. F.; Williams, E. R.; Rizzo, T. R. *J. Am. Chem. Soc.* **2006**, *128*, 905 - 916.
21. Locke, M. J.; McIver, R. T. *J. Am. Chem. Soc.* **1983**, *105*, 4226 - 4232.
22. Chapo, C. J.; Paul, J. B.; Provencal, R. A.; Roth, K.; Saykally, R. J. *J. Am. Chem. Soc.* **1998**, *120*, 12956 - 12957.
23. Bachrach, S. M.; Nguyen, T. T.; Demoin, D. W. *J. Phys. Chem. A* **2009**, *113* (21), 6172 - 6181.
24. Ahn, D.-S.; Park, S.-W.; Jeon, I.-S.; Lee, M.-K.; Kim, N.-H.; Han, Y.-H.; Lee, S. J. *Phys. Chem. B* **2003**, *107*, 14109 - 14118.
25. Kassab, E.; Langlet, J.; Evleth, E.; Akacem, Y. *Theochem* **2000**, *531*, 267 - 282.
26. Jensen, J. H.; Gordon, M. S. *J. Am. Chem. Soc.* **1995**, *117*, 8159 - 8170.
27. Fernandez-Ramos, A.; Smedarchina, Z.; Siebrand, W.; Zgierski, M. Z. *J. Chem. Phys.* **2000**, *113*, 9714 - 9721.
28. Xu, S. J.; Nilles, J. M.; Bowen, K. H. *J. Chem. Phys.* **2003**, *119*, 10696 - 10701.
29. Tajkhorshid, E.; Jalkanen, K. J.; Suhai, S. *J. Phys. Chem. B* **1998**, *102*, 5899 - 5913.
30. Blom, M. N.; Compagnon, I.; Polfer, N. C.; von Helden, G.; Meijer, G.; Suhai, S.; Paizs, B.; Oomens, J. *J. Phys. Chem. A* **2007**, *111*, 7309 - 7316.
31. Koyanagi, G. K.; Cheng, P.; Bohme, D. K. *J. Phys. Chem. A* **2010**, *114*, 241 - 246.
32. Shayesteh, A.; Lavrov, V. V.; Koyanagi, G. K.; Bohme, D. K. *J. Phys. Chem. A* **2009**, *113*, 5602 - 5611.
33. Feil, S.; Koyanagi, G. K.; Bohme, D. K. *Int. J. Mass. Spectrom.* **2009**, *280*, 38 - 41.
34. O'Brien, J. T.; Prell, J. S.; Steill, J. D.; Oomens, J.; Williams, E. R. *J. Am. Chem. Soc.* **2009**, *131*, 3905 - 3912.

35. Wu, R.; McMahon, T. B. *J. Am. Chem. Soc.* **2008**, *130*, 3065 - 3078.
36. Raspopov, S. A.; McMahon, T. B. *J. Mass. Spectrom.* **2005**, *40*, 1536 - 1545.
37. Wu, R.; McMahon, T. B. *J. Mass. Spectrom.* **2008**, *43*, 1641 - 1648.
38. Wu, R.; McMahon, T. B. *J. Am. Chem. Soc.* **2007**, *129*, 4864 - 4865.
39. Oh, H.-B.; Lin, C.; Hwang, H. Y.; Zhai, H.; Breuker, K.; Zabrouskov, V.; Carpenter, B. K.; McLafferty, F. W. *J. Am. Chem. Soc.* **2005**, *127*, 4076 - 4083.
40. Rajabi, K.; Fridgen, T. D. *J. Phys. Chem. A*, **2008**, *112*, 23 - 30.
41. Prell, J. S.; Flick, T. G.; Oomens, J.; Berden, G.; Williams, E. R. *J. Phys. Chem. A*, **2010**, *114*, 854 - 860.
42. Talley, J. M.; Cerda, B. A.; Ohanessian, G.; Wesdemiotis, C. *Chem. Eur. J.* **2002**, *8*, 1377 - 1388.
43. Dunbar, R. C.; Polfer, N. C.; Oomens, J. *J. Am. Chem. Soc.* **2007**, *129*, 14562 - 14563.
44. Armentrout, P. B.; Rodgers, M. T.; Oomens, J.; Steill, J. D. *J. Phys. Chem. A*, **2008**, *112*, 2248 - 2257.
45. Cerda, B. A.; Wesdemiotis, C. *Analyst*, **2000**, *125*, 657 - 660.
46. Polfer, N. C.; Oomens, J.; Dunbar, R. C. *Phys. Chem. Chem. Phys.* **2006**, *8*, 2744 - 2751.
47. Bush, M. F.; O'Brien, J. T.; Prell, J. S.; Saykally, R. J.; Williams, E. R. *J. Am. Chem. Soc.* **2007**, *129*, 1612 - 1622.
48. Polfer, N. C.; Oomens, J.; Moore, D. T.; von Helden, G.; Meijer, G.; Dunbar, R. C. *J. Am. Chem. Soc.* **2006**, *128*, 517 - 525.
49. Bush, M. F.; Oomens, J.; Saykally, R. J.; Williams, E. R. *J. Am. Chem. Soc.* **2008**, *130*, 6463 - 6471.
50. Strittmatter, E. F.; Lemoff, A. S.; Williams, E. R. *J. Phys. Chem. A*, **2000**, *104*, 9793 - 9796.

51. Rodriguez-Santiago, L.; Sodupe, M.; Tortajada, J. *J. Phys. Chem. A* **2001**, *105*, 5340 - 5347.
52. Constantino, E.; Rodriguez-Santiago, L.; Sodupe, M.; Tortajada, J. *J. Phys. Chem. A* **2005**, *109*, 224 - 230.
53. Forbes, M. W.; Bush, M. F.; Polfer, N. C.; Oomens, J.; Dunbar, R. C.; Williams, E. R.; Jockusch, R. A. *J. Phys. Chem. A* **2007**, *111*, 11759 - 11770.
54. Lemoff, A. S.; Bush, M. F.; Williams, E. R. *J. Phys. Chem. A* **2005**, *109*, 1903 - 1910.
55. Marino, T.; Tuscano, M.; Russo, N.; Grand, A. *J. Phys. Chem. B* **2006**, *110*, 24666 - 24673.
56. Rodgers, M. T.; Armentrout, P. B.; Oomens, J.; Steill, J. D. *J. Phys. Chem. A* **2008**, *112*, 2258 - 2267.
57. Jockusch, R. A.; Price, W. D.; Williams, E. R. *J. Phys. Chem. A* **1999**, *103*, 9266 - 9274.
58. Kapota, C.; Lemaire, J.; Maitre, P.; Ohanessian, G. *J. Am. Chem. Soc.* **2004**, *126*, 1836 - 1842.
59. Remko, M.; Rode, B. M. *J. Phys. Chem. A* **2006**, *110*, 1960 - 1967.
60. Rogalewicz, F.; Hopilliard, Y.; Ohanessian, G. *Int. J. Mass Spectrom.* **2000**, *201*, 307 - 320.
61. Hoppilliard, Y.; Rogalewicz, F.; Ohanessian, G. *Int. J. Mass Spectrom.* **2000**, *204*, 267 - 280.
62. Rogalewicz, F.; Hopilliard, Y.; Ohanessian, G. *Int. J. Mass Spectrom.* **2001**, *206*, 45 - 52.
63. Rogalewicz, F.; Hopilliard, Y.; Ohanessian, G. *Int. J. Mass Spectrom.* **2003**, *227*, 439 - 451.
64. Rajabi, K.; Easterling, M. L.; Fridgen, T. D. *J. Am. Soc. Mass Spectrom.* **2009**, *20*, 411 - 418.
65. Frisch, M. J.; Trucks, G. W.; Schlegel, H. B.; Scuseria, G. E.; Robb, M. A.; Cheeseman, J. R.; Scalmani, G.; Barone, V.; Mennucci, B.; Petersson, G. A.; Nakatsuji, H.; Caricato, M.; Li, X.; Hratchian, H. P.; Izmaylov, A. F.; Bloino, J.;

- Zheng, G.; Sonnenberg, J. L.; Hada, M.; Ehara, M.; Toyota, K.; Fukuda, R.; Hasegawa, J.; Ishida, M.; Nakajima, T.; Honda, Y.; Kitao, O.; Nakai, H.; Vreven, T.; Montgomery, J. A. Jr.; Peralta, J. E.; Ogliaro, F.; Bearpark, M.; Heyd, J. J.; Brothers, E.; Kudin, K. N.; Staroverov, V. N.; Kobayashi, R.; Normand, J.; Raghavachari, K.; Rendell, A.; Burant, J. C.; Iyengar, S. S.; Tomasi, J.; Cossi, M.; Rega, N.; Millam, J. M.; Klene, M.; Knox, J. E.; Cross, J. B.; Bakken, V.; Adamo, C.; Jaramillo, J.; Gomperts, R.; Stratmann, R. E.; Yazyev, O.; Austin, A. J.; Cammi, R.; Pomelli, C.; Ochterski, J. W.; Martin, R. L.; Morokuma, K.; Zakrzewski, V. G.; Voth, G. A.; Salvador, P.; Dannenberg, J. J.; Dapprich, S.; Daniels, A. D.; Farkas, O.; Foresman, J. B.; Ortiz, J. V.; Cioslowski, J.; Fox, D. J. *Gaussian 09, Revision A.01*; Gaussian, Inc.: Wallingford, CT, 2009.
66. Kuchle, W.; Dolg, M.; Stoll, H.; Preuss, H. *Molecular Physics*. **1991**, *74* (6), 1245 - 1263.
67. Schlegel, H. B.; Peng, C.; Ayala, P. Y.; Frisch, M. J. *J. Comput. Chem.* **1996**, *17*, 49 - 56.
68. Gorman, G. S.; Speir, J. P.; Turner, C. A.; Amster, I. J. *J. Am. Chem. Soc.* **1992**, *114*, 3986 - 3988.
69. Parr, R. G.; Pearson, R. G., *J. Am. Chem. Soc.* **1983**, *105*, 7512 - 7516.
70. Pearson, R. G., *Inorg. Chem.* **1988**, *27*, 734 - 740.

Chapter 4

Gas-phase Structures of Pb²⁺ Cationized Phenylalanine and Glutamic Acid Determined by Infrared Multiple Photon Dissociation Spectroscopy and Computational Chemistry[†]

4.1. Introduction. Gas-phase amino acids primarily exist as their canonical forms, but zwitterionic tautomers can often be stabilized through metal chelation.¹⁻²¹ The extent to which a metal cation alters the structure of an amino acid is dictated by its size and valency.^{6,20,22-28} Most research concerned with the structures of metal cationized amino acids has focused on complexes of the form $[M(\text{Aa})]^{+/2+}$.^{4-10,15-31} These experiments have revealed that, in general, amino acids with nonpolar side chains are more sensitive to the polarizability of the metal cation, whereas those with side chain functional groups are dependent on the effective shielding of the cation due to the greater degree of charge solvation. This means that increasing the size of the metal cation will have opposite effects on aliphatic and functionalized amino acids. For example, when arginine (Arg) is complexed with the alkali metals, Li⁺ forms a charge-solvated complex, $[\text{Na}(\text{Arg})]^+$ exists as a mixture of both isomers, and $[\text{K}(\text{Arg})]^+$, $[\text{Cs}(\text{Arg})]^+$, and $[\text{Rb}(\text{Arg})]^+$ are zwitterionic.³² A similar trend exists for serine (Ser); Li⁺, Na⁺, K⁺, and Rb⁺ each produce three-coordinate charge-solvated structures where the metal is bound between the amine nitrogen, carbonyl oxygen, and side chain hydroxyl group. Starting with K⁺, a bidentate charge-solvated structure begins to contribute to the gas-phase population as the cation size increases, and $[\text{Cs}(\text{Ser})]^+$ is partly zwitterionic.⁶ By contrast, proline (Pro) and *N*-

[†] Adapted from work accepted for publication in *J. Phys. Chem. A*. DOI:10.1021/jp306420e. Published online: September 4, 2012.

methyl-alanine both form salt bridges with Li^+ and Na^+ , while their charge solvated isomers become increasingly stable as the cation size increases through K^+ , Cs^+ , and Rb^+ .²⁰

Chapter 3 focused on using IRMPD spectroscopy³³⁻³⁷ to characterize bare and hydrated Pb^{2+} complexes with glycine (Gly), alanine (Ala), valine (Val), leucine (Leu), isoleucine (Ile), proline (Pro), and lysine (Lys).^{1,3} This work demonstrated that lead(II)-amino acid complexes, which are deprotonated and of the form $[\text{Pb}(\text{Aa-H})]^+$, adopt one of three structures shown in Figure 4.1: an A-type complex, which has a charge solvated Pb^{2+} cation bound between the amine nitrogen and carbonyl oxygen of an N-deprotonated amino acid; a B-type ion, which is similar to the A-type complex but is O-deprotonated instead; and a C-type complex, where Pb^{2+} forms a salt bridge with an O-deprotonated amino acid. Each of the $[\text{Pb}(\text{Aa-H})]^+$ ions involving nonpolar amino acids are A-type complexes, whereas $[\text{Pb}(\text{Lys-H})]^+$ adopts the C-type tautomer. These isomers are spectroscopically distinct; the A-type complexes contain a characteristic COO-H stretch around 3560 cm^{-1} that is absent in the spectra of the O-deprotonated B- and C-type ions. The difference between $[\text{Pb}(\text{Lys-H})]^+$ and the nonpolar amino acids was attributed to Lys's basic side chain. The ϵ -amine group presents an additional binding site that preferentially stabilizes the C-type isomer of $[\text{Pb}(\text{Lys-H})]^+$.

IRMPD experiments were also carried out on monohydrated $[\text{Pb}(\text{Aa-H})]^+$ ions, as solvation plays a critical role in stabilizing zwitterionic amino acids in the condensed phases.^{1,3} The $[\text{Pb}(\text{Aa-H})\text{H}_2\text{O}]^+$ ions were generally determined to be the hydrated

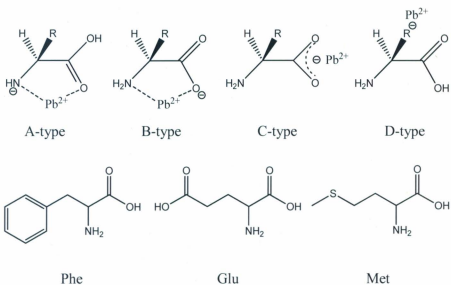


Figure 4.1: Four possible $[Pb(Aa-H)]^+$ isomers. Skeletal drawings of phenylalanine, glutamic acid, and methionine are also shown.

analogues of the bare complexes where water directly attaches to Pb^{2+} ; the attached water remains intact in the B- and C-type ions, but donates a proton to the deprotonated amine group in the A-type complexes. Stepwise microsolvation, however, was seen to stabilize higher-energy tautomers different from those observed for the bare complexes.³⁸⁻⁴³ For example, hydration causes A-type $[\text{Pb}(\text{Pro-H})]^+$ and C-type $[\text{Pb}(\text{Lys-H})]^+$ to isomerize to the C- and B-type $[\text{Pb}(\text{Aa-H})\text{H}_2\text{O}]^+$ complexes, respectively. $[\text{Pb}(\text{Lys-H})\text{H}_2\text{O}]^+$ is also stabilized by an interaction with lysine's side chain, as is the case for the bare complex.

In order to better understand the role additional binding sites play in complexes between Pb^{2+} and the conjugate bases of amino acids, this work uses IRMPD spectroscopy to determine the bare and monohydrated gas-phase structures of Pb^{2+} complexes with three amino acids containing functionalized side chains: phenylalanine (Phe), which has a nonpolar side chain containing an aromatic ring and is often considered as the archetypical system for cation- π interactions^{30,31}; glutamic acid (Glu), whose side chain is polar and contains an acidic γ -carboxyl group capable of binding metal cations²¹; and methionine (Met), which is also nonpolar but contains a sulfur atom at the δ -position. Met is known to form three-coordinate $[\text{M}(\text{Aa})]^+$ complexes with Li^+ , Na^+ , and K^+ , underscoring the ability of the amino acid side chain to influence ionic structure.²⁹

4.2. Methods

4.2.1. IRMPD Spectroscopy. Gas-phase $[\text{Pb}(\text{Phe-H})]^+$, $[\text{Pb}(\text{Met-H})]^+$ and $[\text{Pb}(\text{Glu-H})]^+$ were prepared from 50/50 solutions of methanol (99.8%, ACP Chemicals) and 18.2 M Ω

water (Millipore) containing 0.1 mM $\text{Pb}(\text{NO}_3)_2$ (> 99%, Fluka Chemika) and either 0.1 mM Phe or Glu (Nutritional Biochemicals). Each solution was electrosprayed using the Apollo II ion source of a Bruker Apex Qe 7 T Fourier transform ion cyclotron resonance (FT-ICR) mass spectrometer at a rate of $100 \mu\text{L h}^{-1}$ and allowed to accumulate between $10^{-3} - 1$ s; the voltage across the source exit capillary was 294 V. The ions were then selected by a quadrupole mass filter and stored in a hexapole collision cell for 1.0 - 2.0 s before being accelerated through electrostatic optics and isolated in the ICR cell. The hydrated complexes, $[\text{Pb}(\text{Phe-H})\text{H}_2\text{O}]^+$ and $[\text{Pb}(\text{Glu-H})\text{H}_2\text{O}]^+$, were produced in the hexapole by minimizing the collision gas (Ar) flow and introducing a modest pressure (10^{-2} mbar) of water vapour through a microvalve separating the cell from a degassed water reservoir.⁴⁴

Once trapped in the ICR cell, the isolated complexes were irradiated by a tunable potassium titanyl phosphate optical parametric oscillator (KTP OPO) pumped collinearly using a Brilliant B Nd:YAG laser (Big Sky Laser) as described previously.¹ The ions were irradiated for 1 - 2 s at 1.5 cm^{-1} steps between $3200 - 3800 \text{ cm}^{-1}$, and four mass spectra were averaged per interval. The tunable radiation emitted by the OPO is directed towards the ion packet in the ICR cell through a path purged of CO_2 and H_2O vapour.¹ The cell itself is surrounded by a home-made heating jacket that can be thermalized between 25 - 100 °C. The higher temperatures better facilitate dissociation of the complexes and can yield better spectra. The IRMPD spectra were then prepared by plotting the IRMPD yield, which is the base 10 logarithm of the normalized precursor ion intensity, against the wavenumber of the output of the OPO. The reported intensities were

not adjusted to account for wavelength-dependent variations in the efficiency of the output pulse.

4.2.2. Calculations. The minimum energy structures of the $[\text{Pb}(\text{Aa-H})]^+$ and $[\text{Pb}(\text{Aa-H})\text{H}_2\text{O}]^+$ complexes were determined using the Gaussian 09 software package.⁴⁵ 18 - 110 unique structures were created for each complex by altering the sites of deprotonation and lead chelation in an attempt to fully explore the stabilization of lead by the amino acid functional groups. Bond and torsional angles were also adjusted in order to vary the amount of hydrogen bonding or to relieve molecular strain. Geometry optimizations and harmonic frequency calculations were performed on each isomer using B3LYP density functional theory. The LANL2DZ basis set with relativistic core potential was applied to lead, however 6-31+G(d,p) was used for all other atoms. This method is abbreviated here as B3LYP/6-31+G(d,p) for simplicity, although it should be noted that LANL2DZ is always used for lead. The extracted vibrational modes were scaled by 0.955 in order to better compare computed infrared spectra with the experimental IRMPD data.^{1,3,46} Single point energy calculations were performed on each B3LYP/6-31+G(d,p) optimized structure using the MP2(full)/6-311++G(2d,2p) method (LANL2DZ was still used for lead). The 298 K enthalpies and Gibbs energies determined by this method are reported as MP2(full)/6-311++G(2d,2p)//B3LYP/6-31+G(d,p). This approach is a popular method for determining the relative stabilities of candidate structures, and has been shown to be reasonably accurate for similar complexes.^{6,7}

4.3. Results and Discussion

4.3.1. IRMPD Spectroscopy of $[\text{Pb}(\text{Aa-H})]^+$ and $[\text{Pb}(\text{Aa-H})\text{H}_2\text{O}]^+$. The IRMPD spectra of $[\text{Pb}(\text{Phe-H})]^+$, $[\text{Pb}(\text{Glu-H})]^+$, and their hydrated analogues are shown in Figure 4.2 between 3200 – 3800 cm^{-1} . Each complex loses H_2O when activated by IRMPD using the KTP OPO. This is similar to the IRMPD experiments performed in Chapter 3,^{1,3} and agrees with recent CID work that establishes H_2O loss as the most likely dissociation channel.⁴⁹ The hydrated complexes were also seen to have a secondary loss of H_2O , attributed to the dissociation of $[\text{Pb}(\text{Phe-H})]^+$ and $[\text{Pb}(\text{Glu-H})]^+$; this amounts to 50 – 80% of the first water loss over the O-H stretch region of $[\text{Pb}(\text{Glu-H})\text{H}_2\text{O}]^+$, and 5% of the first water loss for $[\text{Pb}(\text{Phe-H})\text{H}_2\text{O}]^+$.

The IRMPD spectrum of $[\text{Pb}(\text{Glu-H})]^+$ contains a strong absorbance (3580 cm^{-1}) in the O-H stretch region which must be a carboxylic acid O-H stretch. The existence or absence of this band has previously been used to assess whether or not other $[\text{Pb}(\text{Aa-H})]^+$ complexes are carboxyl- or amine-deprotonated.¹ However, glutamic acid contains two carboxylic acid moieties so the lone O-H stretch likely means that $[\text{Pb}(\text{Glu-H})]^+$ is carboxyl deprotonated at either the terminal or side-chain functional group. Since this carboxylic acid O-H stretch is ~ 20 cm^{-1} higher in energy than similar bands observed in the IRMPD spectra of other $[\text{Pb}(\text{Aa-H})]^+$ (Aa = Pro, Ala, Val, Leu, and Ile) complexes, it could suggest that the terminal carboxylic acid is deprotonated instead of the γ -carboxyl group. In contrast to $[\text{Pb}(\text{Glu-H})]^+$, the IRMPD spectrum of $[\text{Pb}(\text{Phe-H})]^+$ contains no bands in the O-H stretch region, but has two N-H stretches visible at 3386 and 3320 cm^{-1} .

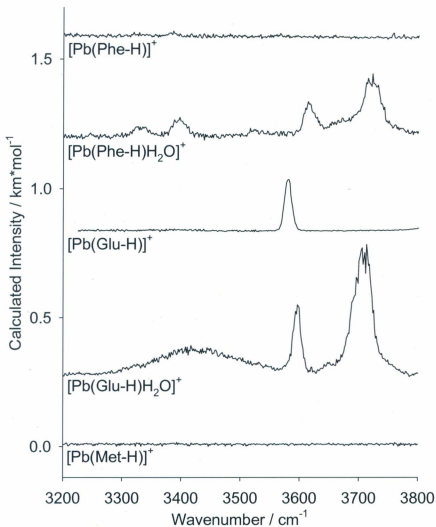


Figure 4.2: The IRMPD spectra of [Pb(Phe-H)]⁺, [Pb(Phe-H)H₂O]⁺, [Pb(Glu-H)]⁺, [Pb(Glu-H)H₂O]⁺, and [Pb(Met-H)]⁺ in the 3200 – 3800 cm⁻¹ region.

Although the N-H bands are very weak, the KTP OPO was observed to be capable of causing $[\text{Pb}(\text{Phe-H})]^+$ to dissociate in the ICR cell, hence the lack of a strong O-H stretch means that $[\text{Pb}(\text{Phe-H})]^+$ is carboxyl-deprotonated with an intact amine group. The IRMPD spectrum of $[\text{Pb}(\text{Met-H})]^+$ is also shown in Figure 4.2. This spectrum is featureless, but the lack of an observable carboxylic acid O-H stretch may indicate that $[\text{Pb}(\text{Met-H})]^+$ is carboxyl-deprotonated; this is consistent with the lowest energy structure, which is a B-type ion (Figure B1 in Appendix B).

The hydrated complexes have slightly more complex IRMPD spectra. The spectrum of $[\text{Pb}(\text{Phe-H})\text{H}_2\text{O}]^+$ has two absorptions in the O-H stretching region at 3615 and 3720 cm^{-1} as well as two pronounced N-H stretches at 3330 and 3395 cm^{-1} . The IRMPD spectrum of $[\text{Pb}(\text{Glu-H})\text{H}_2\text{O}]^+$ also exhibits two O-H stretches at 3597 and 3710 cm^{-1} and contains a broad band centered around 3415 cm^{-1} . The broad band masks any potential N-H stretches that might be observed. $[\text{Pb}(\text{Met-H})]^+$ could not be hydrated in the collision cell, so no IRMPD spectrum of $[\text{Pb}(\text{Met-H})\text{H}_2\text{O}]^+$ could be acquired.

The O-H stretching bands of both $[\text{Pb}(\text{Phe-H})\text{H}_2\text{O}]^+$ and $[\text{Pb}(\text{Glu-H})\text{H}_2\text{O}]^+$ appear at higher wavenumber positions relative to two strong bands observed in the same region for the $[\text{Pb}(\text{Aa-H})\text{H}_2\text{O}]^+$ ions with nonpolar amino acid side chains (Ala, Val, Leu, Ile).^{1,3} It was concluded that for the nonpolar amino acids the addition of water to N-deprotonated $[\text{Pb}(\text{Aa-H})]^+$ lead to an observed structure where a proton was transferred from the water to the deprotonated amine group. In the O-H stretch region this resulted in a carboxylic acid O-H stretch observed at 3570 - 3580 cm^{-1} , and a Pb-O-H stretch observed at 3680 - 3690 cm^{-1} . The intensity of the carboxylic acid O-H stretch was also

observed to be equal to the intensity of the PbO-H stretch, whereas for $[\text{Pb}(\text{Phe-H})\text{H}_2\text{O}]^+$ and $[\text{Pb}(\text{Glu-H})\text{H}_2\text{O}]^+$ the higher energy band is significantly more intense. Figure B2 (Appendix B) clearly shows significant differences in position and intensity for the two bands observed in the O-H stretch region in the IRMPD spectra for $[\text{Pb}(\text{Ala-H})\text{H}_2\text{O}]^+$, compared to when the amino acid is either Phe or Glu.

4.3.2. $[\text{Pb}(\text{Phe-H})]^+$ and $[\text{Pb}(\text{Phe-H})\text{H}_2\text{O}]^+$. Four lowest-energy computed structures for $[\text{Pb}(\text{Phe-H})]^+$ are shown in Figure 4.3 (additional structures can be found in Figure B3 of Appendix B). The most thermodynamically stable structure, Phe-Bi, is a B-type ion where Pb^{2+} is ligated to the NH_2 group, a carboxylate oxygen and the phenyl group. This π -interaction significantly stabilizes Phe-Bi; the most favourable B-type ion without the Pb^{2+} -phenyl π -interaction (Phe-Bii) is 58.4 kJ mol^{-1} higher in Gibbs energy at the MP2 level of theory. In general, the structures that have a Pb^{2+} -phenyl π -interaction (Phe-Ai, -Bi, and -Ci) are significantly more stable than those without it (Phe-Aii, -Bii, and -Cii). It's interesting to note that when the Pb^{2+} -phenyl π -interaction is absent from the structure of $[\text{Pb}(\text{Phe-H})]^+$, the energy ordering of the A-, B-, and C-type isomers is similar to that of the other nonpolar $[\text{Pb}(\text{Aa-H})]^+$ ions (Aa = Gly, Ala, Val, Leu, and Ile).¹ The stabilizing influence of Phe's side chain can be further demonstrated by comparing the thermochemistries of both the N- and O-deprotonated complexes for $[\text{Pb}(\text{Ala-H})]^+$ and $[\text{Pb}(\text{Phe-H})]^+$. N-deprotonation of $[\text{Pb}(\text{Ala})]^{2+}$ is 7.9 kJ mol^{-1} lower in Gibbs energy than O-deprotonation,¹ but is only 0.8 kJ mol^{-1} more favourable for the $[\text{Pb}(\text{Phe})]^{2+}$

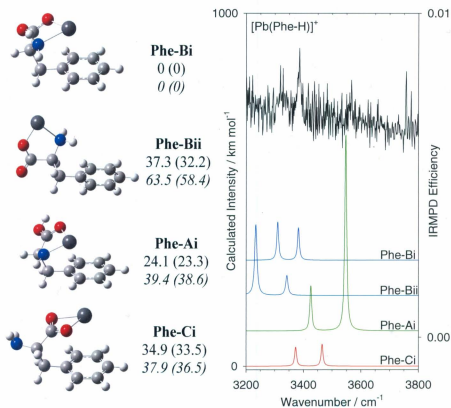


Figure 4.3: The IRMPD spectrum of $[\text{Pb}(\text{Phen-H})]^+$ (black) compared with four computed IR spectra. The computed spectra are from the B3LYP/6-31+G(d,p) optimized structures of Phe-Ai, -Bi, -Bii, and -Ci. The 298 K relative enthalpies and Gibbs energies (in parentheses) have units of kJ mol^{-1} and are provided at the B3LYP/6-31+G(d,p) (top) and MP2(full)/6-311++G(2d,2p) (bottom and italicized) levels of theory. In both cases, the LANL2DZ basis set with effective core potential was applied to Pb^{2+} .

structure without the Pb^{2+} -phenyl π -interaction. However, the additional stabilization of Pb^{2+} by the side-chain in the $[\text{Pb}(\text{Phe})]^{2+}$ structures that include the π -interaction makes O-deprotonation 38.6 kJ mol^{-1} more stable than N-deprotonation. It is also worth noting that the MP2 calculations more strongly favour the π -interaction than the B3LYP calculations. For example, at the B3LYP level of theory, Phe-Bi is 37 kJ mol^{-1} lower in enthalpy than Phe-Bii, but at the MP2 level Phe-Bi is further stabilized by another $\sim 26 \text{ kJ mol}^{-1}$ compared to Phe-Bii. Similar stabilization at the MP2 level of theory of the A and C structures by the Pb^{2+} -phenyl π -interaction are computed.

In Figure 4.3 the computed IR spectra of the $[\text{Pb}(\text{Phe-H})]^+$ isomers are also compared with the experimental IRMPD spectrum of $[\text{Pb}(\text{Phe-H})]^+$. $[\text{Pb}(\text{Phe-H})]^+$ must be O-deprotonated since the IRMPD spectrum does not contain a strong O-H stretch band. Instead, two very weak N-H stretches at 3386 and 3320 cm^{-1} are observed which suggests an intact amine group. This spectroscopically rules out the N-deprotonated structures, Phe-Ai and Phe-Aii, since both have a COO-H stretch expected at about 3560 cm^{-1} . Phe-Bi is by far the most thermodynamically favourable structure and is supported by the IRMPD spectrum. Phe-Bii, -Ci, and -Cii are $36.5 - 98.5 \text{ kJ mol}^{-1}$ higher in Gibbs energy than Phe-Bi and could be ruled out on energetic grounds alone, however, calculated spectra for these isomers also predict N-H stretches at higher or lower wavenumber positions than the two that were observed. Gas-phase $[\text{Pb}(\text{Phe-H})]^+$ is, therefore, most probably a B-type ion where Pb^{2+} is stabilized by the aromatic ring on the side chain.

Three $[\text{Pb}(\text{Phe-H})\text{H}_2\text{O}]^+$ isomers are shown in Figure 4.4. With water binding directly to Pb^{2+} in each structure, it is clear that lead displays a four-coordinate, hemidirected geometry due to the lone pair of electrons which are in orbitals with p-type character.⁴⁷ The B- and C- type ions are simply the hydrated analogues of the $[\text{Pb}(\text{Phe-H})]^+$ structures, however, like the other non-polar amino acids, the lowest energy A-type ion is the result of a subsequent proton transfer from the attached water to the amine group. The Pb^{2+} - π interaction with the side chain of Phe significantly stabilizes the $[\text{Pb}(\text{Phe-H})\text{H}_2\text{O}]^+$ complex by between 22.2 - 52.8 kJ mol^{-1} (Figure 4.4 and B3), similar to the bare complexes. The most thermochemically stable structure is the B-type ion, which is 13.5 kJ mol^{-1} more stable than the A-type structure at the MP2 level of theory. However, the B3LYP calculations actually favour the A-type structure by 6 kJ mol^{-1} . The C-type complex, PheW-Ci, is calculated to be significantly less stable than PheW-Bi and PheW-Ai at both levels of theory.

The computed IR spectra of each $[\text{Pb}(\text{Phe-H})\text{H}_2\text{O}]^+$ structure are also compared with the IRMPD spectrum of $[\text{Pb}(\text{Phe-H})\text{H}_2\text{O}]^+$ in Figure 4.4. The experimental spectrum contains two features at 3330 and 3395 cm^{-1} that are due to the symmetric and antisymmetric NH_2 stretches. The positions of the N-H stretching bands are well reproduced by the calculated spectrum of PheW-Bi; the predicted spectrum for PheW-Ai is similar, but exhibits a significantly larger separation of the NH_2 stretches.

The experimental spectrum also has two strong features at 3615 and 3720 cm^{-1} that are assigned to O-H stretching vibrations. As was discussed above, and as can be

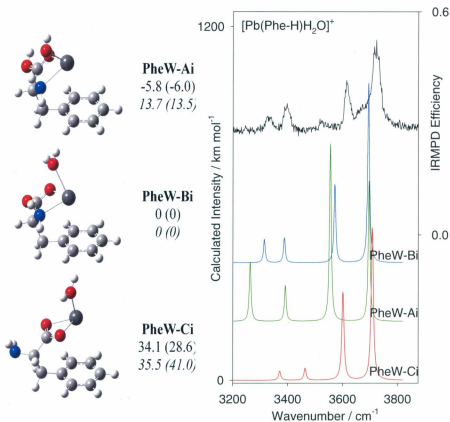


Figure 4.4: The IRMPD spectrum of $[\text{Pb}(\text{Phe-H})\text{H}_2\text{O}]^+$ (black) compared with three computed IR spectra. The computed spectra are from the B3LYP/6-31+G(d,p) optimized structures of PheW-Ai, -Bi, and -Ci. The 298 K relative enthalpies and Gibbs energies (in parentheses) have units of kJ mol^{-1} and are provided at the B3LYP/6-31+G(d,p) (top) and MP2(full)/6-311++G(2d,2p) (bottom and italicized) levels of theory. In both cases, the LANL2DZ basis set with effective core potential was applied to Pb^{2+} .

seen in Figure B2, the shape and positions of the O-H stretching bands in this region are significantly different for $[\text{Pb}(\text{Phe-H})\text{H}_2\text{O}]^+$ (and $[\text{Pb}(\text{Glu-H})\text{H}_2\text{O}]^+$) than for the complexes of other amino acids with non-polar side chains.¹ For $[\text{Pb}(\text{Ala-H})\text{H}_2\text{O}]^+$, the bands at 3569 and 3688 cm^{-1} were assigned to the carboxylic acid O-H stretch and the PbO-H stretch respectively. Furthermore, the two bands were observed to have equal intensity, in agreement with the computed spectrum. The bands for $[\text{Pb}(\text{Phe-H})\text{H}_2\text{O}]^+$ are significantly to the blue of those for $[\text{Pb}(\text{Ala-H})\text{H}_2\text{O}]^+$, and the 3615 cm^{-1} band is much weaker than the 3720 cm^{-1} band. The observed intensity ratio is also in agreement with the predicted spectrum for PheW-Bi. The complexes that are not stabilized by a Pb^{2+} -phenyl π -interaction are too high in energy to have a significant population in the gas phase, and the same is true for PheW-Ci, which is also eliminated spectroscopically based on its higher energy N-H stretches. $[\text{Pb}(\text{Phe-H})\text{H}_2\text{O}]^+$ is best described as a B-type complex in the gas-phase with water directly bound to Pb^{2+} ; the 3615 and 3720 cm^{-1} bands are assigned to the symmetric and antisymmetric stretching vibrations, respectively, of the water ligand.

4.3.3. $[\text{Pb}(\text{Glu-H})]^+$ and $[\text{Pb}(\text{Glu-H})\text{H}_2\text{O}]^+$. Six $[\text{Pb}(\text{Glu-H})]^+$ isomers are shown in Figure 4.5 and an additional ten structures are included in Figure B5 of Appendix B. The most stable A-, B-, and C-type complexes exhibit an additional interaction between Pb^{2+} and the γ -carboxyl side chain. This Pb^{2+} -side chain interaction stabilizes Glu-Ai, -Bi, and -Ci by between 29 and 86 kJ mol^{-1} with respect to the isomers where the side chain has

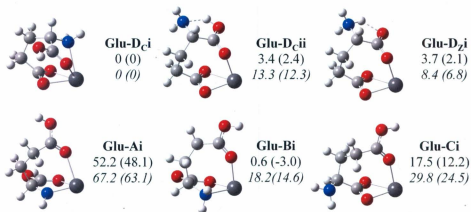


Figure 4.5: The B3LYP/6-31+G(d,p) optimized structures of $[\text{Pb}(\text{Glu-H})]^+$. The 298 K relative enthalpies and Gibbs energies (in parentheses) have units of kJ mol^{-1} and are provided at the B3LYP/6-31+G(d,p) (top) and MP2(full)/6-311++G(2d,2p) (bottom and italicized) levels of theory. Note that the LANL2DZ basis set with effective core potential was applied to Pb^{2+} for both levels of calculation.

no intramolecular non-covalent interaction (Glu-Aiv, -Bii, and -Cii). Furthermore, the relative stabilities of the three complexes are similar to those seen for $[\text{Pb}(\text{Phe-H})]^+$; Glu-Bi is more stable than Glu-Ci and Glu-Ai by 9.8 and 48.5 kJ mol^{-1} in Gibbs energy, respectively. However, unlike $[\text{Pb}(\text{Phe-H})]^+$, $[\text{Pb}(\text{Glu-H})]^+$ is also capable of producing a D-type complex where Pb^{2+} forms a salt bridge with the deprotonated γ -carboxyl group of the side chain (Figure 4.1). Pb^{2+} can be further stabilized by the terminal amine and/or carboxyl groups, which will either be zwitterionic (D_z) or canonical (D_c). The lowest energy D-type structure, and the lowest energy structure overall at the MP2 level of theory, is Glu- D_{ci} , which is coordinated to both side chain carboxylate oxygens, the carbonyl oxygen of the carboxyl group, and the amine group. Two other low-energy D-type structures are also shown in Figure 4.5.

The computed IR spectra for six $[\text{Pb}(\text{Glu-H})]^+$ structures are also compared with the IRMPD spectrum of $[\text{Pb}(\text{Glu-H})]^+$ in Figure 4.6. The experimental spectrum contains one absorbance at 3580 cm^{-1} designated as a COO-H stretch, but no N-H stretches were observed. The lack of N-H stretches may be due to the presence of an intramolecular hydrogen bond, but could also imply that the absorbances are too weak to see, as was previously observed in the case of $[\text{Pb}(\text{Gly-H})]^+$.³ The predicted spectrum for the lowest energy structure, Glu- D_{ci} , is consistent with the observed strong COO-H stretch. Glu-Ai is predicted to have two COO-H stretches and can therefore be ruled out spectroscopically. Both Glu- D_{zi} and $-D_{cii}$ do not have a strong COO-H stretch since there is no carboxyl group in Glu- D_{zi} and the -OH is hydrogen bonded to the amino

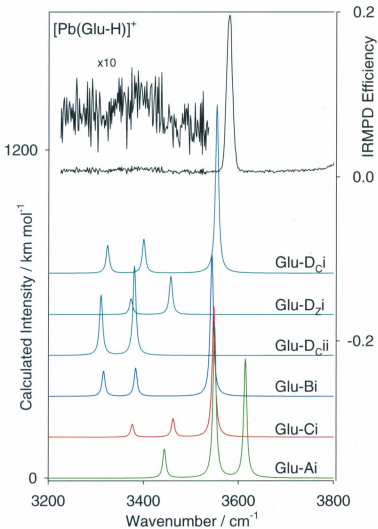


Figure 4.6: The IRMPD spectrum of $[\text{Pb}(\text{Glu-H})]^+$ (black) compared with six computed IR spectra. The computed spectra are from the B3LYP/6-31+G(d,p) optimized structures of Glu-Ai, -Bi, -Ci, -D_{z.i}, -D_{c.i}, and -D_{c.ii} shown in Figure 4.5.

group in Glu-D_Cii. Neither of these structures can be ruled out spectroscopically, however, they cannot account for the strong COO-H stretching absorption. There are three other D-type structures, D_Ciii, D_Civ, and D_Cv (Figure B5) which do explain the COO-H stretch (Figure B6), but each is more than 20 kJ mol⁻¹ less stable than Glu-D_Ci. Glu-Bi and Glu-Ci are calculated to be 14.6 and 24.5 kJ mol⁻¹ higher in energy than the lowest energy structure, respectively. While neither can be ruled out spectroscopically, their calculated thermochemistry predicts that they will not be major contributors to the spectrum.

Eight isomers of [Pb(Glu-H)H₂O]⁺ are collected in Figure 4.7 (ten more are in Figure B7), and their computed IR spectra are compared with the IRMPD spectrum of [Pb(Glu-H)H₂O]⁺ in Figure 4.8. As was observed in the previous Chapter, the most stable hydrated [Pb(Aa-H)]⁺ complexes have water attached directly to Pb²⁺. GluW-Bi and GluW-Ci are simply the hydrated analogues of Glu-Bi and Glu-Ci, and can be ruled out as contributing to the experimental IRMPD spectrum since three bands are expected in the IRMPD spectrum; a COO-H stretch, and two water O-H stretching absorptions (Figure B8). They are also 15.9 and 27.1 kJ mol⁻¹ higher in energy than the most stable structure. Glu-Ai is 41 kJ mol⁻¹ higher in Gibbs energy than the lowest energy structure and is also not expected to be a contributor to the IRMPD spectrum. As was discussed in Section 4.3.1, the bands in the IRMPD spectrum of [Pb(Glu-H)H₂O]⁺ are higher in energy and not of the same intensity as those observed previously for hydrated A-type structures.^{1,3} Furthermore, since the predicted spectrum (Figure B8) has three bands in the

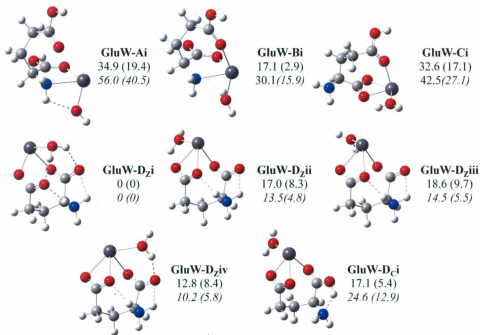


Figure 4.7: The B3LYP/6-31+G(d,p) optimized structures of $[\text{Pb}(\text{Glu-H})\text{H}_2\text{O}]^+$. The 298 K relative enthalpies and Gibbs energies (in parentheses) have units of kJ mol^{-1} and are provided at the B3LYP/6-31+G(d,p) (top) and MP2(full)/6-311++G(2d,2p) (bottom and italicized) levels of theory. Note that the LANL2DZ basis set with effective core potential was applied to Pb^{2+} for both levels of calculation.

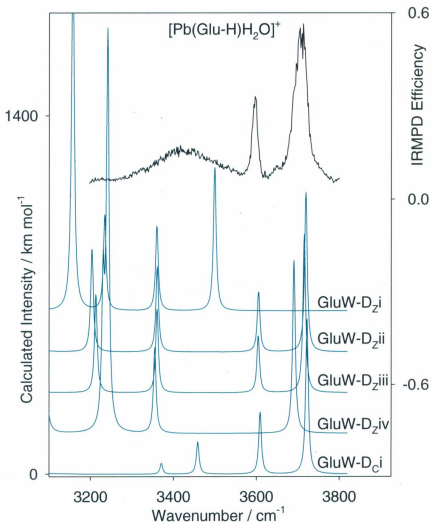


Figure 4.8: The IRMPD spectrum of $[\text{Pb}(\text{Glu-H})\text{H}_2\text{O}]^+$ (black) compared with five computed IR spectra. The computed spectra are from the B3LYP/6-31+G(d,p) optimized structures of GluW-D₂i, -D₂ii, -D₂iii, -D₂iv, and -D_ci shown in Figure 4.7.

O-H stretch region, two COO-H and one PbO-H, it is unlikely that the ion(s) responsible for the present IRMPD spectrum have A-type structures.

The four lowest energy D-type structures are zwitterionic and are separated by less than 6 kJ mol^{-1} . Like $[\text{Pb}(\text{Phe-H})\text{H}_2\text{O}]^+$, these structures are hemidirected; the lone pair on Pb^{2+} repels the ligand. The lowest energy structure, GluW-D_{2i}, has lead bound to one oxygen on each carboxylate and to water. In this structure, water also forms two hydrogen bonds, one with a carbonyl on each of the carboxylate groups. The hydrogen bond strengths are quite different as is evidenced by the bond lengths, one is 1.770 \AA , and the other is 2.099 \AA . There are also two hydrogen bonds with the same carbonyl oxygens, but with two N-H bonds acting as donors. The two N-H--O hydrogen bonds have similarly different strengths. The predicted IR spectrum for this structure is compared with the experimental spectrum in Figure 4.8. Due to hydrogen bonding, it has no free O-H stretching vibrations and therefore cannot account for the two higher energy bands. However, the broad band below 3600 cm^{-1} is similar to other hydrogen bonded features observed previously.^{19,46,48} The weaker O-H--O stretch is the strong band expected at 3500 cm^{-1} . The stronger O-H--O stretch is predicted to be at 3157 cm^{-1} whereas the N-H--O stretches are predicted to occur at 3234 and 2940 cm^{-1} . Based on the inability of these harmonic calculations to accurately predict positions of hydrogen bonded stretching vibrations of this type, it is impossible to say which one(s) are being observed in this spectrum. This broad feature is, however, consistent with what is expected for the lowest-energy structure, GluW-D_{2i}.

The next two lowest energy D_Z -type ions each have water forming only one very weak intramolecular hydrogen bond, and have O-H–O hydrogen bond lengths greater than 2.45 Å. These structures are only about 5 kJ mol⁻¹ higher in Gibbs energy at the MP2 level of theory than the lowest energy structure. The positions of the symmetric and antisymmetric O-H stretches of the water ligand are predicted to occur in the same position as those observed, and with a similar intensity ratio. The fourth D_Z -type structure, GluW- D_{Ziv} , is similar in energy to GluW- D_{Ziii} and - D_{Zii} . In this structure, the water molecule has a strong hydrogen bond with the carboxylate oxygen that does not complex with Pb, and the O-H–O distance is 1.746 Å. This structure cannot be ruled out, but due to the absence of the symmetric O-H stretch due to the hydrogen bond in the O-H stretch region, it cannot by itself account for the experimental spectrum.

The lowest energy D_C -type structure is predicted to be about 13 kJ mol⁻¹ higher in energy than the global minimum structure and has the carboxylate O-H strongly hydrogen bonded to the amine group; the O-H–N bond is 1.805 Å. This higher energy structure can also account for the two bands in the N-H stretching region. The computed IR spectra for other higher-energy structures are compared with the experimental spectrum in Figure B8. Some cannot be ruled out spectroscopically, but their higher relative energies indicate that they will be minor contributors in the gas phase. One final note: the lowest-energy D-type ions deprotonated at the side chain were determined to account for the single O-H stretch observed in the IRMPD spectrum of [Pb(Glu-H)]⁺. The IRMPD spectrum of [Pb(Glu-H)H₂O]⁺ is also accounted for by D-type ions, but

more than one structure is necessary to account for the experimental spectrum of the hydrated ion. These structures are all within 6 kJ mol^{-1} of the lowest-energy isomer.

4.4. Conclusions. IRMPD spectroscopy and electronic structure calculations were used to determine the structures of bare and hydrated $[\text{Pb}(\text{Phe-H})]^+$ and $[\text{Pb}(\text{Glu-H})]^+$ as well as for $[\text{Pb}(\text{Met-H})]^+$. The IRMPD spectrum of $[\text{Pb}(\text{Phe-H})]^+$ is consistent with that of a B-type ion where Pb^{2+} is chelated between the amine nitrogen and deprotonated carboxyl group, and where there is an additional interaction between Pb^{2+} and the aromatic ring on Phe's side chain. $[\text{Pb}(\text{Phe-H})\text{H}_2\text{O}]^+$ is simply the hydrated version of $[\text{Pb}(\text{Phe-H})]^+$ where water binds directly to Pb^{2+} . The featureless IRMPD spectrum of $[\text{Pb}(\text{Met-H})]^+$ in the $3200 - 3800 \text{ cm}^{-1}$ region also suggests that $[\text{Pb}(\text{Met-H})]^+$ is carboxyl-deprotonated, and this is in agreement with its lowest-energy computed structure.

The IRMPD spectrum for $[\text{Pb}(\text{Glu-H})]^+$ is consistent with the lowest-energy canonical D-type structure in which the side chain carboxyl group is deprotonated. The lowest-energy zwitterionic D-type structure, where Pb^{2+} forms a salt bridge with the deprotonated γ -carboxyl group and is further stabilized by Glu's terminal carbonyl oxygen, is only 6.8 kJ mol^{-1} higher in Gibbs energy and cannot be ruled out. $[\text{Pb}(\text{Glu-H})\text{H}_2\text{O}]^+$ exists as at least two, but probably four different low-energy zwitterionic D-type isomers. The lowest-energy structure, where the water participates as a hydrogen bond donor to two different carbonyl oxygens, accounts for the broad feature below 3600 cm^{-1} in the IRMPD spectrum. The three other structures account for the two observed symmetric and antisymmetric O-H stretches for the ligated water molecule.

The amino acid side chain clearly plays a role in stabilizing higher energy tautomers. When the side-chain interaction is removed, calculations predict that $[\text{Pb}(\text{Phe-H})]^+$ and $[\text{Pb}(\text{Glu-H})]^+$ should be A-type ions. This is similar to the IRMPD-determined structures of several $[\text{Pb}(\text{Aa-H})]^+$ and $[\text{Pb}(\text{Aa-H})\text{H}_2\text{O}]^+$ complexes with nonpolar side chains, which generally adopt A-type structures.^{1,3} The structures of lead cationized amino acids are therefore extremely sensitive to the functionalization of the amino acid, as might be expected. Furthermore, the calculations show that the hydrating water in $[\text{Pb}(\text{Phe-H})\text{H}_2\text{O}]^+$ and $[\text{Pb}(\text{Glu-H})\text{H}_2\text{O}]^+$ is bound in the same hemisphere of Pb^{2+} as the deprotonated amino acid. The structure around Pb is therefore hemidirected in that all four ligands are bound to one hemisphere of the complex due to the p character of the orbital containing the lone pair of electrons.⁴⁷

References

1. Burt, M. B.; Decker, S. G. A.; Atkins, C. G.; Rowsell, M.; Peremans, A.; Fridgen T. D. *J. Phys. Chem. B* **2011**, *115*, 11506 - 11518.
2. Chapo, C. J.; Paul, J. B.; Provencal, R. A.; Roth, K.; Saykally, R. J. *J. Am. Chem. Soc.* **1998**, *120*, 12956 -12957.
3. Atkins, C. G.; Banu, L.; Rowsell, M.; Blagojevic, V.; Bohme, D. K.; Fridgen. T. D. *J. Phys. Chem. B* **2009**, *113*, 14457 - 14464.
4. Cerda, B. A.; Wesdemiotis, C. *Analyst*, **2000**, *125*, 657-660.
5. Talley, J. M.; Cerda, B. A.; Ohanessian, G.; Wesdemiotis. C. *Chem. Eur. J.* **2002**, *8*, 1377 - 1388.
6. Armentrout, P. B.; Rodgers, M. T.; Oomens, J.; Steill, J. D. *J. Phys. Chem. A* **2008**, *112*, 2248 - 2257.
7. Rodgers, M. T.; Armentrout, P. B.; Oomens, J.; Steill, J. D. *J. Phys. Chem. A* **2008**, *112*, 2258 - 2267.
8. Moision, R. M.; Armentrout, P. B. *J. Phys. Chem. A* **2002**, *106*, 10350 - 10362.
9. Moision, R. M.; Armentrout, P. B. *J. Phys. Chem. A* **2006**, *110*, 3933 - 3946.
10. Kapota, C.; Lemaire, J.; Maitre, P.; Ohanessian, G. *J. Am. Chem. Soc.* **2004**, *126*, 1836 - 1842.
11. Rogalewicz, F.; Hopilliard, Y.; Ohanessian, G. *Int. J. Mass Spectrom.* **2000**, *201*, 307 - 320.
12. Hoppilliard, Y.; Rogalewicz, F.; Ohanessian, G. *Int. J. Mass Spectrom.* **2000**, *204*, 267 - 280.
13. Rogalewicz, F.; Hopilliard, Y.; Ohanessian, G. *Int. J. Mass Spectrom.* **2001**, *206*, 45 - 52.
14. Rogalewicz, F.; Hopilliard, Y.; Ohanessian, G. *Int. J. Mass Spectrom.* **2003**, *227*, 439 - 451.
15. Bush, M. F.; Forbes, M. W.; Jockusch, R. A.; Oomens, J.; Polfer, N. C.; Saykally, R. J.; Williams, E. R. *J. Phys. Chem. A* **2007**, *111*, 7753 - 7760.

16. Lemoff, A. S.; Bush, M. F.; Williams, E. R. *J. Phys. Chem. A* **2005**, *109*, 1903 - 1910.
17. Polfer, N. C.; Oomens, J.; Moore, D. T.; von Helden, G.; Meijer, G.; Dunbar, R. C. *J. Am. Chem. Soc.* **2006**, *128*, 517 - 525.
18. Polfer, N. C.; Oomens, J.; Dunbar, R. C. *Phys. Chem. Chem. Phys.* **2006**, *8*, 2744 - 2751.
19. Kamariotis, A.; Boyarkin, O. V.; Mercier, S. R.; Beck, R. D.; Bush, M. F.; Williams, E. R.; Rizzo, T. R. *J. Am. Chem. Soc.* **2006**, *128*, 905 - 916.
20. Drayß, M. K.; Armentrout, P. B.; Oomens, J.; Schäfer, M. *Int. J. Mass Spectrom* **2010**, *297*, 18 - 27.
21. O'Brien, J. T.; Prell, J. S.; Steill, J. D.; Oomens, J.; Williams, E. R. *J. Phys. Chem. A* **2008**, *112*, 10823 - 10830.
22. Dunbar, R. C.; Polfer, N. C.; Oomens, J. *J. Am. Chem. Soc.* **2007**, *129*, 14562 - 14563.
23. Marino, T.; Tuscano, M.; Russo, N.; Grand, A. *J. Phys. Chem. B* **2006**, *110*, 24666 - 24673.
24. Bush, M. F.; Oomens, J.; Saykally, R. J.; Williams, E. R. *J. Am. Chem. Soc.* **2008**, *130*, 6463 - 6471.
25. Strittmatter, E. F.; Lemoff, A. S.; Williams, E. R. *J. Phys. Chem. A* **2000**, *104*, 9793 - 9796.
26. Remko, M.; Rode, B. M. *J. Phys. Chem. A* **2006**, *110*, 1960 - 1967.
27. Russo, N.; Belcastro, M.; Marino, T.; Toscano, M. *J. Mass Spectrom.* **2005**, *40*, 300 - 306.
28. Constantino, E.; Rodriguez-Santiago, L.; Sodupe, M.; Tortajada, J. *J. Phys. Chem. A* **2005**, *109*, 224 - 230.
29. Armentrout, P. B.; Gabriel, A.; Moision, R. M. *Int. J. Mass Spectrom.* **2009**, *283*, 56 - 68.
30. Gapeev, A.; Dunbar, R. C. *J. Am. Chem. Soc.* **2001**, *123*, 8360 - 8365.
31. Siu, F. M.; Ma, N. L.; Tsang, C. W. *Chem. Eur. J.* **2004**, *10*, 1966 - 1976.

32. Forbes, M. W.; Bush, M. F.; Polfer, N. C.; Oomens, J.; Dunbar, R. C.; Williams, E. R.; Jockusch, R. A. *J. Phys. Chem. A* **2007**, *111*, 11759 - 11770.
33. Fridgen, T. D. *Mass. Spectrom. Rev.* **2009**, *28*, 586 - 607.
34. Eyler, J. R. *Mass Spectrom. Rev.* **2009**, *28*, 448 - 467.
35. Polfer, N. C.; Oomens, J. *Mass Spectrom. Rev.* **2009**, *28*, 468 - 494.
36. Oepts, D.; van der Meer, A. F. G.; van Amersfoort, P. W. *Infrared Phys. Technol.* **1995**, *36*, 297 - 308.
37. Ortega, J. M.; Berset, J. M.; Chaput, R.; Glotin, F.; Humbert, G.; Jaroszynski, D.; Joly, P.; Kergosien, B.; Lesrel, J. *Nucl. Instrum. Methods Phys. Res., Sect. A* **1996**, *375*, 618 - 625.
38. Snoek, L. C.; Kroemer, R. T.; Simons, J. P. *Phys. Chem. Chem. Phys.* **2002**, *4*, 2130 - 2139.
39. Tajkhorshid, E.; Jalkanen, K. J.; Suhai, S. *J. Phys. Chem. B* **1998**, *102*, 5899 - 5913.
40. Ahn, D.-S.; Park, S.-W.; Jeon, I.-S.; Lee, M.-K.; Kim, N.-H.; Han, Y.-H.; Lee, S. J. *Phys. Chem. B* **2003**, *107*, 14109 - 14118.
41. Jensen, J. H.; Gordon, M. S. *J. Am. Chem. Soc.* **1995**, *117*, 8159 - 8170.
42. Blom, M. N.; Compagnon, I.; Polfer, N. C.; von Helden, G.; Meijer, G.; Suhai, S.; Paizs, B.; Oomens, J. *J. Phys. Chem. A* **2007**, *111*, 7309 - 7316.
43. Xu, S. J.; Nilles, J. M.; Bowen, K. H. *J. Chem. Phys.* **2003**, *119*, 10696 - 10701.
44. Rajabi, K.; Easterling, M. L.; Fridgen, T. D. *J. Am. Soc. Mass Spectrom.* **2009**, *20*, 411 - 418.
45. Frisch, M. J.; Trucks, G. W.; Schlegel, H. B.; Scuseria, G. E.; Robb, M. A.; Cheeseman, J. R.; Scalmani, G.; Barone, V.; Mennucci, B.; Petersson, G. A.; Nakatsuji, H.; Caricato, M.; Li, X.; Hratchian, H. P.; Izmaylov, A. F.; Bloino, J.; Zheng, G.; Sonnenberg, J. L.; Hada, M.; Ehara, M.; Toyota, K.; Fukuda, R.; Hasegawa, J.; Ishida, M.; Nakajima, T.; Honda, Y.; Kitao, O.; Nakai, H.; Vreven, T.; Montgomery, J. A. Jr.; Peralta, J. E.; Ogliaro, F.; Bearpark, M.; Heyd, J. J.; Brothers, E.; Kudin, K. N.; Staroverov, V. N.; Kobayashi, R.; Normand, J.; Raghavachari, K.; Rendell, A.; Burant, J. C.; Iyengar, S. S.; Tomasi, J.; Cossi, M.; Rega, N.; Millam, J. M.; Klene, M.; Knox, J. E.; Cross, J. B.; Bakken, V.; Adamo, C.; Jaramillo, J.; Gomperts, R.; Stratmann, R. E.; Yazyev, O.; Austin, A. J.; Cammi, R.; Pomelli, C.;

- Ochterski, J. W.; Martin, R. L.; Morokuma, K.; Zakrzewski, V. G.; Voth, G. A.; Salvador, P.; Dannenberg, J. J.; Dapprich, S.; Daniels, A. D.; Farkas, O.; Foresman, J. B.; Ortiz, J. V.; Cioslowski, J.; Fox, D. J. Gaussian 09, Revision A.01; Gaussian, Inc.: Wallingford, CT, 2009.
46. Atkins, C. G.; Rajabi, K.; Gillis, E. A. L.; Fridgen, T. D. *J. Phys. Chem. A* **2008**, *112*, 10220 - 10225.
47. Shimoni-Livny, L.; Glusker, J. P.; Bock, C. W. *Inorg. Chem.* **1998**, *37*, 1853 - 1867.
48. Chiavassa, T.; Roubin, P.; Pizzala, L.; Verlaque, P.; Allouche, A.; Marinelli, F. *J. Phys. Chem.* **1992**, *96*, 10659 - 10665.

Chapter 5

Water Binding Energies of $[\text{Pb}(\text{AminoAcid-H})\text{H}_2\text{O}]^+$ Complexes Determined by Blackbody Infrared Radiative Dissociation.[†]

5.1. Introduction. The gas-phase structures of metal (M) cation/amino acid (Aa) complexes can be effectively determined using IRMPD spectroscopy supported by electronic structure calculations.¹⁻²¹ Most of this research has been directed at structurally characterizing $[\text{M}(\text{Aa})]^{+2+}$ ions where M is an alkali, alkaline earth, or first row transition metal, but *p*-block metal/amino acid complexes have been left unexplored. In response, Atkins and coworkers performed IRMPD spectroscopy on Pb^{2+} -bound glycine (Gly) complexes to determine the structures of $[\text{Pb}(\text{Gly-H})]^+$ and $[\text{Pb}(\text{Gly-H})\text{H}_2\text{O}]^+$,⁵ and that work was extended in Chapters 3 and 4 to include $[\text{Pb}(\text{Aa-H})]^+$ and $[\text{Pb}(\text{Aa-H})\text{H}_2\text{O}]^+$ complexes where Aa = proline (Pro), alanine (Ala), valine (Val), leucine (Leu), isoleucine (Ile), phenylalanine (Phe), glutamic acid (Glu), and lysine (Lys).^{4,20} As was detailed in Chapter 1, lead is an excellent candidate for study because it complexes with every amino acid.^{22,23} It also causes dangerous physiological effects within humans ranging from anemia to hypertension, highlighting the biological importance of these structures.²⁴

The dominant gas-phase Pb^{2+} /amino acid complexes formed by electrospray ionization (ESI) are deprotonated and of the form $[\text{M}(\text{Aa-H})]^+$. These structures are not nearly as well characterized as $[\text{M}(\text{Aa})]^{+2+}$ ions and are the focus of this thesis.^{12-16,18,19,21} Pb^{2+} is known to interact with deprotonated amino acids in four ways (Figure 5.1): it can

[†] Adapted from work accepted for publication in *Phys. Chem. Chem. Phys.* DOI:10.1039/c2cp41440f.

bind between the terminal amine and carboxylic acid (A- and B-type structures);^{4,5} lie between the two carbonyl oxygens (a C-type structure);⁴ or attach to a functional group on the amino acid side chain (a D-type structure).²⁰ A-type structures are amine-deprotonated whereas B- and C-type structures are carboxyl-deprotonated. The sites of deprotonation and Pb^{2+} binding are markedly dependent on the polarity and acidity of the amino acid side chains. The $[\text{Pb}(\text{Aa-H})]^+$ structures where Aa = Gly, Pro, Ala, Val, Leu, and Ile form A-type structures, whereas $[\text{Pb}(\text{Phe-H})]^+$ and $[\text{Pb}(\text{Lys-H})]^+$ are B- and C-type ions respectively. The B- and C-type structures are further stabilized by additional interactions with the amino acid side chain; Pb^{2+} binds to the ϵ -amino group in $[\text{Pb}(\text{Lys-H})]^+$, and $[\text{Pb}(\text{Phe-H})]^+$ contains a Pb^{2+} -phenyl π -interaction.^{4,20} $[\text{Pb}(\text{Glu-H})]^+$ is a D-type ion where Pb^{2+} is chelated between the terminal carbonyl oxygen and deprotonated γ -carboxyl group of zwitterionic Glu.²⁰ The $[\text{Pb}(\text{Aa-H})\text{H}_2\text{O}]^+$ structures are generally the hydrated analogues of the $[\text{Pb}(\text{Aa-H})]^+$ complexes where water binds directly to Pb^{2+} through the oxygen atom. It should be noted, however, that water does not always remain intact on the ion; the hydrated A-type structures are the result of a proton shift between the added water and the deprotonated amine group, and water acts as a hydrogen bond donor in the cases of $[\text{Pb}(\text{Lys-H})\text{H}_2\text{O}]^+$ and $[\text{Pb}(\text{Glu-H})\text{H}_2\text{O}]^+$.

Since the $[\text{Pb}(\text{Aa-H})\text{H}_2\text{O}]^+$ ions considered here can adopt at least four distinct isomers, their water binding energies may be noticeably different. In this chapter, blackbody infrared radiative dissociation (BIRD) is used to determine the dissociation

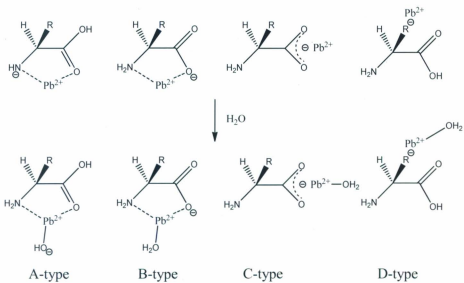


Figure 5.1: The A-, B-, C-, and D-type complexes formed between Pb^{2+} and the conjugate bases of amino acids. The ions resulting from single hydration are also shown.

rate constants and threshold dissociation energies, E_0 , for each $[\text{Pb}(\text{Aa-H})\text{H}_2\text{O}]^+$ complex described above. BIRD is a reliable method for studying the dissociation of solvated ions in low pressure environments (below 10^{-6} mbar) where collision-induced reactions no longer compete with radiative exchange between the ion and the ambient blackbody radiation.^{25,26} BIRD reactions often take seconds or longer, and non-thermal perturbations (such as bath gas collisions, or excitation by radio frequency (RF) fields) can introduce uncertainty into the measured rate constants. Fourier transform ion cyclotron resonance (FT-ICR) mass spectrometry removes these effects by trapping ions in a “zero”-pressure environment (10^{-10} mbar) free of RF fields. This is an excellent technique for making BIRD measurements and is the one used here. BIRD kinetic measurements can be made on ions of any size; however, small molecules are typically within the slow-exchange kinetic limit, meaning that the observed Arrhenius activation energies underestimate the true dissociation energies.^{27,28} Modeling of the observed dissociation rate constants is therefore necessary to extract meaningful values of E_0 . The master equation approach is implemented here to accurately determine the water binding energies for the $[\text{Pb}(\text{Aa-H})\text{H}_2\text{O}]^+$ complexes.²⁹

Since the rate of water loss for different isomers of the same complex may be discernibly different, two sets of BIRD kinetic data were recorded for ions electrosprayed from solutions made from water mixed with either methanol or acetonitrile. The purpose of this is to see whether or not the solvents are causing isomerization while the ions are being desolvated in the ESI source. Ohanessian and coworkers noticed this very issue when they explored the structure of $[\text{Zn}(\text{Gly-H})]^+$ using low-energy CID.³⁰⁻³³ They

observed different fragmentation pathways depending on whether acetonitrile or methanol was used as a solvent, possibly meaning that different structures were produced depending on the solvent from which they were removed.

5.2. Methods.

5.2.1. BIRD Kinetic Measurements. The $[\text{Pb}(\text{Aa-H})]^+$ complexes were prepared by dissolving 0.1 mM $\text{Pb}(\text{NO}_3)_{2(s)}$ (> 99%, Fluka Chemika) and 0.1 mM $\text{Aa}_{(s)}$ (Aa = Pro, Gly, Ala, Val, Leu, Ile, Phe, Glu, and Lys) (Nutritional Biochemicals Corporation) in 50/50 solutions of 18.2 M Ω water (Millipore) with either methanol (99.8%, ACP Chemicals) or acetonitrile (99.9%, Fisher Scientific). An Apollo II ESI source (Bruker Daltonics) was used to pass each solution into a Bruker Apex Qe 7 T FT-ICR mass spectrometer at a flow rate of 100 $\mu\text{L h}^{-1}$. The voltage across the source exit capillary was 294 V. Depending on the complex, the electrosprayed $[\text{Pb}(\text{Aa-H})]^+$ ions were allowed to accumulate in the source for 10^{-3} – 1.0 s. They were then mass selected by a quadrupole mass filter and left to accrue in a hexapole collision cell for 1.0 – 2.0 s. The collision cell has both an argon gas inlet line and a vapour inlet line. $[\text{Pb}(\text{Aa-H})\text{H}_2\text{O}]^+$ complexes were prepared by minimizing the argon gas flow while opening a micro-valve between a water reservoir and the cell.³⁴ Water introduced through the vapour inlet was degassed by a freeze-pump-thaw cycle carried out in triplicate. The $[\text{Pb}(\text{Aa-H})\text{H}_2\text{O}]^+$ ions were then accelerated through electrostatic optics and trapped in the ICR cell. BIRD experiments were carried out on the isolated $[\text{Pb}(\text{Aa-H})\text{H}_2\text{O}]^+$ ions in order to determine the rate constant for its unimolecular dissociation into $[\text{Pb}(\text{Aa-H})]^+$ and water. The peak heights of the precursor ion and fragment ions were monitored as a function of reaction delay

time in order to determine the unimolecular dissociation rate constant (k_{obs}) from the first-order rate equation. The reaction delay increments ranged from 0.10 - 86.00 s, and 2 - 8 mass spectra were averaged per step (generally for 12 - 16 steps) until the dissociation reaction was observed to be nearing completion (90% decay). Some experiments were repeated two to three times to gauge the uncertainty of k_{obs} . In these cases, the average value is reported and the uncertainty is the standard deviation of the mean. The relative uncertainty in k_{obs} was typically about 1%, but was as high as 9% for a small minority of the dissociation reactions.

The vacuum chamber encompassing the ion cell is surrounded by a heating jacket that is thermally controlled by a steady AC input voltage from a variable autotransformer (Variac).^{4,35} The temperature inside the cell was calibrated against the average temperature measured by two thermocouples placed under the heating jacket on opposite sides of the vacuum chamber by temporarily placing a thermocouple inside the cell. The temperatures in and outside the cell were also calibrated against the AC input voltage; allowing the cell temperature to be accurately set between 20 and 120 °C. The uncertainty in the measured average temperature is approximately 2 °C. The BIRD experiments were carried out at 7 - 13 different temperatures, depending on the ion, over the full range of available cell temperatures in order to extract the Arrhenius activation energies from Arrhenius plots ($\ln(k_{\text{obs}})$ vs. $1/T$) for each $[\text{Pb}(\text{Aa-H})\text{H}_2\text{O}]^+$ complex.

5.2.2. Calculations. The structures of the $[\text{Pb}(\text{Aa-H})\text{H}_2\text{O}]^+$ complexes are shown in Figure 5.2 and the structures of the $[\text{Pb}(\text{Aa-H})]^+$ complexes are reported in Chapters 3 and

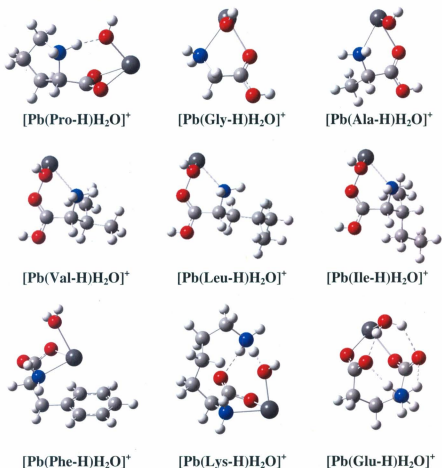


Figure 5.2: The lowest-energy structures of the nine $[\text{Pb}(\text{Aa-H})\text{H}_2\text{O}]^+$ complexes (Aa = Pro, Gly, Ala, Val, Leu, Ile, Phe, Lys, and Glu) determined using IRMPD spectroscopy. Each complex was optimized using the B3LYP/6-31+G(d,p) level of theory. In each case, the LANL2DZ basis set with relativistic core potential was applied to Pb.

4.^{4,20,36} All structures were experimentally verified by IRMPD spectroscopy and are the lowest energy isomers determined computationally. Their vibrational modes and intensities were acquired using the B3LYP/6-31+G(d,p) level of theory, and single-point energies were computed by the MP2(full)/6-311++G(2d,2p)//B3LYP/6-31+G(d,p) method (the vibrational modes and intensities used for H₂O are reported in Table C1 in Appendix C). The effective charge on Pb for each complex was determined using a full natural bond orbital analysis.³⁷ All calculations were performed using Gaussian 09, and in each case, the LANL2DZ basis set with relativistic core potential was applied to lead.⁴¹ The most stable calculated structures for each ion were determined by comparing the 298 K free energies and enthalpies of between 18 – 110 isomers for each complex and finding the minimum energy structure. The 0 K dissociation energies (D_0) for the loss of neutral H₂O from the [Pb(Aa-H)H₂O]⁺ complexes were also obtained using the B3LYP and MP2 theories. The MP2 result added the zero-point energy corrections calculated at the B3LYP/6-31+G(d,p) level of theory to the MP2 single-point energies. Counterpoise (CP) corrections were used to account for basis set superposition errors.^{38,39} Since the reverse association reaction should be barrierless, D_0 can be taken as the threshold dissociation energy, E_0 . In every case, the [Pb(Aa-H)H₂O]⁺ ion was assumed to dissociate into its analogous bare complex (i.e. B-type [Pb(Lys-H)H₂O]⁺ loses water to produce B-type [Pb(Lys-H)]⁺).

5.2.3. Master Equation Modeling. Temperature dependent and E/J -resolved (reaction energy (E) and total angular momentum (J)) unimolecular dissociation rate constants

(k_{uni}) were determined from the master equation (Eq. 5.1) using VariFlex.⁴⁰ The master equation is a set of coupled linear first-order ordinary differential equations that describes the change in population (dN/dt) of a system's internal energy states (i, j) over time.²⁹

$$\frac{dN_i}{dt} = k_d N_i(t) + \sum_j k_{ij} N_j(t) \quad (5.1)$$

In this model, the dissociating ion is treated as a set of weakly-coupled harmonic oscillators. The rate constants for all state-to-state transitions between states i and j due to collisional or radiative processes are the k_{ij} , and k_d is the microcanonical rate constant for population loss from state i due to dissociation. Collisional processes are negligible in these experiments due to the zero-pressure conditions inside the FT-ICR cell, hence the k_{ij} are simply the sum of the rate constants for radiative absorption and emission.^{25,35,41}

VariFlex uses E/J -resolved variable reaction coordinate transition state theory (VRC-TST) and Rice-Ramsperger-Kassel-Marcus (RRKM) theory to minimize the dissociation rate constants (k_d).^{42,43} This method, which requires the vibrational frequencies for the transition state, dissociating ion, and dissociation products, has been described in detail in Section 2.4.2, and its implementation is only briefly discussed here. Vibrational frequencies were extracted from the lowest energy B3LYP/6-31+G(d,p) structures of the IRMPD-determined $[\text{Pb}(\text{Aa-H})\text{H}_2\text{O}]^+$ and $[\text{Pb}(\text{Aa-H})]^+$ complexes, and were scaled by 0.955 to account for anharmonic effects.⁴⁻⁶ Assigning a structure to the transition state is more difficult since the reverse association reaction is expected to be barrierless. For this reason, VRC-TST defines the reaction coordinate as the bond being broken through dissociation, the Pb^{2+} -water oxygen bond, and alters its length until the

calculated RRKM rate constants are minimized.⁴⁴⁻⁴⁹ The radiative exchange rate constants (k_{ij}) are determined using Boltzmann statistics by extracting the Einstein coefficients from the IR absorption intensities associated with the vibrational frequencies.⁵⁰⁻⁵⁵

Trial values of E_0 were suggested using the theoretical 0 K dissociation energies; typical inputs for the threshold dissociation energy ranged between $D_0 \pm 2000 \text{ cm}^{-1}$ in steps of 200 cm^{-1} . The calculated unimolecular dissociation rate constants returned by VariFlex are compared to k_{obs} by constructing Arrhenius plots. The water binding energy is the E_0 which results in the best fit for the experimental slope.^{41,56} The uncertainty in the master equation-derived threshold dissociation energies, when comparing with the experimental Arrhenius plots, is generally $\pm 100 \text{ cm}^{-1}$ ($\sim 1.2 \text{ kJ mol}^{-1}$). The errors reported for E_0 are derived from the error in the slopes of the Arrhenius plots.

5.3. Results and Discussion.

5.3.1. BIRD Kinetic Data. Exposure to ambient black-body photons causes $[\text{Pb}(\text{Aa-H})\text{H}_2\text{O}]^+$ complexes to dissociate into neutral water and $[\text{Pb}(\text{Aa-H})]^+$. $[\text{Pb}(\text{Glu-H})]^+$ was also observed to lose another neutral water molecule at a slower rate. $[\text{Pb}(\text{Pro-H})\text{H}_2\text{O}]^+$ did not lose water at the highest temperature examined and so unimolecular dissociation rate constants could not be obtained. A typical example of $[\text{Pb}(\text{Aa-H})\text{H}_2\text{O}]^+$ dissociation is given in Figure 5.3, which compares the dissociation of $[\text{Pb}(\text{Ala-H})\text{H}_2\text{O}]^+$ at 386.6 K at different reaction times.

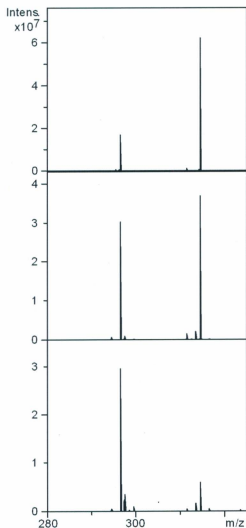


Figure 5.3: The dissociation of $[\text{Pb}(\text{Ala-H})\text{H}_2\text{O}]^+$ ($m/z = 314$ Da) into $[\text{Pb}(\text{Ala-H})]^+$ ($m/z = 296$ Da) and neutral water at 386.6 K monitored as a function of reaction time by FT-ICR mass spectrometry. The relative abundances of the ions are plotted after 6.01 s (a), 24.01 s (b), and 78.01 s (c).

Dissociation rate constants (k_{obs}) were extracted from the $[\text{Pb}(\text{Aa-H})\text{H}_2\text{O}]^+$ and $[\text{Pb}(\text{Aa-H})]^+$ signal intensities by normalizing their abundances (I_{AlaW} and I_{Ala} respectively) and plotting them as a function of reaction time. Because the dissociation reaction is unimolecular, plotting $\ln[I_{\text{AlaW}}/(I_{\text{AlaW}} + I_{\text{Ala}})]$ against reaction time allows the reaction rate constant to be determined by linearly fitting the integrated first-order rate law. In the case of $[\text{Pb}(\text{Glu-H})\text{H}_2\text{O}]^+$, the abundance of the second water loss product ($[\text{Pb}(\text{Glu-H-H}_2\text{O})]^+$) was also taken into account when normalizing the signal intensities. Figure 5.4A exhibits the normalized intensities of $[\text{Pb}(\text{Ala-H})\text{H}_2\text{O}]^+$ and $[\text{Pb}(\text{Ala-H})]^+$ at 386.6 K as functions of reaction time. Following a short induction period to allow ions to thermalize, precursor ions undergo a smooth exponential decay, resulting in linear plots of $\ln[I_{\text{AlaW}}/(I_{\text{AlaW}} + I_{\text{Ala}})]$ versus reaction time (Figure 5.4B), in this case yielding a k_{obs} of $0.0213 \pm 0.0003 \text{ s}^{-1}$ at 386.6 K. The excellent linear fit ($R^2 > 0.996$) indicates that the ions trapped in the ICR cell reached a steady-state energy distribution prior to dissociation. Kinetic data for the dissociation of the other $[\text{Pb}(\text{Aa-H})\text{H}_2\text{O}]^+$ complexes at multiple (7 - 9) temperatures between 292 - 388 K are plotted in Figure C1a - g; the extracted rate constants are also tabulated in Appendix C.

5.3.2. Arrhenius Parameters. Arrhenius plots for each complex were prepared from the temperature-dependent kinetic data to ascertain the activation energy for H_2O removal from each complex. The Arrhenius plots for the dissociation of each $[\text{Pb}(\text{Aa-H})\text{H}_2\text{O}]^+$ ion are shown in Figure 5.5. The linearity of each plot is good ($R^2 = 0.8838 - 0.9975$), and

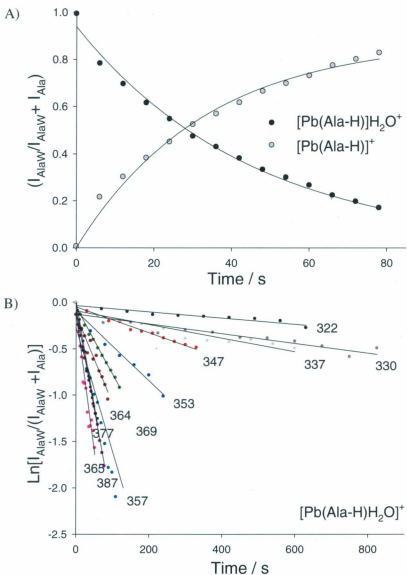


Figure 5.4: a) The normalized intensities of $[Pb(Ala-H)]^+$ and $[Pb(Ala-H)]H_2O^+$ as a function of reaction time. Both ions exhibit first-order kinetic behaviour. b) The BIRD kinetic data for the dissociation of $[Pb(Ala-H)]H_2O^+$ is fit to the integrated first-order rate law ($\ln[I_{AlaW} / (I_{AlaW} + I_{Ala})]$ versus reaction time) at 11 temperatures between 322 – 387 K.

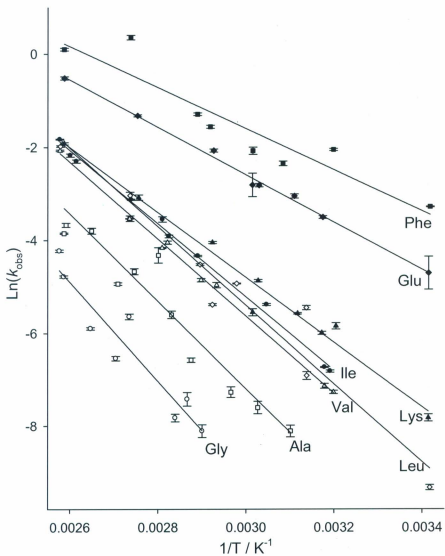


Figure 5.5: Comparison of the Arrhenius plots ($\ln(k_{\text{obs}})$ versus $1/T$) for the $[\text{Pb}(\text{Aa-H})\text{H}_2\text{O}]^+$ complexes (Aa = Gly (\circ), Ala (\square), Val (Δ), Leu (\diamond), Ile (\bullet), Phe (\blacksquare), Lys (\blacktriangle), and Glu (\blacklozenge)).

there are no abrupt changes in slope to suggest other dissociative mechanisms over the temperature range considered. The measured zero-pressure Arrhenius activation energies (E_a) and preexponential factors (A) are provided in Table 5.1. The error associated with the Arrhenius parameters is the standard deviation of the line of best fit.

As mentioned above, the $[\text{Pb}(\text{Aa-H})\text{H}_2\text{O}]^+$ complexes are small enough (36 – 78 vibrational degrees of freedom) that the rate of photon exchange is expected to be slower than the rate of unimolecular decay. This means that their equilibrium distributions of internal energies are truncated by the continuous removal of the most energetic ions. The observed decay rate therefore depends only on the rate of photon absorption and not the rate of thermal unimolecular dissociation. Under these conditions, the measured Arrhenius activation energies underestimate the true dissociation energies, and master equation modeling was performed as a consequence in order to extract meaningful water binding energies to $[\text{Pb}(\text{Aa-H})]^+$.

5.3.3. Master Equation Modeling. The threshold H_2O dissociation energies of the $[\text{Pb}(\text{Ala-H})\text{H}_2\text{O}]^+$ complexes obtained by solving the master equation are collected in Table 5.2. These are compared with theoretical values of E_0 computed at the B3LYP/6-31+G(d,p) and MP2(full)/6-311++G(2d,2p) levels of theory. Since the reverse association reaction is expected to be barrierless, E_0 is essentially the same as D_0 and is found by calculating the energy difference between the reactant and product ground states. In general, the agreement between experiment and calculations is very good.

Table 5.1: Measured $[\text{Pb}(\text{Aa-H})\text{H}_2\text{O}]^+$ Zero-Pressure Arrhenius Parameters

$[\text{Pb}(\text{Aa-H})\text{H}_2\text{O}]^+$ Complex	E_a (kJ mol ⁻¹)	ln(A)
Gly	88.7 +/- 12.1	22.8 +/- 4.0
Ala	74.8 +/- 6.9	20.0 +/- 2.3
Val	68.9 +/- 1.4	19.2 +/- 0.5
Leu	68.1 +/- 4.5	19.2 +/- 1.6
Ile	65.4 +/- 1.5	18.4 +/- 0.5
Phe	36.6 +/- 5.6	11.6 +/- 0.2
Lys	58.0 +/- 3.6	16.1 +/- 1.3
Glu	42.3 +/- 1.2	12.7 +/- 0.4

Table 5.2: Threshold Dissociation Energies

[Pb(Aa-H)H ₂ O] ⁺ Complex	B3LYP/6-31+G(d,p) (kJ mol ⁻¹)		MP2(full)/6-311++G(2d,2p) (kJ mol ⁻¹)		Master Equation (kJ mol ⁻¹)
	<i>U</i>	<i>CP</i>	<i>U</i>	<i>CP</i>	
Pro	159.5	150.2	167.4	142.3	-
Gly	104.5	93.2	108.1	81.8	113.6 +/- 12.1
Ala	105.4	96.2	106.2	80.5	105.3 +/- 8.5
Val	104.1	95.1	103.8	77.4	102.9 +/- 1.4
Leu	106.1	97.3	105.8	80.8	101.7 +/- 4.8
Ile	109.9	100.9	111.8	86.5	102.9 +/- 1.5
Phe	73.1	68.7	75.1	67.0	76.6 +/- 5.6
Lys	93.6	84.3	98.7	73.0	95.7 +/- 3.6
Glu	80.5	72.8	87.6	72.2	76.6 +/- 1.2

U = Uncorrected binding energies, *CP* = Counterpoise corrected binding energies

The water binding energies are determined by inputting a trial value of E_0 into VariFlex, and then adjusting it in steps of 200 cm^{-1} until the solutions to the master equation adequately fit the experimental slope. As an example, consider the dissociation of $[\text{Pb}(\text{Val-H})\text{H}_2\text{O}]^+$ in Figure 5.6. The experimental slope is $-8282.2 \pm 170.4\text{ cm}^{-1}$. Choosing $E_0 = 8500$ and 8700 cm^{-1} returns values of -8180.9 and -8494.8 cm^{-1} respectively; this gives an upper and lower bound to the RRKM-determined value of E_0 that is smaller than the experimental error of the slope of the Arrhenius plot. The E_0 for $[\text{Pb}(\text{Val-H})\text{H}_2\text{O}]^+$ is therefore determined to be $102.9 \pm 1.4\text{ kJ mol}^{-1}$, reflecting the experimental error.

The Arrhenius pre-exponential factors determined using the master equation are reported in Table 5.3. For the most part, they are within the uncertainty of the experimental Arrhenius parameters. Changing the scaling factor for the vibrational frequencies from 0.95 to $0.90 - 1.10$ (Figure C2 in Appendix C) alters the Arrhenius pre-exponential factors of $[\text{Pb}(\text{Val-H})\text{H}_2\text{O}]^+$ by about two percent, and changes the determined threshold dissociation energy by less than four percent.

5.3.4. Factors Affecting $[\text{Pb}(\text{Aa-H})\text{H}_2\text{O}]^+$ Dissociation.

5.3.4.1. Pb^{2+} Stabilization by Amino Acid Conjugate Bases. IRMPD spectroscopy determined that most nonpolar $[\text{Pb}(\text{Aa-H})\text{H}_2\text{O}]^+$ (Aa = Gly, Ala, Val, Leu, and Ile) complexes have A-type structures where the lead-bound water donates a proton to the amino acid's deprotonated amine moiety (Figure 5.2).^{4,5} By contrast, $[\text{Pb}(\text{Phe-H})\text{H}_2\text{O}]^+$ and $[\text{Pb}(\text{Lys-H})\text{H}_2\text{O}]^+$ have B-type structures, and $[\text{Pb}(\text{Glu-H})\text{H}_2\text{O}]^+$ is a D-type complex

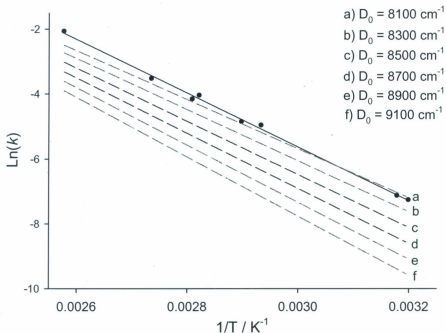


Figure 5.6: The Arrhenius plot of $[\text{Pb}(\text{Val-H})\text{H}_2\text{O}]^+$ (solid line) fit by k_{uni} values calculated using the master equation (dashed lines). The trial E_0 values, 8500 and 8700 cm^{-1} (black dashed lines) produce slopes that are slightly less and slightly more negative than the experimental line, hence the water binding energy is $8600 \pm 100 \text{ cm}^{-1}$ based on a comparison of the experimental Arrhenius plot with the master-equation calculated lines.

Table 5.3: Master Equation Arrhenius Pre-exponential Factors

[Pb(Aa-H)H ₂ O] ⁺ Complex	Master Equation ln(A)
Gly	19.5 +/- 4.0
Ala	19.3 +/- 2.3
Val	18.3 +/- 0.5
Leu	18.2 +/- 1.6
Ile	18.0 +/- 0.5
Phe	11.0 +/- 0.2
Lys	16.2 +/- 1.3
Glu	13.1 +/- 0.4

where Pb^{2+} forms a salt bridge with the γ -carboxyl group and is additionally stabilized by the terminal carbonyl oxygen of zwitterionic Glu.²⁰ The $[\text{Pb}(\text{Aa-H})\text{H}_2\text{O}]^+$ threshold dissociation energies given in Table 5.2 demonstrate that the complexes with the strongest water binding energies are those where the addition of water results in the formation of a covalent N-H bond by transfer of a proton from water to the originally deprotonated nitrogen. Each of the nonpolar A-type complexes, for example, have threshold dissociation energies greater than 100 kJ mol^{-1} , whereas the B-type $[\text{Pb}(\text{Phe-H})\text{H}_2\text{O}]^+$ complex only has a water binding energy of 76.6 kJ mol^{-1} . The main difference between the structures of these ions is that the A-type complexes only have Pb^{2+} bound to the deprotonated nitrogen and to the carbonyl oxygen of the carboxyl group, whereas $[\text{Pb}(\text{Phe-H})\text{H}_2\text{O}]^+$ has Pb^{2+} additionally stabilized by a π -interaction with its side chain. This means that the B-type $[\text{Pb}(\text{Phe-H})\text{H}_2\text{O}]^+$ structure has more electron density on Pb^{2+} than the A-type structures, resulting in a lower charge density and weaker Pb^{2+} -water binding. This is expected for the ion-dipole interactions that exist between water and these $[\text{Pb}(\text{Aa-H})]^+$ complexes.

The structures of $[\text{Pb}(\text{Lys-H})\text{H}_2\text{O}]^+$ and $[\text{Pb}(\text{Glu-H})\text{H}_2\text{O}]^+$ are also stabilized by side chain interactions. The threshold dissociation energy of $[\text{Pb}(\text{Glu-H})\text{H}_2\text{O}]^+$ is similar to that of $[\text{Pb}(\text{Phe-H})\text{H}_2\text{O}]^+$. This is likely due to the multiple basic sites of Glu donating electron density to Pb^{2+} , resulting in a more weakly bound water molecule. The water binding energy of $[\text{Pb}(\text{Lys-H})\text{H}_2\text{O}]^+$ is closer to those of the A-type complexes, and this is reflected by its water acting as a hydrogen bond donor to the ϵ -amine group.

The predicted water binding energy for $[\text{Pb}(\text{Pro-H})\text{H}_2\text{O}]^+$ is significantly higher ($167.4 \text{ kJ mol}^{-1}$) than the other complexes. $[\text{Pb}(\text{Pro-H})\text{H}_2\text{O}]^+$ is a C-type isomer stabilized by hydrogen bonding between water and the secondary amine. This interaction is further stabilized by the inductive effect of proline's ring, which provides additional electron density to the amine. Both of these factors lead to tighter water binding, explaining why $[\text{Pb}(\text{Pro-H})\text{H}_2\text{O}]^+$ was not observed to dissociate in the ICR cell.

The binding energy of $[\text{Pb}(\text{Aa-H})\text{H}_2\text{O}]^+$ complexes therefore depends on the extent of Pb^{2+} stabilization by the amino acid, as well as any extra binding that water participates in, in the form of hydrogen bonding. It is also worthwhile mentioning the expected dissociation pathways for the loss of water from these complexes. $[\text{Pb}(\text{Phe-H})\text{H}_2\text{O}]^+$ and $[\text{Pb}(\text{Glu-H})\text{H}_2\text{O}]^+$ should lose water through a barrierless process simply by breaking the non-covalent Pb-OH_2 bond. The A-type structures, on the other hand, need to restore the proton transferred to the amine group back to the hydroxyl moiety bound to Pb^{2+} . The enthalpy barrier with respect to this process was previously determined, computationally, to be 60.6 kJ mol^{-1} for $[\text{Pb}(\text{Gly-H})\text{H}_2\text{O}]^+$.⁵ Since this barrier for proton transfer is significantly lower than the water binding energy it would not be expected to interfere with the loss of water.

5.3.4.2. Amino Acid Gas-Phase Basicity. The water binding energies of the aliphatic $[\text{Pb}(\text{Aa-H})\text{H}_2\text{O}]^+$ complexes generally decrease as the amino acid side chains become larger, reflecting the electron donating ability of the larger non-polar side chains. Among the A-type structures, the gas-phase basicity (GB) of Gly, 847 kJ mol^{-1} , is the weakest

because its side chain consists of a single hydrogen atom.⁵⁷ The other nonpolar amino acids (Ala, Val, Leu, and Ile) have more electron donating groups in their side chains, and are therefore more basic ($GB = 888 - 898 \text{ kJ mol}^{-1}$). The inductive effect of the larger alkyl side chains results in more electron density donation to the Pb^{2+} atom, weakening the lead-water oxygen bond. Glycine, which has the most electron withdrawing side chain of the A-type structures, will therefore bind water the strongest. The close threshold dissociation energies of the other nonpolar amino acids reflect their similar gas-phase basicities. Table 5.4 illustrates this by comparing the basicities of the aliphatic amino acids with the computed charge on lead as well as the lengths of the bonds that Pb^{2+} forms with water and the two binding sites on the amino acid. It's clear that an increase in amino acid basicity corresponds to a reduced charge on the lead cation, and this results in Pb^{2+} becoming more tightly bound between the amine nitrogen and carbonyl oxygen. For example, the Pb-N bond length is 2.497 Å for $[\text{Pb}(\text{Gly-H})\text{H}_2\text{O}]^+$ (Pb charge = 1.547), but only 2.461 Å for $[\text{Pb}(\text{Ile-H})\text{H}_2\text{O}]^+$ (Pb charge = 1.534), and is even longer for the B-type $[\text{Pb}(\text{Phe-H})\text{H}_2\text{O}]^+$ (2.442 Å). The Pb-OH₂ bond distance follows the reverse trend. The complex with the shortest Pb-OH₂ bond (2.027 Å), and hence the strongest water binding energy, is the one with the most positive charge on Pb, $[\text{Pb}(\text{Gly-H})\text{H}_2\text{O}]^+$.

The gas-phase basicities of Phe, Glu, and Lys are stronger ($GB_{\text{Phe}} = 910 \text{ kJ mol}^{-1}$, $GB_{\text{Glu}} = 936 \text{ kJ mol}^{-1}$, $GB_{\text{Lys}} = 946 \text{ kJ mol}^{-1}$) than the amino acids that produce A-type complexes and, as was mentioned earlier, their water binding energies are weaker. Each complex, however, has an additional interaction between Pb^{2+} and the amino acid side

Table 5.4: The Effect of Amino Acid Basicity on Bond Lengths Around the Pb²⁺ Binding Site

Amino Acid	Gas-phase Basicity (kJ mol ⁻¹)	Pb-N Bond Length (Å)	Pb-O Bond Length (Å)	Pb-OH ₂ Bond Length (Å)	Pb Charge
Gly	847 +/- 13	2.498	2.401	2.028	1.547
Ala	888 +/- 11	2.478	2.398	2.032	1.542
Val	888 +/- 11	2.465	2.389	2.034	1.540
Leu	899 +/- 13	2.467	2.388	2.035	1.536
Ile	899 +/- 13	2.462	2.394	2.034	1.534
Phe	910 +/- 11	2.442	2.110	2.499	1.558

chain that preferentially stabilizes a B- ($[\text{Pb}(\text{Phe-H})\text{H}_2\text{O}]^+$ and $[\text{Pb}(\text{Lys-H})\text{H}_2\text{O}]^+$) or D-type ($[\text{Pb}(\text{Glu-H})\text{H}_2\text{O}]^+$) isomer. This makes it unreasonable to estimate the relative $[\text{Pb}(\text{Aa-H})\text{H}_2\text{O}]^+$ water binding energies solely using gas-phase basicities. As a consequence, this approach should only be used when comparing similar structures.

To the best of the authors' knowledge, the water binding energy of Pb^{2+} has yet to be experimentally defined. However, the hydration energies of the first-row transition metals have been determined to range between 121 – 163 kJ/mol using collision-induced dissociation,⁵⁸ and were previously computed for the alkali and alkaline earth metals.^{59,60} Sr^{2+} , which has a similar effective ionic radius to Pb^{2+} , has an estimated water binding energy of 198 kJ/mol.^{60,61} The fact that these values are larger than the $[\text{Pb}(\text{Aa-H})]^+$ hydration energies highlights the destabilizing effect that electron donation from the amino acid conjugate base has on the Pb^{2+} -water bond. Hydration energies have also been determined for Na^+ -bound valine and glutamine using a similar method to the one presented here. Their water binding energies are 67 and 53 kJ/mol, respectively.^{62,63}

5.3.5. Electrospray Solvents. The data used in Figures 5.4B, 5.5, and C1 come from two sets: ions that were electrosprayed in 50/50 18.2 M Ω $\text{H}_2\text{O}/\text{MeOH}$ or 50/50 18.2 M Ω $\text{H}_2\text{O}/\text{MeCN}$. This approach was based off a concern raised by Ohanessian and coworkers that the solvent binding energies play a role in shaping molecular structure during the last desolvation step of the electrospray process.³⁰⁻³³ It was initially supposed that if different electrospray solvents led to the formation of different $[\text{Pb}(\text{Aa-H})\text{H}_2\text{O}]^+$ isomers, then the

mechanism for water loss in each structure may be different, and hence the isomerism might be noticeable as a change in the water binding energy.

The similarity of the Arrhenius plots clearly demonstrates that, in this case, the electrospray solvent has no effect on the water binding energies of the $[\text{Pb}(\text{Aa-H})\text{H}_2\text{O}]^+$ complexes. Table 5.5 compares the threshold dissociation energies for the two solvent systems. Most data pairs agree within experimental uncertainty, E_0 is identical in each solvent system for $[\text{Pb}(\text{Val-H})\text{H}_2\text{O}]^+$ and $[\text{Pb}(\text{Lys-H})\text{H}_2\text{O}]^+$, and the widest gap is only 6.0 kJ mol^{-1} for $[\text{Pb}(\text{Ala-H})\text{H}_2\text{O}]^+$. It's very unlikely then that the electrospray solvent is affecting the gas-phase structures of these ions. However, to be sure, an IRMPD spectrum was acquired of $[\text{Pb}(\text{Ala-H})\text{H}_2\text{O}]^+$ solvated in 50/50 18.2 MΩ $\text{H}_2\text{O}/\text{MeCN}$ and compared the IRMPD spectrum of $[\text{Pb}(\text{Ala-H})\text{H}_2\text{O}]^+$ in 50/50 18.2 MΩ $\text{H}_2\text{O}/\text{MeOH}$ shown in Chapter 3. As can be seen in Appendix C (Figure C3), the two spectra are identical: each spectrum contains two strong peaks in the O-H stretching region at 3580 and 3690 cm^{-1} , and their positions and intensities are virtually the same regardless of the solvent system used. If the data with the biggest discrepancy ($[\text{Pb}(\text{Ala-H})\text{H}_2\text{O}]^+$) demonstrates no solvent-dependent structural differences it is unlikely that that any exists with the other complexes.

5.4. Conclusions. The threshold dissociation energies and thermal unimolecular dissociation rate constants were determined for water detachment from eight $[\text{Pb}(\text{Aa-H})\text{H}_2\text{O}]^+$ (Aa = Gly, Ala, Val, Leu, Ile, Phe, Glu, and Lys) complexes using blackbody

Table 5.5: Measured E_0 in Different Electrospray Solvent Systems

[Pb(Aa-H)H ₂ O] ⁺ Complex	Master Equation E_0 (kJ mol ⁻¹) (50/50 18.2 MΩ H ₂ O/MeOH)	Master Equation E_0 (kJ mol ⁻¹) (50/50 18.2 MΩ H ₂ O/MeCN)
Gly	110.1 +/- 16.9	105.3 +/- 23.8
Ala	102.9 +/- 5.3	99.3 +/- 16.8
Val	102.9 +/- 1.9	102.9 +/- 1.7
Leu	101.7 +/- 5.2	99.3 +/- 2.1
Ile	104.1 +/- 1.5	102.9 +/- 1.6
Phe	76.6 +/- 6.3	73.0 +/- 3.8
Lys	95.7 +/- 6.3	95.7 +/- 1.2
Glu	76.6 +/- 1.5	77.8 +/- 1.2

infrared radiative dissociation. The determined water binding energies should be equivalent to the dissociation energies because the barrier with respect to the reverse association reaction is expected to be negligible. Since these complexes have relatively few vibrational degrees of freedom, this information was extracted from the BIRD kinetic data using a master equation analysis. The water binding energies ranged from 76.6 to 113.6 kJ mol⁻¹ and were roughly 30 – 100 % larger than the Arrhenius activation energies. This is typical of the slow-exchange limit, where dissociation of the precursor ion is fast compared to photon exchange and the observed dissociation rate constant is much lower than k_{uni} . The threshold dissociation energies were in good agreement with the 0 K dissociation energies calculated using the B3LYP/6-31+G(d,p) and MP2(full)/6-311++G(2d,2p)//B3LYP/6-31+G(d,p) methods.

The water binding energies reflect the different structural isomers of the [Pb(Aa-H)H₂O]⁺ complexes. The A-type structures (Aa = Gly, Ala, Val, Leu, and Ile) must isomerize prior to dissociation, but the threshold for isomerization is small compared to the binding energy. In contrast, water can directly dissociate from the B- (Aa = Phe, Lys) and D-type (Aa = Glu) ions. Steric and electronic considerations affect the relative binding energies of these ions. There is a link between the gas-phase basicities of the amino acids and the ability of [Pb(Aa-H)]⁺ to attach water. Amino acids with stronger basicities donate more electron density to Pb²⁺ and weaken its bond with the water oxygen. [Pb(Gly-H)H₂O]⁺ therefore has the strongest water binding energy in part because Gly is the least basic amino acid. Interactions between Pb²⁺ and the amino acid side chains can also lower the water binding energy. For example, Lys further stabilizes

Pb^{2+} through an additional interaction with the ϵ -amino group. This destabilizes the Pb^{2+} -water bond due to increased electron donation, but it also sterically hinders the water from attaching to the ion.

References

1. Fridgen, T. D. *Mass. Spectrom. Rev.* **2009**, 28, 586 - 607.
2. Eyler, J. R. *Mass. Spectrom. Rev.* **2009**, 28, 448 - 467.
3. Polfer, N. C.; Oomens, J. *Mass Spectrom. Rev.* **2009**, 28, 468 - 494.
4. Burt, M. B.; Decker, S. G. A.; Atkins, C. G.; Rowsell, M.; Peremans, A.; Fridgen T. *J. Phys. Chem. B* **2011**, 115, 11506 - 11518.
5. Atkins, C. G.; Banu, L.; Rowsell, M.; Blagojevic, V.; Bohme, D. K.; Fridgen, T. D. *J. Phys. Chem. B* **2009**, 113, 14457 - 14464.
6. Atkins, C. G.; Rajabi, K.; Gillis, E. A. L.; Fridgen, T. D. *J. Phys. Chem. A* **2008**, 112, 10220 - 10225.
7. Cagmat, E. B.; Szczepanski, J.; Pearson, W. L.; Powell, D. H.; Eyler, J. R.; Polfer, N. C. *Phys. Chem. Chem. Phys.* **2010**, 12, 3474 - 3479.
8. Bush, M. F.; O'Brien, J. T.; Prell, J. S.; Wu, C.-C.; Saykally, R. J.; Williams, E. R. *J. Am. Chem. Soc.* **2009**, 131, 13270 - 13277.
9. Bush, M. F.; O'Brien, J. T.; Prell, J. S.; Saykally, R. J.; Williams, E. R. *J. Am. Chem. Soc.* **2007**, 129, 1612 - 1622.
10. Oh, H.; Breuker, K.; Sze, S. K.; Ge, Y.; Carpenter, B. K.; McLafferty, F. W. *Proc. Natl. Acad. Sci. U.S.A.* **2002**, 99 (25), 15863.
11. Prell, J. S.; Flick, T. G.; Oomens, J.; Berden, G.; Williams, E. R. *J. Phys. Chem. A* **2010**, 114, 854 - 860.
12. Dunbar, R. C.; Polfer, N. C.; Oomens, J. *J. Am. Chem. Soc.* **2007**, 129, 14562 - 14563.
13. Armentrout, P. B.; Rodgers, M. T.; Oomens, J.; Steill, J. D. *J. Phys. Chem. A* **2008**, 112, 2248 - 2257.
14. Polfer, N. C.; Oomens, J.; Dunbar, R. C. *Phys. Chem. Chem. Phys.* **2006**, 8, 2744 - 2751.
15. Polfer, N. C.; Oomens, J.; Moore, D. T.; von Helden, G.; Meijer, G.; Dunbar, R. C. *J. Am. Chem. Soc.* **2006**, 128, 517 - 525.

16. Bush, M. F.; Oomens, J.; Saykally, R. J.; Williams, E. R. *J. Am. Chem. Soc.* **2008**, *130*, 6463 - 6471.
17. Forbes, M. W.; Bush, M. F.; Polfer, N. C.; Oomens, J.; Dunbar, R. C.; Williams, E. R.; Jockusch, R. A. *J. Phys. Chem. A* **2007**, *111*, 11759 - 11770.
18. Lemoff, A. S.; Bush, M. F.; Williams, E. R. *J. Phys. Chem. A* **2005**, *109*, 1903 - 1910.
19. Rodgers, M. T.; Armentrout, P. B.; Oomens, J.; Steill, J. D. *J. Phys. Chem. A* **2008**, *112*, 2258 - 2267.
20. Burt, M. B.; Fridgen, T. D. *J. Phys. Chem. A*. DOI:10.1021/jp306420e. Published online: September 4, 2012.
21. Drayß, M. K.; Armentrout, P. B.; Oomens, J.; Schäfer, M. *Int. J. Mass Spectrom.* **2010**, *297*, 18 - 27.
22. Burford, N.; Eelman, M. D.; LeBlanc, W. G.; Cameron, S.; Robertson, K.N. *Chem. Commun.* **2004**, 332 - 333.
23. Burford, N.; Eelman, M. D.; LeBlanc, W. G. *Can. J. Chem.* **2004**, *82*, 1254 - 1259.
24. Patrick, L. *Altern. Med. Rev.* **2006**, *11* (1), 2 - 22.
25. Dunbar, R. C. *Mass Spectrom. Rev.* **2004**, *23*, 127 - 158.
26. Dunbar, R. C.; McMahon, T. B. *Science* **1998**, *279*, 194 - 197.
27. Price, W. D.; Williams, E. R. *J. Phys. Chem. A* **1997**, *101*, 8844 - 8852.
28. Price, W. D.; Schnier, P. D.; Jockusch, R. A.; Strittmatter, E. F.; Williams, E. R. *J. Am. Chem. Soc.* **1996**, *118*, 10640 - 10644.
29. Gilbert, R. G.; Smith, S. C., *Theory of unimolecular and recombination reactions*. Blackwell Scientific Publications: Oxford, 1990.
30. Rogalewicz, F.; Hopilliard, Y.; Ohanessian, G. *Int. J. Mass Spectrom.* **2000**, *201*, 307 - 320.
31. Hoppilliard, Y.; Rogalewicz, F.; Ohanessian, G. *Int. J. Mass Spectrom.* **2000**, *204*, 267 - 280.

32. Rogalewicz, F.; Hopilliard, Y.; Ohanessian, G. *Int. J. Mass Spectrom.* **2001**, *206*, 45 – 52.
33. Rogalewicz, F.; Hopilliard, Y.; Ohanessian, G. *Int. J. Mass Spectrom.* **2003**, *227*, 439 – 451.
34. Rajabi, K.; Easterling, M. L.; Fridgen, T. D. *J. Am. Soc. Mass Spectrom.* **2009**, *20*, 411 - 418.
35. Stevens, S. M., Jr.; Dunbar, R. C.; Price, W., D.; Sena, M.; Watson, C. H.; Nichols, L. S.; Riveros, J. M.; Richardson, D. E.; Eyler, J. R. *J. Phys. Chem. A* **2002**, *106*, 9686 - 9694.
36. Frisch, M. J.; Trucks, G. W.; Schlegel, H. B.; Scuseria, G. E.; Robb, M. A.; Cheeseman, J. R.; Scalmani, G.; Barone, V.; Mennucci, B.; Petersson, G. A.; Nakatsuji, H.; Caricato, M.; Li, X.; Hratchian, H. P.; Izmaylov, A. F.; Bloino, J.; Zheng, G.; Sonnenberg, J. L.; Hada, M.; Ehara, M.; Toyota, K.; Fukuda, R.; Hasegawa, J.; Ishida, M.; Nakajima, T.; Honda, Y.; Kitao, O.; Nakai, H.; Vreven, T.; Montgomery, J. A. Jr.; Peralta, J. E.; Ogliaro, F.; Bearpark, M.; Heyd, J. J.; Brothers, E.; Kudin, K. N.; Staroverov, V. N.; Kobayashi, R.; Normand, J.; Raghavachari, K.; Rendell, A.; Burant, J. C.; Iyengar, S. S.; Tomasi, J.; Cossi, M.; Rega, N.; Millam, J. M.; Klene, M.; Knox, J. E.; Cross, J. B.; Bakken, V.; Adamo, C.; Jaramillo, J.; Gomperts, R.; Stratmann, R. E.; Yazyev, O.; Austin, A. J.; Cammi, R.; Pomelli, C.; Ochterski, J. W.; Martin, R. L.; Morokuma, K.; Zakrzewski, V. G.; Voth, G. A.; Salvador, P.; Dannenberg, J. J.; Dapprich, S.; Daniels, A. D.; Farkas, O.; Foresman, J. B.; Ortiz, J. V.; Cioslowski, J.; Fox, D. J. *Gaussian 09, Revision A.01*; Gaussian, Inc.: Wallingford, CT, 2009.
37. Glendening, E. D.; Badenhop, J. K.; Reed, A. E.; Carpenter, J. E.; Bohmann, J. A.; Morales, C. M.; Weinhold, F. NBO 5.9. (Theoretical Chemistry Institute, U. o. W.; Madison, W., 2009); <http://www.chem.wisc.edu/~nbo5>.
38. Boys, S. F.; Bernardi, F. *Mol. Phys.* **1970**, *19*, 553.
39. Simon, S.; Duran, M.; Dannenberg, J. J. *J. Chem. Phys.* **1996**, *105* (24), 11024 - 11031.
40. Klippenstein, S. J.; Wagner, A. F.; Dunbar, R. C.; Wardlaw, D. M.; Robertson S. H. VariFlex, Version 1.00 1999, July 16.
41. Price, W. D.; Schnier, P. D.; Williams, E. R. *J. Phys. Chem. B* **1997**, *101*, 664 - 673.
42. Steinfeld, J. I.; Francisco, J. S.; Hase, W. L., *Chemical Kinetics and Dynamics*. 2nd ed.; Prentice Hall: 1999.

43. Forst, W., *Unimolecular Reactions: A Concise Introduction*. Cambridge University Press: 2003.
44. Klippenstein, S. J. *J. Chem. Phys. Lett.* **1990**, *170* (1), 71 - 77.
45. Klippenstein, S. J. *J. Chem. Phys.* **1991**, *94* (10), 6469 - 6482.
46. Klippenstein, S. J. *J. Chem. Phys.* **1992**, *96* (1), 367 - 371.
47. Klippenstein, S. J. *J. Phys. Chem.* **1994**, *98*, 11459 - 11464.
48. Robertson, S. H.; Wagner, A. F.; Wardlaw, D. M. *Faraday Discuss.* **1995**, *102*, 65 - 83.
49. Beyer, T.; Swinehart, D. F. *Commun. ACM.* **1973**, *16* (6), 379.
50. Dunbar, R. C. *J. Chem. Phys.* **1989**, *90* (12), 7369 - 7375.
51. Dunbar, R. C. *J. Chem. Phys.* **1991**, *95* (4), 2537 - 2548.
52. Dunbar, R. C. *J. Phys. Chem.* **1994**, *98*, 8705 - 8712.
53. Dunbar, R. C.; McMahon, T. B.; Thölmann, D.; Tonner, D. S.; Salahub, D. R.; Wei, D. *J. Am. Chem. Soc.* **1995**, *117*, 12819 - 12825.
54. Lin, C.-Y.; Dunbar, R. C. *J. Phys. Chem.* **1996**, *100*, 655 - 659.
55. Dunbar, R. C.; Zaniewski, R. C. *J. Chem. Phys.* **1992**, *96* (7), 5069 - 5075.
56. Jockusch, R. A.; Williams, E. R. *J. Phys. Chem. A.* **1998**, *102*, 4543 - 4550.
57. Gorman, G. S.; Speir, J. P.; Turner, C. A., Amster, I. J. *J. Am. Chem. Soc.* **1992**, *114*, 3986 - 3988.
58. Magnera, T. F.; David, D. E.; Michl, J. *J. Am. Chem. Soc.* **1989**, *111*, 4100 - 4101.
59. Glendening, E. D.; Feller, D. *J. Phys. Chem.* **1995**, *99*, 3060 - 3067.
60. Glendening, E. D.; Feller, D. *J. Phys. Chem.* **1996**, *100*, 4790 - 4797.
61. Shannon, R. D. *Acta Crystallogr. A* **1976**, *32*, 751 - 767.

62. Lemoff, A. S.; Bush, M. F.; Wu, C.-C.; Williams, E. R. *J. Am. Chem. Soc.* **2005**, *127*, 10276 - 10286.
63. Lemoff, A. S.; Bush, M. F.; Williams, E. R. *J. Am. Chem. Soc.* **2003**, *125*, 13576 - 13584.

Chapter 6

Gas-phase Structures of M^{2+} -Cationized Alanine and β -methylaminoalanine Investigated by Computational Chemistry and IRMPD Spectroscopy

6.1. Introduction. IRMPD spectroscopy and electronic structure calculations revealed that lead-cationized amino acids, which are deprotonated and of the form $[\text{Pb}(\text{Aa-H})]^+$, can adopt four of the five structures shown in Figure 6.1. A key feature of this work was that Pb^{2+} can be significantly stabilized by the presence of a functional group on the amino acid side chain. Without side-chain interactions, Pb^{2+} forms an A-type complex by binding between the amine nitrogen and carbonyl oxygen of an N-deprotonated amino acid. This is attributed to Pb^{2+} being a soft (or intermediate) Lewis acid according to hard-soft acid-base theory (HSAB), which states that Lewis acid-base complexes are stabilized by hard-hard or soft-soft interactions.^{1,2} Since NH^- is a softer base than either the NH_2 or carboxylate groups, it provides additional stabilization for Pb^{2+} that favours the formation of an A-type ion. Interactions with side chain functional groups, however, stabilize B-, C-, and D-type ions by providing a new source of electron density for Pb^{2+} . For B- and C-type ions, this extra stabilization allows deprotonation to occur at the carboxylic acid rather than the amine, and enables Pb^{2+} to bind with the carboxylate anion in the case of C-type complexes. D-type ions arise when Pb^{2+} is bound directly with the side chain, and illustrate the significant impact of amino acid basic sites on the structures of metal-cationized amino acids.

With the exception of the $[\text{Pb}(\text{Aa-H})]^+$ and $[\text{Pb}(\text{Aa-H})\text{H}_2\text{O}]^+$ complexes described

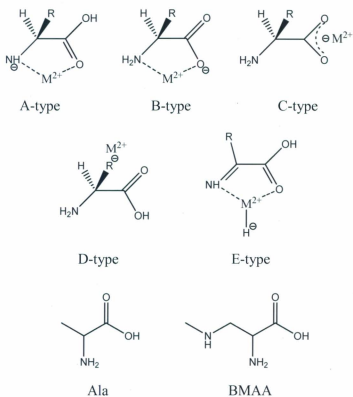


Figure 6.1: The five principle $[M(Aa-H)]^+$ isomers. Skeletal drawings of alanine and β -methylaminoalanine are also shown.

in Chapters 3 and 4, the structures of $[M(\text{Aa-H})]^+$ have not been well characterized. Prior research is limited to Atkins' use of IRMPD spectroscopy to determine that $[\text{Pb}(\text{Gly-H})]^+$ and $[\text{Pb}(\text{Gly-H})\text{H}_2\text{O}]^+$ are A-type ions (Section 2.3.1),³ as well as CID experiments performed on $[\text{Zn}(\text{Gly-H})]^+$ by Ohanessian and coworkers that revealed the existence of four possible isomers.⁴⁻⁷ Intriguingly, one of these $[\text{Zn}(\text{Gly-H})]^+$ structures, the E-type isomer in Figure 6.1, is distinct from those observed for the $[\text{Pb}(\text{Aa-H})]^+$ complexes. E-type $[\text{Zn}(\text{Gly-H})]^+$ ions have the metal ion bound in the same position as A- and B-type structures but appear to result from the A-type structure undergoing a β -hydride transfer reaction that produces a Zn-H bond. It's clear then, that the IRMPD-determined $[\text{Pb}(\text{Aa-H})]^+$ complexes described earlier do not represent the full range of possible $[M(\text{Aa-H})]^+$ isomers.

In order to develop a broader understanding of $[M(\text{Aa-H})]^+$ complexes, this chapter describes the structural determination of $[M(\text{Ala-H})]^+$ ($M^{2+} = \text{Be}^{2+}, \text{Mg}^{2+}, \text{Ca}^{2+}, \text{Sr}^{2+}, \text{Ba}^{2+}, \text{and Zn}^{2+}$) ions by IRMPD spectroscopy and electronic structure calculations.^{8,9} This method has previously been used to analyze several $[M(\text{Aa})]^{+2+}$ complexes, but no $[M(\text{Aa-H})]^+$ structures with alkaline earth metals have been studied.^{3,10-20} The most similar examples are a series of $[\text{Ba}(\text{Aa})]^{2+}$ complexes involving proline, valine, serine, arginine, glutamine, and tryptophan that were determined by IRMPD spectroscopy to form salt bridges.¹⁹ Density functional theory calculations have also suggested that zwitterionic structures become more stable with increasing cation size. $[\text{M}(\text{Trp})]^{2+}$, for example, adopts a charge-solvated structure with Be^{2+} and Mg^{2+} , but

produces zwitterions with Ca^{2+} , Sr^{2+} , and Ba^{2+} .¹⁸ A similar pattern was predicted for $[\text{M}(\text{Gly})]^{2+}$ ions, but suggests that $[\text{Mg}(\text{Gly})]^{2+}$ is also zwitterionic.^{21,22}

Each of the $[\text{Ba}(\text{Aa})]^{2+}$ ions described above bind Ba^{2+} between the oxygen atoms of a carboxylate anion, and are further stabilized by side-chain functional groups in the cases of $[\text{Ba}(\text{Arg})]^{2+}$, $[\text{Ba}(\text{Gln})]^{2+}$, and $[\text{Ba}(\text{Trp})]^{2+}$. These interactions appear to preferentially stabilize charge-solvated structures, suggesting that smaller alkaline earth metal complexes may form nonzwitterionic tautomers. In order to further explore the nature of side chain interactions in $[\text{M}(\text{Aa-H})]^+$ ions, M^{2+} (including Pb^{2+}) complexes with the non-proteinogenic amino acid β -methylaminoalanine (BMAA) will also be considered. BMAA is a particularly interesting candidate for study because it has been linked with the development of amyotrophic lateral sclerosis/Parkinsonism-dementia (ALS/PD).²³⁻²⁷ BMAA excessively activates the glutamate neurotransmitter in the presence of bicarbonate; this degenerates neurons and leads to cell death. It is also known to have a strong binding affinity for Zn^{2+} .²⁴ Determining the structures of $[\text{M}(\text{BMAA-H})]^+$ complexes is therefore biologically relevant, and will help determine the influence of metal cations and side-chain functional groups on amino acid structure.

6.2. Methods

6.2.1. Ion Generation and Activation. Gas-phase $[\text{Sr}(\text{Ala-H})]^+$, $[\text{Ba}(\text{Ala-H})]^+$, $[\text{Sr}(\text{BMAA-H})]^+$, $[\text{Ba}(\text{BMAA-H})]^+$, and $[\text{Pb}(\text{BMAA-H})]^+$ were prepared from 50/50 solutions of methanol (99.8%, ACP Chemicals) and 18.2 M Ω water (Millipore) using electrospray ionization. The Sr^{2+} and Ba^{2+} solutions contained 2.5 mM SrCl_2 or BaCl_2 and

5 mM Ala (Nutritional Biochemicals) or BMAA; $[\text{Pb}(\text{BMAA-H})]^+$ was generated from a solution comprised of 0.1 mM $\text{Pb}(\text{NO}_3)_2$ (> 99%, Fluka Chemika) and 0.1 mM BMAA. Each solution was introduced into the Apollo II ion source of a Bruker Apex Qe 7 T Fourier transform ion cyclotron resonance (FT-ICR) mass spectrometer at a flow rate of 100 – 150 $\mu\text{L h}^{-1}$. The voltage across the capillary exit was 294 V, and the ions were allowed to accumulate in the ion source for 10^{-3} – 1 s before being accelerated through a quadrupole mass filter into a hexapole collision cell. $[\text{M}(\text{Aa-H})\text{H}_2\text{O}]^+$ ions were produced in this region by minimizing the collision gas (Ar) flow and adding 10^{-2} mbar of water vapour from a degassed solvent reservoir.²⁸ The bare and hydrated ions were then trapped for 1.0 – 2.0 s before being accelerated into the ICR cell for isolation.

Infrared multiple photon dissociation (IRMPD) spectroscopy was performed on the ions trapped in the ICR cell by irradiating them between 3200 – 3800 cm^{-1} in 1.5 cm^{-1} steps for 1 – 2 s using the tunable potassium titanyl phosphate optical parametric oscillator (KTP OPO) described in Chapter 2. Four mass spectra were averaged per step. The radiation produced by the OPO enters the ICR cell through a path free of CO_2 and H_2O vapour and is focused towards the orbiting ion packet. To facilitate dissociation, the temperature of the cell was thermalized at ~360 K using a heating jacket that surrounds the ICR cell. The IRMPD spectra were then acquired by plotting the IRMPD yield, which is the base 10 logarithm of the normalized precursor ion intensity, against the wavenumber of the output of the OPO.

6.2.2. Calculations. Gaussian 09 was used to determine the minimum energy structures of the $[M(\text{Aa-H})]^+$ and $[M(\text{Aa-H})\text{H}_2\text{O}]^+$ complexes by a two step process:²⁹ geometry optimizations and harmonic frequency calculations were performed on a series of potential isomers using B3LYP/6-31+G(d,p) density functional theory; and single point energy calculations were carried out on the B3LYP-optimized structures using MP2(full)/6-311++G(2d,2p) in order to determine their relative 298 K enthalpies and Gibbs energies. It should be noted that the LANL2DZ basis set with relativistic core potential was applied to Sr, Ba, and Pb, but the 6-31+G(d,p) and 6-311++G(2d,2p) basis sets were used for all other atoms. Six to seventy-one possible structures were prepared for each complex, but only a selection of the lowest energy complexes are presented here. These isomers differ by the site of metal chelation, deprotonation, and the degree of intramolecular hydrogen bonding. Bond and torsional angles were also altered in order to reduce molecular strain. Computed infrared spectra were compared with experimental IRMPD spectra by scaling the calculated vibrational modes by 0.955.^{3,30,31} In each case, energy minima were verified by the absence of any imaginary frequencies.

6.3. Results and Discussion

6.3.1. IRMPD Spectroscopy of $[M(\text{Ala-H})]^+$, $[M(\text{Ala-H})\text{H}_2\text{O}]^+$, and $[M(\text{BMAA-H})]^+$.

Five metal-cationized amino acids were generated in the gas phase with sufficient intensity to perform IRMPD spectroscopy: $[\text{Sr}(\text{Ala-H})]^+$, $[\text{Ba}(\text{Ala-H})]^+$, $[\text{Sr}(\text{BMAA-H})]^+$, $[\text{Ba}(\text{BMAA-H})]^+$, and $[\text{Pb}(\text{BMAA-H})]^+$. These ions do not dissociate when irradiated by light from a KTP/OPO between 3200 – 3800 cm^{-1} , and efforts to induce fragmentation by

raising the temperature of the ICR cell from room temperature to 360 K were unsuccessful. To circumvent this issue, the complexes were singly hydrated in the hexapole collision cell. This method was used in Chapter 4 to help confirm the structure of $[\text{Pb}(\text{Phe-H})]^+$, and requires that the energy necessary for solvent removal be lower than the dissociation threshold of the bare complex; this was the case for the $[\text{Pb}(\text{Aa-H})\text{H}_2\text{O}]^+$ complexes described earlier, as was demonstrated by their loss of H_2O upon BIRD- or IRMPD activation.

At the time of writing, the only complex to be successfully hydrated was $[\text{Ba}(\text{Ala-H})]^+$. $[\text{Ba}(\text{Ala-H})\text{H}_2\text{O}]^+$ loses H_2O when irradiated between 3200 – 3800 cm^{-1} , and its IRMPD spectrum is shown in Figure 6.2. The spectrum contains one band in the O-H stretching region at 3715 cm^{-1} that is in a similar position to the PbO-H stretches exhibited by several $[\text{Pb}(\text{Aa-H})\text{H}_2\text{O}]^+$ (Aa = Pro, Gly, Ala, Val, Leu, Ile, and Lys) complexes. This peak is consequently assigned as a BaO-H stretch, and suggests that one of the water protons has transferred to the amino acid; it is difficult to tell from the IRMPD spectrum, however, whether or not the proton has completely transferred to an amino acid basic site due to the lack of identifiable peaks in the N-H stretching region. The fact that no peaks are observed over this range may be due to the existence of an intramolecular hydrogen bond, as was the case for $[\text{Pb}(\text{Pro-H})\text{H}_2\text{O}]^+$ and $[\text{Pb}(\text{Lys-H})\text{H}_2\text{O}]^+$ in Chapter 3, but could also mean that they are simply too weak to see. The absence of a second O-H stretch indicates that the proton is likely donated to the amine group. A-type $[\text{Pb}(\text{Aa-H})\text{H}_2\text{O}]^+$ ions were confirmed by the presence of a carboxylic acid

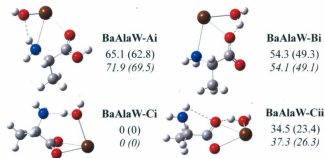
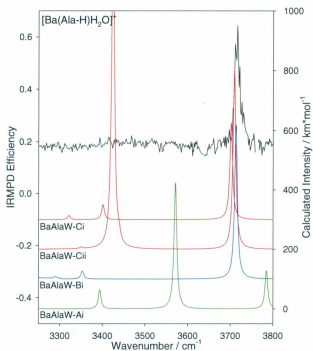


Figure 6.2: The IRMPD spectrum of $[\text{Ba}(\text{Ala-H})\text{H}_2\text{O}]^+$ (black) compared with four computed IR spectra. The computed spectra are from the B3LYP/6-31+G(d,p) optimized structures of BaAlaW-Ai, -Bi, -Ci, and -Cii. The 298 K relative enthalpies and Gibbs energies (in parentheses) have units of kJ mol^{-1} and are provided at the B3LYP/6-31+G(d,p) (top) and MP2(full)/6-311++G(2d,2p) (bottom and italicized) levels of theory. In both cases, the LANL2DZ basis set with effective core potential was applied to Ba^{2+} .

O-H stretch at 3560 cm^{-1} , since a similar band does not exist in the spectrum of $[\text{Ba}(\text{Ala}-\text{H})\text{H}_2\text{O}]^+$, the complex is likely carboxyl-deprotonated.

The experimental IRMPD spectrum in Figure 6.2 is also compared with computed IR spectra derived from four $[\text{Ba}(\text{Ala}-\text{H})\text{H}_2\text{O}]^+$ isomers. The lowest energy isomer, BaAlaW-Ci, is a C-type ion with a hydrogen bond between the water and amine moieties. This structure is 69.5 and 49.1 kJ mol^{-1} more stable than the lowest energy A- and B-type ions, BaAlaW-Ai and -Bi, respectively. BaAlaW-Ai can be spectroscopically eliminated by its prediction of a carboxylic acid O-H stretch at 3570 cm^{-1} , but BaAlaW-Ci and -Bi are both consistent with the IRMPD spectrum. Each of the two complexes explains the absence of a second O-H stretch as the result of an intramolecular hydrogen bond; the proton transfers to the amine group in BaAlaW-Ci and to the carboxylate moiety in BaAlaW-Bi. Both structures also predict weak N-H stretches, which is in keeping with their absence in the IRMPD spectrum. Although these two ions cannot be distinguished spectroscopically, BaAlaW-Bi is significantly higher in energy than BaAlaW-Ci and is 22.8 kJ mol^{-1} less stable than a second C-type isomer, BaAlaW-Cii, that can be disregarded based on its prediction of an intense N-H stretch at 3425 cm^{-1} . BaAlaW-Bi therefore does not likely form a significant part of the gas-phase population, and $[\text{Ba}(\text{Ala}-\text{H})\text{H}_2\text{O}]^+$ is consequently assigned as BaAlaW-Ci.

6.3.2. Computational Comparisons of $[\text{M}(\text{Ala}-\text{H})]^+$ and $[\text{M}(\text{BMAA}-\text{H})]^+$ Complexes.

In Chapters 3 and 4, IRMPD spectroscopy of $[\text{Pb}(\text{Aa}-\text{H})\text{H}_2\text{O}]^+$ complexes demonstrated that their structures are generally the hydrated counterparts of their bare forms where

water attaches to Pb^{2+} . One exception was $[\text{Pb}(\text{Pro-H})\text{H}_2\text{O}]^+$, which isomerizes from an A- to C-type ion upon hydration. $[\text{Pb}(\text{Ala-H})\text{H}_2\text{O}]^+$ and $[\text{Pb}(\text{Ala-H})]^+$, by contrast, are both A-type complexes. The C-type $[\text{Pb}(\text{Ala-H})\text{H}_2\text{O}]^+$ and $[\text{Pb}(\text{Pro-H})\text{H}_2\text{O}]^+$ isomers are 4.5 and 14.4 kJ mol^{-1} more favourable than their lowest energy A-type structures at the MP2(full)/6-311++G(2d,2p)/B3LYP/6-31+G(d,p) level of theory (LANL2DZ was used for Pb), while their A-type bare ions are $\sim 25 \text{ kJ mol}^{-1}$ more stable than the C-type $[\text{Pb}(\text{Aa-H})]^+$ structures. The reason that $[\text{Pb}(\text{Ala-H})\text{H}_2\text{O}]^+$ remains an A-type ion upon solvation while $[\text{Pb}(\text{Pro-H})\text{H}_2\text{O}]^+$ isomerizes was attributed to $[\text{Pb}(\text{Ala-H})\text{H}_2\text{O}]^+$ requiring 84.2 kJ mol^{-1} more Gibbs energy to change lead's binding site than $[\text{Pb}(\text{Pro-H})\text{H}_2\text{O}]^+$ (Figure 3.14).

$[\text{Ba}(\text{Ala-H})\text{H}_2\text{O}]^+$ is significantly more stable, 49.1 – 69.5 kJ mol^{-1} , as a C-type structure than as an A- or B-type ion. Unlike $[\text{Pb}(\text{Ala-H})]^+$ and $[\text{Pb}(\text{Pro-H})]^+$ however, the most favourable $[\text{Ba}(\text{Ala-H})]^+$ isomer is also a C-type ion. The lowest energy A-, B-, C-, and E-type structures of $[\text{Ba}(\text{Ala-H})]^+$ are shown in Figure 6.3. The most stable C-type structure, BaAla-Ci, is 104.9, 36.2, and 207.8 kJ mol^{-1} lower in energy than the A-, B-, and E-type ions, respectively. It's likely then, that $[\text{Ba}(\text{Ala-H})\text{H}_2\text{O}]^+$ is generated by hydrating a C-type $[\text{Ba}(\text{Ala-H})]^+$ complex rather than through isomerization of a hydrated structure. Gas-phase $[\text{Ba}(\text{Ala-H})]^+$ is therefore expected to have a C-type structure.

Geometry optimizations and single point energy calculations were also performed on $[\text{M}(\text{Ala-H})]^+$ complexes involving Be^{2+} , Mg^{2+} , Ca^{2+} , Sr^{2+} , and Zn^{2+} . The lowest energy isomers are collected in Figure D1 in Appendix D, and their relative MP2(full)/6-

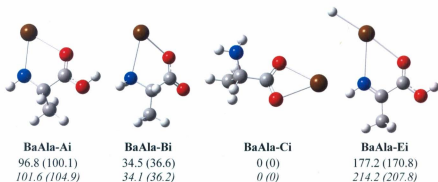


Figure 6.3: The B3LYP/6-31+G(d,p) optimized structures of $[\text{Ba}(\text{Ala-H})]^+$. The 298 K relative enthalpies and Gibbs energies (in parentheses) are provided at the B3LYP/6-31+G(d,p) (top) and MP2(full)/6-311++G(2d,2p) (bottom and italicized) levels of theory. Note that the LANL2DZ basis set with effective core potential was applied to Ba^{2+} for both levels of calculation.

311+G(2d,2p)//B3LYP/6-31+G(d,p) Gibbs energies are summarized in Figure 6.4. The computed results suggest that $[\text{Be}(\text{Ala-H})]^+$ and $[\text{Mg}(\text{Ala-H})]^+$ form B-type ions, whereas $[\text{Ca}(\text{Ala-H})]^+$, $[\text{Sr}(\text{Ala-H})]^+$, and $[\text{Ba}(\text{Ala-H})]^+$ adopt C-type isomers. $[\text{Zn}(\text{Ala-H})]^+$ is expected to be an E-type ion, and $[\text{Pb}(\text{Ala-H})]^+$ was shown in Chapter 3 to be an A-type ion. In Figure 6.4, $\Delta G_{\text{SB-CS}}$ is the MP2-derived Gibbs energy difference between the salt bridge (C-type) and charge-solvated (B-type) ions, and the metals are arranged in order of decreasing chemical hardness. Values for the difference in Gibbs energy between the C- and E-type $[\text{Zn}(\text{Ala-H})]^+$ ions, as well as between the C- and A-type $[\text{Pb}(\text{Ala-H})]^+$ complexes are also shown to demonstrate the stability of their lowest energy isomers with respect to their B-type structures. The B-type alkaline earth metal complexes become more stable as the hardness of the metal cation increases from Be^{2+} to Ba^{2+} . This is the opposite of the trend predicted by HSAB theory. In the case of alanine, the carboxylate anion of the C-type complexes is harder than the corresponding M^{2+} binding sites of the B-type ions, but C-type ions are only observed with the softer cations. This indicates that the most stable structures of the $[\text{M}(\text{Ala-H})]^+$ complexes cannot be justified based solely on their chemical hardness.

$\Delta G_{\text{SB-CS}}$ is also shown as a function of ion size in Figure 6.5. The effective ionic radii of the M^{2+} ions decrease as $\text{Ba}^{2+} > \text{Pb}^{2+} \approx \text{Sr}^{2+} > \text{Ca}^{2+} > \text{Zn}^{2+} \approx \text{Mg}^{2+} > \text{Be}^{2+}$.³² B-type ions become less stable as the size of the metal cation increases. This tendency is consistent with similar trends determined for alkali metal complexes ($[\text{M}(\text{Aa})]^+$) with serine, arginine, and lysine, and is credited to the metal cation being more difficult to

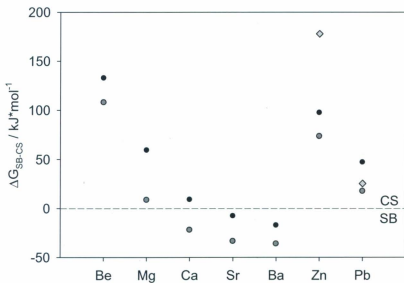


Figure 6.4: The difference in MP2(full)/6-311++G(2d,2p)//B3LYP/6-31+G(d,p) Gibbs energy (ΔG_{SB-CS}) between salt-bridge (C-type) and charge-solvated (B-type) $[M(\text{Aa-H})]^+$ isomers as a function of decreasing chemical hardness. $[M(\text{Ala-H})]^+$ and $[M(\text{BMAA-H})]^+$ complexes are represented by ◐ and ● respectively. Also shown are the ΔG_{SB-CS} values for the E-type $[\text{Zn}(\text{Ala-H})]^+$ and A-type $[\text{Pb}(\text{Ala-H})]^+$ structures relative to their C-type isomers (◐).

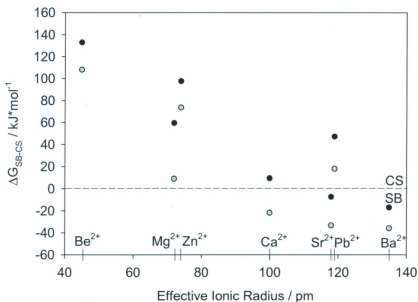


Figure 6.5: The difference in MP2(full)/6-311++G(2d,2p)/B3LYP/6-31+G(d,p) Gibbs energy (ΔG_{SB-CS}) between salt-bridge (C-type) and charge-solvated (B-type) $[\text{M}(\text{Aa-H})]^+$ isomers as a function of the effective ionic radius of the metal cation.³² $[\text{M}(\text{Ala-H})]^+$ and $[\text{M}(\text{BMAA-H})]^+$ complexes are represented by ● and ○ respectively.

charge solvate due to steric effects.^{10,13,17,33} Among the alkaline earth metals, this is reflected by the increasing stability of C-type ions from Be^{2+} to Ba^{2+} . Since carboxylate anions are relatively harder than the basic sites of the B-type ions, the metal interaction in C-type complexes is more electrostatic in nature and is therefore less reliant on charge solvation for stability.

The B-type $[\text{Zn}(\text{Aa-H})]^+$ and $[\text{Pb}(\text{Aa-H})]^+$ complexes are more stable than the effective ionic radii of their metal cations would suggest. This can be attributed to the relative softness of Zn^{2+} and Pb^{2+} compared to similarly sized alkaline earth metal cations (Mg^{2+} and Sr^{2+}). Both metals are intermediate (or borderline soft in the case of Pb) Lewis acids, and are preferentially stabilized by the softer binding sites of B-type ions as a consequence. In the case of $[\text{Pb}(\text{Ala-H})]^+$, Pb^{2+} is soft enough to be stabilized by the NH group rather than the intact amine.^{1,2} Chapter 3 demonstrated that this stabilization is sufficient to overcome the energy required to deprotonate the amine group, and results in $[\text{Pb}(\text{Ala-H})]^+$ forming an A-type complex.

The most stable structure of $[\text{Zn}(\text{Ala-H})]^+$ is computed to be an E-type ion, and this isomer is 110.3 and 104.5 kJ mol^{-1} more stable than the analogous A- and B-type structures. A detailed investigation into the mechanism for E-type ion formation is beyond the scope of this thesis, but the simplest explanation is that $[\text{Zn}(\text{Ala-H})]^+$ results from a β -hydride transfer between the α -carbon of an A-type complex and the metal cation.^{4,5} This reaction is made possible by Zn^{2+} having an empty valence s -orbital, and the same reasoning can be used to explain the relative stability of the E-type $[\text{Be}(\text{Ala-H})]^+$ and $[\text{Mg}(\text{Ala-H})]^+$ complexes since alkaline earth metal cations also have empty

valence *s*-orbitals.¹⁴ The B-type [Be(Ala-H)]⁺ ion, for example, is only 9.2 and 12.4 kJ mol⁻¹ more stable than its E- and A-type isomers, respectively, whereas the A-type [Pb(Ala-H)]⁺ complex is 87.7 kJ mol⁻¹ lower in energy than the E-type structure. This can be explained by Pb²⁺ having an inert pair of electrons in its 6*s* orbital (Section 1.3) that prevent the hydride transfer. The E-type [Ca(Ala-H)]⁺, [Sr(Ala-H)]⁺, and [Ba(Ala-H)]⁺ ions decrease in stability with respect to the B-type structures as the size of the cation increases. Since larger metal cations are less efficiently charge solvated by the basic sites of B-type ions, this is likely a consequence of the growing distance between the cation and the β-hydrogen.

Figures 6.4 and 6.5 also contain the relative energies of seven [M(BMAA-H)]⁺ ions (M²⁺ = Be²⁺, Mg²⁺, Ca²⁺, Sr²⁺, Ba²⁺, Zn²⁺, and Pb²⁺). The lowest energy isomers of these complexes can be found in Figure D2, and five representative isomers of [Ba(BMAA-H)]⁺ are shown in Figure 6.6. The relative stabilities of these complexes follow a similar trend to the [M(Ala-H)]⁺ ions, however, Δ*G*_{SB-CS} is more positive in every case. This demonstrates that the secondary amine group of BMAA's side chain provides additional stabilization to the metal cation that preferentially stabilizes the B-type isomers over the C-type complexes. In the case of [Ca(BMAA-H)]⁺, for example, the additional electron donation makes the B-type structure the most favoured, whereas [Ca(Ala-H)]⁺ is predicted to be a C-type ion.

[Pb(BMAA-H)]⁺ and [Zn(BMAA-H)]⁺ also adopt different isomers than their [M(Ala-H)]⁺ counterparts. The lowest energy isomer of [Pb(BMAA-H)]⁺ is a B-type ion

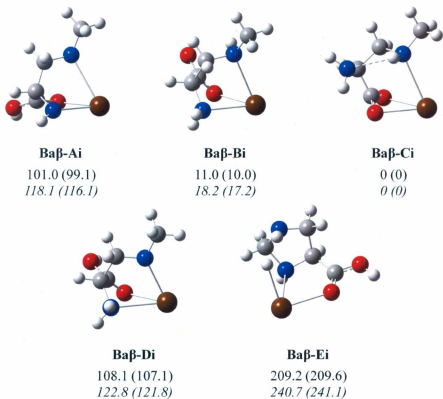


Figure 6.6: The B3LYP/6-31+G(d,p) optimized structures of $[\text{Ba}(\text{BMAA-H})]^+$. The 298 K relative enthalpies and Gibbs energies (in parentheses) are provided at the B3LYP/6-31+G(d,p) (top) and MP2(full)/6-311++G(2d,2p) (bottom and italicized) levels of theory. Note that the LANL2DZ basis set with effective core potential was applied to Ba^{2+} for both levels of calculation.

that is 34.3 kJ mol^{-1} more favourable than the most stable A-type structure. That a B-type ion is predicted for $[\text{Pb}(\text{BMAA-H})]^+$ instead of an A-type can be attributed to the extra stabilization of Pb^{2+} by the side chain NH group. This enables deprotonation at the carboxylic acid and stabilizes the B-type $[\text{Pb}(\text{BMAA-H})]^+$ complex. The most stable structure of $[\text{Zn}(\text{BMAA-H})]^+$ is also a B-type ion, but a nearly isoenergetic E-type complex was also found. In this case, the side-chain interaction between Zn^{2+} and the β -methylamine nitrogen facilitates a β -hydride transfer from the side-chain methyl group to the metal cation. This results in the formation of the Zn-H bond, and also causes the amino acid side chain to produce a five-membered ring with the terminal NH group. The B-type ion is likely more stable than the E-type structure due to the additional stabilization of the metal cation provided by the side chain. The increased electron density on the metal center diminishes the likelihood of a hydride transfer, and also explains why the E-type $[\text{Be}(\text{BMAA-H})]^+$ and $[\text{Mg}(\text{BMAA-H})]^+$ complexes are significantly higher in energy, 123.5 and $115.8 \text{ kJ mol}^{-1}$ respectively, than their B-type structures.

The structures of the $[\text{M}(\text{Ala-H})]^+$ and $[\text{M}(\text{BMAA-H})]^+$ complexes are therefore controlled by the size of the cation, its chemical hardness, and the presence of additional basic sites on the amino acid side chain. This latter point was seen to preferentially stabilize B-type complexes in Chapters 3 and 4, and is responsible for the increased stability of the $[\text{M}(\text{BMAA-H})]^+$ complexes with respect to the $[\text{M}(\text{Ala-H})]^+$ ions. It is the size of the metal cation, however, that has the most significant structural impact. Large

cations are less effectively stabilized by the basic sites of B-type ions than small ones, and C-type ions become more stable with increasing ion size as a consequence.

6.3.3. Computed Structures of $[\text{Ba}(\text{BMAA-H})\text{H}_2\text{O}]^+$. In order to better compare alanine and β -methylaminoalanine, potential isomers of $[\text{Ba}(\text{BMAA-H})\text{H}_2\text{O}]^+$ were also analysed computationally. Eight $[\text{Ba}(\text{BMAA-H})\text{H}_2\text{O}]^+$ structures are compared in Figure 6.7. The most stable structure, Ba β W-Ci, is a C-type ion that is stabilized by an intramolecular hydrogen bond with the side chain amino group. This configuration is 1.0 and 29.5 kJ mol⁻¹ more stable than two similar C-type isomers, Ba β W-Cii and -Ciii, that form hydrogen bonds with the carbonyl oxygen and terminal amine moieties. Ba β W-Ci is also 49.9 – 61.6 kJ mol⁻¹ lower in energy than the most stable A- and D-type structures, but is nearly isoenergetic with the most favourable B-type structure, Ba β W-Bi. This is a much smaller energy difference than what was predicted for the analogous $[\text{Ba}(\text{Ala-H})]^+$ complexes, and demonstrates the stabilizing effect of BMAA's secondary amine. These results, combined with the calculations performed on the $[\text{Ba}(\text{BMAA-H})]^+$ described above, predict that $[\text{Ba}(\text{BMAA-H})\text{H}_2\text{O}]^+$ is a C-type ion formed by hydrating a C-type complex. It is therefore expected to be virtually identical to the case of $[\text{Ba}(\text{Ala-H})\text{H}_2\text{O}]^+$, with the exception that the intramolecular hydrogen bond forms between water and the secondary amine, rather than the terminal amine group.

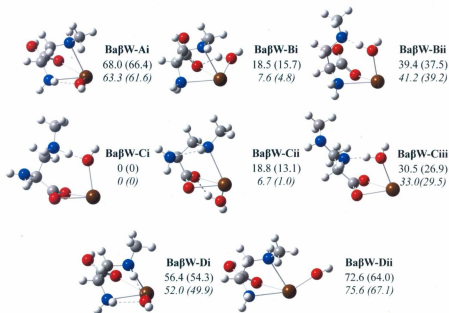


Figure 6.7: The B3LYP/6-31+G(d,p) optimized structures of $[\text{Ba}(\text{BMAA-H})\text{H}_2\text{O}]^+$. The 298 K relative enthalpies and Gibbs energies (in parentheses) are provided at the B3LYP/6-31+G(d,p) (top) and MP2(full)/6-311++G(2d,2p) (bottom and italicized) level of theories. Note that the LANL2DZ basis set with effective core potential was applied to Ba^{2+} for both levels of calculation.

6.4. Conclusions. $[\text{Sr}(\text{Ala-H})]^+$, $[\text{Ba}(\text{Ala-H})]^+$, $[\text{Sr}(\text{BMAA-H})]^+$, $[\text{Ba}(\text{BMAA-H})]^+$, and $[\text{Pb}(\text{BMAA-H})]^+$ were generated in the gas phase by electrospray ionization but were either too strongly bound to perform IRMPD spectroscopy using a KTP/OPO or no absorption occurred. Hydrating these complexes also proved to be difficult, but an IRMPD spectrum of $[\text{Ba}(\text{Ala-H})\text{H}_2\text{O}]^+$ was acquired that confirmed its structure to be a C-type ion where one of the water hydrogen atoms forms an intramolecular hydrogen bond with alanine's amine group.

In order to reveal further information about the $[\text{M}(\text{Ala-H})]^+$ and $[\text{M}(\text{BMAA-H})]^+$ complexes, geometry optimizations and single-point energy calculations were carried out using the B3LYP/6-31+G(d,p)//MP2(full)/6-311++G(2d,2p) method (LANL2DZ was applied to Sr, Ba, and Pb). These calculations predict that $[\text{Ba}(\text{Ala-H})\text{H}_2\text{O}]^+$ is formed by hydrating a C-type $[\text{Ba}(\text{Ala-H})]^+$ complex. This is similar to the $[\text{Pb}(\text{Aa-H})\text{H}_2\text{O}]^+$ complexes shown in Chapters 3 and 4, which generally have the same type of structure as their bare forms. Additional electronic structure calculations on $[\text{Ba}(\text{BMAA-H})\text{H}_2\text{O}]^+$ demonstrated that both it and $[\text{Ba}(\text{BMAA-H})]^+$ are also expected to have C-type structures. The lowest energy structure of $[\text{Ba}(\text{BMAA-H})\text{H}_2\text{O}]^+$ is similar to that of $[\text{Ba}(\text{Ala-H})\text{H}_2\text{O}]^+$, but its hydrogen bond is between the water hydrogen and the secondary amine group.

The computed structures of the $[\text{M}(\text{Aa-H})]^+$ complexes revealed that the M^{2+} binding site depends primarily on the size of the metal cation. Among the $[\text{M}(\text{Ala-H})]^+$ ions, Be^{2+} , Mg^{2+} , Zn^{2+} , and Pb^{2+} are predicted to have charge-solvated isomers, while Ca^{2+} , Sr^{2+} , and Ba^{2+} form salt bridge structures. This demonstrates that large cations are

less effectively stabilized by the basic sites of charge-solvated ions, and that salt bridges become more favourable with increasing ion size. There is also a secondary trend among ions with similar ionic radii that indicates that the softer cation is better at stabilizing charge-solvated structures. This occurs because NH^+ and NH_2 are softer bases than carboxylate anions and will provide extra stabilization to softer cations. Another factor to consider is M^{2+} stabilization by the amino acid side chain. The $[\text{M}(\text{BMAA-H})]^+$ ions, for example, follow the same pattern as the $[\text{M}(\text{Ala-H})]^+$ complexes, but their B-type isomers are preferentially stabilized by a side-chain interaction between the metal cation and secondary amine. The structures of $[\text{M}(\text{Aa-H})]^+$ complexes therefore depend on several competing factors: the size of the cation, its chemical hardness, and the presence or absence of functional groups on the amino acid side chain.

References

1. Parr, R. G.; Pearson, R. G., *J. Am. Chem. Soc.* **1983**, *105*, 7512 - 7516.
2. Pearson, R. G., *Inorg. Chem.* **1988**, *27*, 734 - 740.
3. Atkins, C. G.; Banu, L.; Rowsell, M.; Blagojevic, V.; Bohme, D. K.; Fridgen, T. D., *J. Phys. Chem. B* **2009**, *113*, 14457 - 14464.
4. Rogalewicz, F.; Hopilliard, Y.; Ohanessian, G. *Int. J. Mass Spectrom.* **2000**, *201*, 307 - 320.
5. Hoppilliard, Y.; Rogalewicz, F., Ohanessian, G. *Int. J. Mass Spectrom.* **2000**, *204*, 267 - 280.
6. Rogalewicz, F.; Hopilliard, Y.; Ohanessian, G. *Int. J. Mass Spectrom.* **2001**, *206*, 45 - 52.
7. Rogalewicz, F.; Hopilliard, Y.; Ohanessian, G. *Int. J. Mass Spectrom.* **2003**, *227*, 439 - 451.
8. Fridgen, T. D. *Mass. Spectrom. Rev.* **2009**, *28*, 586 - 607.
9. Polfer, N. C.; Oomens, J. *Mass Spectrom. Rev.* **2009**, *28*, 468 - 494.
10. Armentrout, P. B.; Rodgers, M. T.; Oomens, J.; Steill, J. D., *J. Phys. Chem. A* **2008**, *112*, 2248 - 2257.
11. Rodgers, M. T.; Armentrout, P. B.; Oomens, J.; Steill, J. D., *J. Phys. Chem. A* **2008**, *112*, 2258 - 2267.
12. Kapota, C.; Lemaire, J.; Maitre, P.; Ohanessian, G., *J. Am. Chem. Soc.* **2004**, *126*, 1836 - 1842.
13. Bush, M. F.; Forbes, M. W.; Jockusch, R. A.; Oomens, J.; Polfer, N. C.; Saykally, R. J.; Williams, E. R., *J. Phys. Chem. A* **2007**, *111*, 7753 - 7760.
14. Polfer, N. C.; Oomens, J.; Moore, D. T.; Helden, G. v.; Meijer, G.; Dunbar, R. C., *J. Am. Chem. Soc.* **2006**, *128*, 517 - 525.
15. Polfer, N. C.; Oomens, J., Dunbar, R. C., *Phys. Chem. Chem. Phys.* **2006**, *8*, 2744 - 2751.

16. Kamariotis, A.; Boyarkin, O. V.; Mercier, S. R.; Beck, R. D.; Bush, M. F.; Williams, E. R.; Rizzo, T. R., *J. Am. Chem. Soc.* **2006**, *128*, 905 - 916.
17. Drayß, M. K.; Armentrout, P. B.; Oomens, J.; Schäfer, M., *Int. J. Mass Spectrom.* **2010**, *297*, 18 - 27.
18. Dunbar, R. C.; Polfer, N. C.; Oomens, J., *J. Am. Chem. Soc.* **2007**, *129*, 14562 - 14563.
19. Bush, M. F.; Oomens, J.; Saykally, R. J.; Williams, E. R., *J. Am. Chem. Soc.* **2008**, *130*, 6463 - 6471.
20. O'Brien, J. T.; Prell, J. S.; Steill, J. D.; Oomens, J.; Williams, E. R., *J. Phys. Chem. A* **2008**, *112*, 10823 - 10830.
21. Remko, M.; Rode, B. M., *J. Phys. Chem. A* **2006**, *110*, 1960 - 1967.
22. Strittmatter, E. F.; Lemoff, A. S.; Williams, E. R., *J. Phys. Chem. A* **2000**, *104*, 9793 - 9796.
23. Bradley, W. G.; Mash, D. C., *Amyotroph. Lateral Scler.* **2009**, *10* (2), 7 - 20.
24. Nunn, P. B., *Amyotroph. Lateral Scler.* **2009**, *10* (2), 26 - 33.
25. Banack, S. A.; Murch, S. J., *Amyotroph. Lateral Scler.* **2009**, *10* (2), 34 - 40.
26. Vyas, K. J.; Weiss, J. H., *Amyotroph. Lateral Scler.* **2009**, *10* (2), 50 - 55.
27. Lobner, D., *Amyotroph. Lateral Scler.* **2009**, *10* (2), 56 - 60.
28. Rajabi, K.; Easterling, M. L.; Fridgen, T. D. *J. Am. Soc. Mass Spectrom.* **2009**, *20*, 411 - 418.
29. Frisch, M. J.; Trucks, G. W.; Schlegel, H. B.; Scuseria, G. E.; Robb, M. A.; Cheeseman, J. R.; Scalmani, G.; Barone, V.; Mennucci, B.; Petersson, G. A.; Nakatsuji, H.; Caricato, M.; Li, X.; Hratchian, H. P.; Izmaylov, A. F.; Bloino, J.; Zheng, G.; Sonnenberg, J. L.; Hada, M.; Ehara, M.; Toyota, K.; Fukuda, R.; Hasegawa, J.; Ishida, M.; Nakajima, T.; Honda, Y.; Kitao, O.; Nakai, H.; Vreven, T.; Montgomery, J. A. Jr.; Peralta, J. E.; Ogliaro, F.; Bearpark, M.; Heyd, J. J.; Brothers, E.; Kudin, K. N.; Staroverov, V. N.; Kobayashi, R.; Normand, J.; Raghavachari, K.; Rendell, A.; Burant, J. C.; Iyengar, S. S.; Tomasi, J.; Cossi, M.; Rega, N.; Millam, J. M.; Klene, M.; Knox, J. E.; Cross, J. B.; Bakken, V.; Adamo, C.; Jaramillo, J.; Gomperts, R.; Stratmann, R. E.; Yazyev, O.; Austin, A. J.; Cammi, R.; Pomelli, C.; Ochterski, J. W.; Martin, R. L.; Morokuma, K.; Zakrzewski, V. G.; Voth, G. A.;

Salvador, P.; Dannenberg, J. J.; Dapprich, S.; Daniels, A. D.; Farkas, O.; Foresman, J. B.; Ortiz, J. V.; Cioslowski, J.; Fox, D. J. Gaussian 09, Revision A.01; Gaussian, Inc.: Wallingford, CT, 2009.

30. Atkins, C. G.; Rajabi, K.; Gillis, E. A. L.; Fridgen, T. D., *J. Phys. Chem. A* **2008**, *112*, 10220 - 10225.
31. Burt, M. B.; Decker, S. G. A.; Atkins, C. G.; Rowsell, M.; Peremans, A.; Fridgen T. D. *J. Phys. Chem. B* **2011**, *115*, 11506 - 11518.
32. Shannon, R. D., *Acta Cryst.* **1976**, *A32*, 751 - 767.
33. Jockusch, R. A.; Price, W., D.; Williams, E. R. *J. Phys. Chem. A* **1999**, *103*, 9266 - 9274.

Chapter 7

Summary

7.1. Overview. The structures and physical properties of gas-phase ions can be determined by monitoring the effects of ion activation. IRMPD spectroscopy, for example, has been repeatedly demonstrated throughout this thesis to be capable of assigning unique structures to small ions, and was used to characterize the metal-cationized amino acids presented in Chapters 3, 4, and 6. This approach relies on comparing the IRMPD spectrum of an ion with computed IR spectra derived from putative isomers, and is most appropriate when the ion under study exhibits clearly identifiable vibrational bands.

The structures of nine Pb^{2+} -cationized amino acids (Aa = Pro, Ala, Val, Leu, Ile, Phe, Met, Lys, and Glu) were determined in Chapters 3 and 4 by acquiring their IRMPD spectra between $3200 - 3800 \text{ cm}^{-1}$. Those spectra confirmed that Pb^{2+} interacts with the amino acid conjugate bases in four ways: it can bind between the terminal amine and carboxylic acid (A- and B-type structures); lie between the two carbonyl oxygens (a C-type structure); or attach to a functional group on the amino acid side chain (a D-type structure). A-type structures are amine-deprotonated whereas B- and C-type complexes are carboxyl-deprotonated. This allows A-type ions to be spectroscopically distinguished from the other isomers by the presence of a carboxylic acid O-H stretch that appears around 3560 cm^{-1} . This band was used to confirm that the $[\text{Pb}(\text{Aa-H})]^+$ complexes with nonpolar side chains (Aa = Ala, Val, Leu, Ile, and Pro) have A-type structures, while its

absence helped indicate that $[\text{Pb}(\text{Phe-H})]^+$ and $[\text{Pb}(\text{Met-H})]^+$ are B-type ions, that $[\text{Pb}(\text{Lys-H})]^+$ is a C-type complex, and that $[\text{Pb}(\text{Glu-H})]^+$ has a D-type structure. These conclusions were supported by comparing the IRMPD spectra with computed IR spectra derived from the lowest energy isomers of each complex. In cases where it was difficult to distinguish between isomers spectroscopically, their relative 298 K enthalpies and Gibbs energies were calculated using the MP2(full)/6-311++G(2d,2p)//B3LYP/6-31+G(d,p) method (with LANL2DZ applied to Pb) in order to evaluate which structure has the largest gas-phase population.

A key feature of the above work was that Pb^{2+} can be significantly stabilized by interactions with a basic site on the amino acid side chain. $[\text{Pb}(\text{Aa-H})]^+$ complexes without side chain functional groups adopt A-type isomers whereas those with them have B-, C-, or D-type structures. This difference can be explained using hard-soft acid-base theory; Pb^{2+} is a soft Lewis acid and in the absence of additional binding sites will produce A-type complexes by preferentially binding to the NH^+ group. By contrast, side chain functional groups provide a separate source of electron density for Pb^{2+} that allows it to bind with the harder bases. This stabilizes the B-, C-, and D-type isomers observed for $[\text{Pb}(\text{Phe-H})]^+$, $[\text{Pb}(\text{Met-H})]^+$, $[\text{Pb}(\text{Lys-H})]^+$, and $[\text{Pb}(\text{Glu-H})]^+$.

The ability of side-chain interactions to stabilize metal cations was further explored in Chapter 6, where the most stable $[\text{M}(\text{Ala-H})]^+$ and $[\text{M}(\text{BMAA-H})]^+$ isomers ($\text{M}^{2+} = \text{Be}^{2+}$, Mg^{2+} , Ca^{2+} , Sr^{2+} , Ba^{2+} , Zn^{2+} , and Pb^{2+}) were predicted using computational chemistry. These calculations suggest that $[\text{M}(\text{BMAA-H})]^+$ complexes are stabilized by an additional interaction between the metal cation and the secondary amine on the side

chain of BMAA, and that they are more stable as charge solvated isomers than the $[M(\text{Ala-H})]^+$ complexes.

Chapter 6 also demonstrated that the size of the metal cation has a greater impact on the structure of $[M(\text{Ala-H})]^+$ and $[M(\text{BMAA-H})]^+$ complexes than its chemical hardness. C-type isomers become more stable as the size of the metal cation is increased, and this was attributed to the softer basic sites becoming less efficient at charge solvating larger metals. When the cations are of a similar size, however, the softer metal is preferentially stabilized by the NH^+ or NH_2 groups on the amino acid. The structures of $[M(\text{Aa-H})]^+$ complexes therefore depend on several competing factors: the size of the cation, its chemical hardness, and the presence or absence of functional groups on the amino acid side chain.

Hydrating the $[\text{Pb}(\text{Aa-H})]^+$ complexes causes water to chelate with lead; it remains intact when bound to a B-, C-, or D-type isomer, but donates a proton to the deprotonated amine group when attached to A-type ions. This results in a PbO-H stretch that appears in the IRMPD spectra of the A-type complexes near 3680 cm^{-1} , and which was confirmed by an isotopic labeling experiment using oxygen-18-labeled water. A-type $[\text{Pb}(\text{Aa-H})\text{H}_2\text{O}]^+$ ions can therefore be distinguished from the other isomers by the presence of this band. The addition of water to the $[\text{Pb}(\text{Aa-H})]^+$ complexes also increases the opportunity for hydrogen bonding, and this was observed in the structures of $[\text{Pb}(\text{Pro-H})\text{H}_2\text{O}]^+$, $[\text{Pb}(\text{Lys-H})\text{H}_2\text{O}]^+$, and $[\text{Pb}(\text{Glu-H})\text{H}_2\text{O}]^+$. In general, the $[\text{Pb}(\text{Aa-H})\text{H}_2\text{O}]^+$ complexes are simply the hydrated analogues of their bare forms. The exceptions are

$[\text{Pb}(\text{Pro-H})]^+$, which isomerizes to a C-type ion upon hydration, and $[\text{Pb}(\text{Lys-H})\text{H}_2\text{O}]^+$, which is a B-type complex.

The thermal unimolecular dissociation rate constants and threshold dissociation energies for water loss from eight of the $[\text{Pb}(\text{Aa-H})\text{H}_2\text{O}]^+$ complexes described above (Aa = Gly, Ala, Val, Leu, Ile, Phe, Lys, and Glu) were determined by BIRD kinetic measurements and master equation modeling in Chapter 5. The BIRD-determined water binding energies reflect the different isomers of the $[\text{Pb}(\text{Aa-H})\text{H}_2\text{O}]^+$ complexes and are dependent on the degree of Pb^{2+} stabilization by the amino acid conjugate bases. The A-type $[\text{Pb}(\text{Aa-H})\text{H}_2\text{O}]^+$ ions, for example, have stronger water binding energies than the B- and D-type ions, which have additional electron density on Pb^{2+} due to their side-chain interactions. This results in a smaller charge density on the metal cation that weakens the Pb^{2+} -water bond. Some complexes, such as the B-type $[\text{Pb}(\text{Lys-H})\text{H}_2\text{O}]^+$ ion, are also stabilized by intramolecular hydrogen bonding between water and the amino acid, and this is expressed by their stronger water binding energies. $[\text{Pb}(\text{Lys-H})\text{H}_2\text{O}]^+$ has a water binding energy that is 19.1 kJ mol^{-1} greater than that of $[\text{Pb}(\text{Phe-H})\text{H}_2\text{O}]^+$, a B-type ion without hydrogen bonding, a value that is roughly the strength of a hydrogen bond. The aliphatic A-type ions also exhibit a trend whereby the water binding energies decrease as the size of the amino acid side chain increases. This is attributed to the inductive effect of the larger alkyl side chains donating more electron density to Pb^{2+} .

7.2. Future and Current Projects. Mass spectrometric techniques are excellent tools for the characterization of ion structure and reactivity, and have been instrumental in

understanding the nature of solvated cations, metal clusters, and metal-ion complexes with biomolecules. The experiments reviewed and presented in this thesis have particularly emphasized research into the nature of metal-cationized nucleobases and amino acids, and have helped set the stage for more interesting experiments on biological ions; for example, investigations into the nature of protein aggregates or larger DNA subunits. IRMPD spectroscopy in the 3000 – 4000 cm^{-1} region, BIRD kinetics, and other activation methods such as CID provide a direct method for the structural and thermochemical characterization of these biomolecules, and may reveal the driving forces behind their formation.

The results advanced by this thesis fall in two categories: the IRMPD-determined structures of $[\text{M}(\text{Aa-H})]^+$ and $[\text{M}(\text{Aa-H})\text{H}_2\text{O}]^+$ complexes, and the BIRD-derived water dissociation energies of $[\text{M}(\text{Aa-H})\text{H}_2\text{O}]^+$. At the time of writing, the Fridgen research group at Memorial University is continuing to use these techniques to investigate the structures of M^{2+} complexes with amino acids or small peptides, and the preliminary results are different from those of the Pb^{2+} complexes presented in Chapters 3 and 4. $[\text{Zn}(\text{Pro-H})]^+$, for example, loses neutral Zn upon IRMPD or collisional activation rather than H_2O , which was originally expected based on the dissociation of $[\text{Pb}(\text{Pro-H})]^+$ (Section 3.3.4). Intriguingly, hydrating $[\text{Zn}(\text{Pro-H})]^+$ results in a structure where Zn^{2+} is bound to the carbonyl oxygen of an α -carbon-deprotonated proline monomer. This complex also contains a hydrogen bond between the zinc-bound water moiety and the amine group, and a proton transfer has occurred from the attached water to the metal cation, resulting in a Zn-H bond. A $[\text{Zn}(\text{Pro-H})(\text{Pro})]^+$ complex is also quite prevalent in

the electrospray mass spectrum whereas no $[\text{Pb}(\text{Pro-H})(\text{Pro})]^+$ ion had previously been observed. $[\text{Zn}(\text{Pro-H})(\text{Pro})]^+$ loses two H_2 molecules upon activation rather than neutral proline. In an effort to further characterize $[\text{Zn}(\text{Aa-H})(\text{Aa})]^+$ systems, complexes with glycine, alanine, and β -alanine were examined and found to lose water instead. However, when sarcosine (N-methyl glycine) is the amino acid, H_2 is lost like in the case of proline, suggesting that this dissociation channel is only promoted in secondary amines. Further comparisons between these results and those of Zn^{2+} complexes with the conjugate bases of alanine, β -alanine, and N-methyl glycine are currently producing a detailed picture of the structures and decomposition pathways of $[\text{Zn}(\text{Aa-H})(\text{Aa})]^+$ complexes.

Steps have also been taken to explore larger structures, such as metal-cationized peptide and nucleobase complexes. For example, work has begun on determining the structures of metal-cationized AlaGly dipeptides by IRMPD spectroscopy. Preliminary results for $[\text{Na}(\text{AlaGly-H})(\text{H}_2\text{O})_n]^+$ and $[\text{Ca}(\text{AlaGly-H})(\text{H}_2\text{O})_n]^+$ ($n = 1 - 3$) complexes indicate that these structures have strong intramolecular hydrogen bonds. This research will eventually be extended to biologically relevant peptides such as glutathione (γ -Glu-Cys-Gly). An investigation into the structures of metal cationized guanine/guanosine complexes has also been initiated because guanine tetramers comprise the telomeres in the DNA of chromosomes. The detailed structure of these complexes could have an impact in aging studies as well as cancer research. Currently, this work is in the exploratory stages as guanine's insolubility makes cluster preparation difficult.

The research described in Chapter 6 is particularly ripe for further study. β -methylaminoalanine has been linked to the onset of amyotrophic lateral sclerosis (ALS),

so using IRMPD spectroscopy and CID/IRMPD activation to determine the structures and reactivity of these complexes could shed light on possible therapies. Computational chemistry predicted that $[M(\text{BMAA-H})]^+$ complexes adopt different isomers depending on the size of the metal cation. However, it has proved difficult to experimentally confirm this using IRMPD spectroscopy because these ions either do not absorb in the 3200 – 3800 cm^{-1} region or are too strongly bound to be induced to dissociate by the KTP/OPO. To circumvent this issue, we are planning to improve our spectroscopic sensitivity by using a high-power CO_2 laser to activate the $[M(\text{BMAA-H})]^+$ complexes before irradiation by the tunable KTP/OPO. This will allow more strongly bound complexes to be examined, and could enable a thorough investigation of the $[M(\text{BMAA-H})]^+$ complexes.

The combination of mass spectrometry with gas-phase ion activation techniques makes it possible to accumulate an enormous amount of information about biologically important species. The information provided by this thesis provides a base from which to more fully explore the structures of larger metal-cationized peptides. Considering the sheer number and complexity of these ions, there is clearly a lot of work left to be done.

Appendix A – Supporting Information for Chapter 3

Isomerization of A- to C-type [Pb(Ala-H)]⁺ and [Pb(Pro-H)]⁺ complexes: Computed potential energy surfaces for the isomerization of A-type [Pb(Ala-H)]⁺ and [Pb(Pro-H)]⁺ complexes to their C-type isomers are shown in Figures A1 and A2 respectively. Geometry optimizations and relative Gibbs energies were determined using the B3LYP/6-31+G(d,p) method, and all calculations were performed using Gaussian 09.¹ Transition states were confirmed by the presence of one imaginary vibrational mode that corresponds to the reaction coordinate.

C-type [Pb(Ala-H)]⁺ and [Pb(Pro-H)]⁺ ions can be produced from their A-type isomers by two hydrogen transfer reactions followed by a change in lead binding site. The first hydrogen transfer is from the carboxylic acid O-H to the oxygen atom bonded with lead, while the second is from the lead-bound oxygen to the deprotonated amine nitrogen. In both cases, isomerization is endothermic by 29.4 – 33.1 kJ mol⁻¹ of Gibbs energy and the barriers with respect to hydrogen transfer are too high to be expected to occur. It is therefore unlikely that C-type [Pb(Ala-H)]⁺ and [Pb(Pro-H)]⁺ complexes exist in the gas phase.

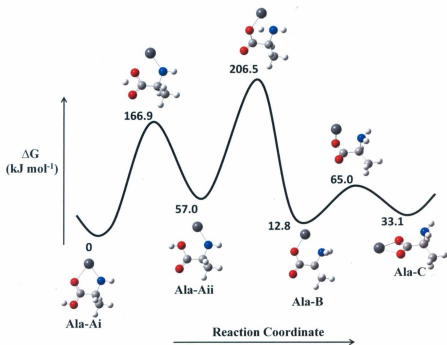


Figure A1: Potential energy surface for the isomerization of A- to C-type [Pb(Ala-H)]⁺. The optimized geometries and reported Gibbs energies were determined using the B3LYP/6-31+G(d,p) method.

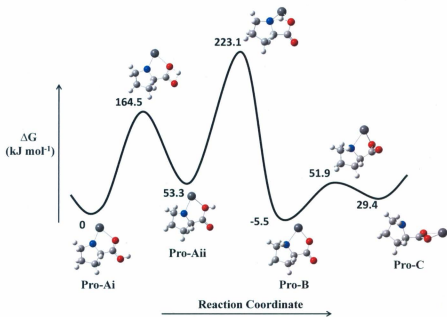


Figure A2: Potential energy surface for the isomerization of A- to C-type $[\text{Pb}(\text{Pro-H})]^+$. The optimized geometries and reported Gibbs energies were determined using the B3LYP/6-31+G(d,p) method.

References

I. Frisch, M. J.; Trucks, G. W.; Schlegel, H. B.; Scuseria, G. E.; Robb, M. A.; Cheeseman, J. R.; Scalmani, G.; Barone, V.; Mennucci, B.; Petersson, G. A.; Nakatsuji, H.; Caricato, M.; Li, X.; Hratchian, H. P.; Izmaylov, A. F.; Bloino, J.; Zheng, G.; Sonnenberg, J. L.; Hada, M.; Ehara, M.; Toyota, K.; Fukuda, R.; Hasegawa, J.; Ishida, M.; Nakajima, T.; Honda, Y.; Kitao, O.; Nakai, H.; Vreven, T.; Montgomery, J. A. Jr.; Peralta, J. E.; Ogliaro, F.; Bearpark, M.; Heyd, J. J.; Brothers, E.; Kudin, K. N.; Staroverov, V. N.; Kobayashi, R.; Normand, J.; Raghavachari, K.; Rendell, A.; Burant, J. C.; Iyengar, S. S.; Tomasi, J.; Cossi, M.; Rega, N.; Millam, J. M.; Klene, M.; Knox, J. E.; Cross, J. B.; Bakken, V.; Adamo, C.; Jaramillo, J.; Gomperts, R.; Stratmann, R. E.; Yazyev, O.; Austin, A. J.; Cammi, R.; Pomelli, C.; Ochterski, J. W.; Martin, R. L.; Morokuma, K.; Zakrzewski, V. G.; Voth, G. A.; Salvador, P.; Dannenberg, J. J.; Dapprich, S.; Daniels, A. D.; Farkas, O.; Foresman, J. B.; Ortiz, J. V.; Cioslowski, J.; Fox, D. J. Gaussian 09, Revision A.01; Gaussian, Inc.: Wallingford, CT, 2009.

Appendix B – Supporting Information for Chapter 4

IRMPD Spectroscopy and Computed Structures of $[\text{Pb}(\text{Met-H})]^+$: The IRMPD spectrum of $[\text{Pb}(\text{Met-H})]^+$ is shown in Figure B1 and compared with the computed B3LYP/6-31+G(d,p) IR spectra of three $[\text{Pb}(\text{Met-H})]^+$ isomers shown in Figure B2. Gaussian 09 was used for all calculations.¹ Although the experimental spectrum is featureless, the lack of a carboxylic acid O-H stretch may imply that $[\text{Pb}(\text{Met-H})]^+$ is carboxyl-deprotonated. This is consistent with the computed IR spectra of the lowest energy B- and C-type isomers (Met-Bi and -Ci), but these two structures cannot be further distinguished in the 3200 – 3800 cm^{-1} region without observable N-H stretches. The most stable $[\text{Pb}(\text{Met-H})]^+$ structure is predicted to be Met-Bi, which is 21.3 kJ mol^{-1} of Gibbs energy lower in energy than Met-Ci according to the MP2(full)/6-311++G(2d,2p)//B3LYP/6-31+G(d,p) method (the LANL2DZ basis set with relativistic core potential was applied to lead), and 40.8 kJ mol^{-1} more favourable than Met-Ai. Hence, Met-Bi may be the most likely structure for $[\text{Pb}(\text{Met-H})]^+$, although it cannot be confirmed spectroscopically. It should also be noted that, in each case, Pb^{2+} is predicted to be stabilized by the δ -sulfur atom in a similar manner to the structures of $[\text{Pb}(\text{Phe-H})]^+$ and $[\text{Pb}(\text{Glu-H})]^+$. Removing this interaction destabilizes $[\text{Pb}(\text{Met-H})]^+$ by 40.8 - 87.7 kJ mol^{-1} of Gibbs energy depending on the type of complex.

Computed Structures of $[\text{Pb}(\text{Phe-H})]^+$ and $[\text{Pb}(\text{Phe-H})\text{H}_2\text{O}]^+$: Two $[\text{Pb}(\text{Phe-H})]^+$ and three $[\text{Pb}(\text{Phe-H})\text{H}_2\text{O}]^+$ isomers are shown in Figure B4, and their computed IR spectra

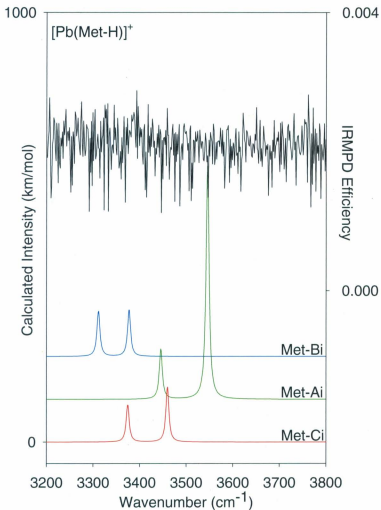


Figure B1: The IRMPD spectrum of $[\text{Pb}(\text{Met-H})]^+$ (black) compared with three computed IR spectra. The computed spectra were derived from the B3LYP/6-31+G(d,p) optimized structures of Met-Ai, -Bi, and Ci shown in Figure B2.

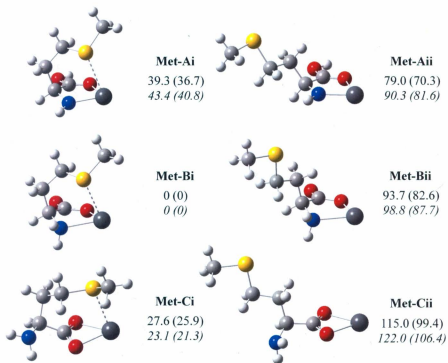


Figure B2: The B3LYP/6-31+G(d,p) optimized structures of $[\text{Pb}(\text{Met-H})]^+$. The 298 K relative enthalpies and Gibbs energies (in parentheses) have units of kJ mol^{-1} and are provided at the B3LYP/6-31+G(d,p) (top) and MP2(full)/6-311++G(2d,2p) (bottom and italicized) levels of theory. Note that the LANL2DZ basis set with effective core potential was applied to Pb^{2+} for both levels of calculation.

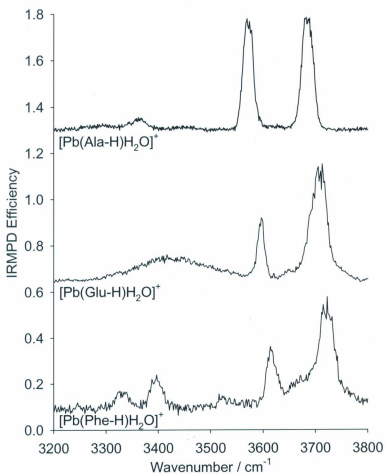


Figure B3: Comparison of the IRMPD spectra for [Pb(Phe-H)H₂O]⁺, [Pb(Glu-H)H₂O]⁺, and [Pb(Ala-H)H₂O]⁺.²

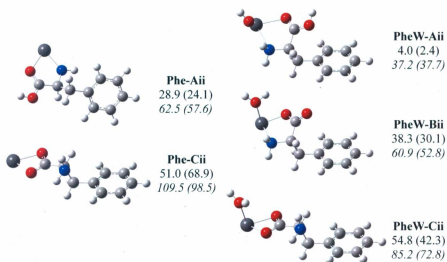


Figure B4: The B3LYP/6-31+G(d,p) optimized structures of (a) $[\text{Pb}(\text{Phe-H})]^+$ and (b) $[\text{Pb}(\text{Phe-H})\text{H}_2\text{O}]^+$. The B3LYP/6-31+G(d,p) energies are reported as ΔH_{298K} (ΔG_{298K}) and have units of kJ mol^{-1} . The MP2(full)/6-311++G(2d,2p) energies are italicized. In each case, the LANL2DZ basis set with effective core potential was applied to Pb^{2+} .

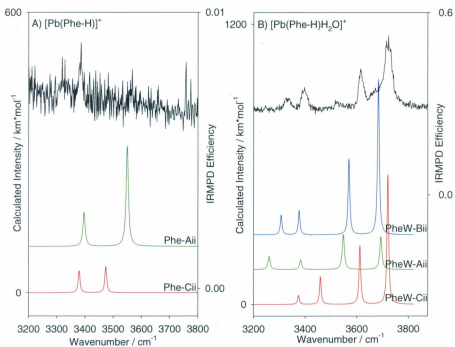


Figure B5: The IRMPD spectra (black) of (a) $[\text{Pb}(\text{Phe-H})]^+$ and (b) $[\text{Pb}(\text{Phe-H})\text{H}_2\text{O}]^+$ compared with computed IR spectra derived from the B3LYP/6-31+G(d,p) optimized structures in Figure B4.

are compared with the IRMPD spectra of $[\text{Pb}(\text{Phe-H})]^+$ and $[\text{Pb}(\text{Phe-H})\text{H}_2\text{O}]^+$ in Figure B5. The structural geometries were initially optimized using the B3LYP/6-31+G(d,p) method, and these calculations were further refined using MP2(full)/6-311++G(2d,2p)//B3LYP/6-31+G(d,p) in order to determine single point energies. In both cases, the LANL2DZ basis set with relativistic core potential was applied to lead. The $[\text{Pb}(\text{Phe-H})]^+$ complexes without the Pb^{2+} -phenyl π -interaction, Phe-Aii and -Cii, are 19.0 and 62.0 kJ mol^{-1} of Gibbs energy more stable at the MP2 level of theory than their respective analogues with the π -interaction, Phe-Ai and -Ci. In a similar manner, the $[\text{Pb}(\text{Phe-H})\text{H}_2\text{O}]^+$ complexes without the π -interaction (PheW-Aii, -Bii, and Cii) are 24.2 – 52.8 kJ mol^{-1} less favourable than PheW-Ai, -Bi, and -Ci, the complexes with the π -interaction. Each of these complexes is significantly higher in energy than their most stable tautomers (Phe-Bi and PheW-Bi), and are not expected to exist in the gas phase. Additionally, the computed IR spectra of Phe-Aii, Phe-Cii, PheW-Aii, and PheW-Cii do not match their associated IRMPD spectra and can be ruled out spectroscopically.

Computed Structures of $[\text{Pb}(\text{Glu-H})]^+$ and $[\text{Pb}(\text{Glu-H})\text{H}_2\text{O}]^+$: Figures B6 and B8 each contain ten structures of $[\text{Pb}(\text{Glu-H})]^+$ or $[\text{Pb}(\text{Glu-H})\text{H}_2\text{O}]^+$, and their computed IR spectra are compared with the IRMPD spectra of $[\text{Pb}(\text{Glu-H})]^+$ or $[\text{Pb}(\text{Glu-H})\text{H}_2\text{O}]^+$ in Figures B7 and B9. The structural geometries were determined using the same method described above. The $[\text{Pb}(\text{Glu-H})]^+$ structures without a Pb^{2+} - γ -carbonyl oxygen interaction are higher in energy than structures that include it. The lowest-energy A-type

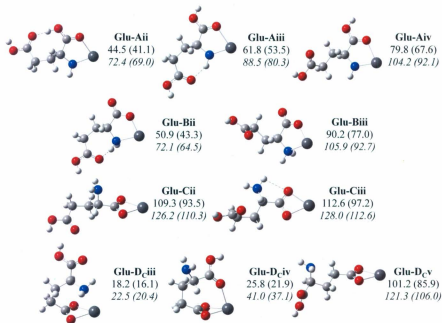


Figure B6: The B3LYP/6-31+G(d,p) optimized structures of $[\text{Pb}(\text{Glu-H})]^+$. The B3LYP/6-31+G(d,p) energies are reported as $\Delta H_{298\text{K}}$ ($\Delta G_{298\text{K}}$) and have units of kJ mol^{-1} . The MP2(full)/6-311++G(2d,2p) energies are italicized. In each case, the LANL2DZ basis set with effective core potential was applied to Pb^{2+} .

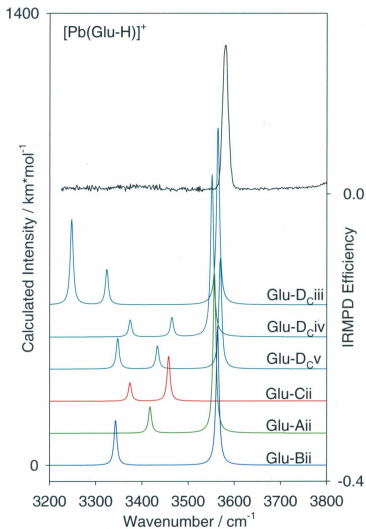


Figure B7: The IRMPD spectrum (black) of $[\text{Pb}(\text{Glu-H})]^+$ compared with computed IR spectra derived from the B3LYP/6-31+G(d,p) optimized structures in Figure B6.

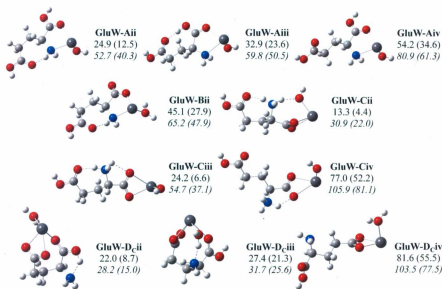


Figure B8: The B3LYP/6-31+G(d,p) optimized structures of $[\text{Pb}(\text{Glu-H})\text{H}_2\text{O}]^+$. The B3LYP/6-31+G(d,p) energies are reported as $\Delta H_{298\text{K}}$ ($\Delta G_{298\text{K}}$) and have units of kJ mol^{-1} . The MP2(full)/6-311++G(2d,2p) energies are italicized. In each case, the LANL2DZ basis set with effective core potential was applied to Pb^{2+} .

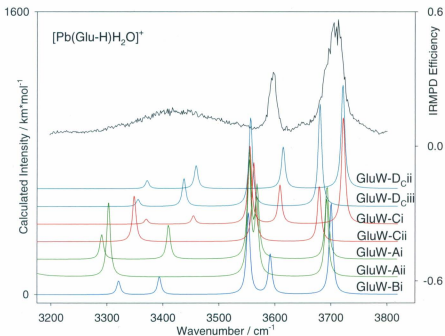


Figure B9: The IRMPD spectrum (black) of $[\text{Pb}(\text{Glu-H})\text{H}_2\text{O}]^+$ compared with computed IR spectra derived from the B3LYP/6-31+G(d,p) optimized structures in Figure B8.

isomer without this interaction (Glu-Aii) is 5.8 kJ mol^{-1} higher in energy than the most stable A-type structure, Glu-Ai. Glu-Aii is stabilized by a hydrogen bond between the terminal O-H group and the γ -carbonyl oxygen. If this interaction is replaced by a hydrogen bond between the amine and the side chain (Glu-Aiii) or is removed completely (Glu-Aiv), the energy gap with respect to Glu-Ai jumps to 11.3 and 29.0 kJ mol^{-1} , respectively. In a similar manner, Glu-Bii is stabilized by a hydrogen bond between the amine group and the γ -carbonyl oxygen, and is 49.9 kJ mol^{-1} higher in energy than Glu-Bi. Removing this interaction (Glu-Biii) destabilizes the ion by another 28.2 kJ mol^{-1} . Glu-Cii, which is not stabilized by hydrogen bonding, is 85.9 kJ mol^{-1} less stable than Glu-Ci. Since Glu-Ai, -Bi, and -Ci are already significantly higher in energy than the global minimum structure, Glu-Dzi, the aforementioned isomers are not likely to be stable in the gas-phase. The picture is similar for the D-type complexes where Pb^{2+} binds to the deprotonated γ -carboxyl group and is stabilized by a terminal oxygen atom. For example, the most stable D-type isomer without Pb^{2+} stabilized by the terminal carboxyl group (Glu-DCv) is 99.1 kJ mol^{-1} higher in Gibbs energy at the MP2 level of theory than Glu-Dzi, and is 93.6 kJ mol^{-1} less stable than the lowest energy DC-type ion, Glu-DCi. Since the N-H stretch region is featureless, it is difficult to eliminate most of these isomers spectroscopically. However, their significantly high relative energies mean they can be ruled out thermochemically.

Similar trends are not predicted for the hydrated complexes. For example, the removal of the Pb^{2+} - γ -carbonyl oxygen interaction in the A-type ions makes it possible for a hydrogen bond to form between the amine nitrogen and side-chain carbonyl group

(GluW-Aii). This makes GluW-Aii 5.4 kJ mol^{-1} more stable than GluW-Ai. GluW-Aiii, which has a similar configuration to Glu-Aii, is 4.8 kJ mol^{-1} less stable than GluW-Ai, while GluW-Aiv, which contains no hydrogen bonding, is further disfavoured by another 10.8 kJ mol^{-1} . The B-type analogue of GluW-Aii (GluW-Bii) is 32.0 kJ mol^{-1} higher in energy than GluW-Bi. The removal of the side-chain interaction also allows the C-type ions to relax further. GluW-Cii contains two hydrogen bonds: one between the amine and the γ -carbonyl oxygen, and another between the amine and one of the water O-H groups. This makes GluW-Cii more stable than GluW-Ci by 5.1 kJ mol^{-1} . Removing one (GluW-Ciii) or both (GluW-Civ) of these interactions, however, increases the energy of the ion with respect to GluW-Ci by 10.2 and 21.0 kJ mol^{-1} respectively. Despite all of this, the A-, B-, and C-type ions are still significantly higher in energy than the lowest energy D-type ion (GluW-Dzi), and will therefore not be present in the gas phase. As was the case for the D-type $[\text{Pb}(\text{Glu-H})]^+$ complexes, removing the additional stabilization imparted by the terminal carboxyl group (GluW-Dciv) significantly destabilizes $[\text{Pb}(\text{Glu-H})\text{H}_2\text{O}]^+$ complexes. For example, GluW-Dciv is 77.5 kJ mol^{-1} and 64.6 kJ mol^{-1} higher in Gibbs energy than GluW-Dzi and GluW-Dci at the MP2 level of theory.

References

1. Frisch, M. J.; Trucks, G. W.; Schlegel, H. B.; Scuseria, G. E.; Robb, M. A.; Cheeseman, J. R.; Scalmani, G.; Barone, V.; Mennucci, B.; Petersson, G. A.; Nakatsuji, H.; Caricato, M.; Li, X.; Hratchian, H. P.; Izmaylov, A. F.; Bloino, J.; Zheng, G.; Sonnenberg, J. L.; Hada, M.; Ehara, M.; Toyota, K.; Fukuda, R.; Hasegawa, J.; Ishida, M.; Nakajima, T.; Honda, Y.; Kitao, O.; Nakai, H.; Vreven, T.; Montgomery, J. A. Jr.; Peralta, J. E.; Ogliaro, F.; Bearpark, M.; Heyd, J. J.; Brothers, E.; Kudin, K. N.; Staroverov, V. N.; Kobayashi, R.; Normand, J.; Raghavachari, K.; Rendell, A.; Burant, J. C.; Iyengar, S. S.; Tomasi, J.; Cossi, M.; Rega, N.; Millam, J. M.; Klene, M.; Knox, J. E.; Cross, J. B.; Bakken, V.; Adamo, C.; Jaramillo, J.; Gomperts, R.; Stratmann, R. E.; Yazyev, O.; Austin, A. J.; Cammi, R.; Pomelli, C.; Ochterski, J. W.; Martin, R. L.; Morokuma, K.; Zakrzewski, V. G.; Voth, G. A.; Salvador, P.; Dannenberg, J. J.; Dapprich, S.; Daniels, A. D.; Farkas, O.; Foresman, J. B.; Ortiz, J. V.; Cioslowski, J.; Fox, D. J. *Gaussian 09, Revision A.01*; Gaussian, Inc.: Wallingford, CT, 2009.
2. Burt, M. B.; Decker, S. G. A.; Atkins, C. G.; Rowsell, M.; Peremans, A.; Fridgen T. D. *J. Phys. Chem. B* **2011**, *115*, 11506 - 11518.

Appendix C – Supporting Information for Chapter 5

Vibrational Frequencies and Intensities of H₂O: The vibrational modes and intensities of water were determined using the B3LYP/6-31+G(d,p) method as implemented by Gaussian 09 and are given in Table C1.¹ VariFlex scales these frequencies by a factor of 0.955 to account for anharmonic effects.²

Measured Dissociation Rate Constants: Table C2 lists the dissociation rate constants extracted by fitting the BIRD kinetic measurements to the integrated first-order rate law (Figures C1a - g) over the temperature range 292 – 388 K. In general, the linearity of each plot is good ($R^2 = 0.7073 - 0.9990$, with the majority being > 0.99). In cases where experiments were repeated (in italics), $\ln(k_{\text{obs}})$ is the mean value and the reported uncertainty is the standard deviation of the mean. The relative uncertainty of $\ln(k_{\text{obs}})$ is typically about 1%, but is as high as 9% for a small minority of the longer reactions. In examples where experiments were only performed once, $\sigma \ln(k_{\text{obs}})$ is the natural logarithm of the uncertainty in the slope of the integrated first-order rate law. The uncertainty in temperature is ± 1 K.

Master Equation Modeling Using Different Frequency Scaling Factors: Figure C2 demonstrates the effect of altering the frequency scaling factor (α) used for master equation modeling. In the case of $[\text{Pb}(\text{Val-H})\text{H}_2\text{O}]^+$, varying α between 0.90 – 1.10 results in water binding energies between 99.5 – 103.6 kJ mol⁻¹, and Arrhenius pre-

Table C1: Vibrational Frequencies and Intensities of H₂O

Vibrational Mode	Frequency (cm ⁻¹)	Intensity (km mol ⁻¹)
Bend	1603.23	91.2215
Symmetric Stretch	3809.23	6.4100
Antisymmetric Stretch	3931.29	57.2896

Table C2: Observed Dissociation Rate Constants

[Pb(Aa-H)H ₂ O] ²⁺ Complex	Temperature (K)	ln(<i>k</i> _{obs}) (s ⁻¹)	o(ln(<i>k</i> _{obs})) (s ⁻¹)
Gly	344.(8)	-8.1117	0.1383
	348.(8)	-7.4186	0.1461
	352.(2)	-7.8240	0.0835
	365.(7)	-5.6417	0.0598
	369.(8)	-6.5368	0.0488
	377.(8)	-5.8963	0.0257
	386.(7)	-4.7795	0.0238
	388.(2)	-4.2267	0.0274
Ala	322.(5)	-8.1117	0.1277
	330.(4)	-7.6009	0.1357
	337.(2)	-7.2644	0.1167
	347.(8)	-6.5713	0.0481
	353.(3)	-5.5994	0.0811
	357.(0)	-4.3200	0.1654
	364.(2)	-4.6670	0.0638
	365.(5)	-3.5268	0.0612
	377.(5)	-3.7958	0.0629
	385.(9)	-3.6691	0.0431
386.(6)	-3.8490	0.0141	
Val	312.(6)	-7.2644	0.0379
	314.(6)	-7.1309	0.0523
	340.(9)	-4.9618	0.0571
	345.(1)	-4.8540	0.0363
	354.(4)	-4.0456	0.0343
	356.(0)	-4.1605	0.0128
	365.(6)	-3.5302	0.0048
	388.(0)	-2.0684	0.0168
Leu	292.(6)	-8.5172	0.1644
	318.(7)	-6.9078	0.0833
	335.(7)	-4.9268	0.0098
	342.(0)	-5.3817	0.0217
	345.(4)	-4.5190	0.0183
	365.(4)	-3.0275	0.0730
	387.(8)	-1.9763	0.0163
Ile	313.(3)	-6.8124	0.0384
	314.(6)	-6.7254	0.0210
	328.(2)	-5.3817	0.0217
	346.(0)	-4.3351	0.0153
	354.(0)	-3.9120	0.0300
	355.(9)	-3.5439	0.0588
	365.(2)	-3.1168	0.0127

Table C2: Observed Dissociation Rate Constants (continued)

[Pb(Aa-H)H ₂ O] ⁺ Complex	Temperature (K)	ln(<i>k</i> _{obs}) (s ⁻¹)	σln(<i>k</i> _{obs}) (s ⁻¹)
Ile	382.(5)	-2.2986	0.0349
	384.(5)	-2.1698	0.0350
	388.(0)	-1.8274	0.0101
Phe	292.(6)	-3.2728	0.0075
	312.(6)	-2.0512	0.0231
	324.(3)	-2.3476	0.0492
	331.(6)	-2.0750	0.0771
	342.(6)	-1.5583	0.0323
	346.(0)	-1.2899	0.0283
	365.(3)	0.3581	0.0499
	386.(5)	0.1024	0.0299
Lys	292.(9)	-7.8240	0.0787
	312.(0)	-5.8430	0.0690
	315.(2)	-5.9915	0.0333
	320.(8)	-5.5728	0.0159
	330.(3)	-4.8665	0.0260
	331.(7)	-5.5468	0.0769
	342.(0)	-4.0456	0.0229
	362.(8)	-3.0716	0.0577
	386.(5)	-1.9174	0.0250
Glu	292.(9)	-4.7020	0.3546
	315.(0)	-3.4999	0.0298
	321.(6)	-3.0428	0.0461
	330.(1)	-2.8096	0.0363
	331.(7)	-2.8050	0.2513
	341.(7)	-2.0699	0.0325
	363.(2)	-1.3214	0.0224
	386.(5)	-0.5150	0.0341

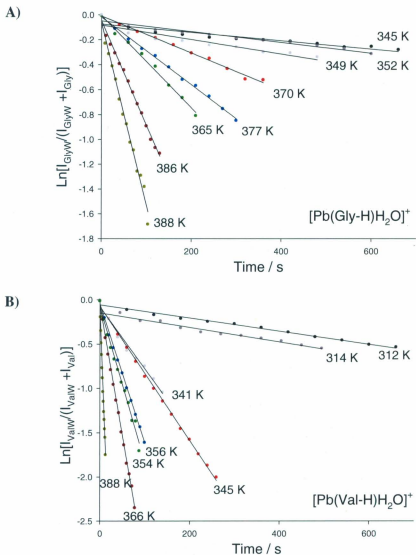


Figure C1a-b: BIRD kinetic data for the dissociation of seven $[\text{Pb}(\text{Aa-H})\text{H}_2\text{O}]^+$ complexes (Aa = Gly, Val, Leu, Ile, Phe, Lys, and Glu) fit to the integrated first order rate law ($\text{Ln}[I_{\text{AaW}}/(I_{\text{AaW}} + I_{\text{Aa}})]$ versus reaction time).

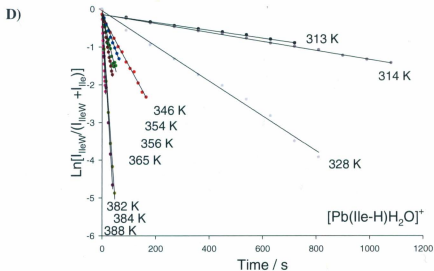
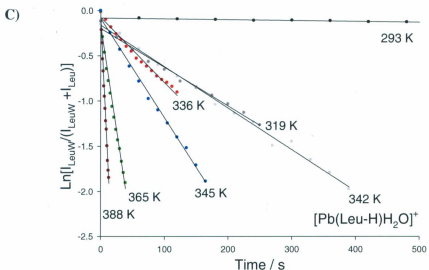


Figure C1c-d: BIRD kinetic data for the dissociation of seven $[\text{Pb}(\text{Aa-H})\text{H}_2\text{O}]^+$ complexes (Aa = Gly, Val, Leu, Ile, Phe, Lys, and Glu) fit to the integrated first order rate law ($\ln[I_{\text{AaW}}/(I_{\text{AaW}} + I_{\text{Aa}})]$ versus reaction time).

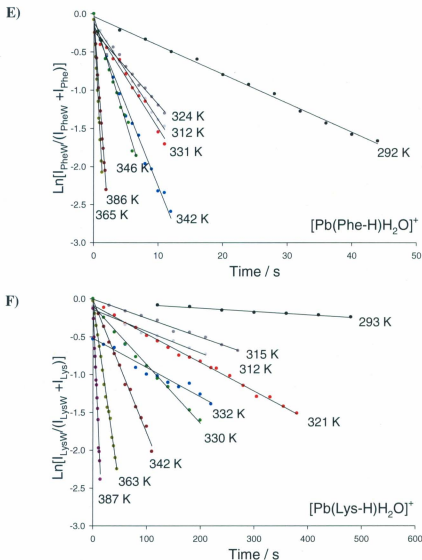


Figure C1e-f: BIRD kinetic data for the dissociation of seven $[\text{Pb}(\text{Aa-H})\text{H}_2\text{O}]^+$ complexes (Aa = Gly, Val, Leu, Ile, Phe, Lys, and Glu) fit to the integrated first order rate law ($\ln[I_{\text{AaW}}/(I_{\text{AaW}} + I_{\text{Aa}})]$ versus reaction time).

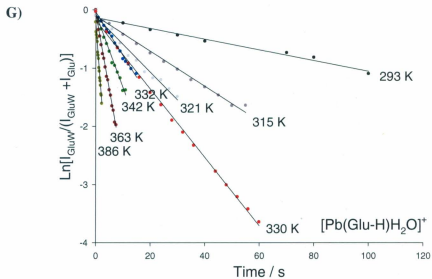


Figure C1g: BIRD kinetic data for the dissociation of seven $[\text{Pb}(\text{Aa-H})\text{H}_2\text{O}]^+$ complexes (Aa = Gly, Val, Leu, Ile, Phe, Lys, and Glu) fit to the integrated first order rate law ($\ln[I_{\text{AaW}}/(I_{\text{AaW}}+I_{\text{Aa}})]$ versus reaction time).

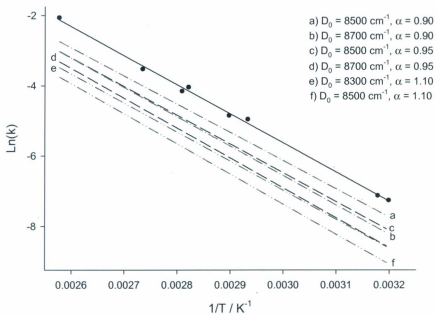


Figure C2: The Arrhenius plot of $[\text{Pb}(\text{Val-H})\text{H}_2\text{O}]^+$ (solid line) fit by k_{uni} values obtained by master equation modeling using frequency scaling factors (α) between 0.90 – 1.10 (dashed lines).

exponential factors ($\ln(A)$) ranging from 17.6 – 18.6. This is compared to the reported $[\text{Pb}(\text{Val-H})\text{H}_2\text{O}]^+$ values of $E_0 = 102.9 \pm 1.4 \text{ kJ mol}^{-1}$ and $\ln(A) = 18.3 \pm 0.5$ using an α of 0.95. Consequently, different scaling factors do not significantly alter the results of the master equation.

IRMPD Spectra of $[\text{Pb}(\text{Ala-H})\text{H}_2\text{O}]^+$: The IRMPD spectra of $[\text{Pb}(\text{Ala-H})\text{H}_2\text{O}]^+$ complexes generated from two electrospray solvents (50/50 18.2 M Ω H₂O/MeOH and 50/50 18.2 M Ω H₂O/MeCN) are compared in Figure C3 along with the computed infrared spectra for the A-, B-, and C-type ions described in Figure 5.1. The method used to prepare, isolate, and irradiate these complexes has been described previously.³ In brief, the ions are generated by the route described in the methods section, and then irradiated for approximately two seconds by photons emitted from a potassium titanyl phosphate optical parametric oscillator (KTP OPO). The OPO was scanned over a spectroscopic range of 3200 – 3800 cm^{-1} at intervals of 1.5 cm^{-1} , and four mass spectra were averaged per wavelength step. The computed spectra were scaled by 0.955 to account for anharmonic effects. The locations and intensities of each vibrational mode in the compared spectra are virtually identical; hence there is no reason to believe that isomerism is being induced by the solvent during the electrospray process.

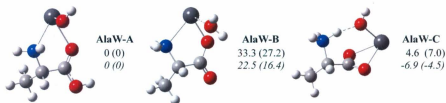
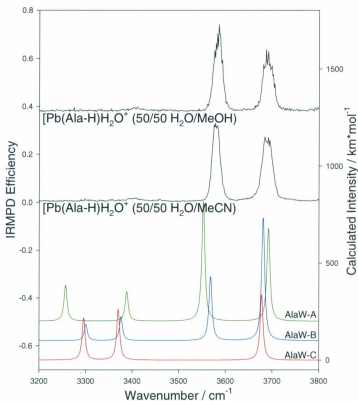


Figure C3: IRMPD spectra in the 3200 - 3800 cm⁻¹ region for [Pb(Ala-H)H₂O]⁺ solvated in 50/50 18.2 MΩ H₂O/MeOH and 50/50 18.2 MΩ H₂O/MeCN. The spectra are compared to computed infrared spectra for A- (green), B- (blue), and C-type (red) [Pb(Ala-H)H₂O]⁺ complexes.²

References

1. Klippenstein, S. J.; Wagner, A. F.; Dunbar, R. C.; Wardlaw, D. M.; Robertson S. H. VariFlex, Version 1.00 1999, July 16.
2. Frisch, M. J.; Trucks, G. W.; Schlegel, H. B.; Scuseria, G. E.; Robb, M. A.; Cheeseman, J. R.; Scalmani, G.; Barone, V.; Mennucci, B.; Petersson, G. A.; Nakatsuji, H.; Caricato, M.; Li, X.; Hratchian, H. P.; Izmaylov, A. F.; Bloino, J.; Zheng, G.; Sonnenberg, J. L.; Hada, M.; Ehara, M.; Toyota, K.; Fukuda, R.; Hasegawa, J.; Ishida, M.; Nakajima, T.; Honda, Y.; Kitao, O.; Nakai, H.; Vreven, T.; Montgomery, J. A. Jr.; Peralta, J. E.; Ogliaro, F.; Bearpark, M.; Heyd, J. J.; Brothers, E.; Kudin, K. N.; Staroverov, V. N.; Kobayashi, R.; Normand, J.; Raghavachari, K.; Rendell, A.; Burant, J. C.; Iyengar, S. S.; Tomasi, J.; Cossi, M.; Rega, N.; Millam, J. M.; Klene, M.; Knox, J. E.; Cross, J. B.; Bakken, V.; Adamo, C.; Jaramillo, J.; Gomperts, R.; Stratmann, R. E.; Yazyev, O.; Austin, A. J.; Cammi, R.; Pomelli, C.; Ochterski, J. W.; Martin, R. L.; Morokuma, K.; Zakrzewski, V. G.; Voth, G. A.; Salvador, P.; Dannenberg, J. J.; Dapprich, S.; Daniels, A. D.; Farkas, O.; Foresman, J. B.; Ortiz, J. V.; Cioslowski, J.; Fox, D. J. Gaussian 09, Revision A.01; Gaussian, Inc.: Wallingford, CT, 2009.
3. Burt, M. B.; Decker, S. G. A.; Atkins, C. G.; Rowsell, M.; Peremans, A.; Fridgen T. D. *J. Phys. Chem. B* **2011**, *115*, 11506 - 11518.

Appendix D – Supporting Information for Chapter 6

Computed Structures of [M(Ala-H)]⁺ and [M(BMAA-H)]⁺ Complexes: The lowest energy isomers for a series of [M(Ala-H)]⁺ and [M(BMAA-H)]⁺ complexes (M²⁺ = Be²⁺, Mg²⁺, Ca²⁺, Sr²⁺, Ba²⁺, Zn²⁺, and Pb²⁺) are shown in Figures D1 and D2 respectively. Geometry optimizations as well as relative 298 K enthalpies and Gibbs energies were determined using the MP2(full)/6-311++G(2d,2p)//B3LYP/6-31+G(d,p) method as implemented by Gaussian 09.¹ It should be noted, however, that the LANL2DZ basis set and effective core potential were used for Sr, Ba, and Pb. All reported energies have units of kJ mol⁻¹.

The calculations suggest that [Be(Ala-H)]⁺ and [Mg(Ala-H)]⁺ have B-type structures; [Ca(Ala-H)]⁺, [Sr(Ala-H)]⁺, and [Ba(Ala-H)]⁺ are predicted to be C-type ions; and [Zn(Ala-H)]⁺ and [Pb(Ala-H)]⁺ are expected to have E- and A-type structures, respectively. In contrast to the [M(Ala-H)]⁺ complexes, the [M(BMAA-H)]⁺ ions are stabilized by an additional interaction with the secondary amine on the amino acid side chain. This stabilizes B-type ions for [M(BMAA-H)]⁺ complexes involving Be²⁺, Mg²⁺, Ca²⁺, Zn²⁺, and Pb²⁺. [Sr(BMAA-H)]⁺ and [Ba(BMAA-H)]⁺ are predicted to be C-type complexes.

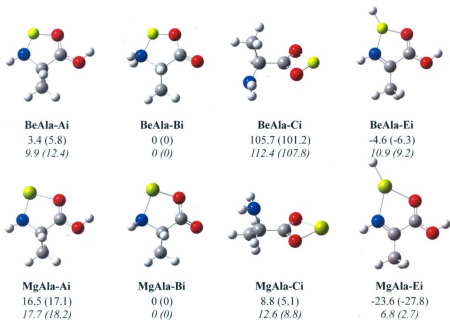


Figure D1a-b: The B3LYP/6-31+G(d,p) optimized structures of $[\text{Be}(\text{Ala-H})]^+$ and $[\text{Mg}(\text{Ala-H})]^+$. The 298 K relative enthalpies and Gibbs energies (in parentheses) have units of kJ mol^{-1} and are provided at the B3LYP/6-31+G(d,p) (top) and MP2(full)/6-311+G(2d,2p) (bottom and italicized) levels of theory.

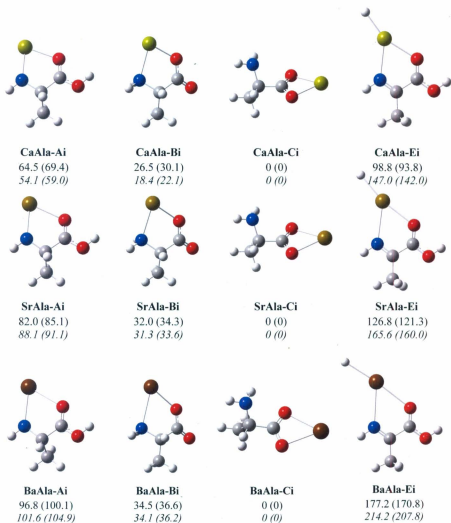


Figure D1c-e: The B3LYP/6-31+G(d,p) optimized structures of [Ca(Ala-H)]⁺, [Sr(Ala-H)]⁺ and [Ba(Ala-H)]⁺. The 298 K relative enthalpies and Gibbs energies (in parentheses) have units of kJ mol⁻¹ and are provided at the B3LYP/6-31+G(d,p) (top) and MP2(full)/6-311++G(2d,2p) (bottom and italicized) levels of theory. Note that the LANL2DZ basis set with effective core potential was applied to Sr²⁺ and Ba²⁺ for both levels of calculation.

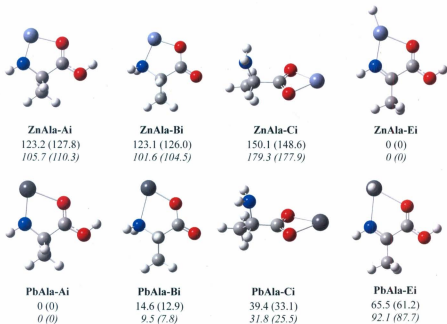


Figure D1f-g: The B3LYP/6-31+G(d,p) optimized structures of $[\text{Zn}(\text{Ala-H})]^+$ and $[\text{Pb}(\text{Ala-H})]^+$. The 298 K relative enthalpies and Gibbs energies (in parentheses) have units of kJ mol^{-1} and are provided at the B3LYP/6-31+G(d,p) (top) and MP2(full)/6-311++G(2d,2p) (bottom and italicized) levels of theory. Note that the LANL2DZ basis set with effective core potential was applied to Pb^{2+} for both levels of calculation.

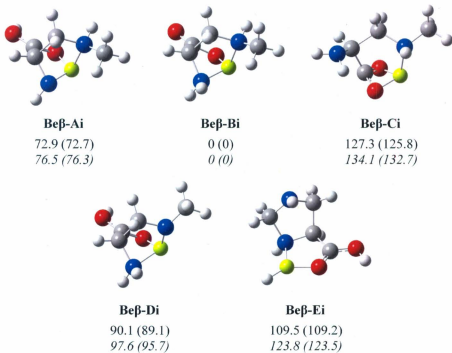


Figure D2a: The B3LYP/6-31+G(d,p) optimized structures of $[\text{Be}(\text{BMAA-H})]^+$. The 298 K relative enthalpies and Gibbs energies (in parentheses) have units of kJ mol^{-1} and are provided at the B3LYP/6-31+G(d,p) (top) and MP2(full)/6-311++G(2d,2p) (bottom and italicized) levels of theory.

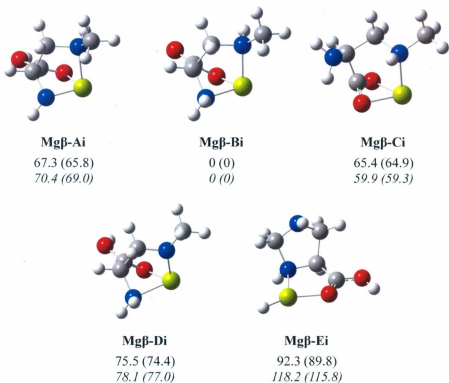


Figure D2b: The B3LYP/6-31+G(d,p) optimized structures of $[\text{Mg}(\text{BMAA-H})]^+$. The 298 K relative enthalpies and Gibbs energies (in parentheses) have units of kJ mol^{-1} and are provided at the B3LYP/6-31+G(d,p) (top) and MP2(full)/6-311++G(2d,2p) (bottom and italicized) levels of theory.

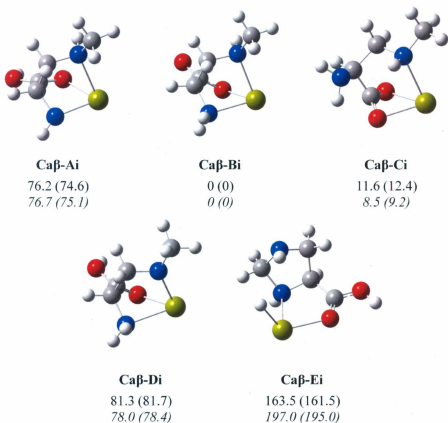


Figure D2c: The B3LYP/6-31+G(d,p) optimized structures of $[\text{Ca}(\text{BMAA-H})]^+$. The 298 K relative enthalpies and Gibbs energies (in parentheses) have units of kJ mol^{-1} and are provided at the B3LYP/6-31+G(d,p) (top) and MP2(full)/6-311++G(2d,2p) (bottom and italicized) levels of theory.

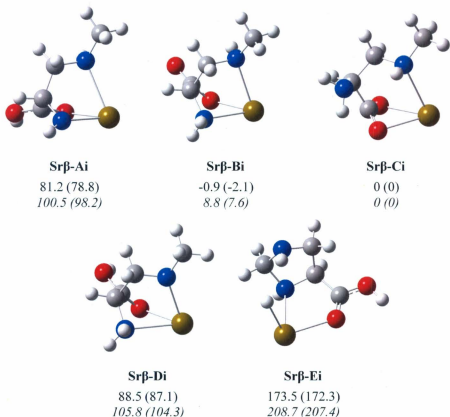


Figure D2d: The B3LYP/6-31+G(d,p) optimized structures of $[\text{Sr}(\text{BMAA-H})]^+$. The 298 K relative enthalpies and Gibbs energies (in parentheses) have units of kJ mol^{-1} and are provided at the B3LYP/6-31+G(d,p) (top) and MP2(full)/6-311++G(2d,2p) (bottom and italicized) levels of theory. Note that the LANL2DZ basis set with effective core potential was applied to Sr^{2+} for both levels of calculation.

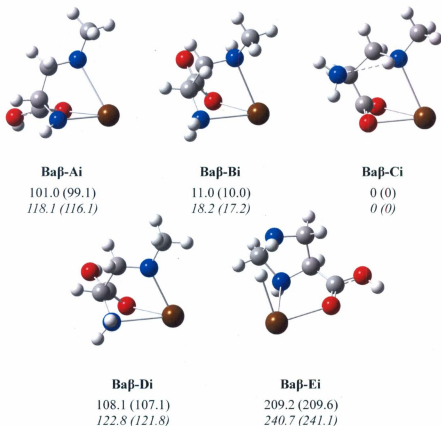


Figure D2e: The B3LYP/6-31+G(d,p) optimized structures of $[\text{Ba}(\text{BMAA-H})]^+$. The 298 K relative enthalpies and Gibbs energies (in parentheses) have units of kJ mol^{-1} and are provided at the B3LYP/6-31+G(d,p) (top) and MP2(full)/6-311++G(2d,2p) (bottom and italicized) levels of theory. Note that the LANL2DZ basis set with effective core potential was applied to Ba^{2+} for both levels of calculation.

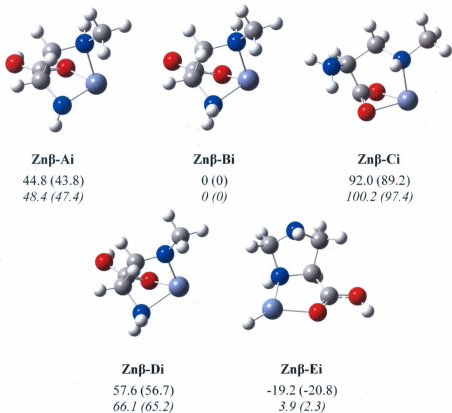


Figure D2f: The B3LYP/6-31+G(d,p) optimized structures of $[\text{Zn}(\text{BMAA-H})]^+$. The 298 K relative enthalpies and Gibbs energies (in parentheses) have units of kJ mol^{-1} and are provided at the B3LYP/6-31+G(d,p) (top) and MP2(full)/6-311++G(2d,2p) (bottom and italicized) levels of theory.

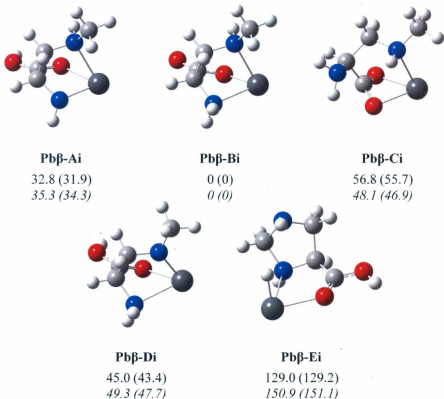


Figure D2g: The B3LYP/6-31+G(d,p) optimized structures of $[\text{Pb}(\text{BMAA-H})]^+$. The 298 K relative enthalpies and Gibbs energies (in parentheses) have units of kJ mol^{-1} and are provided at the B3LYP/6-31+G(d,p) (top) and MP2(full)/6-311++G(2d,2p) (bottom and italicized) levels of theory. Note that the LANL2DZ basis set with effective core potential was applied to Pb^{2+} for both levels of calculation.

References

I. Frisch, M. J.; Trucks, G. W.; Schlegel, H. B.; Scuseria, G. E.; Robb, M. A.; Cheeseman, J. R.; Scalmani, G.; Barone, V.; Mennucci, B.; Petersson, G. A.; Nakatsuji, H.; Caricato, M.; Li, X.; Hratchian, H. P.; Izmaylov, A. F.; Bloino, J.; Zheng, G.; Sonnenberg, J. L.; Hada, M.; Ehara, M.; Toyota, K.; Fukuda, R.; Hasegawa, J.; Ishida, M.; Nakajima, T.; Honda, Y.; Kitao, O.; Nakai, H.; Vreven, T.; Montgomery, J. A. Jr.; Peralta, J. E.; Ogliaro, F.; Bearpark, M.; Heyd, J. J.; Brothers, E.; Kudin, K. N.; Staroverov, V. N.; Kobayashi, R.; Normand, J.; Raghavachari, K.; Rendell, A.; Burant, J. C.; Iyengar, S. S.; Tomasi, J.; Cossi, M.; Rega, N.; Millam, J. M.; Klene, M.; Knox, J. E.; Cross, J. B.; Bakken, V.; Adamo, C.; Jaramillo, J.; Gomperts, R.; Stratmann, R. E.; Yazyev, O.; Austin, A. J.; Cammi, R.; Pomelli, C.; Ochterski, J. W.; Martin, R. L.; Morokuma, K.; Zakrzewski, V. G.; Voth, G. A.; Salvador, P.; Dannenberg, J. J.; Dapprich, S.; Daniels, A. D.; Farkas, O.; Foresman, J. B.; Ortiz, J. V.; Cioslowski, J.; Fox, D. J. Gaussian 09, Revision A.01; Gaussian, Inc.: Wallingford, CT, 2009.

Vita

Name: Michael Brian Burt

Birth Date: February 18th, 1986

Education: Doctor of Philosophy, Memorial University of Newfoundland,
St. John's, Newfoundland and Labrador (2008 – 2012)

Bachelor of Science (Hons), Memorial University of Newfoundland,
St. John's, Newfoundland and Labrador (2004 – 2008)

Publications: 7. "Water binding energies of $[\text{Pb}(\text{Aa-H})\text{H}_2\text{O}]^+$ complexes measured by blackbody infrared radiative dissociation"
M. B. Burt, S. G. A. Decker, and T. D. Fridgen. *Phys. Chem. Chem. Phys.*, accepted. DOI:10.1039/c2cp41440f.

6. "IRMPD spectroscopic and computational study of gas phase $[\text{M}(\text{Ura-H})(\text{Ura})]^+$ and $[\text{M}(\text{Ura-H})(\text{H}_2\text{O})_n]^+$ ($\text{M}=\text{Sr}, \text{Ba}; n=1,2$) complexes"

A. A. Power, O. Y. Ali, M. B. Burt, and T. D. Fridgen. *Int. J. Mass Spectrom.*, accepted. DOI:10.1016/j.ijms.2012.08.020.

5. "Gas-phase structures of Pb^{2+} cationized phenylalanine and glutamic acid determined by infrared multiple photon dissociation spectroscopy and computational chemistry"

M. B. Burt and T. D. Fridgen. *J. Phys. Chem. A*, accepted.
DOI:10.1021/jp306420e.

4. "Structures and physical properties of gaseous metal cationized biological ions"

M. B. Burt and T. D. Fridgen. *E. J. Mass Spectrom.* **2012**, *18* (2), 235 - 250.

3. "Structures of bare and hydrated $[\text{Pb}(\text{AminoAcid-H})]^+$ complexes using infrared multiple photon dissociation spectroscopy."

M. B. Burt, C. G. Atkins, S. G. A. Decker, M. Rowsell, and T. D. Fridgen. *J. Phys. Chem. B* **2011**, *115*, 11506 - 11518.

2. "Theoretical ring-chain equilibria of R-but-3-enoate esters; a quantum mechanical study of reactivity profiles."

M. B. Burt, A. K. Crane, N. Su, N. Rice and R. A. Poirier. *Can. J. Chem.* **2010**, *88* (11), 1094 - 1103.

1. "Heterogeneous proton-bound dimers with a high dipole moment monomer: how could we experimentally observe these anomalous ionic hydrogen bonds?"
M. B. Burt and T. D. Fridgen, *J. Phys. Chem. A* **2007**, *111*, 10738-10744.

Conference Proceedings:

1. 60th ASMS Conference on Mass Spectrometry and Allied Topics, Vancouver, British Columbia, May 20 – 24, 2012.
Poster Presentation: Structures of bare and hydrated [Pb(AminoAcid-H)]⁺ complexes using infrared multiple photon dissociation spectroscopy
M. B. Burt, S. Decker, C. G. Atkins M. Rowsell, and T. D. Fridgen

Contributed Presentations:

18. 29th Annual Trent Conference on Mass Spectrometry, Orillia, Ontario, August 13 - 16, 2012.
Oral Presentation: "Water binding energies of [Pb(AminoAcid-H)H₂O]⁺ complexes determined by blackbody infrared radiative dissociation"
M. B. Burt, C. G. Atkins, S. Decker, M. Rowsell, and T. D. Fridgen

17. 95th Canadian Chemistry Conference and Exhibition, Calgary, Alberta, May 26 – 30, 2012.
Oral Presentation: "Structures of bare and hydrated [Pb(AminoAcid-H)]⁺ complexes using infrared multiple photon dissociation spectroscopy"
M. B. Burt, S. Decker, C. G. Atkins M. Rowsell, and T. D. Fridgen

16. 19th Annual Chemistry Colloquium Contest, St. John's, Newfoundland and Labrador, January 26, 2012.
Oral Presentation: "Petroleomics: the chemical history of crude oil"
M. B. Burt

15. Caffeinating with Chemists, St. John's, Newfoundland and Labrador, October 21, 2011.
Oral Presentation: "The chemical mosaic: quasicrystals and the 2011 Nobel Prize in Chemistry"
M. B. Burt

14. 28th Annual Trent Conference on Mass Spectrometry, Orillia, Ontario, August 8 - 11, 2011.
Oral Presentation: "Structures of bare and hydrated [Pb(AminoAcid-H)]⁺ complexes using infrared multiple photon dissociation spectroscopy"

M. B. Burt, C. G. Atkins, S. Decker, M. Rowsell, and T. D. Fridgen

13. 2011 Gordon Research Conference on Gaseous Ions: Structures, Energetics & Reactions, Galveston, Texas, February 27 - March 4, 2011.

Poster Presentation: "Structures of bare and hydrated $[\text{Pb}(\text{AminoAcid-H})]^+$ complexes using infrared multiple photon dissociation spectroscopy"

M. B. Burt, S. Decker, C. G. Atkins, M. Rowsell, and T. D. Fridgen

12. 18th Annual Chemistry Colloquium Contest, St. John's, Newfoundland, January 27, 2011.

Oral Presentation: "Cold fusion: a story of science gone wrong"

M. B. Burt

11. 27th Annual Trent Conference on Mass Spectrometry, Orillia, Ontario, July 26 – 29, 2010.

Poster Presentation: "Structures and solvent binding energies of $[\text{Pb}(\text{AminoAcid-H})\text{H}_2\text{O}]^+$ by IRMPD spectroscopy, BIRD kinetics and computational studies"

M. B. Burt, S. Decker and T. D. Fridgen

10. 57th ASMS Conference on Mass Spectrometry and Allied Topics, Salt Lake City, Utah, May 23 - 27, 2010.

Oral Presentation: "Structures of bare and hydrated $\text{Pb}[\text{Aa-H}]^+$ complexes by IRMPD spectroscopy and computational chemistry"

M. B. Burt, S. Decker, C. Atkins, M. Rowsell, and T. D. Fridgen

9. 17th Annual Chemistry Colloquium Contest, St. John's, Newfoundland, January 28, 2010.

Oral Presentation: "Chemistry and the hive: how scent enables communication between bees"

M. B. Burt

8. 2009 Asilomar Conference on Mass Spectrometry, Pacific Grove, California, October 8 - 12, 2009.

Poster Presentation: "Structural determination of $[\text{Pb}(\text{AminoAcid-H})]^+$ complexes using infrared multiple photon dissociation spectroscopy"

M. B. Burt, C. G. Atkins, S. Decker, M. Rowsell, and T. D. Fridgen

7. 3rd Annual Summer Student Symposium, St. John's, Newfoundland, August 12, 2009.

Poster Presentation: "Structural determination of $[\text{Pb}(\text{AminoAcid-}$

H)]⁺ complexes using infrared multiple photon dissociation spectroscopy”
S. Decker, M. B. Burt, C. G. Atkins, M. Rowsell, and T. D. Fridgen

6. ChemCon 2009, St. Francis Xavier University, Antigonish, NS, May 14 - 16, 2009.

Oral Presentation: “The structural identification of gas-phase amino acid complexes containing Pb²⁺ ions”
M. Rowsell, C. G. Atkins, M. B. Burt and T. D. Fridgen

5. 26th Annual Trent Conference on Mass Spectrometry, Orillia, Ontario, July 27 - 30, 2009.

Oral Presentation: “Structural determination of [Pb(AminoAcid-H)]⁺ complexes using infrared multiple photon dissociation spectroscopy”
M. B. Burt, C. G. Atkins, S. Decker, M. Rowsell, and T. D. Fridgen

4. 16th Annual Chemistry Colloquium Contest, St. John’s, Newfoundland, February 5, 2009.

Oral Presentation: “The impact of protostellar shocks on molecular clouds: the chemistry of interstellar matter”
M. B. Burt

3. 24th Annual Trent Conference on Mass Spectrometry, Orillia, Ontario, July 30 - August 2, 2007.

Oral Presentation: “Binding energy determination for the dimerization of protonated nucleic acids with methanol in the gas phase using HPMS”
M. B. Burt, K. R. Eldridge and T. B. McMahon.

2. 2006 Atlantic Theoretical Chemistry Symposium, Antigonish, Nova Scotia, August 11 -13, 2006.

Oral Presentation: “The thermochemistry and structures of heterogeneous proton-bound dimers”
M. B. Burt and T. D. Fridgen.

1. 23rd Annual Trent Conference on Mass Spectrometry, Orillia, Ontario, July 31- August 3, 2006.

Poster Presentation: “Structures and binding energies of proton-bound dimers containing high dipole-moment monomers”
M. B. Burt and T. D. Fridgen.

001311

